# THÈSE POUR OBTENIR LE GRADE DE DOCTEUR DE L'UNIVERSITÉ DE MONTPELLIER

**Spécialité : Électronique**

**École doctorale : Information, Structures, Systèmes**

**Unité de recherche : Institut d'Électronique et des Systèmes – UMR 5214**

**En partenariat international avec Università Degli Studi di Bari Aldo Moro, Italie**

## Long Wavelength QCLs for BTEX and Propane Detection through QEPAS


**Présentée par Kumar KINJALK**
**le 13 Décembre 2023**

**Sous la direction de Alexeï BARANOV**
**et Angelo SAMPAOLO**


**Devant le jury composé de**

| | |
|---|---|
| Roberto LI VOTI, Professeur, Sapienza Università di Roma, Roma, Italy | Président |
| Guilhem ALMUNEAU, Directeur de recherche, LAAS-CNRS, Toulouse, France | Rapporteur |
| Marco GENOVESE, Directeur de recherche, INRIM, Torino, Italy | Membre |
| Anna Maria COCLITE, Maître de conférences, Institute of Solid State Physics, TU Graz, Austria | Membre |
| Alexeï BARANOV, Directeur de recherche, CNRS, IES, Université de Montpellier, France | Directeur de thèse |
| Angelo SAMPAOLO, Maître de conférences, Università degli Studi di Bari Aldo Moro, Italy | Co-directeur de thèse |

UNIVERSITÉ DE MONTPELLIER




**UNIVERSITÀ DEGLI STUDI DI BARI ALDO MORO**

**DIPARTIMENTO INTERATENEO DI FISICA "M. MERLI"**


**Dottorato di ricerca in FISICA – Ciclo XXXVI**

**Settore Scientifico Disciplinare: FIS/01**

# Long Wavelength QCLs for BTEX and Propane Detection through QEPAS


**Dottorando: Kumar KINJALK**

**Supervisori: Dr. Alexeï BARANOV e Dr. Angelo SAMPAOLO**

**Coordinatore: Prof. G. Gonnella**


**ESAME FINALE 2023**

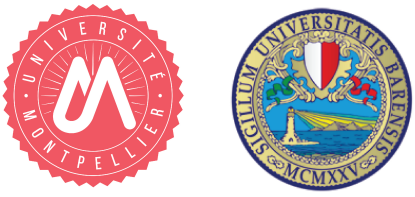

# Long Wavelength QCLs for BTEX and Propane Detection through QEPAS

by

**Kumar Kinjalk**

($13^{th}$ December, 2023)

A thesis presented for the degree of
Doctor of Philosophy

**Université de Montpellier, France**
École doctorale : Information, Structures, Systèmes
Unité de recherche : Institut d'Électronique et des Systèmes

**Università Degli Studi di Bari Aldo Moro, Italy**
Dipartimento Interateneo di Fisica"M. Merlin"
Laboratorio di Ricerca: Polysense

The thesis was prepared in 2020 – 2023 at host: Institut d'Électronique et des Systèmes, Université de Montpellier, France and co-host: Polysense, Università Degli Studi di Bari Aldo Moro, Italy.

The thesis is defended at Università Degli Studi di Bari Aldo Moro, Italy

Supervisor:
**Dr. Alexei N. Baranov** (CNRS/Université de Montpellier)

Co-supervisor:
**Dr. Angelo Sampaolo** (Polysense/Politecnico di Bari)

*To my parents*

# Acknowledgment

Embarking on this thesis journey has been an enlightening odyssey, woven together by the guidance, support, and encouragement of numerous exceptional individuals. I would like to extend my gratitude to each and every one who contributed to this journey. My sincere apologies if I inadvertently missed mentioning your name.

First and foremost, I extend a heartfelt appreciation to Dr. Alexei Baranov, my supervisor. Alex, your unwavering support, continuous sharing of knowledge, and your accessibility despite your busy schedule have been invaluable to me. Thank you for consistently pushing me to excel and for your exceptional patience and understanding throughout.

I'd also like to extend my thanks to my second supervisor, Dr. Angelo Sampaolo, for his priceless insights and willingness to share his expertise. Angelo, I'm grateful to you not only for imparting knowledge but also for being an exceptionally engaging and humorous supervisor, making my experience in Bari incredibly enjoyable and entertaining.

Thanks to Dr. Guilhem Almuneau and Prof. Marco Andrea Marangoni for agreeing to be my reporters. I would also like to thank Dr. Guilhem Almuneau, Dr. Marco Genovese, Prof. Roberto Li Voti and Prof. Anna Maria Coclite for participating in my jury.

A special mention goes to Dr. Michael Bahriz for always being available for discussions, and to Prof. Eric Tournie for your unwavering encouragement and support, whether related to research or administrative tasks.

I owe a particular acknowledgment to Ms. Ariane Meguekam for her patience while guiding me in the clean room. Your teaching style instilled confidence in me and made handling tasks independently a seamless experience. I'm deeply thankful.

I'd like to express my appreciation to the entire Nanomir and Polysense group for being incredible colleagues. A special nod to the Polysense team for their concern about whether I took my lunch—it always brought a smile. Also, heartfelt thanks to the colleagues in the Optaphi consortium; it's been a pleasure working alongside such remarkable individuals.

A heartfelt shout-out to my dear friends Daniel, Jordan, Gabriele, Gautam, and Luigi. Daniel and Jordan, our escapades and shared memories remain unforgettable. The Uber story still is the funniest; we must catch up on those missed tradition nights. Thank you for being a patient ear through personal and professional matters. Gabriele, Gautam, and Luigi, your patience and constant support amid my complaints mean the world. Gabrielle and Gautam, those lengthy calls were a lifeline, and although our time together was brief, it was truly memorable.

My heartfelt thanks also go to my dear friends Abhinav Gautam and Chandraprakash for their belief in me, imparting life lessons, and unwavering support akin to older brothers.

I cannot forget to express my gratitude to Fred, Vero, Marie-Paul, and their entire family for their warmth, hospitality and constant encouragement. Your kindness knows no bounds, and I'm deeply grateful for your generosity. Thank you immensely.

Finally, I'm immensely grateful to my family for their unwavering love and support that has been a rock-solid foundation in my life. Mom, Dad, and every cherished member of our family, your boundless love, sacrifices, and steadfast backing have shaped who I am today. You are my source of strength and the guiding light behind my accomplishments. The constant love from you has been an unceasing well of inspiration, teaching me invaluable lessons in resilience, compassion, and perseverance. My love for all of you transcends mere words.

*This journey wouldn't have been the same without each and every one of you. Thank you from the bottom of my heart for being a part of this incredible experience.*

Kumar Kinjalk

# Contents

**List of Figures** **v**

**List of Tables** **xiii**

**Introduction** **1**

Motivation . . . . . 1
Organization of the Manuscript . . . . . 5
Bibliography . . . . . 7

**1 QCL Design** **9**

1.1 Introduction . . . . . 9
1.2 Quantum Cascade Lasers . . . . . 9
1.2.1 Inception to The State of Art . . . . . 9
1.2.2 Principle of Operation . . . . . 12
1.2.3 Population Inversion . . . . . 15
1.2.4 Intersubband Gain . . . . . 18
1.2.5 InAs/AlSb Material System . . . . . 21
1.2.6 Active Region Design Considerations . . . . . 24
1.3 InAs-based QCLs with Extremely Low Threshold . . . . . 25
1.3.1 Design Evolution . . . . . 25
1.3.2 QCL Modeling . . . . . 29
1.3.3 QCL Waveguide . . . . . 30
1.3.4 Experimental Results and Discussion . . . . . 34
1.4 Conclusion . . . . . 41
Bibliography . . . . . 42

**2 Technology of InAs-based QCLs** **47**

2.1 Introduction . . . . . 47
2.2 QCL Fabrication Process . . . . . 47
2.2.1 Ridge Definition: Wet Etching . . . . . 50
2.2.2 Insulation: Hard-Baked Photoresist . . . . . 51

2.2.3 Metallization . . . 53
2.2.4 Polishing, Lift-off, and Mounting . . . 53
2.3 Characterization of QCLs . . . 55
2.4 Improvement of QCL Technology . . . 56
2.4.1 Issues with Photoresist Insulation . . . 56
2.4.2 Simulation for Alternative Insulation Material . . . 63
2.4.3 $SiO_2$ Insulation using PECVD . . . 71
2.4.4 $SiO_2$ Insulation using Spin-on-Glass . . . 74
2.4.4.1 Spin-on-Glass . . . 74
2.4.4.2 Fabrication Modifications . . . 75
2.4.4.3 Characteristics of QCLs Insulated with $SiO_2$ using SOG . 79
2.5 Conclusion . . . 83
Bibliography . . . 85

**3 DFB QCLs for BTEX and Propane Detection 89**
3.1 Introduction . . . 89
3.2 Distributed Feedback Lasers . . . 90
3.2.1 Working Principle . . . 90
3.2.2 DFB Design Choice . . . 94
3.2.3 Wavelength Tuning . . . 95
3.3 DFB Design Optimization . . . 96
3.4 Fabrication of DFB QCLs . . . 105
3.4.1 Grating Fabrication . . . 105
3.4.2 Experimental Results . . . 108
3.5 Characteristics of DFB QCLs . . . 112
3.6 Conclusion . . . 116
Bibliography . . . 117

**4 Spectroscopic Investigation of BTEX and Propane 119**
4.1 Introduction . . . 119
4.2 Gas Detection Techniques . . . 121
4.2.1 Non-Optical . . . 121
4.2.2 Optical . . . 122
4.3 Photoacoustic Spectroscopy . . . 124
4.4 Quartz Enhanced Photoacoustic Spectroscopy . . . 127
4.4.1 Background . . . 127
4.4.2 Custom Tuning Fork . . . 129
4.4.3 Spectrophone Design . . . 132
4.4.4 Wavelength Modulation . . . 133
4.4.5 Long-term Stability Analysis of QEPAS Sensor . . . 135

4.5 Highly Selective QEPAS Detection of BTEX and Propane . . . . . 137
4.5.1 Experimental Setup . . . . . 137
4.5.2 Sensor Optimization, Calibration and Minimum Detection Limit . . 141
4.5.3 Selectivity Analysis . . . . . 147
4.6 Coupling of Long-Wavelength QCLs with Hollow Core Waveguide . . . . . 152
4.6.1 Theoretical Overview . . . . . 153
4.6.2 Experimental Setup . . . . . 155
4.6.3 Results and Discussion . . . . . 156
4.7 Conclusion . . . . . 161
Bibliography . . . . . 163

**Summary and Future Perspective** **169**

**List of Publications** **175**

# List of Figures


0.1 Normalized absorption spectra of Benzene, Toluene, Ethylbenzene, Xylene, and Propane, along with some atmospheric absorbers and lighter alkanes. . 2

1.1 Statistical summary of QCLs demonstrated in CW and Pulsed mode using different material system. . . . . 12

1.2 (a) Interband and (b) Intersubband transition along with the respective gain profiles. $e_{if}$ is the energy difference between initial and final lasing states. . . . . 13

1.3 Simplified schematic band diagram of a QCL under applied electric field. Each stage of the structure consists of an active region, a extractor and an injection region. . . . . 14

1.4 Schematic of active zone of QCLs showing carrier transitions and the corresponding carrier lifetimes. . . . . 15

1.5 Schematic representation of the active medium geometry. $y$ is the light propagation direction; $z$ is the growth direction. . . . . 18

1.6 The different III–V material systems, as defined by their lattice constants. 22

1.7 Light-Current characteristics of QC like structure based on different material systems. Adapted from [28]. . . . . 23

1.8 Schematic of (Left) Vertical and (Right) Diagonal transition schemes in active region. . . . . 24

1.9 Conduction band profile of the active region of an InAs-based QCL emitting at 19 $\mu$m and moduli squared of the electron wavefunctions. The lasing transition involves red and green energy states. Adapted from [32]. . . . . 26

1.10 Band diagram of the design EQ62 used as a reference for the development of long-wavelength QCLs at nanoMIR group. The lasing transition occurs between the states $e_3$ and $e_2$. . . . . 27

1.11 Schematic presentation of the thermally excited carrier escape from the upper level of the lasing transition. Adapted from [34]. . . . . 28

1.12 Band diagram of the proposed design C1771 calculated using (Top) WECA and (Bottom) Nextnano NEGF software . . . . . 30

1.13 Illustration of the modeled QCL structure. $W_r$ and $W_i$ are the ridge and insulation widths respectively. . . . . 32
1.14 Absorption loss as a function of ridge width for fundamental and first two higher order modes. . . . . 34
1.15 Threshold current density of QCLs measured at RT as a function of ridge width in pulsed (blue, 330 ns × 12 kHz) and CW mode (red). A QCL mounted on the AlN heatsink is shown in the inset. Emission spectra of a 3.6-mm-long laser measured in pulsed mode at 300 K and in the CW regime at 310 K are also shown. . . . . 36
1.16 PIV characteristics of a QCL measured at different temperatures (330 ns × 12 kHz). . . . . 36
1.17 Threshold current density and slope efficiency of large ($d = 16 - 20$ $\mu$m) QCLs as a function of temperature (330 ns × 12 kHz). . . . . 37
1.18 Threshold current density of the large lasers as a function of inverse resonator length. The blue line shows an expected behavior if the waveguide absorption is the only loss inside the laser cavity. . . . . 39
1.19 Material gain spectrum calculated close to the threshold at RT. . . . . 40

2.1 Pictorial representation of the processing steps of InAs-based QCLs insulated with hard-baked photoresist. . . . . 49
2.2 Electron microscopy image of QCL ridge formed using wet etching. . . . . 51
2.3 Electron microscopy images of a QCL ridge after wet etching and citric acid treatment, resulting in the formation of corrugated side walls in the active region. (Left) Complete mesa structure and (Right) zoomed image showing the corrugated side wall. . . . . 51
2.4 Electron microscopy image of fabricated QCL ridge after hard-baked photoresist insulation and metallization. . . . . 52
2.5 Schematic illustrations of (Left) epilayer-up and (Right) epilayer-down mounting configurations of QCLs. . . . . 54
2.6 Illustration of experimental setup for electrical and optical characterization of QCLs in pulsed operation. . . . . 55
2.7 PIV characteristics of FP QCL, insulated with photoresist, in different temperature cycles. The emission wavelength is 14 $\mu$m. . . . . 58
2.8 PIV characteristics of DFB QCL, insulated with photoresist, in different temperature cycles. The emission wavelength is 7.7 $\mu$m. . . . . 59
2.9 Threshold current density as a function of temperature showing the gradual recovery of the original threshold current density over time. . . . . 60
2.10 Emission spectra of DFB QCLs in two temperature cycles and the gradual recovery of the emission wavelength over time. . . . . 61

2.11 Effect of temperature on the state of stress of a photoresist sample. Adapted from [16] . . . 62
2.12 The extinction coefficient of AZ1518 as a function of wavelength. . . . 62
2.13 An optical image of the fabricated QCLs showing surface damage after wire bonding attempts. . . . 63
2.14 Optical leakage factor as a function of insulation width for different insulating materials. . . . 65
2.15 Figure of merit as a function of insulation width for different insulating materials. . . . 66
2.16 Optical loss as a function of insulation width for different insulating materials. 67
2.17 Optical loss as a function of ridge width for different insulating materials with fixed width. . . . 68
2.18 Thermal simulation of a QCL structure with a 14 $\mu$m wide ridge insulated with photoresist in epilayer-down mounting configuration at 293 K. . . . 69
2.19 Thermal resistance of QCLs at 293 K as a function of insulation width for different insulating materials. . . . 71
2.20 Electron microscopy image of fabricated QCL ridge insulated with $SiO_2$ using PECVD. . . . 72
2.21 Comparison of (Left) pulsed PIV characteristics and (Right) threshold current density as a function of ridge width for QCLs insulated with photoresist and $SiO_2$ using PECVD. . . . 73
2.22 Polymeric structure of (Left) Silicate and (Right) Siloxane SOG. R represents organic group. . . . 74
2.23 The SOG film densified using RF plasma treatment exhibits poor adhesion as it peels off during the Scotch Tape Test. . . . 76
2.24 (Left) Discontinuity in single coat SOG film. (Right) No discontinuity in two coat SOG film. . . . 78
2.25 Post-etch electron microscopy image of fabricated QCL ridge insulated with $SiO_2$ using SOG, with a photoresist layer utilized to shield the lateral $SiO_2$ layer during etching. . . . 79
2.26 (Left) Comparison of pulsed PIV characteristics and (Right) threshold current density as a function of ridge width for QCLs insulated with photoresist, $SiO_2$ using PECVD and SOG. . . . 80
2.27 PIV characteristics of FP QCL, insulated with $SiO_2$, in different temperature cycles. The emission wavelength is 14 $\mu$m. . . . 80
2.28 Threshold current density as a function of temperature shows no change in different temperature cycles. . . . 81

2.29 Threshold current density as function of temperature in pulsed and continuous wave operation for QCLs insulated with (Left) Photoresist and (Right) $SiO_2$ using Spin on Glass shows the reduction in thermal resistance in later case. . . . . 82
2.30 An optical image of the fabricated QCLs insulated with $SiO_2$ using spin on glass show successful wire bonding attempts. . . . . 83
2.31 n and k of $SiO_2$ thin film as a function of wavelength [24] . . . . . 83

3.1 A schematic illustration of Bragg resonator showing the reflection occurring at each interface. $n_1$ and $n_2$ are the refractive index of the materials with $n_1 > n_2$. . . . . 91
3.2 (Top Left) Optical band diagram, (Top Right) Spatial response of DFB and (Bottom) Local electric field distribution of two standing waves in a grating with periodic perturbation of refractive index. . . . . 91
3.3 Illustration of (Top Left) Buried index, (Top Right) Lateral surface etched and (Bottom Left) Top surface etched gratings. . . . . 94
3.4 Illustration of simulated DFB QCL structure. . . . . 96
3.5 Electric field distribution of (Left) Semiconductor and (Right) Metal modes in the DFB laser for grating etch dept of 0.65 $\mu$m. . . . . 98
3.6 The wavelength of the modes in the DFB structure as a function of the grating etch depth for two cladding thicknesses. . . . . 99
3.7 The loss experienced by the modes in the DFB structure as a function of grating etch depth for two cladding thicknesses. . . . . 100
3.8 The optical confinement factor of modes in the DFB structure as a function of the etching depth for two cladding thicknesses. . . . . 101
3.9 The figure of merit of modes in the DFB structure as a function of grating etch depth for two cladding thicknesses. . . . . 102
3.10 Schematic diagrams of longitudinal variation of spatial intensity distribution of a DFB with different coupling levels. Adapted from [6] . . . . . 103
3.11 (Left) The coupling coefficient of modes in the DFB structure as a function of the etching depth for two cladding thicknesses. (Right) Surface plasmon mode located at the interface of the Bragg grating and the cladding . . . . 104
3.12 Schematic of an electron-beam lithography machine. . . . . 106
3.13 (Left) appropriately developed and (Right) over developed grating patterns. 108
3.14 Electron microscopy image of gratings etched using ICP. . . . . 108
3.15 (Left) Comparison of position of emission spectra of DFB QCL ($\Lambda$ = 2.12 $\mu$m) with the emission spectra of FP devices at various temperatures in pulsed operation. (Right) comparison of PIV characteristics of DFB and FP QCLs at 300 K in pulsed operation. . . . . 109

3.16 (Left) Emission spectra of DFB QCL ($\Lambda = 2.12$ $\mu$m) and (Right) Comparison of emission wavelengths of FP and DFB QCLs at different temperatures in CW regime. . . . . 110
3.17 (Top Left) CW PIV characteristics, (Top Right) emission wavelength as a function of temperature, (Bottom Left) wavenumber as the function of current at different temperatures accessible by Peltier cooling element and (Bottom Right) emission spectra at 270 K in dB scale showing the SMSR of DFB QCL with $\Lambda = 2.16$ $\mu$m. . . . . 112
3.18 Simulation results for the DFB QCLs operating at 13.71 $\mu$m. (Top Left) Wavelength, (Top Right) loss, (Bottom Left) coupling coefficient as the function of grating depth for two cladding thicknesses. . . . . 114
3.19 (Left) CW PIV characteristics, (Right) wavenumber as the function of current at different temperatures. The laser is suitable for Toluene detection at 13.71 $\mu$m. . . . . 115
3.20 (Left) CW PIV characteristics, (Right) wavenumber as the function of current at different temperatures. The laser is suitable for Benzene detection at 14.85 $\mu$m. . . . . 115
3.21 (Left) CW PIV characteristics, (Right) wavenumber as the function of current. The laser is suitable for Propane detection at 13.36 $\mu$m. . . . . 116

4.1 (Left) Symmetric and (Right) First in-plane flexural antisymmetric mode of a QTF. . . . . 128
4.2 Laser beam focused between the prongs of tuning fork to localize the acoustic wave between the prongs. . . . . 129
4.3 Custom tunning forks. Adapted from [35]. . . . . 130
4.4 QTF with T-shaped prongs where $T_1 = 2$ mm, $T_2 = 1.4$ mm, $L_0 = 2.4$ mm, $L_1 = 7$ mm. Adapted from [35]. . . . . 131
4.5 (Left) On-beam and (Right) Off-beam QEPAS configuration. . . . . 132
4.6 Internal view of the collimated and packaged DFB QCLs. . . . . 137
4.7 (a) PIV characteristics of DFB QCLs operating at $-10$°C, $-5$°C and 3°C for $QCL_T$, $QCL_B$ and $QCL_P$ respectively. (b)–(d) Solid lines represent the simulation of the absorption spectrum for pure Toluene, Benzene, and Propane. The absorption spectra of Toluene and Benzene are extracted from the absorption coefficient spectra of the NIST database, while the Propane spectrum is extracted from the cross-sections spectra of the HITRAN spectroscopic database. The dotted lines indicate the QCL wavelength tuning as a function of injected current. . . . . 138
4.8 The schematic of the QEPAS sensor system employing InAs-base long-wavelength QCL. . . . . 139

4.9 (Left) The electrical characteristics of the QTF showing the resonance frequency and quality factor as a function of pressure. (Right) Resonance profile of the QTF at 760 Torr. . . . . 140
4.10 (Left) Normalized QEPAS signal of Toluene plotted against modulation amplitude at various pressures. (Right) QEPAS spectra of 150 ppm of Toluene at optimal working conditions. . . . . 142
4.11 (Left) Normalized QEPAS signal of Benzene plotted against modulation amplitude at various pressures. (Right) QEPAS spectra of 100 ppm of Benzene at optimal working conditions. . . . . 143
4.12 (Left) Normalized QEPAS signal of Propane plotted against modulation amplitude at various pressures. (Right) QEPAS spectra of 10000 ppm of Propane at optimal working conditions. . . . . 143
4.13 (Left) QEPAS spectra of Toluene depicted as a function of laser current at optimal working conditions for various concentration levels. (Right) Peaks of most intense features plotted against concentration for Toluene . . . . . 145
4.14 (Left) QEPAS spectra of Benzene depicted as a function of laser current at optimal working conditions for various concentration levels. (Right) Peaks of most intense features plotted against concentration for Benzene . . . . . 145
4.15 (Left) QEPAS spectra of Propane depicted as a function of laser current at optimal working conditions for various concentration levels. (Right) Peaks of most intense features plotted against concentration for Propane . . . . . 146
4.16 (a)-(c) Allan-Werle deviation analysis of Toluene, Benzene, and Propane, respectively, demonstrating the minimum detection limit (MDL) as a function of lock-in integration time. . . . . 146
4.17 Left) Comparison of QEPAS spectra obtained for 240 ppm of Benzene and 150 ppm of Ethylbenzene with the spectrum obtained for pure Nitrogen. (Right) Comparison of QEPAS signals for 30 ppm Toluene with two mixtures: 30 ppm of Toluene mixed with 40 ppm Ethylbenzene, and 30 ppm Toluene mixed with 192 ppm of Benzene at 200 Torr and 200 mVpp modulation depth. . . . . 148
4.18 (Left) Comparison of QEPAS spectra obtained for 144 ppm of Toluene with the spectrum obtained for pure Nitrogen. (Right) Comparison of QEPAS signals for 10 ppm Benzene with a mixture of 10 ppm of Benzene and 144 ppm Toluene at 500 Torr and 225 mVpp modulation depth. . . . . 149
4.19 (Left) Comparison of QEPAS spectra obtained for 10000 ppm of Methane and Ethane with the spectrum obtained for pure Nitrogen.(Right) Comparison of QEPAS signal for 500 ppm Propane with two mixtures: 500 ppm of Propane mixed with 9000 ppm Methane, and 500 ppm Propane mixed with 9000 ppm of Ethane at 400 Torr and 325 mVpp modulation depth. . 150

4.20 Transmissivity of uncoated Ge optical window as a function of wavelength. Adapted from [42]. . . . . 151
4.21 Schematic of the experimental setup used to optically couple long-wavelength QCL with the HCW. . . . . 155
4.22 Beam profiles of the $QCL_T$ emitting at 13.71 $\mu$m recorded by positioning the infrared pyro-camera (Top Left) close to the QCL exit, (Top Middle) and (Top Right) close to the exit of the HCW of length 20 cm and 40 cm coupled with lens of focal length 50 mm respectively, (Bottom Left) and (Bottom Right) close to the exit of the HCW of length 20 cm and 40 cm coupled with lens of focal length 75 mm respectively. . . . . 157
4.23 Measured and theoretical total loss as a function of HCW length for coupling lens of different focal lengths. . . . . 160

# List of Tables


1.1 Effective electronic mass in different material systems. . . . . 22
1.2 Refractive index and thicknesses of different layers in the modeled QCL structure. . . . . 33

2.1 Refractive index of dielectrics used as insulating materials. . . . . 64
2.2 Thermal conductivity of different layers and insulating materials. . . . . 70
2.3 Parameters and test results for thermal treatment of SOG samples. . . . . 77

3.1 The refractive indices and the thickness of different layers in the modeled DFB structure. . . . . 97

4.1 Measured beam radius, $W$, and calculated beam waist radius, $w_0$, at the focal plane of the coupling lens having focal length $f$. . . . . 157
4.2 Divergence angles and $M^2$ values for both QCL and HCWs, coupled using lens of focal length $f$. . . . . 159
4.3 Comparison of measured and calculated coupling efficiency. . . . . 160

# Introduction

## Motivation

The detection of trace gases is crucial in a variety of fields, including atmospheric science, environmental monitoring in urban and industrial areas, and life science research applications. The need for accurate detection and quantification of volatile organic compounds (VOCs) has finally gained, during the last decade, the deserved level of attention within the environmental research community due to their high toxicity. Moreover, in medical diagnostics, an increasing number of studies have demonstrated the direct correlation between these VOCs in exhaled breath and certain diseases [1–4]. This correlation paves the way for leveraging VOCs as biomarkers and the development of noninvasive diagnostic tools.

Among all the VOCs, this thesis places particular emphasis on Benzene, Toluene, Ethylbenzene, and Xylene, collectively called BTEX, as well as on Propane. BTEX has been identified as a significant contributor to air pollution and have severe detrimental effects on human health, even in trace concentrations. The International Agency for Research on Cancer (IARC) and the United States Environmental Protection Agency (EPA) have both identified Benzene as a human carcinogen [5] [6]. Neurological, respiratory diseases [7], [8], and fetal development issues have also all been related to long-term exposure to Benzene and other gases in the BTEX family [9]. On the other hand, exposure to low concentrations of Propane is generally considered safe. However, its detection is crucial in safe handling, storage, and usage. In industrial environments, accurate detection of Propane

is critical for preventing leaks, ensuring compliance with safety protocols, and optimizing fuel usage.

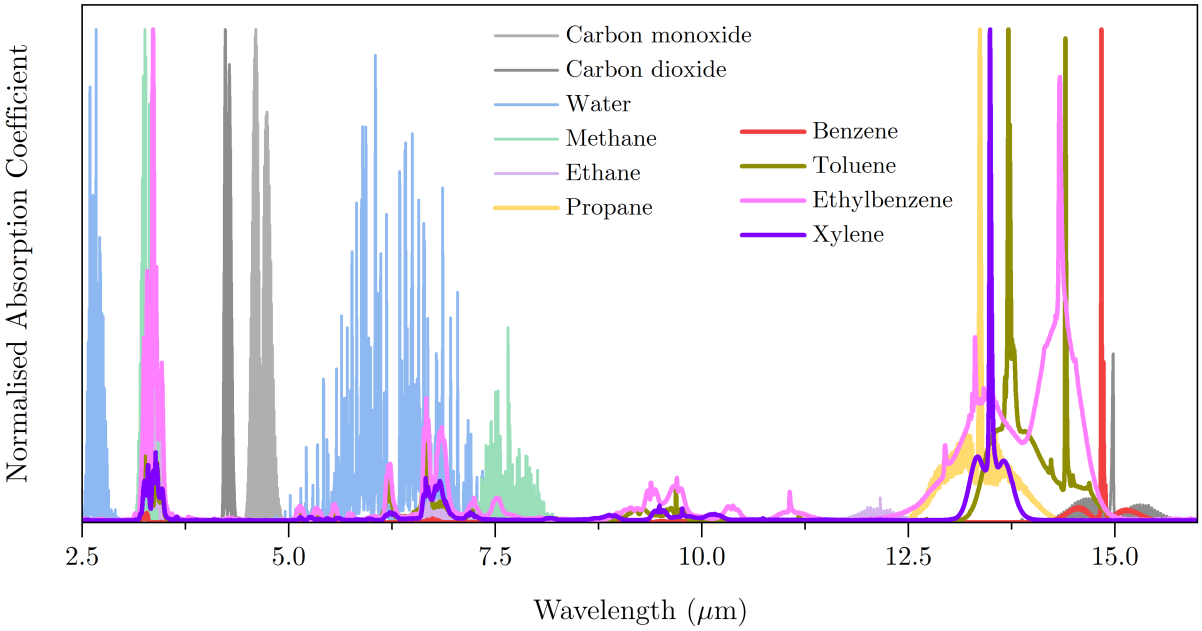


**Figure. 0.1:** Normalized absorption spectra of Benzene, Toluene, Ethylbenzene, Xylene, and Propane, along with some atmospheric absorbers and lighter alkanes.

Considering the widespread production of these VOCs in industrial processes, transportation, and various other areas, their identification and quantification is necessary. Over the years, significant advancements have been made in developing a wide range of sensing techniques specifically designed for the detection of trace gases. These encompass a range of sensor types, such as solid-state [10], catalytic, electrochemical [11], and optical gas sensors, among others.

Among the different sensing techniques, optical/spectroscopic sensors stand out because of their unique characteristics of sensitivity and specificity. Spectroscopic sensors are based on laser absorption: excitation of the molecules from their ground state to excited state through absorption of photons.

Spectroscopic approaches can be divided in two major groups: *i*) direct absorption techniques, in which the residual light is analyzed to evaluate the absorbing species concen-

tration, and *ii*) indirect techniques, where the absorbed radiation determines the variation of other physical quantities that can be measured. All the spectroscopic techniques place a particular emphasis on the mid-infrared (mid-IR) region, often referred to as the "molecular fingerprint" region because it gives access to the fundamental roto-vibrational transitions of many gas species and offers a treasure trove of information about their chemical composition and molecular structure [12]. The fundamental vibrational modes of molecules allow us to discern unique spectral signatures, especially when it comes to complex compounds and structures. For instance, the wavelength range of $12-15$ $\mu$m, is particularly suitable for unambiguous discrimination of specific chemical bonds and functional groups, such as BTEXs. Moreover, with respect to the overtones and other combination bands, absorption coefficients and cross-sections are larger in the $12-15$ $\mu$m range and the spectral separation between compounds represent the optimum starting point for pursuing highly accurate spectroscopy measurements.

Figure 0.1 displays the normalized absorption spectra of BTEX and Propane alongside typical atmospheric absorbers and lighter alkanes like methane and ethane. The data from this figure highlights that the absorption strengths of BTEX and Propane within $12-15$ $\mu$m wavelength range is significantly stronger compared to shorter wavelengths. Furthermore, unlike at shorter wavelengths where the spectral range is plagued with other absorbers, the absorption features in $12-15$ $\mu$m range remain distinct and do not overlap with atmospheric absorbers. This unique characteristic is particularly interesting because it can potentially enable interference-free detection with exceptional sensitivity.

Tunable Laser Diode Absorption Spectrometry (TDLAS) [13] has emerged in the last few decades as one of the most frequently employed spectroscopic techniques. In this approach, the laser diode's wavelength is tuned to scan the absorption line of the targeted gas, and detection relies on quantifying the intensity of light received by the photodiode. TDLAS offers impressive selectivity and sensitivity; nevertheless, its main limitation is that sensitivity is directly linked to the optical path length. Consequently, TDLAS gas sensors tend to be rather bulky. Furthermore, III–V Quantum Well (QW) diode lasers widely utilized in TDLAS are unsuitable for operating within the spectral range of $12-$

15 $\mu$m.

The first issue can be addressed by using relatively newer techniques like Quartz-Enhanced Photoacoustic Spectroscopy (QEPAS) [14], which can be adopted as a point sensing technique. In QEPAS, sensitivity remains unaffected by the optical path length, enabling the design of compact sensing systems. This approach presents additional advantages, including immunity to external noise and eliminating the need for optical detectors. Furthermore, it offers wavelength independence, meaning that various gas species can be detected simply by replacing the laser source once the system is developed. Thanks to this last feature, accessing $12 - 15$ $\mu$m spectral window depends only on the development of suitable emitters capable of effectively probing this spectral range. In fact, this spectroscopic region has remained largely unexplored till now mainly because of the unavailability of laser sources capable to provide optical power at the mW level, ambient temperature operations and low power consumption.

As a result, the need for suitable long-wavelength mid-IR sources has surged in parallel with our increasing awareness of the vast potential inherent in the mid-IR spectral range. Quantum Cascade Lasers (QCLs) present a viable option for accessing this spectral range, as they have demonstrated the capability to cover the entire mid-IR spectrum. Various material systems have been employed in the development of QCLs, with the InP family being the most mature. However, QCLs based on InP have exhibited poor performance within the targeted wavelength range. In particular, InP-based QCLs are not able to operate in the continuous wave (CW) regime close to room temperature, which is required for the most of existing spectroscopic techniques. The solution to this challenge lies in the utilization of InAs-based QCLs. These QCLs, thanks to the low electron effective mass of InAs, yield higher intersubband gain and have consequently been proven to operate in the CW regime at room temperature (RT) in the desired wavelength regime.

This thesis aims to bridge the gap between the demand for accurate BTEX and Propane detection and the limitations imposed by existing technologies. By harnessing the capabilities of long-wavelength InAs-based QCLs and QEPAS, this work endeavors to unlock

new possibilities in the gas sensing scenario, offering a pathway to overcome current challenges and pave the way for enhanced monitoring, improved air quality, and safer industrial practices.

The main goals of the thesis include:

- Design high-performance long-wavelength InAs-based QCLs emitting at $12-15$ $\mu$m.
- Refine the fabrication process to further improve the device performance.
- Fabricate single-frequency QCLs suitable for BTEX and Propane spectroscopy.
- Demonstrate highly selective and sensitive detection of BTEX and Propane through QEPAS.

## Organization of the Manuscript

This manuscript is divided into four chapters:

**Chapter 1** starts by presenting the historical progression of QCLs and their underlying operational principles. Subsequently, it delves into the rationale behind selecting the InAs/AlSb material system. The chapter then addresses various design considerations before delving into the evolution of InAs-based QCL designs, ultimately leading to a comprehensive discussion of the novel design proposed in this work. A concise overview of the QCL waveguide is provided before the chapter concludes by presenting experimental results pertaining to device performance using the proposed design.

**Chapter 2** centers on the processing technology of InAs-based QCLs, shedding light on the challenge related to fluctuations in device performance arising from the commonly utilized photoresist insulation. The origins of these issues are explored. Subsequently, the chapter delves into a comprehensive discussion of an alternative insulating material selection. Upon determining the suitable material, the chapter proceeds to explore techniques for material deposition. It becomes evident in this chapter that conventional deposition methods lead to device degradation and inefficiency when depositing insulating material.

Finally, the chapter introduces a novel insulation technology founded on Spin-on Glass (SOG) to address this concern. The implementation of meticulous process optimization is then explored, demonstrating the achievement of high-performance QCLs while effectively addressing the challenges associated with photoresist insulation.

**Chapter 3** starts with a brief overview of the theoretical background of Distributed Feedback (DFB) lasers, including the various grating designs and the wavelength tuning mechanism. It then provides an in-depth discussion of the simulations to design and optimize the DFB structure in order to achieve single longitudinal mode operation. Finally, it discusses the fabrication technique and characteristics of the fabricated devices suitable for detecting BTEX and Propane.

**Chapter 4** presents the spectroscopic investigation of BTEX and Propane through QEPAS. The chapter starts with a brief overview of the available gas detection techniques, followed by the origin and theoretical background of photoacoustic spectroscopy (PAS) and QEPAS. The chapter then discusses the developed sensing system, followed by a detailed discussion of results obtained for QEPAS of BTEX and Propane, demonstrating high selectivity and sensitivity. Finally, the coupling of long-wavelength QCL with a Hollow Core Waveguide (HCW) is explored by investigating the coupling conditions, beam quality, and losses.

*The design, growth, and fabrication of the QCL devices were carried out at the Institut d'electronique et des systèmes, University of Montpellier, France. The spectroscopic investigation was conducted at the PolySense Lab at the University of Bari Aldo Moro, Italy. This collaborative effort operates under the OPTAPHI consortium, funded by the European Union's Horizon 2020 research and innovation program through the Marie Skłodowska-Curie grant agreement No. 860808.*

# Bibliography


[1] Frank S. Cikach and Raed A. Dweik. Cardiovascular Biomarkers in Exhaled Breath. *Progress in Cardiovascular Diseases*, 55(1):34–43, jul 2012. doi:10.1016/j.pcad.2012.05.005.

[2] Célia Lourenço and Claire Turner. Breath Analysis in Disease Diagnosis: Methodological Considerations and Applications. *Metabolites*, 4(2):465–498, jun 2014. doi:10.3390/metabo4020465.

[3] Anju Sharma, Rajnish Kumar, and Pritish Varadwaj. Smelling the Disease: Diagnostic Potential of Breath Analysis. *Molecular Diagnosis & Therapy*, 27(3):321–347, feb 2023. doi:10.1007/s40291-023-00640-7.

[4] Diana Poli, Paolo Carbognani, Massimo Corradi, Matteo Goldoni, Olga Acampa, Bruno Balbi, Luca Bianchi, Michele Rusca, and Antonio Mutti. Exhaled volatile organic compounds in patients with non-small cell lung cancer: cross sectional and nested short-term follow-up study. *Respiratory Research*, 6(1), jul 2005. doi:10.1186/1465-9921-6-71.

[5] A. Trakoli. IARC Monographs on the Evaluation of Carcinogenic Risks to Humans. Volume 99: Some Aromatic Amines, Organic Dyes, and Related Exposures. International Agency for Research on Cancer. *Occupational Medicine*, 62(3):232–232, apr 2012. doi:10.1093/occmed/kqs011.

[6] United States Environmental Protection Agency. Benzene. URL: https://www.epa.gov/sites/default/files/2016-09/documents/benzene.pdf.

[7] Mark M Greenberg. The Central Nervous System and Exposure to Toluene: A Risk Characterization. *Environmental Research*, 72(1):1–7, jan 1997. doi:10.1006/enrs.1996.3686.

[8] Bian Yu, Zhang Yuan, Zhou Yu, and Feng Xue-song. BTEX in the environment: An update on sources, fate, distribution, pretreatment, analysis, and removal techniques. *Chemical Engineering Journal*, 435:134825, may 2022. doi:10.1016/j.cej.2022.134825.

[9] Abbas Norouzian Baghani, Armin Sorooshian, Maryam Heydari, Razieh Sheikhi, Somayeh Golbaz, Qadir Ashournejad, Majid Kermani, Faranak Golkhorshidi, Abdullah Barkhordari, Ahmad Jonidi Jafari, Mahdieh Delikhoon, and Abbas Shahsavani. A case study of BTEX characteristics and health effects by major point sources of pollution during winter in Iran. *Environmental Pollution*, 247:607–617, apr 2019. doi:10.1016/j.envpol.2019.01.070.

[10] G. Korotcenkov. Metal oxides for solid-state gas sensors: What determines our choice? *Materials Science and Engineering: B*, 139(1):1–23, apr 2007. doi:10.1016/j.mseb.2007.01.044.

[11] František Opekar and Karel Štulík. *Electrochemical Gas Sensors*. Wiley, sep 2009. doi:10.1002/9780470027318.a9074.

[12] Andreas Schwaighofer, Markus Brandstetter, and Bernhard Lendl. Quantum cascade lasers (QCLs) in biomedical spectroscopy. *Chemical Society Reviews*, 46(19):5903–5924, 2017. doi:10.1039/c7cs00403f.

[13] H. I. Schiff, G. I. Mackay, and J. Bechara. The use of tunable diode laser absorption spectroscopy for atmospheric measurements. *Research on Chemical Intermediates*, 20(3-5):525–556, jan 1994. doi:10.1163/156856794x00441.

[14] Pietro Patimisco, Gaetano Scamarcio, Frank Tittel, and Vincenzo Spagnolo. Quartz-Enhanced Photoacoustic Spectroscopy: A Review. *Sensors*, 14(4):6165–6206, mar 2014. doi:10.3390/s140406165.

# Chapter 1

# QCL Design

## 1.1 Introduction

We begin by presenting the historical development of Quantum Cascade Lasers (QCLs) and the fundamental principles governing their operation. We discuss the rationale behind selecting the InAs/AlSb material system. We then explore different design aspects before delving into the InAs-based QCL design evolution, ultimately leading to the proposed novel design, where we study the influence of energy separation between the upper lasing level and the next immediate level. Finally, a concise overview of the QCL waveguide is provided before concluding by discussing experimental results on device performance using the proposed design.

## 1.2 Quantum Cascade Lasers

### 1.2.1 Inception to The State of Art

The fundamental notion of the QCL, the utilization of "intersubband transitions" for radiation amplification in a superlattice structure, was first theorized in 1971 by Kazarinov and Suris [1, 2]. However, it took almost 20 years to bring this idea to life. In 1994, followed by the development of Molecular Beam Epitaxy (MBE), Faist, et al. [3] demon-

strated the first QCL. These devices had modest characteristics: emitting at 4.26 $\mu$m, in pulsed mode, with a maximal operating temperature of 90 K. However, it was a very important milestone in the development of sources of mid-IR radiation.

In 1994, F. Capasso's group made a significant breakthrough by showcasing THz radiation through difference frequency generation, which laid the foundation for THz QCL [4]. Merely a year later, the same team proved that QCLs could operate up to temperatures of 160 K and fine-tuned the active region to achieve lasing within the 8 to 9 $\mu$m range [5]. This pivotal year also witnessed the first continuous wave (CW) QCL operating at cryogenic temperatures, emitting at 8.15 $\mu$m [6]. The following year, in 1996, marked the first demonstration of room temperature pulsed QCL [7].

In the years 1998–2000, this group continued to push the boundaries of QCL technology, achieving emission wavelengths of 11 $\mu$m [8], 17 $\mu$m [9], and 19 $\mu$m [10]. A buried heterostructure [11] to enhance heat dissipation was also introduced. This was a crucial step towards achieving room temperature CW QCL which in 2002, lead to the demonstration of the very first CW QCL operating at room temperature. These devices had a maximum optical output power of approximately 17 mW at 292 K and emission wavelength of 9.1 $\mu$m [12].

The ability of QCLs to function at room temperature invigorated their application in molecular spectroscopy, leading to numerous QCL demonstrations in the long-wavelength spectrum using diverse material systems. A group in Vienna demonstrated QCLs at 15 $\mu$m and 23 $\mu$m [13], Capasso's group grew a 19 $\mu$m QCL using MOCVD [14], Kazuue et al. published devices emitting at 15 $\mu$m [15], Gmachl's group reported one at 14 $\mu$m [16]. In 2014, Faist's group achieved another milestone by demonstrating QCLs emitting at 24.4 $\mu$m [17]. However, despite these advancements, the utilization of long-wavelength QCLs for spectroscopic purposes remained a challenge due to their elevated threshold current density, limited power output, and the prevalent need for cryogenic cooling.

In 2015, nanoMIR group at Institut d'Electronique et des Systèmes within University of Montpellier, France, shattered all the records by demonstrating the ability of the

InAs/AlSb material system to produce a high optical intersubband gain in the far-infrared region even at a higher temperature. They reported QCL emitting at 20 $\mu$m at room temperature, with a low threshold current density of 4.5 kA/cm$^2$ and a maximum operating temperature of 80°C [18]. In 2016, they demonstrated the first InAs/AlSb-based QCLs in CW operation up to 20°C. The laser was emitting at 15 $\mu$m and had significantly lower threshold current density of just 0.730 kA/cm$^2$ at room temperature in pulsed mode [19]. The low threshold current density was a major milestone towards CW operation of long-wavelength QCLs at room temperature.

Again, in 2018, they demonstrated QCLs emitting at 11 $\mu$m with a threshold current density as low as 1 kA/cm$^2$ at room temperature in pulsed mode [20]. They achieved a single-frequency operation of around 11 $\mu$m using distributed feedback architecture and were able to operate in CW up to 295 K. In 2019, they showed InAs/AlSb-based QCLs operating at 25 $\mu$m with a low threshold current density of 1.1 kA/cm$^2$ at 80 K [21]. In the same year, they showed DFB QCL operating in CW and emitting at $>$ 17 $\mu$m [22] and between 10 $\mu$m and 18 $\mu$m [23]. In 2021, they demonstrated Fabry Perot QCls emitting at 18 $\mu$m at 40°C, and up to 21 $\mu$m on Peltier cooler, with threshold current densities below 1 kA/cm$^2$ [24]. These devices were capable of CW operation up to room temperature. The ability to design QCLs operating in CW at room temperature opened up the possibility to exploit long-wavelength mid-IR spectral range for molecular spectroscopy along with many other applications.

Figure 1.1 presents the statistical summary of the QCLs utilizing various material systems and operating modes, spanning over a range of temperatures. Notably, the data reveals that InAs-based QCLs outperform others, particularly excelling in both very short wavelengths and the long-wavelength mid-IR region. In the later sections will discuss basic theoretical background of the QCLs and the factors contributing to the better performance of InAs-based QCLs in the context of long wavelengths.

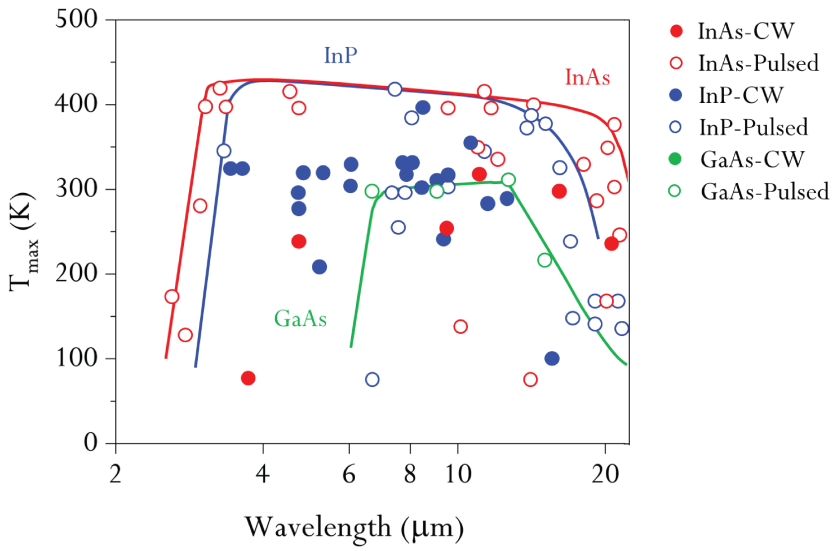


**Figure. 1.1:** Statistical summary of QCLs demonstrated in CW and Pulsed mode using different material system.

### 1.2.2 Principle of Operation

QCLs are fundamentally different from conventional semiconductor diode lasers. While the conventional diode lasers work on the principle of interband transition i.e., the lasing transition occurring between the conduction and the valence band of the semiconductor material, in QCLs, the lasing transitions occur between conduction band energy states (subbands), arising from size quantization within the quantum wells, i.e., intersubband transition [3]. This confers a significant edge to QCLs. In diode lasers, the emission wavelength is primarily dictated by the band gap energy of the active layer material. However, in the case of QCLs, the emission wavelength is contingent on the energy separation between the subbands. This separation can be finely adjusted by varying the thickness of individual structural layers, allowing for precise control over the emitted wavelength.

Additionally, intersubband transition offers several other features. In these transitions processes electrons remain within the conduction band consequently making the device unipolar. The unipolar nature of QCLs results in an increased robustness of the devices because there is no surface recombination. In contrast to interband transitions, for which the joint density of states is constant for energies larger than the transition energy, in-

tersubband transitions have an atomic-like joint density which results in symmetric and narrow gain linewidth [25]. Furthermore, because the initial and final subbands have the same curvature (neglecting nonparabolicity), this linewidth depends only indirectly on the subband populations through collision processes. Simplified illustration of interband and intersubband transitions along with respective gain profiles are shown in Figure 1.2.

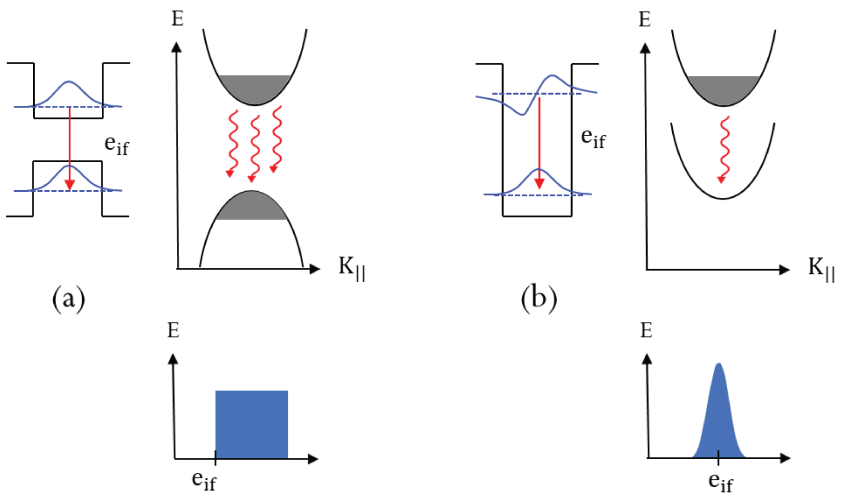


**Figure. 1.2:** (a) Interband and (b) Intersubband transition along with the respective gain profiles. $e_{if}$ is the energy difference between initial and final lasing states.

Historically, QCLs uses a multistage cascade scheme, where electrons are recycled from period to period, contributing each time to the gain and the photon emission. The period is essentially divided into three sections: injector, active, and extractor regions, and is made up of multiple quantum wells and barriers formed by semiconductors with different bandgaps [3, 26]. The Lower bandgap material forms the quantum well while semiconductor with higher bandgap forms barriers. The periodic repetition of wells and barriers is called superlattice. When the superlattice is biased appropriately, it produces a cascading scheme, as shown in Figure 1.3. In a properly designed QCL, the bias voltage sustains resonant states in each period of the structure. The electrons are selectively injected into the upper state $e_3$ by resonant tunnelling from the preceding injection region (blue arrow). Doped regions are added in the injection regions in order to provide electrons required for the QCL operation and to eliminate formation of electric field domains at

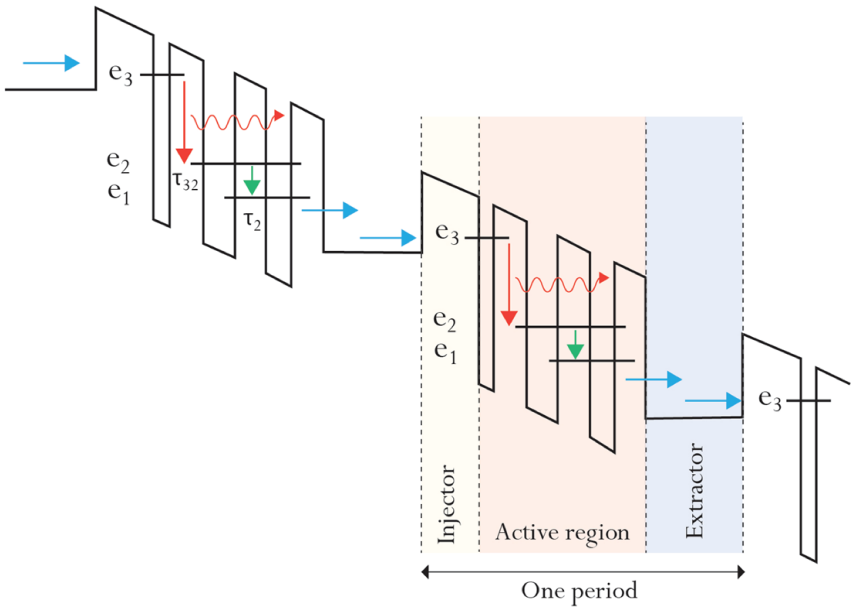


**Figure. 1.3:** Simplified schematic band diagram of a QCL under applied electric field. Each stage of the structure consists of an active region, a extractor and an injection region.

high currents. The radiative transition takes place between $e_3$ and $e_2$ (red arrow) states resulting in the emission of photons. The carriers then quickly scatter to the lower state $e_1$ (green arrow) via a non-radiative transition guaranteed by the resonance between the transition $e_{21}$ and longitudinal optical (LO) phonon of the well material. This process is very efficient and therefore the lifetime of the upper state is controlled by electron-LO phonon scattering, typically of the order of $\sim$ 1 ps. Finally, $e_1$ state is depopulated into the miniband of the consequent superlattice. The miniband allows the electrons to traverse this region before tunnelling through the injection region into the upper state $e_3$ (blue arrow) of the next period. Ideally, this process repeats over the entire length of the structure: essentially a single electron can produce as many photons as there are the periods, providing the internal quantum efficiency of the QCLs greater than 1. This recycling of electrons leads to larger optical output powers.

Having gained basic understanding of electron transport within the QCL superlattice and the process of photon generation, our next focus will be on exploring population inversion and intersubband gain.

### 1.2.3 Population Inversion

A simplified, sub-threshold three-level active region and the electronic transitions associated with it, as shown in Figure 1.4, can be used to derive the conditions for population inversion required for lasing action. In this model, we consider an injector with a single level having a constant population, $n_g$ and aligned with the $e_3$ of the next period. The lasing transition occurs between subband levels $e_3$ and $e_2$.

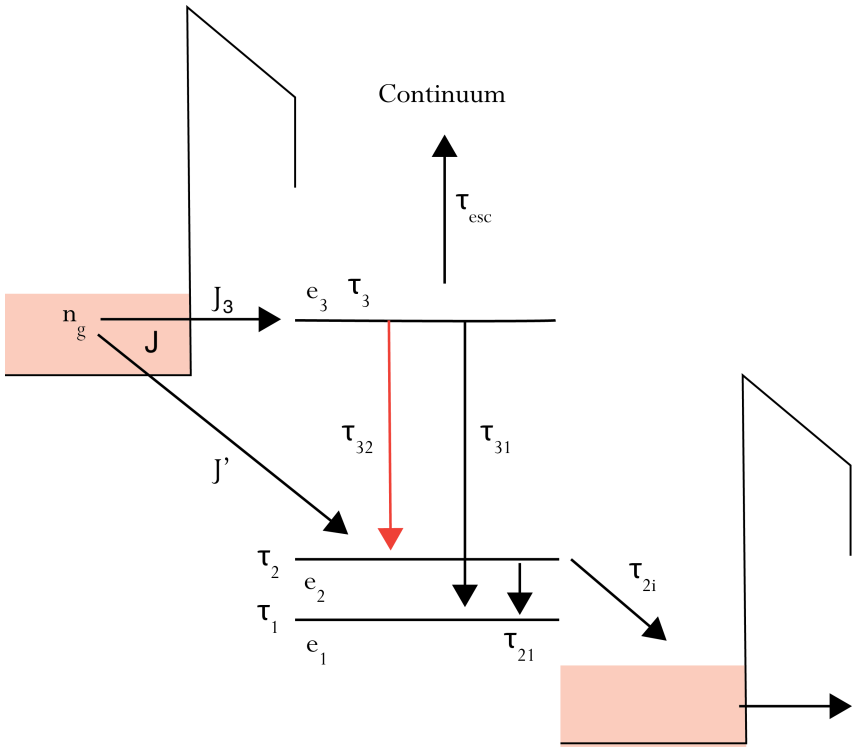


**Figure. 1.4:** Schematic of active zone of QCLs showing carrier transitions and the corresponding carrier lifetimes.

In an ideal scenario, our anticipation is that the total current ($J$) supplied by the injector will be channeled exclusively to $e_3$ in the subsequent period. However, the reality is that there is always a possibility of direct tunneling of electrons from the injection level to the $e_2$ of the next active region. This gives rise to parasitic current ($J^{'}$) and decrease the current being injected to $e_3$, thereby diminishing the extent of the population inversion. The fraction of total current actually being injected to $e_3$ ($J_3$) can be thought in terms of injection efficiency defined as

$$\eta_i = \frac{J_3}{J} \tag{1.1}$$

Additionally, there are several other possible transition pathways for the electrons in $e_3$, each associated with a transition rate $\tau^{-1}$, where, $\tau$ is the lifetime of the electrons in particular levels. Electrons may scatter to $e_2$ followed by a transition to $e_1$ with the rate $\tau_{32}^{-1}$ and $\tau_{21}^{-1}$ respectively, before exiting the active region via resonant tunnelling. They can also transit directly from $e_2$ to the injection level with rate $\tau_{2i}^{-1}$ without transiting to $e_1$. Apart from these paths, there are other nonradiative transitions such as a direct escape of electrons from $e_3$ to the continuum with the rate $\tau_{esc}^{-1}$, and direct transitions from $e_3$ to $e_1$ with the rate $\tau_{31}^{-1}$. These nonradiative processes decrease the QCL efficiency.

Considering all these transition pathways, the rate of change $(dn/dt)$ of population $n_3$ in $e_3$ can be written as

$$\frac{dn_3}{dt} = \frac{J_3}{e} - \frac{n_3}{\tau_{32}} - \frac{n_3}{\tau_{31}} - \frac{n_3}{\tau_{esc}} \tag{1.2}$$

similarly, for $n_2$

$$\frac{dn_2}{dt} = \frac{J^{'}}{e} + \frac{n_3}{\tau_{32}} - \frac{n_2}{\tau_{21}} - \frac{n_2}{\tau_{2i}} \tag{1.3}$$

where, $n_i$ is the electron sheet density of level $i$ and $e$ is the electronic charge. Assuming that there is no change in population of electrons below threshold i.e.,

$$\frac{dn_2}{dt} = \frac{dn_3}{dt} = 0 \tag{1.4}$$

we can write

$$n_3 = \frac{J_3}{e}\left(\frac{1}{\tau_{32}} + \frac{1}{\tau_{31}} + \frac{1}{\tau_{esc}}\right)^{-1} \tag{1.5}$$

$$\frac{n_2}{n_3} = \frac{J^{'}}{en_3}\left(\frac{1}{\tau_{21}} + \frac{1}{\tau_{2i}}\right)^{-1} + \frac{1}{\tau_{32}}\left(\frac{1}{\tau_{21}} + \frac{1}{\tau_{2i}}\right)^{-1} \tag{1.6}$$

From these equations and assuming the parasitic current between injection level and $e_2$, $J^{'}$ is much smaller than the injection current between injection level and $e_3$ of the active zone i.e., $J^{'}/J_3 \rightarrow 0$. We may write,

$$\frac{n_2}{n_3} \approx \frac{1}{\tau_{32}}\left(\frac{1}{\tau_{21}} + \frac{1}{\tau_{2i}}\right)^{-1} \tag{1.7}$$

assuming $\tau_2 = \left(\frac{1}{\tau_{21}} + \frac{1}{\tau_{2i}}\right)^{-1}$ where, $\tau_2$ represents the total time for which electrons populate $e_2$. We obtain a directly proportional relation between the ratios of electron populations $n_3$ and $n_2$ and lifetime of transition between $e_3 \rightarrow e_2$ and $e_2$ i.e.,

$$\frac{n_3}{n_2} \approx \frac{\tau_{32}}{\tau_2} \tag{1.8}$$

From this relation we can see that the population inversion ($n_3/n_2 > 1$) is maintained only when the transition lifetime between $e_3$ and $e_2$ is greater than the lifetime of electrons occupying $e_2$. Now, assuming the rates of electron escaping directly into the continuum and the current injected directly into $e_2$ are negligible i.e., $1/\tau_{esc}$ and $J^{'} \approx 0$ and applying the steady state condition $dn/dt = 0$. We can write

$$n_3 = \frac{J_3}{e}\tau_3 \text{ and } \tau_3 = \left(\frac{1}{\tau_{31}} + \frac{1}{\tau_{32}}\right)^{-1} \tag{1.9}$$

and

$$n_2\left(\frac{\tau_{32}}{\tau_2}\right) = n_3 \tag{1.10}$$

From above equation we get

$$n_3 - n_2 = n_2 \left( \frac{\tau_{32}}{\tau_2} - 1 \right) \tag{1.11}$$

$$n_2 = \frac{\tau_2}{\tau_{32}} \frac{J_3}{e} \tau_3 \tag{1.12}$$

Finally, the population difference between $e_3$ and $e_2$ reads

$$\Delta n = n_3 - n_2 = \frac{\eta_i J}{e} \tau_3 \left( 1 - \frac{\tau_2}{\tau_{32}} \right) \tag{1.13}$$

From this equation we can clearly see that the in order to maximize the difference in population between the upper level $e_3$ and lower level $e_2$, $\tau_3$ should also be maximized.

Moreover, the thermal excitation of electrons from bottom miniband to $e_2$, referred to as thermal backfilling as well as thermally excited electrons form $e_3$ to upper levels can disturb the population inversion. Therefore, the design of the band structure must be optimized to improve $\tau_3$ and reduce the thermal backfilling and excitation of electrons from $e_3$ to upper levels.

### 1.2.4 Intersubband Gain

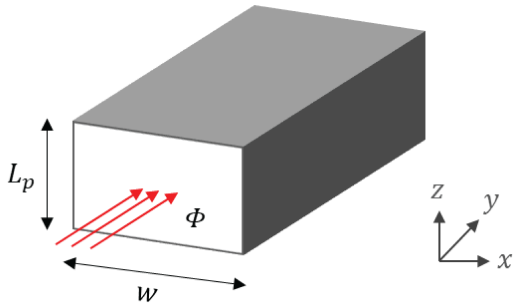


**Figure. 1.5:** Schematic representation of the active medium geometry. $y$ is the light propagation direction; $z$ is the growth direction.

To determine the propagation gain of a QCL active region, one must factor in the device's

geometry as shown in Figure 1.5. Consider an electromagnetic plane wave traveling across a width, $w$, in the plane of a heterostructure. This heterostructure has a thickness of $L_p$ and encompasses a single QC active period, comprising the three levels illustrated in Figure 1.4. The power density, $P$, carried by the plane wave, with an amplitude denoted as $E_0$ and the number of photons of energy $\hbar\omega$ crossing the structure per unit time i.e., photon flux ($\phi$) can be formulated as

$$P = \frac{1}{2}\epsilon_0 n c E_0^2 \tag{1.14}$$

$$\phi = \frac{1}{2}\frac{\epsilon_0 n c E_0^2}{\hbar\omega} w L_p \tag{1.15}$$

Now considering $\hbar\omega = e_{32}$ i.e., maximum stimulated emission rate for transition from $e_3 \rightarrow e_2$, $W_{32}^{max}$, the photon flux variation propagating along $y$ direction in the medium at the distance $dy$ is given by

$$d\phi = W_{32}^{max} n_3 w dy - W_{32}^{max} n_2 w dy \tag{1.16}$$

where $n_i w dy$ is the total number electrons in level $e_i$ $(i = 2, 3)$ in a slice of length $dy$. $W_{32}^{max}$ is represented in terms of transition width, $\gamma$ and dipole matrix element between the two levels $e_3$ and $e_2$, $|\langle z_{32}\rangle|^2$ as

$$W_{32}^{max} = \frac{e^2 E_0^2 |\langle z_{32}\rangle|^2}{2\gamma\hbar} \tag{1.17}$$

The first term in Equation (1.16) corresponds to the stimulated emission of photons due to the presence of electrons in $e_3$, while the second corresponds to the absorption of photons due to the presence of electrons in $e_2$.

The propagation gain (or material gain), $G$, is defined as the variation of the photon flux

divided by the number of photons

$$G = \frac{d\phi/dy}{\phi} \tag{1.18}$$

Hence, using Equations (1.16) to (1.18) one can express the propagation gain

$$G = \frac{2e^2\langle z_{32}\rangle^2\omega}{2\epsilon_0 n c\gamma L_p}(n_3 - n_2) \tag{1.19}$$

With the expression of the population inversion in Equation (1.13) and by using the wavelength $\lambda = 2\pi c/\omega$ (in vacuum) of the propagating light, one finally gets the usual expression of the gain of a QC laser, proportional to the current density

$$G = gJ \tag{1.20}$$

where $g$ is a gain coefficient defined as

$$g = \frac{4\pi e\langle z_{32}\rangle^2}{2\epsilon_0 n\lambda\gamma L_p}\eta_i\tau_3\left(1 - \frac{\tau_2}{\tau_{32}}\right) \tag{1.21}$$

$g$ can also be expressed in terms of oscillator strength ($f_{32}$) of the intersubband transition $e_3 \rightarrow e_2$ and electron effective mass ($m^*$) as follows

$$g = \eta_i\frac{e\hbar}{\epsilon_0 c m^*}\frac{1}{2\gamma n L_p}f_{32}\left(1 - \frac{\tau_2}{\tau_{32}}\right) \tag{1.22}$$

$$f_{32} = \frac{2m^*\omega}{\hbar}\langle z_{32}\rangle^2 \tag{1.23}$$

In a QC laser, normally the guided optical mode extends in the $z$ direction outside of the active region. The gain is then reduced in the proportion of the spatial overlap, $\Gamma$, of the

guided mode with the active zone

$$G = \Gamma g J \tag{1.24}$$

It is important to note that the above gain is for one period of the active zone. If we have an active region of $N_p$ periods having comparable modal overlap $\Gamma_p$ the expression becomes

$$G = \Gamma_p N_p g J \tag{1.25}$$

### 1.2.5 InAs/AlSb Material System

The different III–V materials that have been investigated for QC lasers are presented in Figure 1.6. Among all the possible combinations, the heterostructures that have already been used to realize QCLs are indicated by the dashed red ovals. This thesis however is focused on InAs/AlSb material system. This material system exhibits a large conduction band offset, $\Delta E_c = 2.1$ eV, between InAs and AlSb. Historically, this giant offset was a primary factor that initially prompted the choice of this material system for development of QCLs, allowing the demonstration of the shortest QCL emission wavelength of 2.6 $\mu$m [27].

The effective mass of electron has a direct influence on the transition energy, squared dipole matrix element, $\langle z_{32} \rangle^2$, and the lifetime of the electron in the upper transition state, $\tau_3$. It can be shown that squared dipole matrix element and lifetime is inversely proportional to $m^*$ and $\sqrt{m^*}$ respectively. Therefore, the gain coefficient, $g$, becomes proportional to $(m^*)^{-3/2}$ [28].

$$g \propto \langle z_{32} \rangle^2 \tau_3 \propto (m^*)^{-3/2} \tag{1.26}$$

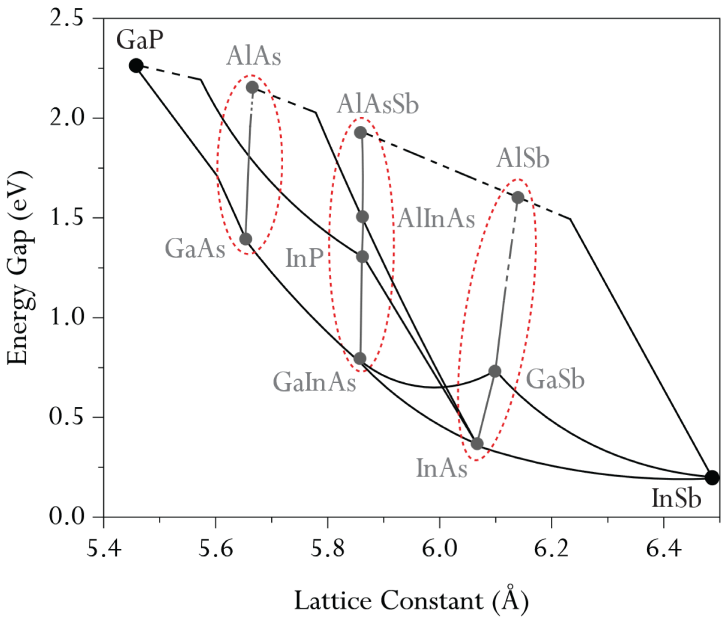


**Figure. 1.6:** The different III–V material systems, as defined by their lattice constants.

| Material (well/barrier) | Substrate | $m^*(m_0)$ |
|---|---|---|
| GaAs/AlGaAs | GaAs | 0.067 |
| InGaAs/AlInAs | InP | 0.043 |
| InGaAs/AlAsSb | InP | 0.043 |
| InAs/AlSb | InAs | 0.023 |

**Table 1.1:** Effective electronic mass in different material systems.

Thus, the smaller effective mass should result in higher intersubband gain. The comparison of electronic effective mass for different materials is presented in Table 1.1. From this table we can see that the InAs/AlSb material system has the least effective electron mass thereby should provide highest gain. The high intersubband gain in this material system is clearly evident from Figure 1.7, presenting the experimental results on the light current characteristics of QC like structure based on different material systems [28] emitting at 10 $\mu$m.

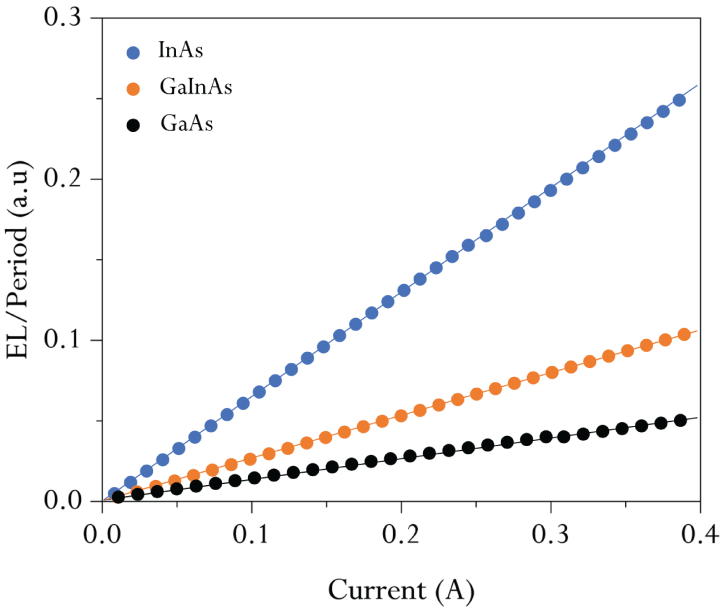


**Figure. 1.7:** Light-Current characteristics of QC like structure based on different material systems. Adapted from [28].

Other advantages of using InAs/AlSb material system is related to the absorption. The absorption bands of phonons in InAs are shifted towards lower energies compared to the InGaAs/InAlAs and GaAs/AlGaAs systems. Unlike these materials, there is no absorption in InAs linked to the combination of two phonons up to a wavelength of 20 $\mu$m [29]. This phenomenon provides access to wavelengths close to the Reststrahlen Band (a frequency zone where light is strongly absorbed by phonons: $30 - 60$ $\mu$m) [30] thus paving the way for even longer wavelength QCLs.

Apart from the advantages, this material system does have some drawbacks . The large conduction band discontinuity between InAs and AlSb becomes an issue in the realm of longer wavelengths. Due to the exponential decay of the squared wavefunction in the barriers, for a given coupling strength the materials with larger conduction band discontinuity, much thinner barriers are needed, in the order of the atomic monolayer [31], which makes the growth complicated and requires great expertise and precision. Another issue with this material system is the low thermal conductivity compared to InP based material system. Nonetheless, InAs/AlSb material system remains an attractive choice

for long-wavelength QCLs.

### 1.2.6 Active Region Design Considerations

Based on the earlier discussions, it's clear that achieving laser emission necessitates meeting several critical prerequisites within the active region's design. The foremost requirement is the establishment of population inversion. To achieve a large population inversion, the design must efficiently inject carriers into the upper excited state of the lasing transition ($e_3$), minimizing carrier escape to the continuum, other non-radiative processes and thermal backfilling of the $e_2$. Furthermore, it's vital to optimize carrier lifetimes in the lasing levels, specifically ensuring a high $\tau_{32}/\tau_2$ ratio. Moreover, the formation of electric field domains at high current must be suppressed by adding appropriately doped regions in injector regions.

Referring to Equation (1.22) within the intersubband gain derivation, we encounter two fundamental parameters that govern the intersubband gain within the active region of QCLs: the electron lifetime in the upper state of the active transition, $\tau_3$, and the oscillator strength, $f_{32}$. It's noteworthy that these two parameters exhibit a reciprocal relationship to each other thus, the design of the active region in QCLs can be tailored to favor one of these parameters. Consequently, two basic design approaches emerge: the"vertical transition scheme" and the"diagonal transition scheme" as shown in Figure 1.8.

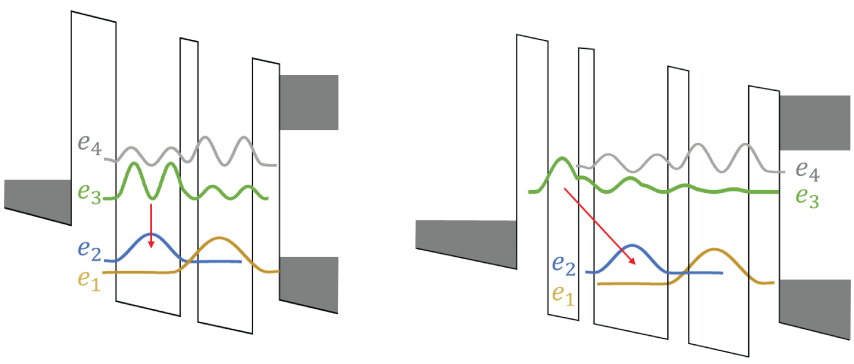


**Figure. 1.8:** Schematic of (Left) Vertical and (Right) Diagonal transition schemes in active region.

In vertical transitions the wave functions in $e_2$ and $e_3$ are mainly localized in the first quantum well while those of $e_1$ and $e_4$ in the second one. The strong spatial overlap of the wave functions in $e_3$ and $e_2$, between which laser transition occurs, allows one to obtain a high value of the oscillator strength, so the transition is strong and contributes to increasing gain. However, this strong spatial overlap also reduces $\tau_{32}$, which contributes to lowering gain. On the other hand, diagonal transition active region is adopted to favor the electron lifetime $\tau_3$ in the state $e_3$. This is achieved by addition of a thin well close to the injection barrier which spatially separates wave functions of the upper state of the laser transition localized in the first thin quantum well from the wave functions of states $e_2$ and $e_1$. Since the wavefunction is resonant across the barrier between these wells, the transition from $e_3$ to $e_2$ state is diagonal. In this case the spatial overlap between the wavefunctions of $e_3$ and $e_2$ is reduced leading to the lower oscillator strength which results in lower gain. However, $\tau_{32}$ is higher which allows for more inversion. Thus, depending on the parameters of the structure the longer lifetimes can allow a higher gain if they compensate the smaller $f_{32}$.

## 1.3 InAs-based QCLs with Extremely Low Threshold

### 1.3.1 Design Evolution

As mentioned in Section 1.2.5, the giant conduction band offset of this material system allowed for demonstration of shortest QCL emission. However, in lasers operating at such wavelengths, the relevant states involved in the lasing transition are located at exceedingly high energy levels, $2-3$ times higher than InAs bandgap [27]. Thus, due to the strong nonparabolicity, the InAs electron effective mass in the upper transition level increases up to $(0.1-0.2)\ m_0$ compared with $0.023\ m_0$ in the bottom of the conduction band. This elevated effective mass adversely impacts the available intersubband optical gain. Conversely, for long-wavelengths, the lasing states are located close to the bottom of conduction band, where nonparabolicity effect becomes negligible leading to low electron effective mass in InAs. Thus, the low effective mass, as we have seen earlier

Equation (1.22) can be effectively leveraged in achieving a high QCL gain. This situation can be illustrated by the band diagram of an InAs-based QCL emitting at 19 $\mu$m as shown in Figure 1.9.

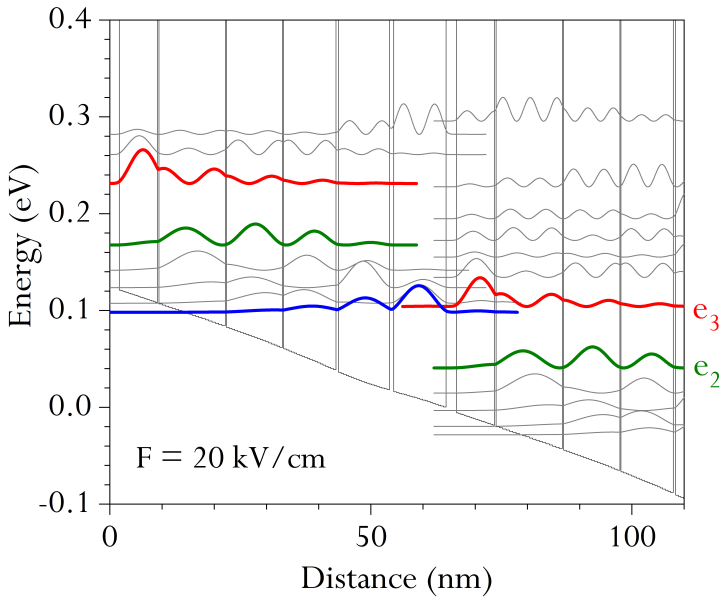


**Figure. 1.9:** Conduction band profile of the active region of an InAs-based QCL emitting at 19 $\mu$m and moduli squared of the electron wavefunctions. The lasing transition involves red and green energy states. Adapted from [32].

The upper state of the lasing transition is situated at only 110 meV from the bottom of the InAs conduction band and the effective mass in this level is just 0.03 $m_0$, which results in an extremely high optical gain [32]. The use of InAs with light electrons resulted in significant performance improvement of long-wavelength QCLs with the first demonstration of semiconductor lasers emitting at room temperature (RT) at 18 $\mu$m in pulsed mode. Further optimization of the laser waveguide and the active region design allowed achieving the first RT CW operation of QCLs at 15 $\mu$m [19]. The vertical transition scheme employed in this work as shown in Figure 1.10 has been used with slight modifications for subsequent developments of long-wavelength QCLs at the nanoMIR group.

This transition scheme, as discussed earlier, provides a large oscillator strength intended to diminish the role of the interface scattering supposed to be essential in the InAs/AlSb

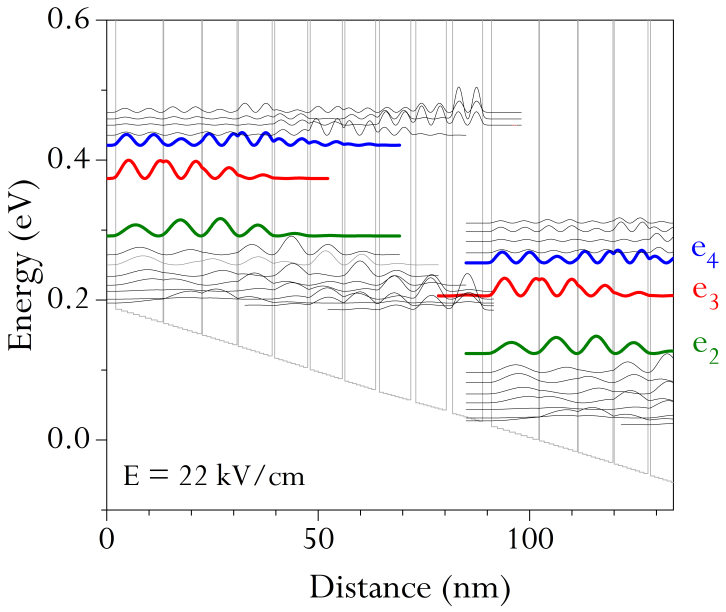


**Figure. 1.10:** Band diagram of the design EQ62 used as a reference for the development of long-wavelength QCLs at nanoMIR group. The lasing transition occurs between the states $e_3$ and $e_2$.

system because of the giant band offset of 2.1 eV and the chemical nature of the interfaces without common atoms [33]. The high oscillator strength, on its own, does not reduce the interface scattering, but does makes its impact less dramatic because of the faster radiative transition. The next upper level in the active region $e_4$ is about 50 meV above the upper transition state $e_3$ state and the width of the injector miniband $\Delta_{inj}$ is 100–105 meV under operating conditions. A drawback of this design is a proximity of the last injector levels and the lower lasing state $e_2$, which can potentially result in a substantial leakage current originated from the direct injection to $e_2$. Another design parameter that can be improved is a relatively small $e_4 - e_3$ distance. The electron concentration in upper transition state decreases because of the thermal excitation to $e_4$ and subsequent scattering to bottom states in the active quantum wells as illustrated in Figure 1.11, resulting in shortening of the lasing transition [34]. In the presence of elastic scattering, such as interface scattering and alloy disordering, the undesired effect of this recombination path becomes stronger, further reducing the lasing efficiency [34]. This mechanism results in a shunt-type leakage current that can significantly affect the QCL operation if the $e_4 - e_3$ distance is small.

Thus, we developed a novel design aimed at reduction of both mentioned types of leakage current.

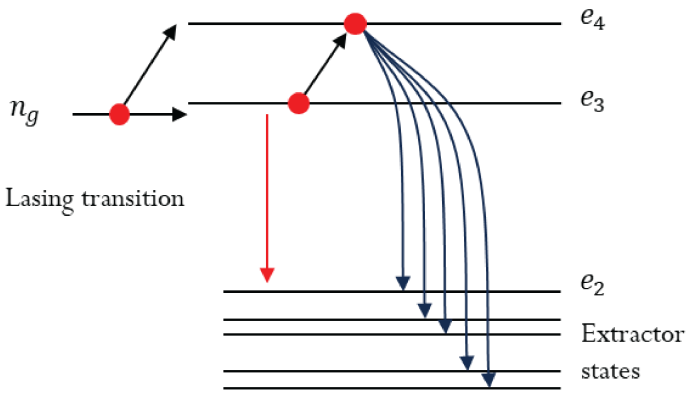


**Figure. 1.11:** Schematic presentation of the thermally excited carrier escape from the upper level of the lasing transition. Adapted from [34].

The vertical design used in previous generation of devices does not have enough flexibility to improve the separation $e_4 - e_3$ because an increase in the distance between the upper transition states is always accompanied by the same effect in the bottom miniband of the structure, which deteriorates electron extraction from the lower transition level $e_2$. In the new structure (C1771) designed to emit near 14 $\mu$m ($e_3 - e_2 = 88$ meV), we added a thin quantum well after the injection barrier, which allowed us to increase the $e_4 - e_3$ separation to 65 meV at a bias corresponding to the expected threshold without significant spreading of the bottom levels. The width of the injector miniband at the threshold was moderately increased to $\Delta_{inj} = 141$ meV from 105 meV. Two quantum wells in the middle of the injector region were doped with Si at $n = 8 \times 10^{16}$ cm$^{-3}$ whereas the thickness of the injection barrier in the new structure was increased from 2.1 to 2.6 nm to weaken the undesired consequences of the higher doping. The larger injector miniband in the employed design, which is partially a consequence of the modification of the $e_4 - e_3$ separation, limits additional thermal backfilling of the $e_2$ level resulting from the increased doping (Figure 1.12). The active zone of the QCL consists of 45 repetitions of the following layer sequence, in $\AA$ and starting from the injection barrier: **26**/41/**1**/62/**1**/67/**2**/66/**2**/64/**6**/64/**6**/62/**6**/59/**9**/58/**10**/57/**11**/56, where AlSb

layers are in bold and the Si-doped layers are underlined. The total electron sheet density $N_s$ in the structure, taking into account residual doping of InAs ($n \sim 5 \times 10^{15}$ cm$^{-3}$, estimated) is considered to be $1 \times 10^{11}$ cm$^{-2}$ per period.

### 1.3.2 QCL Modeling

In this study, QCL modelling was carried out using two simulation tools. The first tool, WECA software, was developed at nanoMIR by Roland Teissier. This interactive software is designed to compute the electronic band structures of semiconductor heterostructures by self-consistently solving the Schrödinger-Poisson equations. Additionally, the software calculates essential parameters related to intersubband transitions, including energies and oscillator strength. It also takes into account properties influenced by optical phonon scattering, tunnelling, and interface roughness. The software's validation was performed through modelling InAs/AlSb QCLs, leveraging the wealth of experimental data available for these devices accumulated at nanoMIR.

The nextnano NEGF software, developed by NEXTNANO company, is designed for simulating electron dynamics in heterostructures, including superlattices and quantum cascade lasers (QCLs). This software is built upon a quantum transport method that adheres to the nonequilibrium Green's function (NEGF) framework. It offers a convenient platform for conducting simulations of electron transport within QCL structures, enabling the calculation of current-voltage characteristics and gain/absorption properties. Furthermore, it facilitates modeling the behavior of QCLs above the threshold. Adjustable parameters of the model were chosen to match basic results obtained using the WECA software, such as energies of the calculated quantum levels, the shape and overlap of electron wavefunctions. The 3–band model for the effective mass was used in the NEGF calculations.

Band energy diagram of a portion of the QCL active region and moduli squared of the relevant electron wavefunctions of the proposed design C1771 are shown in Figure 1.12. The data calculated with both WECA (Figure 1.12, Top) and nextnano NEGF (Figure 1.12, Bottom) software are very close to each other. At this electric field (26 kV/cm)

the energy of the lasing transition $e_3 - e_2$ is 85 and 87.5 meV and its oscillator strength was calculated to be 50.2 and 52 using WECA and NEGF, respectively.

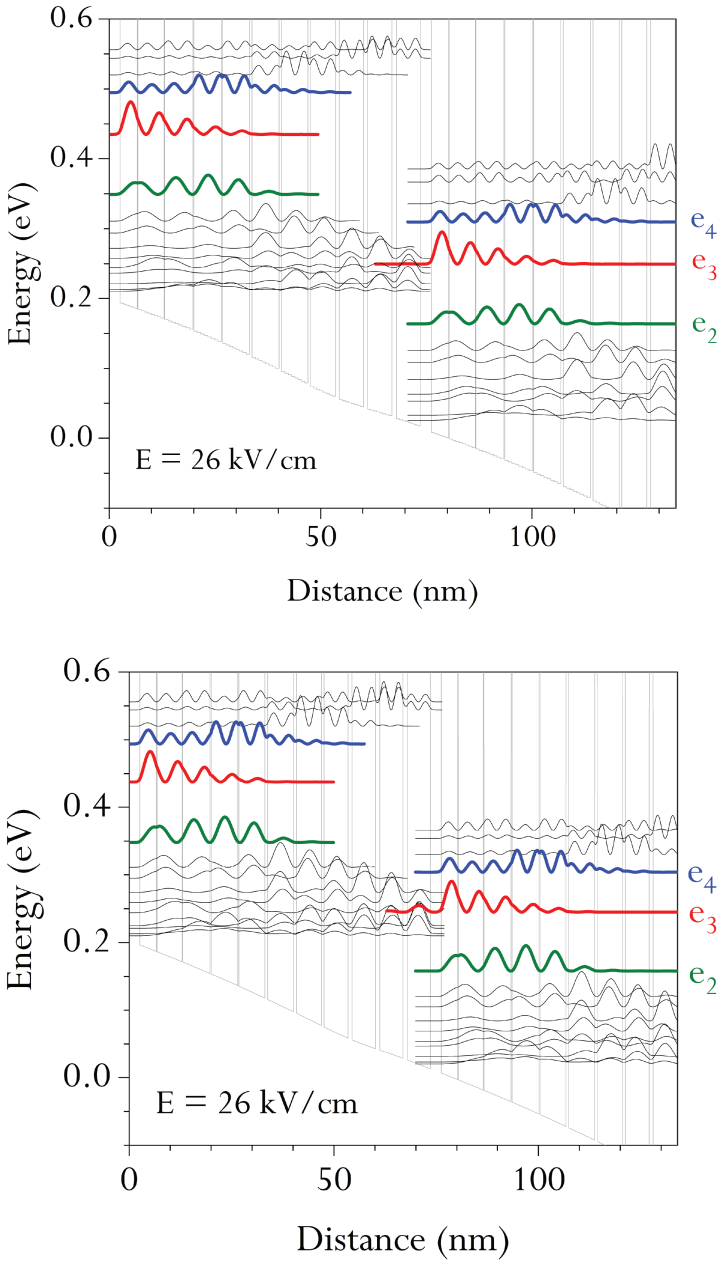


**Figure. 1.12:** Band diagram of the proposed design C1771 calculated using (Top) WECA and (Bottom) Nextnano NEGF software

### 1.3.3 QCL Waveguide

The waveguide serves as the structural foundation for the active region, and its primary purpose is to provide optical confinement. A poorly designed waveguide decreases the

laser performance by increasing the loss, even when the active region itself is functioning optimally. The loss is often due to absorption of the optical mode by various physical phenomena such as: free-carrier absorption, two-phonon absorption, or interband absorption. In the case of a structure emitting in the mid-IR, the most dominant loss arises due to free-carrier absorption. This loss is unavoidable but can be managed.

Using the Drude free electron model, the free carrier loss, $\alpha_{fc}$, can be expressed as [35]:

$$\alpha_{fc} = \frac{e^2 N_d \gamma \omega_p \lambda^2}{4\pi c^3 n_r \epsilon_0 m^*} \tag{1.27}$$

where, $N_d$ is the doping level, $\gamma$ is the damping, $\omega_p$ is the plasma frequency of the material. $n_r$ and $\epsilon_0$ are the low frequency dielectric and real refractive index of the material. From this equation we can see that the free carrier loss increases rapidly with increasing wavelength, $\alpha_{fc} \propto \lambda^2$ and $N_d$. Thus, for a given wavelength, to minimize the loss the doping has to be controlled very precisely.

In InAs-based QCLs the optical confinement is provided by the InAs cladding layers. The index contrast is achieved by heavily doping the cladding layers with Si (to $7 \times 10^{17}$ $\mathrm{cm}^{-3}$ in the proposed design). Such an elevated doping levels will lead to a significant increase in free carrier absorption. Thus, to minimize the loss, undoped InAs spacers are strategically employed to separate the active zone from the cladding layers.

Careful consideration is essential when determining the thickness of these layers. When cladding layers are too thin, there is a risk of optical mode leakage into the metal contact placed on top of the cladding, resulting in elevated losses. Similarly, thin spacers can lead to increased overlap of modes with the absorbing cladding layers. Conversely, if spacers are excessively thick (exceeding 4 $\mu$m), it leads to diminished optical confinement. To attain a low threshold gain, a substantial cladding layer thickness is necessary, as highlighted in [36]. However, it's important to strike a balance, as excessive thickness can elevate thermal resistance, particularly given the low conductivity of InAs. In our proposed QCL design, we opted for 3-$\mu$m-thick spacer and cladding layers.

We employed the finite element method utilizing COMSOL software to evaluate optical confinement factor and loss in the proposed structure. The InAs/AlSb active region of the device has a total thickness of 3.8 $\mu$m. We obtain an effective index of the active zone of 3.37 by taking the weighted average of the various thicknesses of the InAs and AlSb layers. We assume that there are no losses in the spacer layers, i.e., the imaginary part of the refractive index is zero. In the model we assume substrate thickness of 10 $\mu$m. Using the Drude model [37] the complex refractive index of the cladding layer and the substrate is calculated to be $2.89 + i0.009$ [38] and $1.701 + i0.10472$ respectively. The modeled structure is completed with insulation on either side of the QCL ridge, capped by 20 nm of Ti and 400 nm of Au. Figure 1.13 displays a cross-section of the modeled QCL structure, and Table 1.2 presents all the layers and corresponding refractive index and thicknesses.

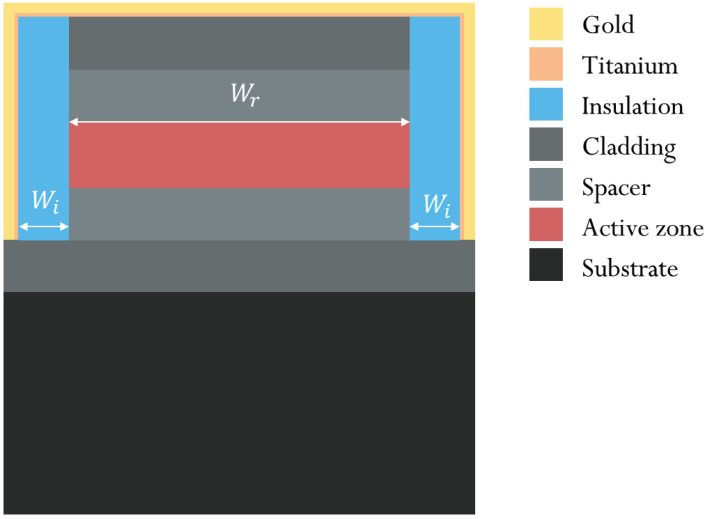


**Figure. 1.13:** Illustration of the modeled QCL structure. $W_r$ and $W_i$ are the ridge and insulation widths respectively.

The loss, $\alpha$, experienced by the modes can be deduced from the imaginary part of the modal frequencies according to the following relationship:

$$\alpha = \frac{4\pi \cdot \mathrm{Img}(\omega) \cdot n_{eff}}{c} \tag{1.28}$$

| Material | Refractive Index | Thickness |
|---|---|---|
| Gold | 22.2+i93.2 [39] | 400 nm |
| Titanium | 27.08+i6.08 [40] | 20 nm |
| Cladding | 2.89+i0.009 [38] | 3 $\mu$m |
| Spacer | 3.4 [41] | 3 $\mu$m |
| Active zone | 3.37 | 3.8 $\mu$m |
| Substrate | 1.701+i0.10472 [36] | 10 $\mu$m |
| Insulation | 1.6+i0.1 [36] | 5 $\mu$m |

**Table 1.2:** Refractive index and thicknesses of different layers in the modeled QCL structure.

Where $\omega$ is the frequency and $n_{eff}$ is the effective index of the mode under consideration. $c$ is the light speed. In addition, we used the ratio of the electric field distribution over the active region ($E_{active}$) to that over the complete waveguide ($E_{total}$) to calculate the confinement factor, $\Gamma$, as shown in the equation below

$$\Gamma = \frac{\int_{active} |E_z|^2 \, dZ}{\int_{total} |E_z|^2 \, dZ} \tag{1.29}$$

Based on this simulation, the overlap of the fundamental mode with the active region, $\Gamma$, and the loss, $\alpha$, for an empty 14-$\mu$m-wide-ridges waveguide were calculated to be 0.5 and 3.6 cm$^{-1}$, respectively.

It's essential to emphasize that the optical power of the laser is constrained by the saturation of gain in the active medium. To enhance the power output, one can enlarge the volume of the active medium, and this expansion can be accomplished through the utilization of a broader waveguide. This however has effect on the modes supported by the waveguide. On the one hand the active zone's small thickness, in relation to the wavelength, ensures single-mode operation in the vertical direction. The supported modes in the lateral direction are determined by the width of the waveguide. A very narrow

waveguide exclusively supports the fundamental mode, whereas a wider waveguide can accommodate higher-order modes. Nevertheless, these modes experience increased loss because the optical field intensity is greater at the lossy insulation/metal sidewall. The increased loss minimizes the spatial mode competition and allows for single transverse mode operation even in wide waveguide. As can be seen from Figure 1.14, displaying the loss characteristics of the fundamental mode and the first two higher-order modes, along with their corresponding mode profiles as a function of ridge width. This becomes especially important while designing single frequency lasers where the waveguide width are comparable to the wavelength.

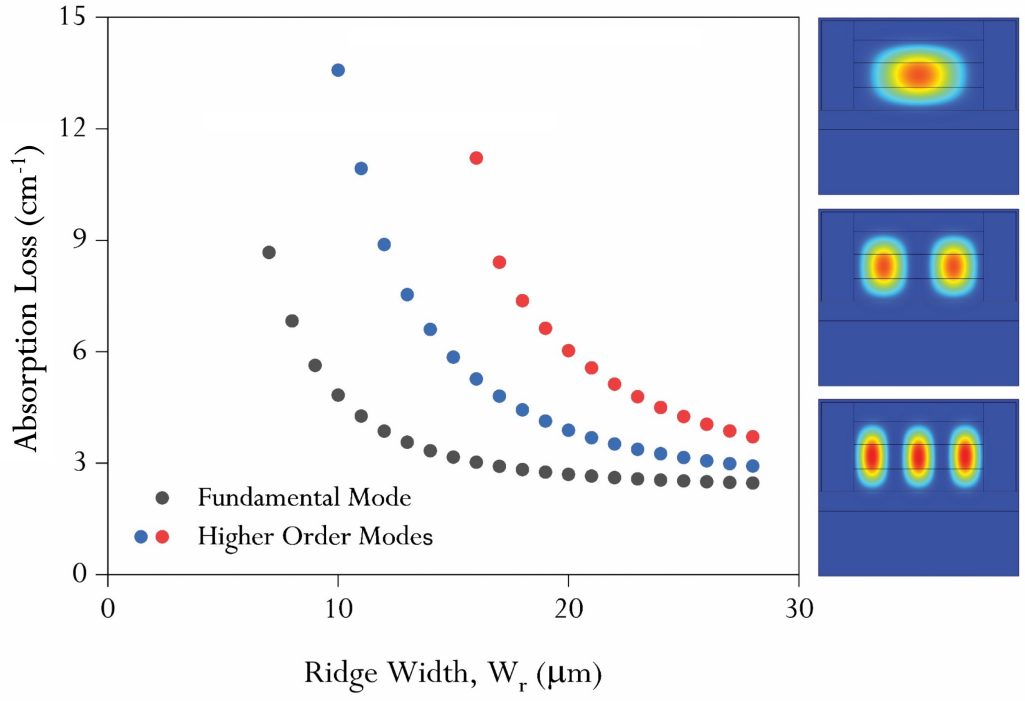


**Figure. 1.14:** Absorption loss as a function of ridge width for fundamental and first two higher order modes.

### 1.3.4 Experimental Results and Discussion

The structure (C1771) was grown by molecular beam epitaxy on an InAs substrate in a RIBER Compact 21 solid source machine equipped with valved cracker cells for the group V elements using growth rates of 0.33 and 0.5 ml/s for AlSb and InAs, respectively, and

then processed into (7-20)-$\mu$m-wide ridge deep mesa devices using standard optical photolithography and wet chemical etching. Hard-baked photoresist was used for electrical insulation. We will discuss the processing steps in detail in Section 2.2.

The QCLs were soldered episide down on Aluminum Nitride (AlN) heatsinks and placed for measurements into a liquid nitrogen flow cryostat. The emission spectra of the lasers were measured using a Bruker V70 infrared Fourier transform spectrometer (FTIR) equipped with a pyroelectric detector. The emitted light was collected with a $f/1$ off-axis parabolic mirror and another $f/1$ off-axis parabolic mirror was employed to collimate the beam for optical power calibrations using a Melles Griot 13PEM001 power meter. Fabricated QCLs with cleaved facets were tested in pulsed mode (330 ns $\times$ 12 kHz). An additional 30 Hz current modulation was applied for pulsed measurements of voltage-current light-current curves (PIV) with the slow FTIR detector. The characterization setup is discussed in further detail in Section 2.3.

The threshold current density, $J_{th}$, of the fabricated laser was lower than in previously reported InAs-based QCLs [19, 22, 42, 43]. In 3.6 mm long devices, it varied from 0.63 to 1.0 kA/cm$^2$ with the ridge width decreasing from 20 to 7 $\mu$m as shown in Figure 1.15. $J_{th}$ of some of these QCLs operated in the CW regime is also shown in this plot as well as the pulsed data for 2.3-mm-long lasers. The best devices operated in CW mode up to $315 - 320$ K. The increase in $J_{th}$ in narrow lasers is due to a larger overlap of the optical mode with absorbing dielectric on the mesa walls [31]. The threshold current density was as low as 0.605 and 0.60 kA/cm$^2$ in 5- and 7.2-mm-long devices, respectively. The emission spectra of the lasers were centered between 14.0 and 14.3 $\mu$m at RT (inset in Figure 1.15), close to the QCL gain peak position expected near the threshold.

Typical PIV characteristics of the devices measured at different temperatures up to 410 K are shown in Figure 1.16. The initial slope efficiency plotted as a function of temperature (Figure 1.17) was also improved compared with the reference design [19] from $80 - 90$ to $90 - 110$ mW/A or by about 20% in 3.6-mm-long lasers despite the smaller number of active stages, 45 instead of 55. The maximum pulsed optical power of 5-mm-long

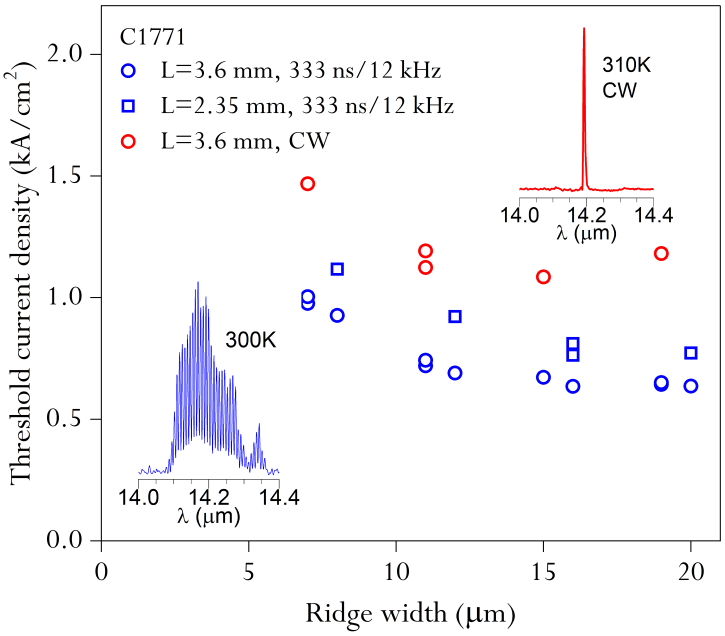


**Figure. 1.15:** Threshold current density of QCLs measured at RT as a function of ridge width in pulsed (blue, 330 ns × 12 kHz) and CW mode (red). A QCL mounted on the AlN heatsink is shown in the inset. Emission spectra of a 3.6-mm-long laser measured in pulsed mode at 300 K and in the CW regime at 310 K are also shown.

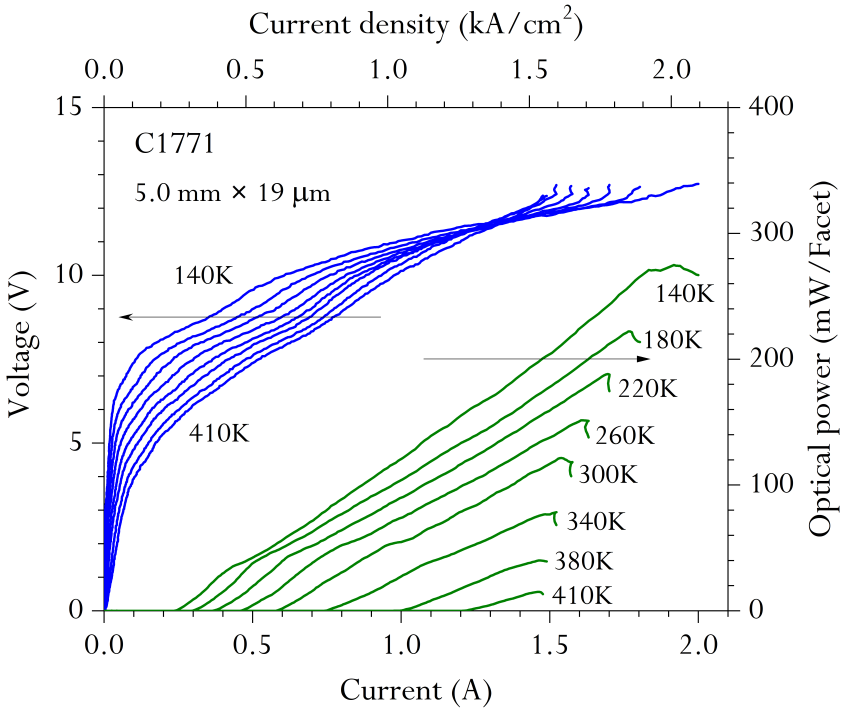


**Figure. 1.16:** PIV characteristics of a QCL measured at different temperatures (330 ns × 12 kHz).

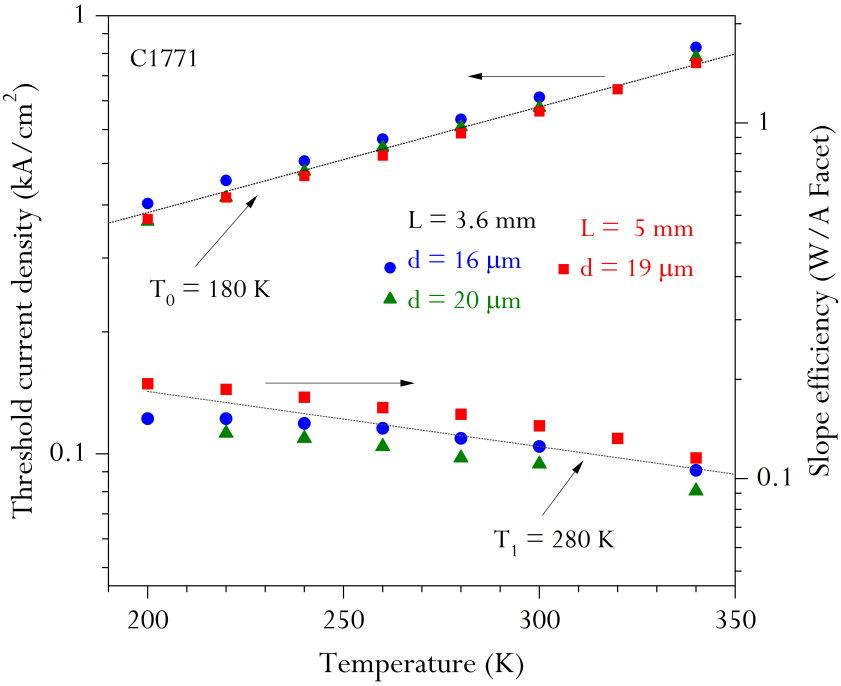


**Figure. 1.17:** Threshold current density and slope efficiency of large ($d = 16 - 20$ $\mu$m) QCLs as a function of temperature (330 ns $\times$ 12 kHz).

lasers reached 120 mW at RT with a slope efficiency of 130 mW/A (Figure 1.16). The characteristic temperature of the threshold current temperature dependence $T_0$ increased up to 180 K from 165 K whereas the $T_1$ value characterizing the reduction of the slope efficiency with temperature increased from 260 to about 280 K in the tested devices (Figure 1.17). The threshold current densities demonstrated in this work are, to the best of our knowledge, the lowest values ever reported for QCLs without facet treatment [44]. The $J_{th}$ values obtained in the present work are $15 - 20\%$ lower than in our InAs-based QCLs of the previous design [19] and the output powers are higher to the same extent.

Direct comparison of these results is complicated because the designs are quite different. The wafers were grown on different machines, and the influence of the growth conditions affecting the interface quality and residual doping is difficult to compare. We can however estimate to what extent the increased $e_3 - e_4$ distance can be responsible for the observed improvements. For further analysis, we can use the general equation for QCL threshold conditions, including the transparency current $J_{tr}$ [45, 46]:

$$J_{th} = J_{tr} + \frac{(\alpha_w + \alpha_m)}{\Gamma g} = J_{leak} + J_{bf} + \frac{\alpha_w}{\Gamma g} - \frac{ln(R)}{\Gamma g}\frac{1}{L} = J_{leak} + J_{bf} + J_0 \tag{1.30}$$

where $J_{leak}$ is the leakage current that can be attributed to parasitic recombination channels involving $e_4$ (the effect of the states above $e_4$ is neglected), $J_{bf}$ is the current corresponding to thermal backfilling of the lower transition level $e_2$ [34], $\alpha_m$ is the mirror loss depending on the laser length $L$. The facet reflectivity $R$ calculated using the Fresnel formula yields $R = 0.29$ for the given dielectric waveguide. Figure 1.18 presents the threshold current density of the studied QCLs as a function of reciprocal resonator length.

With the calculated value of the optical confinement factor $\Gamma = 0.5$, we can find from these data the differential material gain $g$ =46 cm/kA. The interception of the fitted straight line with the $Y$ axis gives a current that is the sum of the threshold current density $J_0$ in the absence of leakage and backfilling and $J_{tr}$. $J_0 = 0.15$ kA/cm$^2$ and $J_{tr} = 0.35$ kA/cm$^2$ can be found from these data using the extracted gain and the calculated waveguide loss $\alpha_m = 3.6$ cm$^{-1}$. These data show that the transparency current is a major contribution to the QCL threshold at RT in long lasers. To estimate the impact of the increased distance $e_3 - e_4$ in the new design on the QCL threshold, we should first calculate $J_{bf}$ , which corresponds to the additional current through $e_3$ required to compensate for a decrease in the population inversion due to electrons thermally excited to $e_2$ from the ground injector states.

$$J_{bf} \approx \frac{qN_s}{\tau_3}\, exp\left(\frac{-\Delta_{inj}}{kT}\right) \tag{1.31}$$

where $q$ is the electron charge, $\tau_3$ is the lifetime in the upper transition level $e_3$ and $kT$ is the thermal energy [47]. Assuming the calculated phonon lifetime $\tau_3 = 0.35$ ps we can obtain an optimistic estimation for $J_{bf} = 0.16$ kA/cm$^2$ and thus $J_{leak} = 0.19$ kA/cm$^2$ in the considered structure. The leakage current is proportional to the electron concentration in $e_4$ which in turn exponentially depends on the $e_3 - e_4$ distance if we neglect the direct tunneling from the upper injector states [45]. The increase of this parameter from 50 to

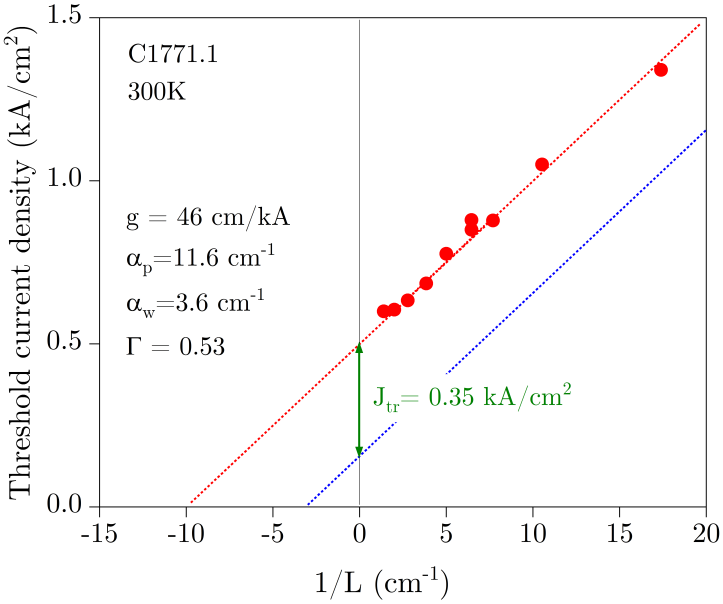


**Figure. 1.18:** Threshold current density of the large lasers as a function of inverse resonator length. The blue line shows an expected behavior if the waveguide absorption is the only loss inside the laser cavity.

65 meV results in 38% reduction of the $e_4$ population and could thus provide a decrease of $J_{leak}$ from 0.31 kA/cm$^2$ to the observed value of 0.19 kA/cm$^2$ at RT. Consequently, the maximum improvement of $J_{th}$ due to the greater separation of the upper transition levels cannot exceed 0.12 kA/cm$^2$ in the studied structure, or 20% calculated as a ratio of $J_0/J_{th}$ at $e_3 - e_4 = 65$ and 50 meV, that is, 0.15 / 0.5 and 0.15 / (0.5 + 0.12). The differential quantum efficiency is proportional to $J_0/J_{th}$ [34], so the maximum increase in output power can also be close to 20%. In presence of the interface recombination or other elastic scattering the thermal backfilling becomes more significant because of the shorter $\tau_3$ and the part of $J_{leak}$ that can be affected by increasing the $e_3 - e_4$ distance correspondingly drops.

To summarize, the expansion of the $e_3 - e_4$ separation in the new design is certainly useful for the device operation but cannot provide a considerable performance improvement. It should be noted that in long-wavelength QCLs this distance approaches the lasing transition energy and its further increase can result in absorption of the laser emission, which is illustrated in Figure 1.19 displaying the gain spectrum of the studied QCL

structure calculated using Nextnano NEGF software close to threshold. It is worth noting that $\Delta_{inj}$ increases with electric field, which will result in weaker backfilling in short lasers. Since $J_{bf}$ is the main component of threshold the $J_{th}(1/L)$ dependence should not be strictly linear. The data for long QCLs are more reliable to extract the differential gain.

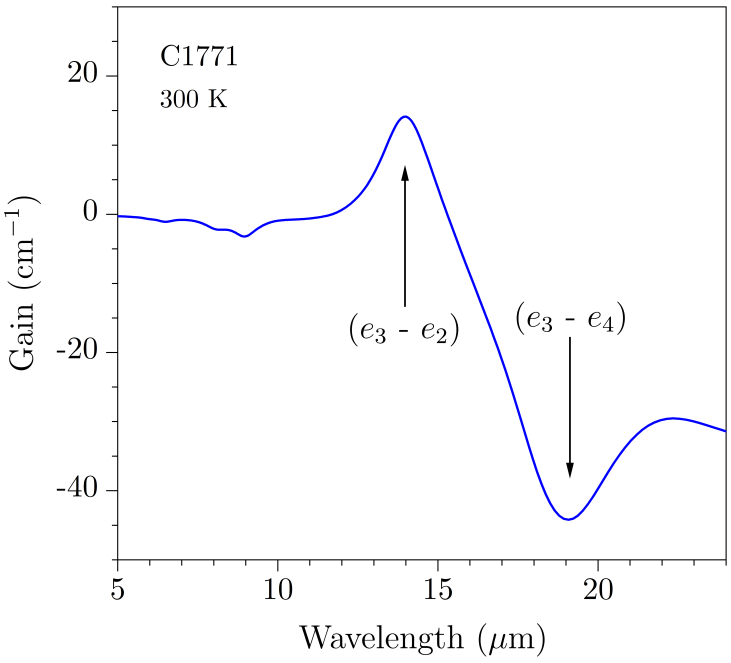


**Figure. 1.19:** Material gain spectrum calculated close to the threshold at RT.

For further performance improvement, it is necessary to reduce the thermal backfilling, Equation (1.31). The injector miniband is already large in the employed design, which can penalize continuous-wave operation because of the increased operating voltage. The doping level can be perhaps optimized in combination with the injection barrier thickness. The most important parameter responsible for the QCL performance is the electron lifetime in the upper transition level. An increased diagonality can be helpful to reduce the parasitic current associated with thermal backfilling. Note that the influence of interface scattering on performance of the InAs-based QCLs is very strong because of the extremely high barriers in the InAs-based QCLs and the chemical nature of the InAs/AlSb interfaces, which limits the advantages of diagonal schemes. Novel designs

with lower barriers in the active quantum wells can be considered to moderate the effect of interface scattering.

## 1.4 Conclusion

In this chapter we discussed the historical development and the working principle of the QCLs followed by derivation of population inversion and intersubband gain. We then present the reason for choosing the InAs/AlSb based material system. Finally we demonstrated InAs-based QCLs emitting at 14.2 $\mu$m with an extremely low threshold current density of 0.6 kA/cm$^2$ at 300 K, which is the best reported result for any QCL without facet treatment. The temperature stability of the threshold current and of the slope efficiency were improved with the corresponding characteristic temperatures $T_0 = 180$ K and $T_1 = 280$ K compared with previously reported long-wavelength InAs-based QCLs. The performance improvement obtained can be partially explained by the increased separation up to 65 meV of the upper transition level and the next one in the new design. We did not consider the population of $e_2$ and $e_4$ due to direct tunneling from the injector, but this parasitic mechanism should be weaker in the used design due to the thicker injection barrier. Optimization of the QCL design aimed at the increase of the lifetime in the upper transition level is necessary for further performance improvement.

# Bibliography


[1] R. Kazarinov and R. Suris. Possible amplification of electromagnetic waves in a semiconductor with a superlattice. *Soviet Physics—Semiconductors*, 4:707–709, 1971.

[2] R Kazarinov and R Suris. Electric and electromagnetic properties of semiconductors with a superlattice. *Soviet Physics Semiconductors*, 6:120–131, 1972.

[3] J. Faist, F. Capasso, D. L. Sivco, C. Sirtori, A. L. Hutchinson, and A. Y. Cho. Quantum Cascade Laser. *Science*, 264, 4 1994. doi:10.1126/science.264.5158.553.

[4] C. Sirtori, F. Capasso, J. Faist, L. N. Pfeiffer, and K. W. West. Far-infrared generation by doubly resonant difference frequency mixing in a coupled quantum well two-dimensional electron gas system. *Applied Physics Letters*, 65, 7 1994. doi:10.1063/1.112328.

[5] C. Sirtori, J. Faist, F. Capasso, A.L. Hutchinson, D.L. Sivco, and A.Y. Cho. Quantum cascade lasers in the $8-9$ $\mu m$ wavelength region. *LEOS '95. IEEE Lasers and Electro-Optics Society 1995 Annual Meeting. 8th Annual Meeting. Conference Proceedings.* doi:10.1109/LEOS.1995.484645.

[6] C. Sirtori, J. Faist, F. Capasso, A. L. Hutchinson, D. L. Sivco, and A. Y. Cho. Continuous Wave Operation of Quantum Cascade Lasers at $8.15\mu m$. *Conference on Lasers and Electro-Optics*, page CPD25, 1995.

[7] J. Faist, F. Capasso, C. Sirtori, D.L. Sivco, A.L. Hutchinson, and A.Y. Cho. Room temperature mid-infrared quantum cascade lasers. *Electronics Letters*, 32, 1996. doi:10.1049/el:19960395.

[8] Gaetano Scamarcio, Claire Gmachl, Federico Capasso, Alessandro Tredicucci, Albert L Hutchinson, Deborah L Sivco, and Alfred Y Cho. Long-wavelength interminiband Fabry-Pérot and distributed feedback quantum cascade lasers. *Semiconductor Science and Technology*, 13, 11 1998. doi:10.1088/0268-1242/13/11/019.

[9] Alessandro Tredicucci, Claire Gmachl, Federico Capasso, Deborah L. Sivco, Albert L. Hutchinson, and Alfred Y. Cho. Long wavelength superlattice quantum cascade lasers at $\lambda \approx 17$ $\mu m$. *Applied Physics Letters*, 74, 2 1999. doi:10.1063/1.123026.

[10] Alessandro Tredicucci, Claire Gmachl, Michael C. Wanke, Federico Capasso, Albert L. Hutchinson, Deborah L. Sivco, Sung-Nee G. Chu, and Alfred Y. Cho. Surface plasmon quantum cascade lasers at $\lambda \sim 19$ $\mu m$. *Applied Physics Letters*, 77, 10 2000. doi:10.1063/1.1316768.

[11] Mattias Beck, Jerome Faist, Claire F. Gmachl, Federico Capasso, Deborah L. Sivco, James N. Baillargeon, and Alfred Y. Cho. Buried heterostructure quantum cascade lasers. page 231, 4 1998. doi:10.1117/12.304449.

[12] M. Beck. Continuous Wave Operation of a Mid-Infrared Semiconductor Laser at Room Temperature. *Science*, 295, 1 2002. doi:10.1126/science.1066408.

[13] Jochen Ulrich, Johann Kreuter, Werner Schrenk, Gottfried Strasser, and Karl Unterrainer. Long wavelength (15 *and* 23 $\mu m$) GaAs/AlGaAs quantum cascade lasers. *Applied Physics Letters*, 80:3691–3693, 5 2002. doi:10.1063/1.1481236.

[14] J.A. Fan, M.A. Belkin, M. Troccoli, S. Corzine, D. Bour, G. Hofler, and F. Capasso. Double-metal waveguide $\approx 19$ $\mu m$ quantum cascade lasers grown by metal organic vapour phase epitaxy. *Electronics Letters*, 43:1284, 2007. doi:10.1049/el:20079450.

[15] Kazuue Fujita, Masamichi Yamanishi, Tadataka Edamura, Atsushi Sugiyama, and Shinichi Furuta. Extremely high T-values ($\sim 450$ $K$) of long-wavelength ($\sim 15$ $\mu m$), low-threshold-current-density quantum-cascade lasers based on the indirect pump scheme. *Applied Physics Letters*, 97, 11 2010. doi:10.1063/1.3518487.

[16] Xue Huang, William O. Charles, and Claire Gmachl. Temperature-insensitive long-wavelength ($\lambda \approx 14 \mu m$) Quantum Cascade lasers with low threshold. *Optics Express*, 19:8297, 4 2011. doi:10.1364/OE.19.008297.

[17] K. Ohtani, M. Beck, and J. Faist. Double metal waveguide InGaAs/AlInAs quantum cascade lasers emitting at 24 $\mu m$. *Applied Physics Letters*, 105, 9 2014. doi:10.1063/1.4896542.

[18] M. Bahriz, G. Lollia, A.N. Baranov, and R. Teissier. High temperature operation of far infrared ($\lambda \approx 20$ $\mu m$) InAs/AlSb quantum cascade lasers with dielectric waveguide. *Optics Express*, 23, 1 2015. doi:10.1364/OE.23.001523.

[19] Alexei N. Baranov, Michael Bahriz, and Roland Teissier. Room temperature continuous wave operation of InAs-based quantum cascade lasers at 15 $\mu m$. *Optics Express*, 24, 8 2016. doi:10.1364/OE.24.018799.

[20] Z. Loghmari, M. Bahriz, D. Díaz Thomas, A. Meguekam, H. Nguyen Van, R. Teissier, and A.N. Baranov. Room temperature continuous wave operation of InAs/AlSb-based quantum cascade laser at $\lambda \sim 11$ $\mu m$. *Electronics Letters*, 54, 8 2018. doi:10.1049/el.2018.5258.

[21] Z. Loghmari, M. Bahriz, A. Meguekam, R. Teissier, and A.N. Baranov. InAs-based quantum cascade lasers emitting close to $25 \mu m$. *Electronics Letters*, 55, 2 2019. doi:10.1049/el.2018.6413.

[22] Hoang Nguyen Van, Zeineb Loghmari, Hadrien Philip, Michael Bahriz, Alexei Baranov, and Roland Teissier. Long Wavelength ($\lambda > 17$ $\mu m$) Distributed Feedback Quantum Cascade Lasers Operating in a Continuous Wave at Room Temperature. *Photonics*, 6, 3 2019. doi:10.3390/photonics6010031.

[23] F. Barho, H. Philip, Z. Loghmari, M. Bahriz, A. N. Baranov, and R. Teissier. Long wavelength ($\lambda = 10 - 18$ $\mu m$) mid-IR quantum cascade lasers operating in a continuous wave at room temperature. *2019 44th International Conference on Infrared, Millimeter, and Terahertz Waves (IRMMW-THz)*, 9 2019. doi:10.1109/IRMMW-THz.2019.8874040.

[24] Zeineb Loghmari, Hadrien Philip, Michaël Bahriz, Alexei N. Baranov, and Roland Teissier. Long wavelength ($\lambda = 10 - 20$ $\mu m$) mid-IR quantum cascade lasers for

spectroscopy applications. *Novel In-Plane Semiconductor Lasers XX*, 3 2021. doi:10.1117/12.2583140.

[25] A. Wittmann, Y. Bonetti, J. Faist, E. Gini, and M. Giovannini. Intersubband linewidths in quantum cascade laser designs. *Applied Physics Letters*, 93, 10 2008. doi:10.1063/1.2993212.

[26] So Edeagu. Mid-Infrared Quantum Cascade Lasers. *Nigerian Journal of Technology*, 31:227–232, 2012.

[27] O. Cathabard, R. Teissier, J. Devenson, J. C. Moreno, and A. N. Baranov. Quantum cascade lasers emitting near 2.6 $\mu m$. *Applied Physics Letters*, 96, 4 2010. doi:10.1063/1.3385778.

[28] E. Benveniste, A. Vasanelli, A. Delteil, J. Devenson, R. Teissier, A. Baranov, A. M. Andrews, G. Strasser, I. Sagnes, and C. Sirtori. Influence of the material parameters on quantum cascade devices. *Applied Physics Letters*, 93, 9 2008. doi:10.1063/1.2991447.

[29] E. S. Koteles and W. R. Datars. Two-phonon absorption in InSb, InAs, and GaAs. *Canadian Journal of Physics*, 54:1676–1682, 8 1976. doi:10.1139/p76-199.

[30] WH STREYER. Reststrahlen band optics for the advancement of far-infrared optical architecture, 2016. URL: http://hdl.handle.net/2142/95367.

[31] Alexei N. Baranov and Roland Teissier. Quantum Cascade Lasers in the InAs/AlSb Material System. *IEEE Journal of Selected Topics in Quantum Electronics*, 21:85–96, 11 2015. doi:10.1109/JSTQE.2015.2426412.

[32] D. Chastanet, G. Lollia, A. Bousseksou, M. Bahriz, P. Laffaille, A. N. Baranov, F. Julien, R. Colombelli, and R. Teissier. Long-infrared InAs-based quantum cascade lasers operating at 291 K ($\lambda = 19\ \mu m$) with metal-metal resonators. *Applied Physics Letters*, 104:021106, 1 2014. doi:10.1063/1.4861465.

[33] P. Laffaille, J. C. Moreno, R. Teissier, M. Bahriz, and A. N. Baranov. High temperature operation of short wavelength InAs-based quantum cascade lasers. *AIP Advances*, 2:022119, 6 2012. doi:10.1063/1.4714363.

[34] Dan Botez, Chun-Chieh Chang, and Luke J Mawst. Temperature sensitivity of the electro-optical characteristics for mid-infrared ($\lambda = 3 - 16\ \mu m$)−emitting quantum cascade lasers. *Journal of Physics D: Applied Physics*, 49:043001, 2 2016. doi:10.1088/0022-3727/49/4/043001.

[35] Paul Harrison and Alex Valavanis. *Quantum Wells, Wires and Dots*. Wiley, 5 2016. doi:10.1002/9781118923337.

[36] Zeineb Loghmar. Lasers à cascades quantiques InAs/AlSb au-delà de 10 $\mu m$ : Emission mono-fréquence et génération du THz par différence de fréquences, 2019.

[37] Neil W. Ashcroft and N. David Mermin. *Solid State Physics*. Holt, Rinehart and Winston, 1976, 33 edition, 1976.

[38] Olivier Cathabard. Lasers à cascade quantique InAs/AlSb : amélioration des performances et fonctionnement monofréquence, 2009.

[39] Mark A. Ordal, Robert J. Bell, Ralph W. Alexander, Larry L. Long, and Marvin R. Querry. Optical properties of Au, Ni, and Pb at submillimeter wavelengths. *Applied Optics*, 26:744, 2 1987. doi:10.1364/AO.26.000744.

[40] Mark A. Ordal, Robert J. Bell, Ralph W. Alexander, Lawrence A. Newquist, and Marvin R. Querry. Optical properties of Al, Fe, Ti, Ta, W, and Mo at submillimeter wavelengths. *Applied Optics*, 27:1203, 3 1988. doi:10.1364/AO.27.001203.

[41] Physico-Technical Institute. IOFFE. URL: http://www.ioffe.ru/SVA/NSM/nk/index.html.

[42] Hoang Nguyen-Van, Alexei N. Baranov, Zeineb Loghmari, Laurent Cerutti, Jean-Baptiste Rodriguez, Julie Tournet, Gregoire Narcy, Guilhem Boissier, Gilles Patriarche, Michael Bahriz, Eric Tournié, and Roland Teissier. Quantum cascade lasers grown on silicon. *Scientific Reports*, 8:7206, 5 2018. doi:10.1038/s41598-018-24723-2.

[43] Z. Loghmari, J.-B. Rodriguez, A. N. Baranov, M. Rio-Calvo, L. Cerutti, A. Meguekam, M. Bahriz, R. Teissier, and E. Tournié. InAs-based quantum cascade lasers grown on on-axis (001) silicon substrate. *APL Photonics*, 5:041302, 4 2020. doi:10.1063/5.0002376.

[44] Fang-Liang Yan, Jin-Chuan Zhang, Dan-Yang Yao, Feng-Qi Liu, Li-Jun Wang, Jun-Qi Liu, and Zhan-Guo Wang. Very low threshold operation of quantum cascade lasers. *Chinese Physics B*, 24:024212, 2 2015. doi:10.1088/1674-1056/24/2/024212.

[45] S. Slivken, A. Evans, W. Zhang, and M. Razeghi. High-power, continuous-operation intersubband laser for wavelengths greater than 10 $\mu m$. *Applied Physics Letters*, 90, 4 2007. doi:10.1063/1.2722190.

[46] Luke J. Mawst and Dan Botez. High-Power Mid-Infrared ($\lambda \sim 3-6\ \mu m$) Quantum Cascade Lasers. *IEEE Photonics Journal*, 14:1–25, 2 2022. doi:10.1109/JPHOT.2021.3132261.

[47] D. Botez, J. C. Shin, L. J. Mawst, I. Vurgaftman, J. R. Meyer, and S. Kumar. Suppression of carrier leakage in 4.8 $\mu m-$ emitting quantum cascade lasers. page 76160N, 2 2010. doi:10.1117/12.842593.

# Chapter 2

# Technology of InAs-based QCLs

## 2.1 Introduction

This chapter provides a thorough description of fabrication of InAs-based Quantum Cascade Lasers (QCLs). It then examines the issues related to the device insulation followed by a discussion on alternative insulating materials and development of a novel fabrication procedure aimed at the performance improvement and production cost reduction.

## 2.2 QCL Fabrication Process

A complete QCL fabrication process is illustrated in Figure 2.1 (A–N). The process can be broadly split into three major stages, each involving many intermediate steps: the ridge definition, Figure 2.1 (A–F), insulation Figure 2.1 (G–I), and metallization, Figure 2.1 (J–N). Typically, the process takes several days due to the multiple lithography and etching steps.

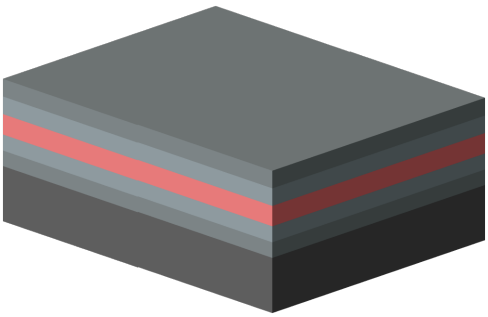

A. Sample preparation

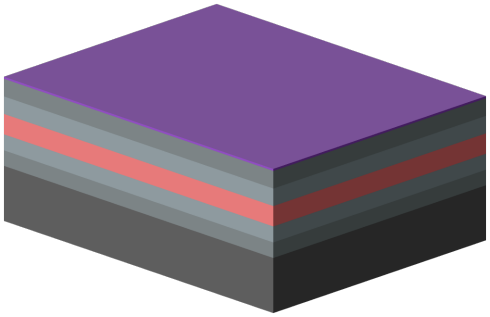

B. Spin coating of -ve photoresist to define ridge patterns

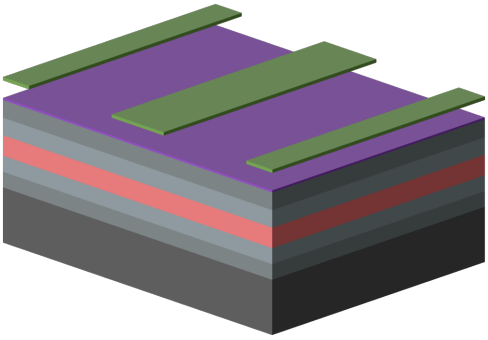

C. Photolithography etching mask

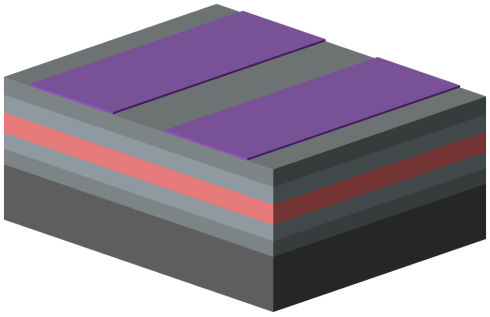

D. Developing to define the ridges

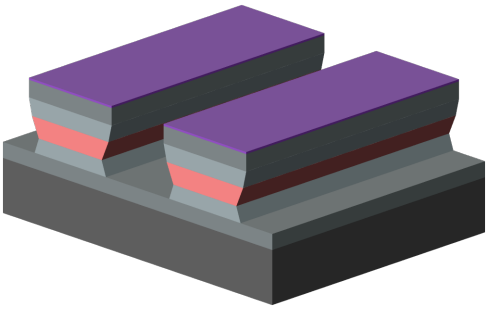

E. Wet chemical etching to define ridges (dovetail etch profile)

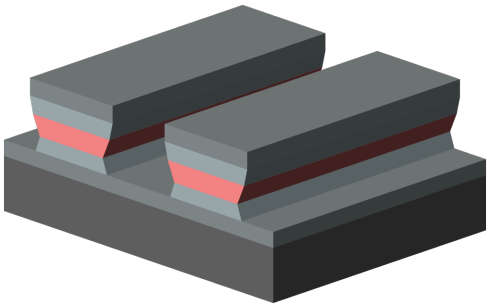

F. Resist removal

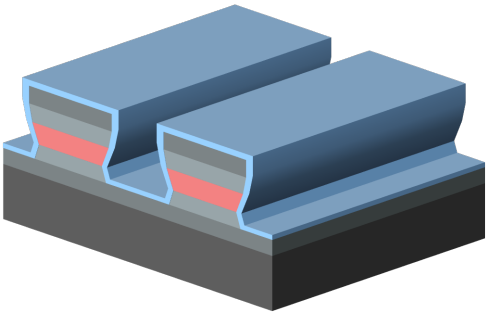

G. Spin coating of +ve photoresist for insulation

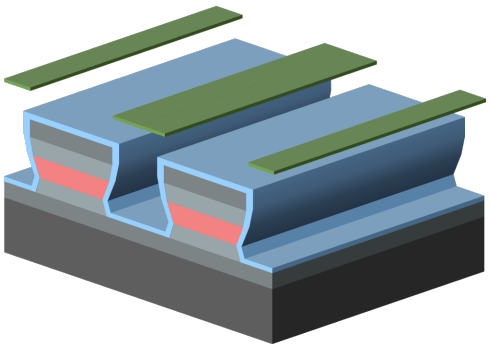

H. Photolithography opening mask

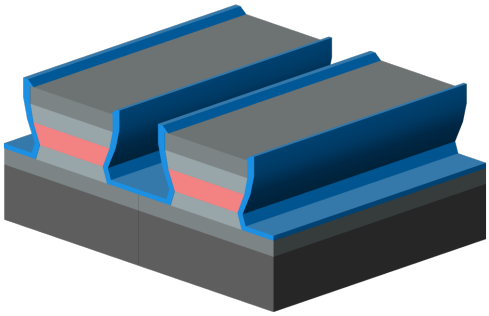

I. Developing followed by hard baking the +ve resist

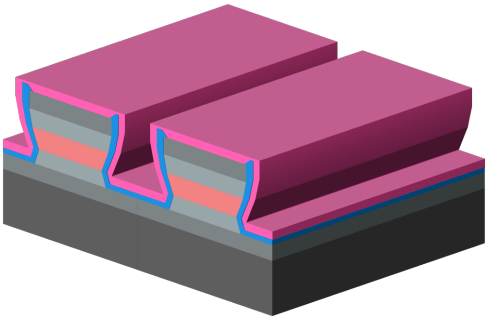

J. Spin coating of thick +ve photoresist for metallization

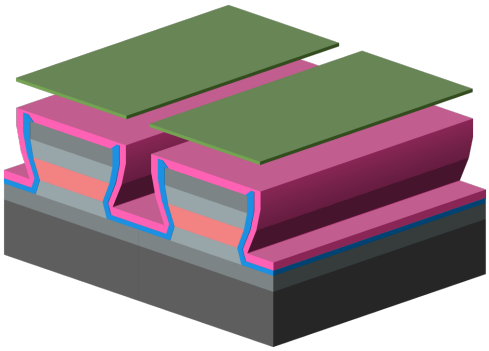

K. Photolithography metallization mask

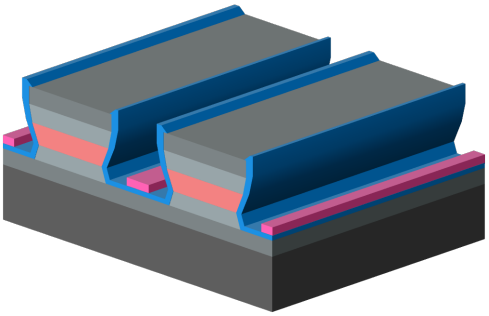

L. Developing

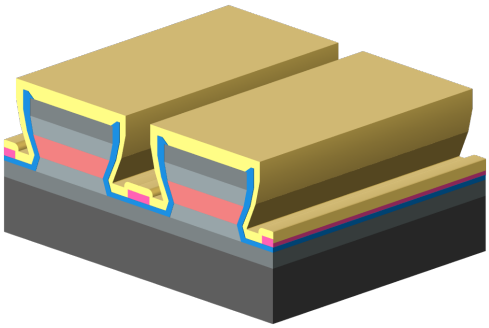

M. Metallization

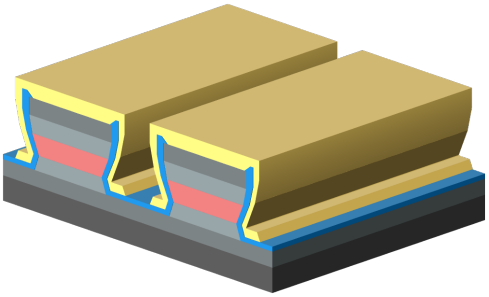

N. Final devices after substrate thinning followed by metal lift-off

**Figure. 2.1:** Pictorial representation of the processing steps of InAs-based QCLs insulated with hard-baked photoresist.

### 2.2.1 Ridge Definition: Wet Etching

The careful and precise formation of laser ridges is critical as it lays the groundwork for superior control over the laser emission properties, allowing for desired performance. The fabrication process starts by thoroughly cleaning the cleaved wafer with a sequence of acetone, ethanol, isopropanol, and deionized water. Such treatment is usually sufficient to remove any residue buildup on the sample surface. However, in cases where impurities persist a low RF power (50 W) reactive ion etching (RIE) with Argon and Oxygen can be used. The low RF power helps to minimize damage of the upper InAs cladding layer. After cleaning the sample is baked on a hot plate to remove any moisture and to promote the adhesion of photoresist in the following steps.

The areas of the wafer that will eventually be transformed into mesa of laser ridges are patterned using ultraviolet (UV) photolithography (SUSS MicroTec MJB4 Mask Aligner) with a negative photoresist, AZ2020 [1]. Typically, for InAs-based QCLs, the mask is aligned to pattern the ridges along $0\bar{1}\bar{1}$ orientation, producing a dovetail etch profile, as shown in Figure 2.1 (E). The patterned sample is etched using a mixture of $H_3PO_4$ (phosphoric acid) : $H_2O_2$ (hydrogen peroxide) : $H_2O$ (deionized water) in the proportion of 2 : 1 : 2. The etching rate is 1 $\mu$m/min at room temperature. The electron microscopy image of the etched laser ridge is shown in Figure 2.2.

To reduce current leakage over the mesa walls the sample is etched again using a solution of citric acid ($C_6H_8O_7$), water, and hydrogen peroxide: $[C_6H_8O_7 : H_2O] : H_2O_2$ in the proportion of $[1 : 1] : 1$. Due to the selective etching of InAs (does not etch high Al-containing layers) in citric acid solution, this step produces AlSb-rich corrugated surface on the side walls of the laser ridge as shown in Figure 2.3. The AlSb oxide has low electrical conductivity, which reduces the current leakage in the processed devices. Finally, the remaining photoresist is stripped off using acetone or remover PG (N-Methylpyrrolidone-based solvent) [2].

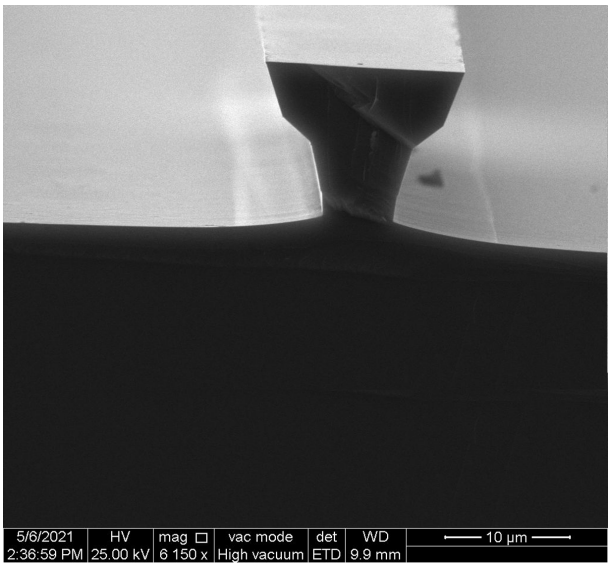


**Figure. 2.2:** Electron microscopy image of QCL ridge formed using wet etching.

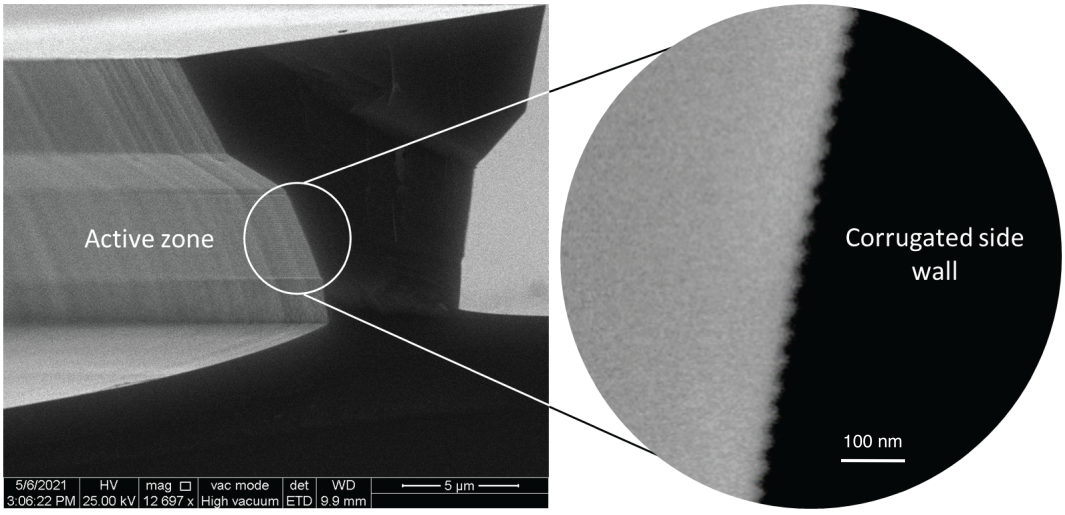


**Figure. 2.3:** Electron microscopy images of a QCL ridge after wet etching and citric acid treatment, resulting in the formation of corrugated side walls in the active region. (Left) Complete mesa structure and (Right) zoomed image showing the corrugated side wall.

### 2.2.2 Insulation: Hard-Baked Photoresist

The next critical stage in fabrication process consists in insulation of the ridge sidewalls. Hard-baked photoresist is historically used at IES for insulation of InAs-based QCLs. In this work we employed for this purpose a positive photoresist AZ1518 [3] baked at 200°C for 2 hours.

The sample is spin-coated with AZ1518, at 3000 rpm for 30 seconds and baked on a hot plate at 110°C for 1 minute. This layer ultimately serves as the insulation. To imprint the desired opening patterns the sample undergoes UV exposure for a duration of 23 seconds through a mask. The mask employed in this step is similar to the one used earlier, however, with a slightly narrower aperture. The narrower opening plays a crucial role in guaranteeing that only the photoresist on top of the mesa remains unexposed, thereby preventing any unintentional removal of the layer from the sidewalls. The unexposed photoresist is then stripped off using a developer. Finally, the sample undergoes a 2 hours hard-baking process at a temperature of 200°C. Figure 2.4 illustrates an electron microscopy image of the QCL ridge after the insulation and metallization.

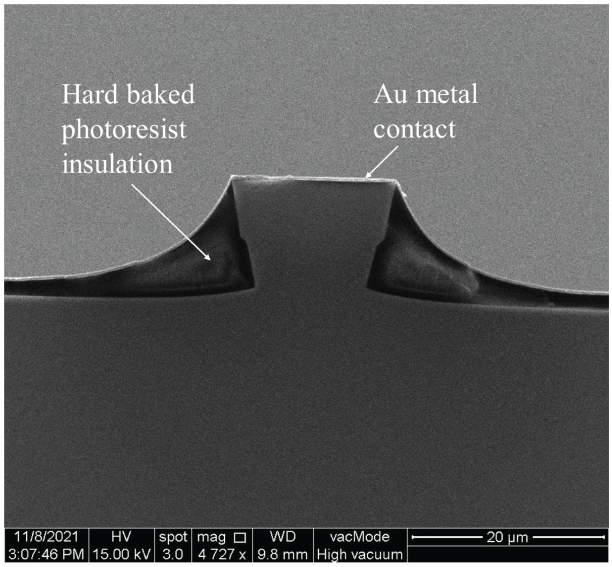


**Figure. 2.4:** Electron microscopy image of fabricated QCL ridge after hard-baked photoresist insulation and metallization.

Indeed, the use of photoresist for insulation has proven to be a simple and effective method, ensuring high performance of the devices [4–6]. The photoresist insulation, however, has some issues concerning its stability. In Section 2.4, we will look into these issues in detail and propose an improved strategy for insulating long-wavelength InAs-based QCLs.

### 2.2.3 Metallization

After insulation, the surface of the sample is metallized using UV photolithography, thermal evaporation and lift-off.

A negative photoresist, AZ2070 [7], is deposited using spin coating at 4000 rpm for 30 seconds followed by a pre-exposure bake for 2 minutes on a hot plate at 110°C, mask alignment, UV exposition for 10 seconds, and a post-exposure bake for 1 minute at 110°C. The exposed photoresist is then developed. The developing time is typically 2 minutes 45 seconds. The developer only dissolves the unexposed photoresist on top of the laser ridge where the final metal layer will be deposited and creates an undercut in the remaining undissolved photoresist. The appropriate undercut depth is essential for successful lift-off and can be controlled by adjusting the exposure time. Typically, for 10 seconds exposure, the undercut depth is upwards of 9 $\mu$m and is sufficient for successful lift-off.

To ensure good adhesion between the deposited metal film and the semiconductor, it is essential to remove any oxide/organic impurities which might have formed on the sample's surface during the preceding steps. This step, referred to as deoxidation, consists in acid treatment of the sample using dilute HCl ($HCl : H_2O = 1 : 4$) solution for 30 seconds, right before metal deposition.

The metal deposition is made in a vacuum evaporation chamber. A thin Ti layer (20 nm) is deposited first to improve adhesion to the semiconductor surface, followed by 200 nm of Au, 30 nm of Cr, and another 200 nm of Au. Ti layer prevents Au contact exfoliating while the Cr layer blocks diffusion of Indium solder used for mounting the lasers bars to the heat sink.

### 2.2.4 Polishing, Lift-off, and Mounting

The top contact deposition is followed by the thinning of the substrate to aid in the cleavage of the laser bars and the formation of mirror facets. The substrate is thinned down to $100 - 150$ $\mu$m by mechanical polishing. The devices are then cleaved into laser bars of desired lengths using a scriber, thus, forming Fabry–Pérot (FP) resonators and

eventually individual laser chips. The laser chips are soldered on copper heatsinks with Indium in one of the two configurations: epilayer-up and epilayer-down, as illustrated in Figure 2.5.

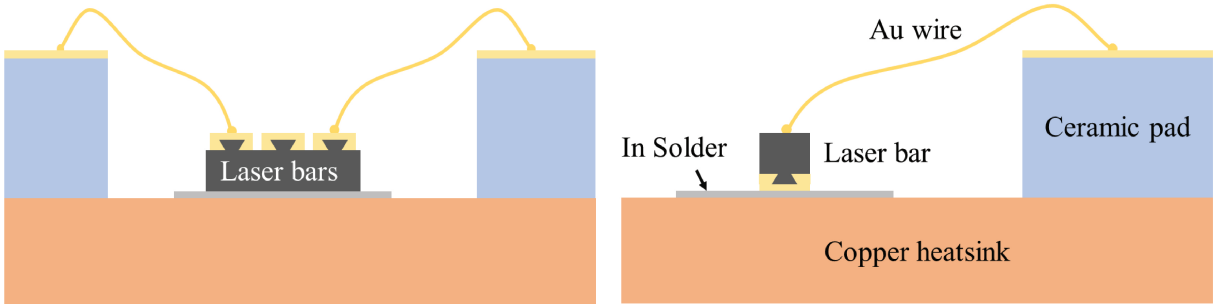


**Figure. 2.5:** Schematic illustrations of (Left) epilayer-up and (Right) epilayer-down mounting configurations of QCLs.

Figure 2.5 (Left) depicts an epilayer-up mounting configuration which is helpful for testing multiple-laser bars. Figure 2.5 (Right) shows a laser soldered epi-side down providing efficient heat dissipation necessary for CW operation. This configuration requires however precise positioning of the laser chip with respect to the edge of the heatsink and careful surface preparation to prevent optical blocking of laser emission and electrical shortening.

Once the QCLs are mounted, gold wires with a diameter of 50 $\mu$m are manually soldered to connect the laser ridge and a metallized ceramic pad on the heatsink serving as a top electrical contact, the bottom contact being the heatsink itself. Afterward, the devices undergo a thorough cleansing process using ethanol in an ultrasound bath to eliminate any remaining traces of the soldering flux.

This concludes FP QCL fabrication process, and the devices are ready for characterization. It is important to clarify that the process outlined in above sections is specific to this work. It should also be noted that the selection of photoresist, chemicals and equipments is not rigid and can be changed/adjusted for further optimization.

## 2.3 Characterization of QCLs

Figure 2.6 illustrates the experimental setup used to investigate the electrical and optical characteristics of the QCLs in pulsed operation. The setup includes an oscilloscope, pulse generator, voltage-current source, lock-in amplifier, and Fourier transform spectrometer (FTIR) equipped with a pyroelectric DTGS detector, all interconnected and computer-controlled. The QCLs are securely fixed on a station equipped with a Peltier cooler and two probes, for current injection and voltage control. The current is delivered by the pulse generator. To provide a rectangular shape of the short pulses of high operating current and voltage, inherent in QCLs, an electronic commutator circuit based on a power MOSFET placed close to the tested device is employed. Each pulse opens the MOSFET, thereby applying to the QCL voltage from a DC current source. The current is controlled by the output voltage of the programmable source. Voltage measurements

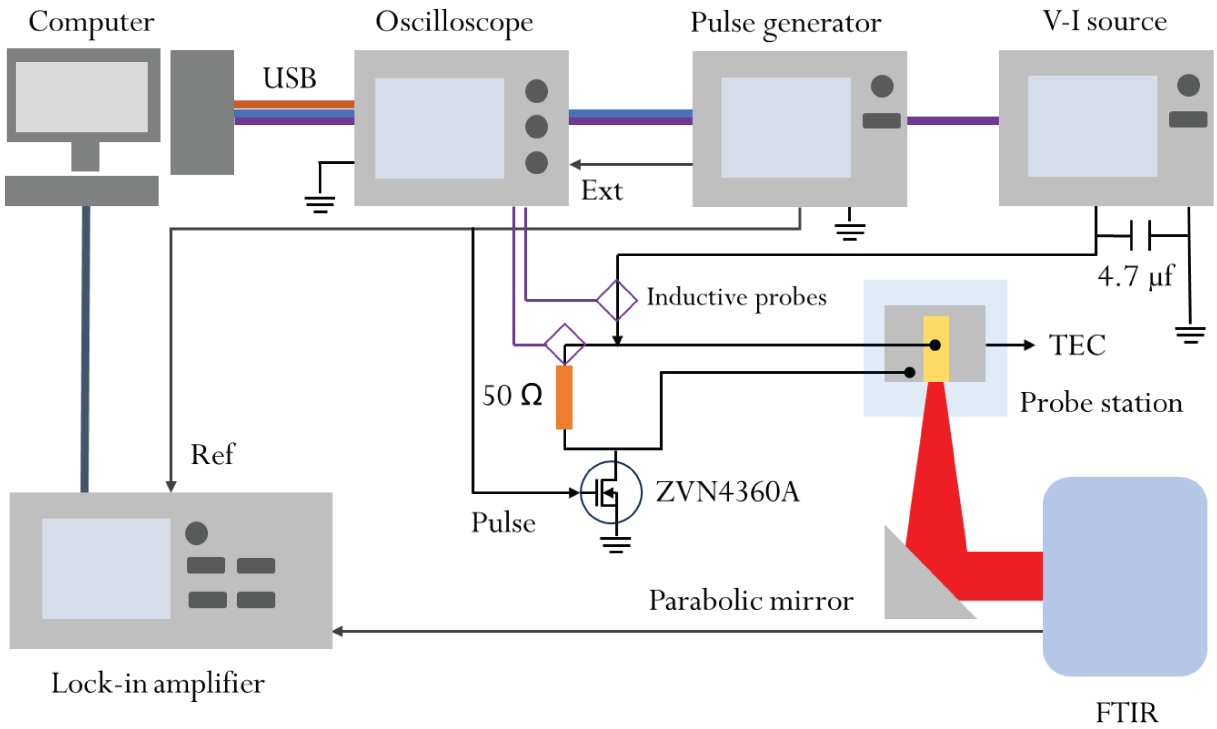


**Figure. 2.6:** Illustration of experimental setup for electrical and optical characterization of QCLs in pulsed operation.

are performed by monitoring the voltage on the inductive probe measuring the current through a 50 Ω resistor connected in parallel to the laser chip. The current is measured using the second inductive probe connected in series with the tested device. The voltage is programmatically varied and the corresponding current and optical power are acquired and saved. The emitted light is collected and directed to the FTIR for spectral analysis by employing a parabolic mirror.

## 2.4 Improvement of QCL Technology

In addition to using a suitable etching process, an appropriate mesa sidewall surface insulation is absolutely crucial in preventing the degradation of the material and minimizing surface leakage currents. As the InAs/AlSb etched mesa sidewall surface is chemically unstable due to the highly reactive nature of In and Al, given enough time and exposure to the surrounding atmosphere, it eventually results in the formation of native oxide on the surface [8]. The oxide semiconductor interface has a high density of interface states, dangling bonds, and defects that introduce trap states within the forbidden band, leading to surface leakage current [9]. Furthermore, the native oxide of Indium as well as InAs itself, due to high electrical conductivity, further surge leakage [10].

The elevated leakage current has a detrimental impact on laser performance, consequently increasing their threshold current and reducing emission efficiency [11]. Passivation of the QCL ridge walls is therefore crucial. In addition, the insulation layer plays a significant role not only in electrical insulation but also in the confinement of the light in the active region and as well as in heat dissipation [12]. Taking into account the numerous responsibilities of insulation, it is mandatory to select a material that effectively minimizes surface leakage, has minimal absorption, a low refractive index, and high thermal conductivity.

### 2.4.1 Issues with Photoresist Insulation

As mentioned earlier, for long-wavelength InAs/AlSb-based QCLs, a hard-baked photoresist is used for insulating the active zone [13–15]. This insulation technique is mature

and robust, as evident from the demonstration of high-performing QCLs emitting from 2.6 $\mu$m [14] to 25 $\mu$m [15]. However, this approach has some drawbacks. In particular, poor thermal conductivity of the photoresist prevents efficient heat extraction required for CW operation. This technique remains however a compelling and straightforward choice solely due to standardized fabrication protocols and ease of deposition by spin-coating. It is adequate for most applications particularly when thermal issues are not too strict, such as when operating the devices in the pulsed regime or in continuous wave mode with limited electrical power [12]. However, the increasing demand for high-temperature operation of QCLs comes with challenges. The use of hard-baked photoresist as an insulation material poses limitations due to its polymeric nature and plastic-like properties. Specifically, the properties of photoresist are susceptible to modification at high temperature often related to CW operation in extreme conditions, which ultimately compromises the performance of the devices.

We studied the susceptibility of QCLs, insulated with hard-baked photoresist, to performance instability associated with operation at elevated temperatures. In this investigation, QCLs with emission wavelengths of 14 $\mu$m and 7.7 $\mu$m were selected and tested at temperatures up to 120°C. We examined the variation in optical power-current and voltage-current (PIV) characteristics before and after the QCLs were subjected to high temperatures.

The mounted devices chosen for this investigation were left undisturbed in a secure location for a period of one week before proceeding with the experiment. This ensured that the insulation had sufficient time to stabilize and eliminate any residual effects that might be induced during soldering. The devices were then placed in a liquid nitrogen flow cryostat and characterized in pulsed mode (333 ns $\times$ 12 kHz). Two sets of measurements were performed, each with varying temperatures. In both sets, the temperature varied from 280 K to 400 K. Before proceeding with the second measurements the devices were cooled down and were maintained at 280 K for 15 minutes. From hereinafter, the first and the second set of measurements are referred to as $1^{st}$ and $2^{nd}$ temperature cycle.

Figure 2.7 and Figure 2.8 show the PIV characteristics of the studied QCLs. The measurements corresponding to the 1st temperature cycle is shown as dotted lines and those to corresponding the 2nd temperature cycle as solid lines. For the temperatures lower than 360 K, the data presented in the figures show a change in the threshold current density after the first temperature cycle. At 280 K, the threshold of the 14-$\mu$m-QCLs increased by about 7% compared with the initial values. The performance change of the 7.7-$\mu$m-devices was even more pronounced, reaching 13%, but the effect was inversed as a threshold reduction was observed.

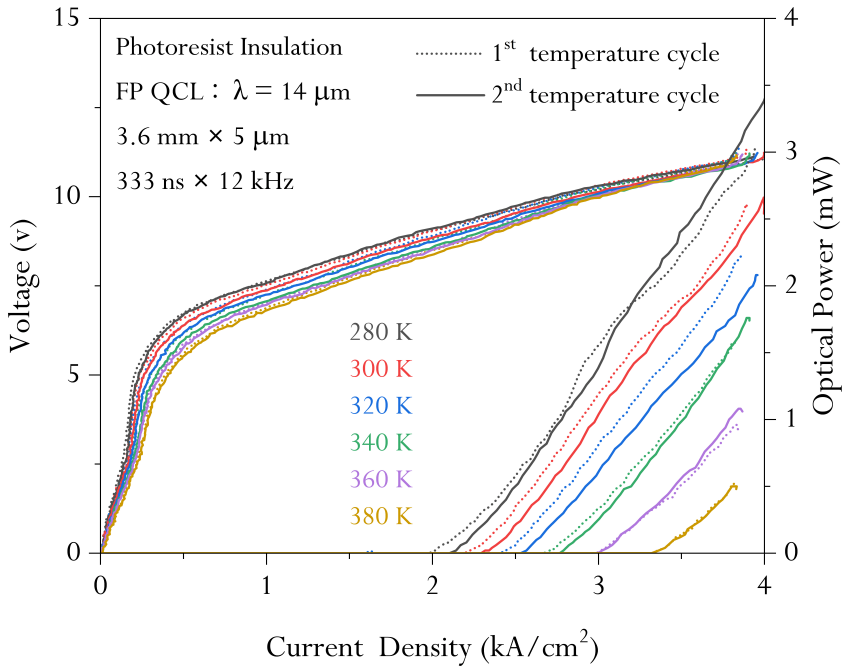


**Figure. 2.7:** PIV characteristics of FP QCL, insulated with photoresist, in different temperature cycles. The emission wavelength is 14 $\mu$m.

Additionally, it is noteworthy that there is no apparent change in the VI characteristics. The VI characteristics observed during the initial cycle are consistent with those observed during the subsequent cycle. The observed consistency implies the absence of any change in the leakage current. Since the leakage current remains constant in both cycles, it can be inferred that any alterations in the threshold current density solely arises from the modification of the optical loss in the lasers, resulting in the observed change in the

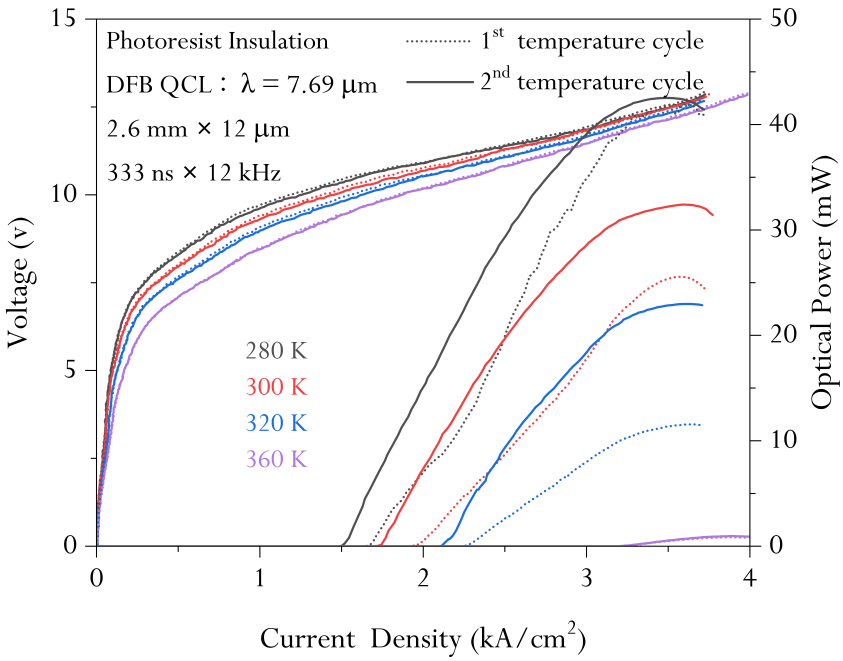


**Figure. 2.8:** PIV characteristics of DFB QCL, insulated with photoresist, in different temperature cycles. The emission wavelength is 7.7 $\mu$m.

threshold.

If the modified value of threshold current densities were maintained permanently, then the modification might not be deemed as performance instability. If only this were true, the photoresist insulation would have been faultless (in terms of optical and electrical characteristics). However, as shown in Figure 2.9, the alteration is not permanent. Over time, the threshold current densities gradually returned to the original values, as if they had retained those values in memory. Figure 2.9 displays the threshold current densities ranging from 280 K to 360 K for both temperature cycles. It also shows the threshold current density values measured 15 and 96 hours after the second temperature cycle. These measurements clearly show the gradual restoration of the original threshold current densities.

In addition, the change of the properties of the photoresist insulation also affected the emission wavelength, as illustrated in Figure 2.10. We observed a shift of 0.63 $cm^{-1}$ in the emission wavelength between the two temperature cycles. Similar to the threshold

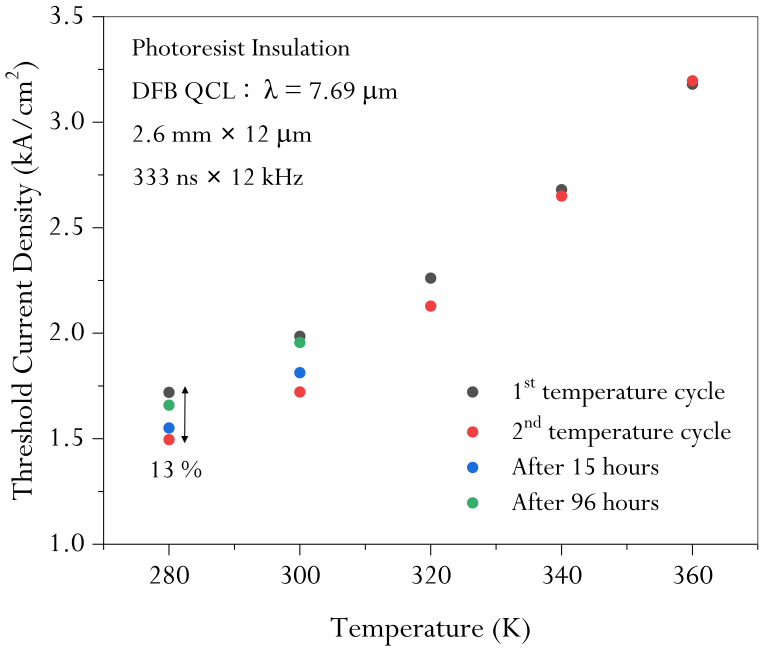


**Figure. 2.9:** Threshold current density as a function of temperature showing the gradual recovery of the original threshold current density over time.

current density, this wavelength shift was also temporary. Over time, the devices gradually returned to the original emission wavelength. Figure 2.10 displays the emission spectra of DFB QCL at 280 K for both temperature cycles. It also presents emission spectra measured 15 and 96 hours after the second temperature showing the gradual restoration.

The modification of the optical properties of photoresist can be attributed to transformation of its structure. When a photoresist is heated close to its glass transition temperature ($T_g$), typically ranging from 100°C to 130°C for AZ1518, it undergoes a transition from a glassy to a rubbery state. This transition leads to increased flexibility and reduced stiffness of the photoresist [17]. Moreover, the resist experiences higher thermal expansion, which can cause dimensional changes and potential thermal stress [16] as shown in Figure 2.11. As a result, the complex refractive index of the resist can be altered, thereby affecting its optical properties. Once the material is cooled below its $T_g$, the molecular mobility decreases, and the material's structure stabilizes, allowing it to restore its original properties. However, it is important to note that certain relaxation processes, such

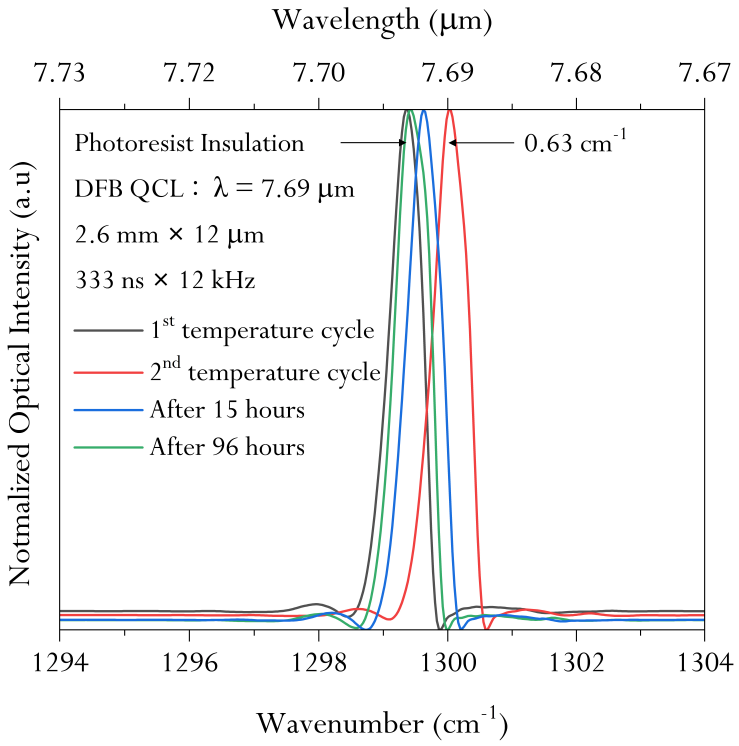


**Figure. 2.10:** Emission spectra of DFB QCLs in two temperature cycles and the gradual recovery of the emission wavelength over time.

as stress relaxation, may continue to occur over longer time scales even after the material has returned below the $T_g$. These processes involve the gradual release of internal stresses and the rearrangement of molecular chains, which we have indirectly observed in our experiments.

The observed opposite trend in the temperature-induced change in the threshold current density of the 14 and 7.7 $\mu$m QCLs can be attributed to the respective increase or decrease in the extinction coefficient of the photoresist insulation after thermal treatment. Figure 2.12 displays an absorption spectrum of the baked photoresist showing strong variation between 7 and 8 $\mu$m. It is reasonable to suppose that a change in the chemical nature of the photoresist can provoke quite strong consequences in this spectral region. The sign of this effect will depend on the initial state of the photoresist insulation with respect to the absorption features in the spectrum. This ambiguity introduces an additional layer of variability in device performance.

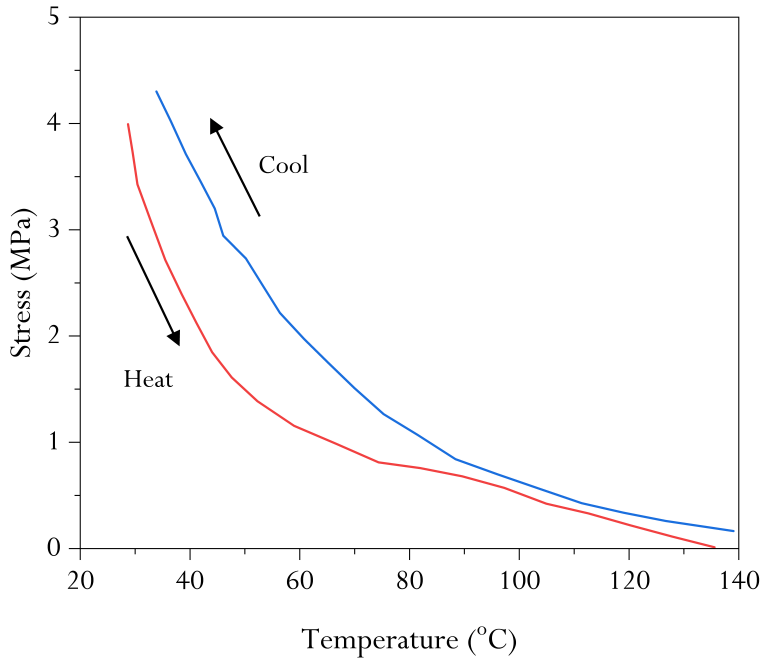


**Figure. 2.11:** Effect of temperature on the state of stress of a photoresist sample. Adapted from [16]

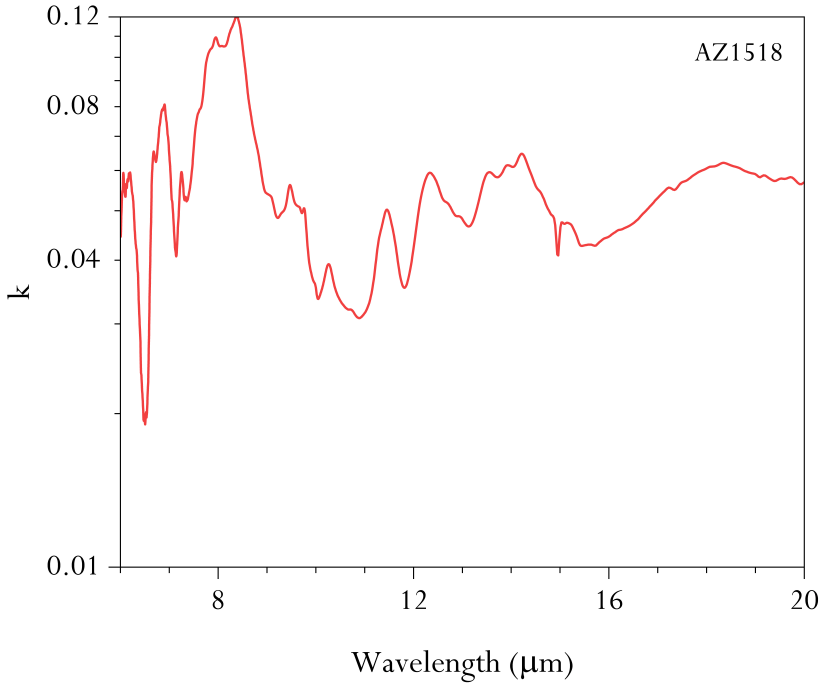


**Figure. 2.12:** The extinction coefficient of AZ1518 as a function of wavelength.

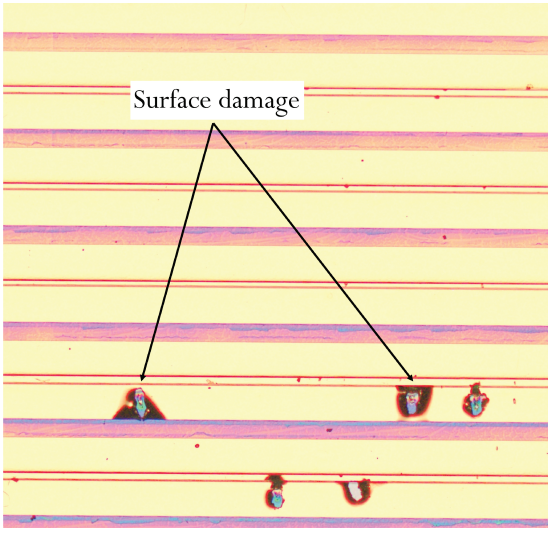


**Figure. 2.13:** An optical image of the fabricated QCLs showing surface damage after wire bonding attempts.

Another concern related to photoresist insulation is wire bonding. The wire bonding process involves the fusion of a wire with the metal on top of the device and an external circuit using ultrasonic vibrations. In addition, for Au wire bonding, the devices are heated to a temperature of approximately 100°C [18]. The intrinsic softness of hard-baked photoresist, along with the high temperature, makes it impossible to successfully bond the wires using this technique. As a result, manual soldering with In of each device is necessary, leading to a laborious and arduous process that restricts mass production capabilities. The optical image of the wire bonding attempts depicted in Figure 2.13 shows the surface damage that occurred on the QCLs insulated with photoresist.

### 2.4.2 Simulation for Alternative Insulation Material

To achieve stability of the QCL performance it is crucial to resolve the issues related to photoresist insulation. One approach to overcome the challenge is to replace the photoresist with a more stable material. Thus, in an effort to address these issues, we conducted research into the potential use of conventional hard dielectrics. These materials, including $SiO_2$, $Si_3N_4$, $TiO_2$ and others have been employed to insulate QCLs [19–22]. Nonetheless, their use in the long-wavelength range is still limited and is being investigated.

This part of the thesis aims to select the dielectric that works best for long-wavelengths. We employed the finite element method utilizing COMSOL software to simulate and evaluate the confinement factor, optical loss, and thermal resistance of QCL structure insulated with a variety of dielectrics ($SiO_2$, $Si_3N_4$, $TiO_2$). Photoresist, AZ1518, insulation was also studied for the comparison. We employed the identical model of the QCL structure, designed to emit at 14 $\mu$m, as detailed in Section 1.3.3 and varied the insulating material. The refractive index of the dielectrics used as insulating materials are shown in Table 2.1.

The primary factor influencing the loss induced by the insulator is its absorption strength, along with its refractive index that governs its interaction with the lasing optical mode. A highly absorbing insulator with a small refractive index can potentially provide low loss.

| Material | Refractive Index |
|---|---|
| AZ1518 | 1.6+i0.1 [23] |
| $SiO_2$ | 1.7778+i0.092814 [24] |
| $TiO_2$ | 0.73014+i1.6878 [24] |
| $Si_3N_4$ | 3.6647+i1.0228 [24] |

**Table 2.1:** Refractive index of dielectrics used as insulating materials.

Throughout the simulations, we played around with the insulation materials and their width, $W_i$, varying from 0.01 $\mu$m to 5 $\mu$m using a parametric sweep with a step of 0.02 $\mu$m. In order to investigate the impact of insulating materials on the guided mode, we used the ratio of the squared electric field over the insulator region including lateral metallization ($E_{insulator}$) to that over the active region ($E_{active}$) as shown in the equation below to calculate the fraction of mode leaking into insulation ($L^*$).

$$L^* = \frac{\int_{insulator} |E_z|^2 \, dZ}{\int_{active} |E_z|^2 \, dZ} \tag{2.1}$$

The leakage factor, $L^*$, for different insulating materials as a function of insulation width is shown in Figure 2.14

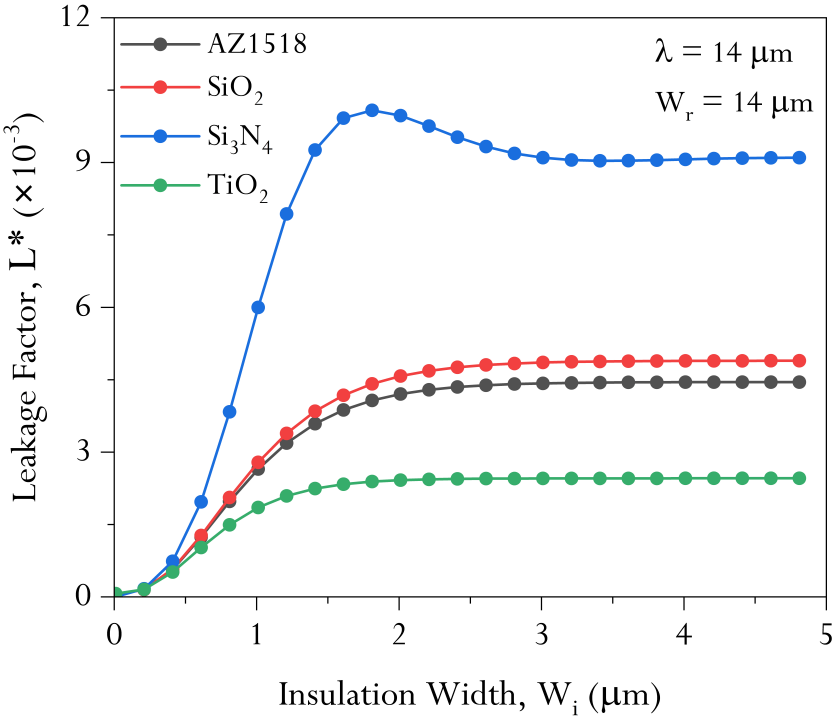


**Figure. 2.14:** Optical leakage factor as a function of insulation width for different insulating materials.

Based on the observations made in Figure 2.14, it is evident that the proportion of mode confined within the insulation material increases as the insulation width increases, up to a width of 2 $\mu$m. Beyond this point, the fraction of confined mode remains relatively constant for larger insulation widths. Comparing the performance of different insulation materials, AZ1518 and $SiO_2$ exhibit similar mode leakage, while $TiO_2$ and $Si_3N_4$ display the lowest and highest leakage values, respectively. The observed trend can be attributed to the similarity in refractive index contrast between the active zone and the insulation materials AZ1518 and $SiO_2$, while a higher contrast is for $TiO_2$ and a lower contrast for $Si_3N_4$. The increasing $L^*$ factor indicates stronger interaction of the optical mode with absorbing insulation material.

Now we should analyze the strength of the mode absorption in the insulator. Absorption

is directly proportional to the extinction coefficient of the absorbing material. To assess the combined effect of both the fraction of mode propagating in the insulation ($L^*$) and the extinction coefficient ($k$) we defined the figure of merit $\chi^*$ as follows

$$\chi^* = \frac{1}{L^* \times k} \tag{2.2}$$

The figure of merit, $\chi^*$, for different insulating materials as a function of insulation width is shown in Figure 2.15.

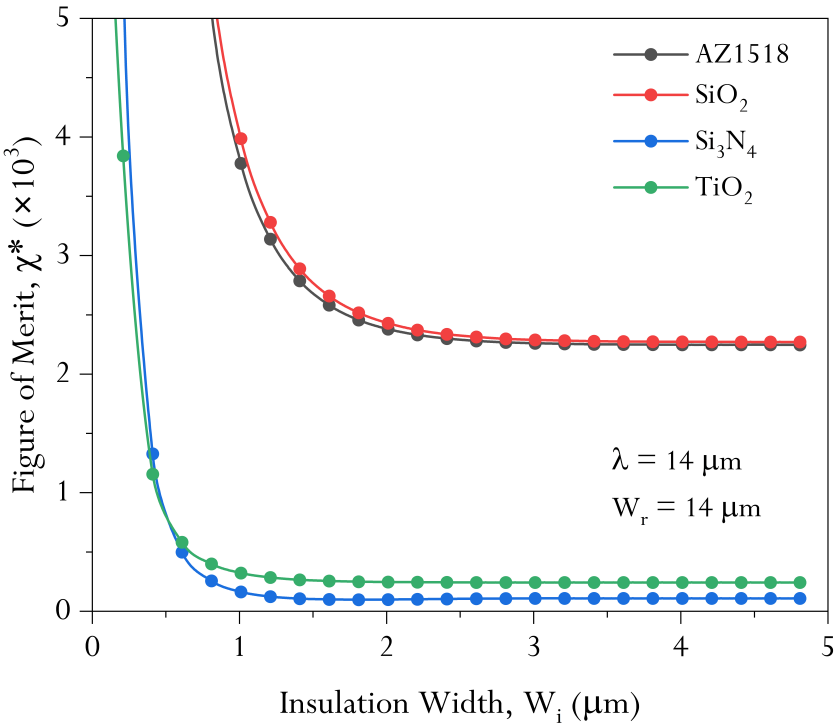


**Figure. 2.15:** Figure of merit as a function of insulation width for different insulating materials.

Based on Figure 2.15, it is evident that the effect of AZ1518 and $SiO_2$ insulation is comparable, with $SiO_2$ showing slightly better performance across the entire range of studied insulation widths. On the other hand, the poor performance of $TiO_2$ and $Si_3N_4$ can be attributed to their much higher extinction coefficients in comparison to AZ1518 and $SiO_2$, as indicated in Table 2.1. In conclusion, $SiO_2$ proves to be the best choice

thanks to the large refractive index contrast and its reasonably low extinction coefficient.

To investigate the impact on the loss, $\alpha$, encountered by the guided mode, we determined $\alpha$ using the imaginary part of the frequencies of the modes using Equation (1.28). The optical loss for different dielectrics as a function of insulation width is shown in Figure 2.16.

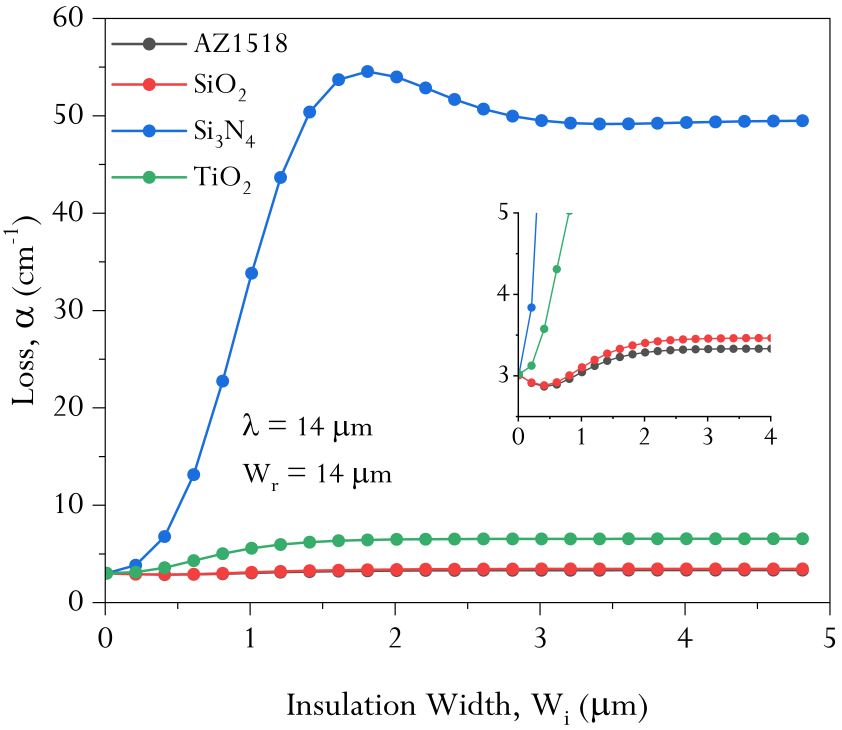


**Figure. 2.16:** Optical loss as a function of insulation width for different insulating materials.

It can be seen from Figure 2.16 that the loss due to $SiO_2$ insulation is comparable to that of the AZ1518 whereas the loss due to $TiO_2$ and $Si_3N_4$, is nearly two and sixteen times higher for thick insulation. It is interesting to note that even though the extinction coefficient of $Si_3N_4$ is lower than that of $TiO_2$, modes encounter a much higher loss. This is due to the lower refractive index contrast between $Si_3N_4$ and active zone, as compared to $TiO_2$. The low refractive index contrast leads to increased mode overlap with the insulating material resulting in higher loss. For the insulation thickness exceeding the penetration depth of the optical mode the loss is constant.

The above trend is maintained even for insulation thicknesses ranging from 0.01 $\mu$m –

2 $\mu$m, specifically, $TiO_2$ and $Si_3N_4$ both displays substantially more losses compared to AZ1518 and $SiO_2$. However, the loss profile is not flat. For $TiO_2$ and $Si_3N_4$, we observe a sharp increase with the increase in insulation thickness, whereas for AZ1518 and $SiO_2$, this dependence demonstrates a minimum around 500 nm, as shown in Figure 2.16 (inset) . Such behavior can be explained by the competition of losses induced by absorption in the lateral ridge metallization and in the insulator itself.

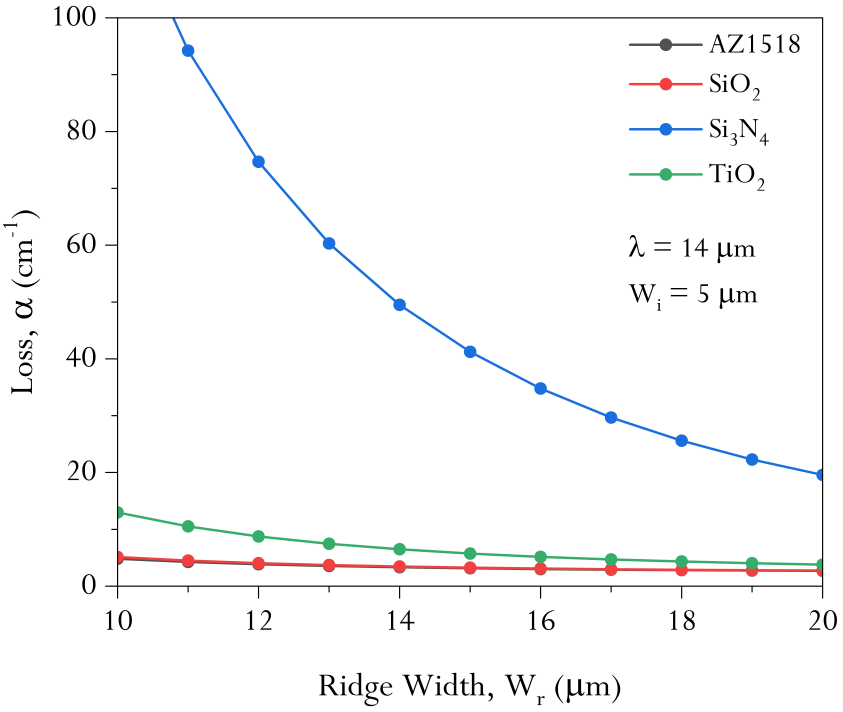


**Figure. 2.17:** Optical loss as a function of ridge width for different insulating materials with fixed width.

These simulations were performed for a typical case when the QCL ridge width is equal to the emission wavelength in vacuum. In practical design scenarios, it is common for the ridge width of the QCL to be narrower than the emission wavelength. This is particularly true when designing single-frequency devices to suppress higher order spatial modes. A narrower ridge width also facilitates continuous wave operation, as it enhances the lateral removal of heat generated within the laser, resulting in better heat dissipation. However, in narrow ridges, the overlap between the mode and the insulating material is higher, which leads to increased optical loss, as depicted in Figure 2.17, displaying the loss for

different insulating materials as a function of ridge width. Consequently, the careful selection of the insulating material becomes even more important in such cases.

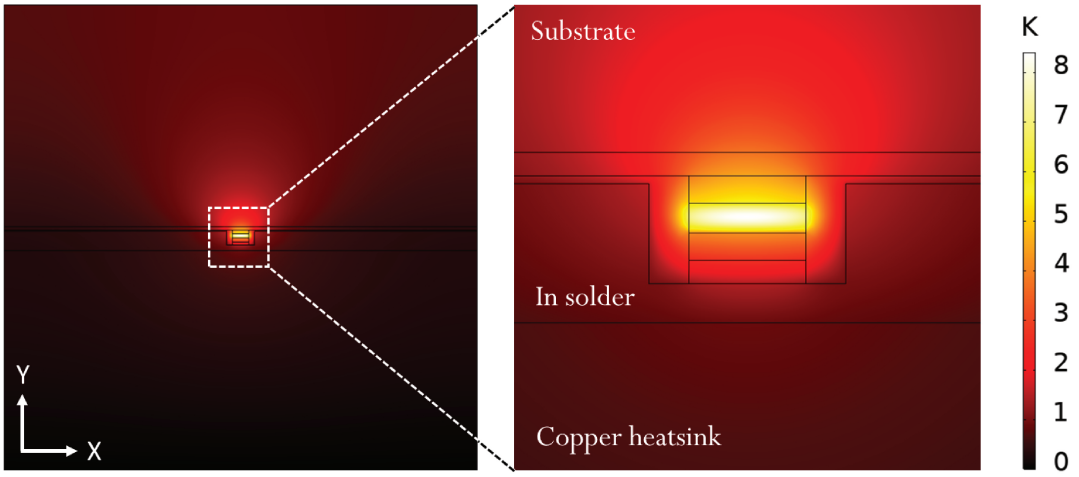


**Figure. 2.18:** Thermal simulation of a QCL structure with a 14 $\mu$m wide ridge insulated with photoresist in epilayer-down mounting configuration at 293 K.

In this section we showed that the optical properties of $SiO_2$ make it a viable alternative of AZ1518. We also compared the efficiency of heat dissipation in QCLs insulated with these materials. We modeled a QCL structure, soldered epi-side down on a copper heatsink with indium as shown in Figure 2.18. In the model, we chose a 400-$\mu$m-wide bottom cladding and 400-$\mu$m-wide, 150-$\mu$m-thick substrate as in the actual devices.

The simulation is based on solving the Fourier equation for the steady-state heat transport

$$Q = C_{th} \cdot \Delta T \tag{2.3}$$

Where $Q$ is the amount of heat, $C_{th}$ is the thermal conductivity, and $\Delta$ is the Laplacian operator. The thermal conductivity of each layer is presented in Table 2.2. We assume that the heat generated due to Joule heating of the cladding and the contacts is insignificant compared to the active area. Hence, the active zone is the only heat source. The

| Material | Thermal conductivity $C_{th}$ $(W \cdot K^{-1} \cdot m^{-1})$ |
|---|---|
| Copper heatsinks | 385 |
| Indium | 84 |
| Cladding | 27 [25] |
| Spacer | 27 [25] |
| Active zone | 27 (X) 3 (Y) 27 (Z) [23] [26] |
| Substrate | 27 [25] |
| AZ1518 | 0.2 [23] |
| $SiO_2$ | 1.3 [27] |

**Table 2.2:** Thermal conductivity of different layers and insulating materials.

Joule heating of the active zone can be expressed as

$$T_{act} = T_{sink} + R_{th} V I \tag{2.4}$$

Where, $T_{act}$, and $T_{sink}$ are the temperature of the active zone and copper heatsink, respectively. $R_{th}$ is the thermal resistance. $V$ is the voltage, and $I$ is the current applied to the laser.

In the simulation, an electrical power, i.e., $VI$, of $1W$ was applied and $T_{sink} = 0$ K was set so that $T_{act}$ would directly give $R_{th}$. Similar to what was discussed before, we varied the insulation material and width to obtained the $R_{th}$ as shown in Figure 2.19. Based on the findings in Figure 2.19, it is apparent that the QCL insulated with $SiO_2$ exhibits a lower thermal resistance compared to AZ1518, owing to its higher thermal conductance. This lower $R_{th}$ is anticipated to enhance the overall performance of the QCL. Through simulation, we estimate that real devices insulated with $SiO_2$ could potentially achieve approximately a 15% improvement in $R_{th}$ compared to AZ1518 insulation.

The lower loss and improved thermal resistance exhibited by $SiO_2$, makes it becomes a viable and practical alternative for hard-baked photoresist insulation in long-wavelength

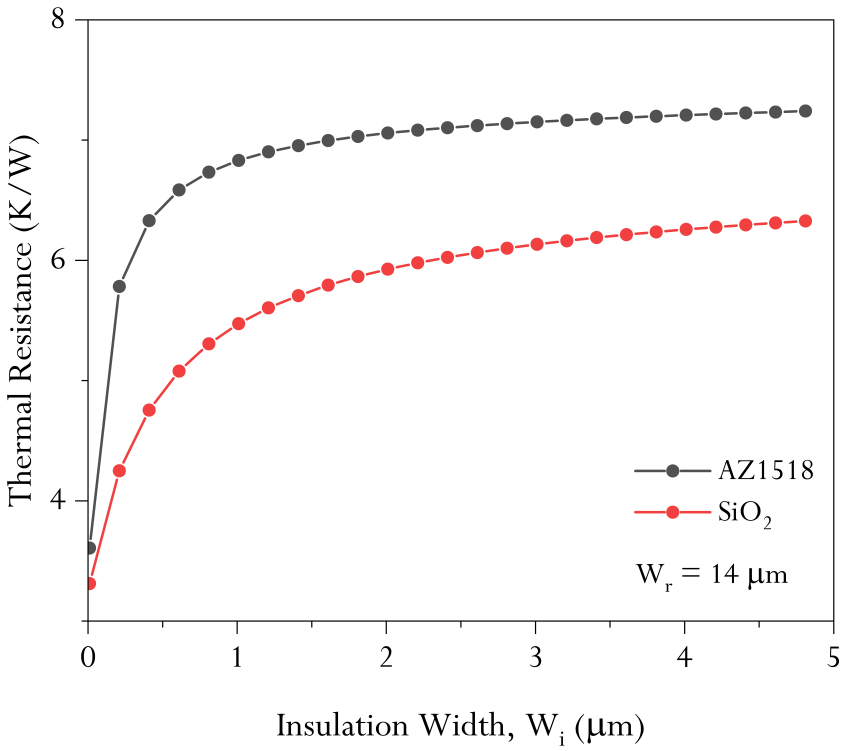


**Figure. 2.19:** Thermal resistance of QCLs at 293 K as a function of insulation width for different insulating materials.

InAs-based QCLs. With a hopeful outlook, by utilizing $SiO_2$ as insulation, we anticipate several improvements in our devices. These improvements include a reduction in threshold current density, enhancement of optical power, and lower thermal resistance. Additionally, employing $SiO_2$ as insulation should help alleviate performance fluctuations associated with photoresist insulation. In order to experimentally verify these results, we fabricated and studied QCLs insulated with $SiO_2$. The fabrication technique and results are discussed in next section.

### 2.4.3 $SiO_2$ Insulation using PECVD

PECVD (Plasma-Enhanced Chemical Vapor Deposition) is a commonly used technique in the microelectronics industry for depositing thin films of $SiO_2$. PECVD involves the use of a plasma to break down precursor gases into their constituent atoms or molecules, which then react and form a $SiO_2$ film on the substrate.

In Silane-Oxygen PECVD, available in our clean room, $SiO_2$ films deposition is performed using $SiH_4$–Ar–$N_2O$ gas mixture. $N_2O$ is used as a source of atomic oxygen. The precursors for $SiO_2$ deposition, $SiH_4$ and O, are created by plasma dissociation of feed gases. Initial surface reactions of the film growth include the surface formation of intermediate molecular oxides such as $(SiH_3)_2O$ and $SiH_3OH$ which, after further oxidation, forms final $SiO_2$ [28]

The QCL structure designed to emit at 14 µm was processed into FP ridge waveguides using standard fabrication technique. We used Silane-Oxygen PECVD at 300°C to deposit a 500-nm-thick $SiO_2$ film for insulation, followed by photolithography for metal contact opening and reactive ion etching to remove the oxide film from the top of the mesa. The fabrication was completed with metallization, polishing, and lift-off. Reference devices with photoresist insulation were also fabricated from the same wafer. The electron microscopy image of a mesa insulated with $SiO_2$ using PECVD is shown in Figure 2.20.

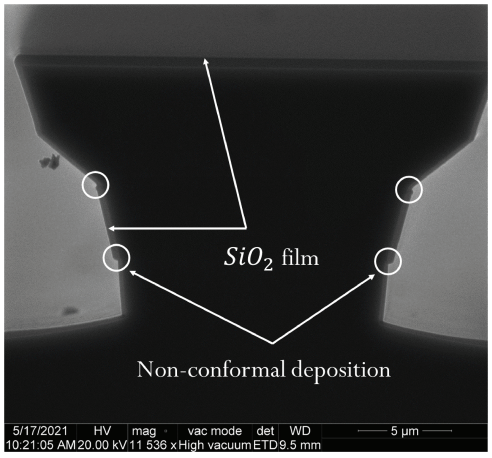


**Figure. 2.20:** Electron microscopy image of fabricated QCL ridge insulated with $SiO_2$ using PECVD.

The samples were then cleaved into 1.5-mm-long devices, mounted epilayer up onto a copper heat sink, and characterized in pulsed mode. The PIV characteristics of the QCLs insulated with photoresist and with $SiO_2$ are presented in Figure 2.21 (Left). The comparisons of the PIV curves reveal pretty unexpected results. Contrary to what was suggested

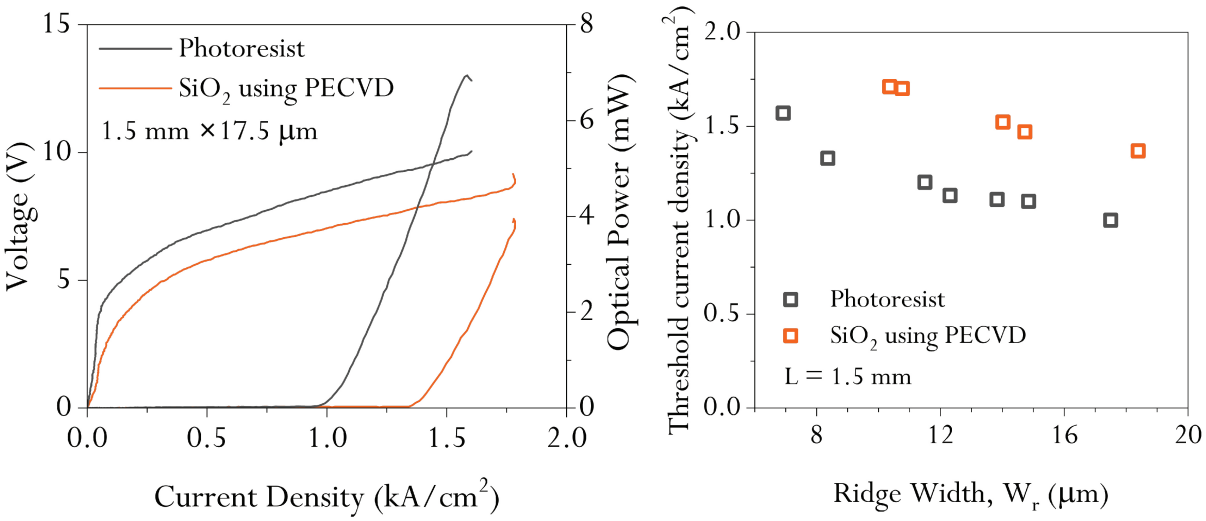


**Figure. 2.21:** Comparison of (Left) pulsed PIV characteristics and (Right) threshold current density as a function of ridge width for QCLs insulated with photoresist and $SiO_2$ using PECVD.

by the simulations, for QCLs insulated with $SiO_2$ using PECVD, both the threshold current and optical power deteriorated significantly. Several devices with varying ridge widths were measured, and we observed the same behavior, as shown in Figure 2.21 (Right) presenting the threshold current density as a function of the ridge width for both devices.

This performance degradation can be associated with the $SiO_2$ deposition environment. As discussed previously, the etched mesa sidewall surface is chemically unstable and quickly reacts with oxygen to form a native oxide on the surface. The native oxide of Indium, being highly conductive, creates parasitic channels and hence increases surface leakage, which in turn deteriorates the threshold current density. The presence of nascent oxygen during PECVD deposition further accelerates the oxide formation. Moreover, in the case of Silane-Oxygen PECVD, the high sticking coefficient of $SiH_3$ radical [28] results in non-conformal film deposition at the angled parts of the mesa, as shown in Figure 2.20. This nonconformality in the deposition can also potentially increase surface leakage.

TEOS (Tetraethylorthosilicate)-Oxygen PECVD can eliminate the problem of non-conformal

deposition [28]. However, due to its unavailability, we could not conduct the studies. Furthermore, the issue of an oxygen-rich environment persists even in this case.

### 2.4.4 $SiO_2$ Insulation using Spin-on-Glass

The previous study shows that the PECVD is not an appropriate technique for the deposition of $SiO_2$ on InAs/AlSb-based QCLs, due to an oxygen-rich deposition environment, at least in the available conditions. Hence, we need to find a suitable alternative for $SiO_2$ deposition.

In this work we proposed to use Spin-on-Glass (SOG) to deposit $SiO_2$. The SOG technique does not require expensive machinery, and the fabrication process is almost identical to that used for photoresist insulation. Furthermore, this technique also eliminates the exposure of the etched mesa to an oxygen-rich environment. However, its use as an insulation technique for long-wavelength QCLs has never been demonstrated.

After a brief introduction to Spin-on-Glass, the following section presents the fabrication of QCLs utilizing spin on glass for insulation, and device characterization.

#### 2.4.4.1 Spin-on-Glass

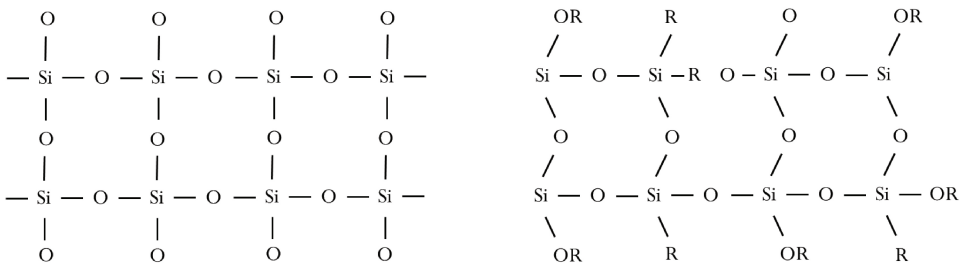

**Figure. 2.22:** Polymeric structure of (Left) Silicate and (Right) Siloxane SOG. R represents organic group.

SOG is a material representing a liquid solution of $SiO_2$ that can be deposited using spin coating, followed by a thermal [29] or RF plasma [30] curing. It has been widely used in the fabrication of integrated circuits [31] and microelectromechanical systems [32]

primarily as an insulation film and as a planarization layer. Additionally, by combining the SOG process with etching techniques, it has found applications in optical devices, biochips, and other devices, providing enhanced functionality and performance [33].

A variety of SOG materials have been synthesized to cater to diverse applications. SOGs that are based on silicates and siloxanes are frequently utilized. Silicate SOGs are made by dehydrating $Si(OH)_4$ during a condensation reaction. The resulting film has a robust Si–O network (Figure 2.22, Left) and is free of –OH groups. However, it shrinks significantly during the curing process, which creates high tensile stress that can lead to cracking problems. On the other hand, siloxane SOGs contain organic groups such as $–CH_3$ or $–C_2H_5$ (Figure 2.22, Right), which modify the Si–O network and reduce film stress. This improves crack resistance and film planarity. Siloxane SOGs are heavier and more viscous than silicate SOGs, which leads to thicker films at the same spin speed [34].

#### 2.4.4.2 Fabrication Modifications

An essential factor to investigate when comparing the advantages of utilizing siloxane versus silicate SOG pertains to the temperature required for curing. Siloxane SOG presents certain benefits concerning reduced curing temperatures compared to silicate SOG. The curing process of siloxane SOG can be accomplished at temperatures typically not exceeding 400°C [35], [36]. On the contrary, the temperatures required for silicate SOG generally are higher, frequently surpassing 800°C [29], [37]. Elevated curing temperatures can cause the sample deformation, thermal stress, or device failure, thereby restricting the scope of viable applications. Utilizing a lower curing temperature is a beneficial aspect of semiconductor fabrication that deals with substrates or devices susceptible to heat damage. The lower temperatures mitigate the likelihood of thermal degradation to fragile structures, thereby enhancing the yield and dependability of the device.

The concern of potential thermal degradation of the QCL structure led us to consider using the siloxane SOG for insulation. However, the recommended curing temperature of 400°C is still relatively high for QCL structures. A few researchers have demonstrated low-temperature curing using RF plasma [38], [30] and low-temperature thermal treatment

[29]. Hence, we explored both techniques to densify the SOG film.

The SOG was deposited on samples of InAs substrate using spin coating at 4000 and 6000 rpm for 30 seconds, followed by a triple hot plate bake sequence, 80°C, 150°C and 250°C each for 60 seconds. The sequential temperature increase allows gradual solvent evaporation, and a low initial hot plate temperature improves planarization and lower film defects [36]. The scotch tape test, commonly used to measure the adhesive strength of thin films to substrates, followed by the wire bonding test, were used to qualitatively assess the densification of the SOG film.

### RF Plasma Treatment

The samples were placed in the center of a barrel-type quartz chamber with electrodes covering half of the cylinder wall. RF power was supplied by a solid-state 13.56 MHz RF power generator. The film was treated with capacitively coupled RF plasma. The chamber was filled with oxygen at a pressure of 330 Pa. The RF power was 100 W and the treatment time was 35 min. As shown in the Figure 2.23, the scotch tape test results were disappointing as the film peeled off the substrate. The weak adhesion can be attributed to incomplete or improper densification of the SOG film. Consequently, due to weak film adhesion and an oxygen-rich environment, this particular SOG densification technique was deemed unsuitable for insulating InAs-based QCLs.

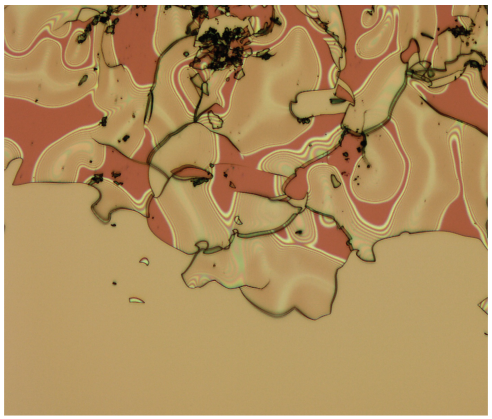

**Figure. 2.23:** The SOG film densified using RF plasma treatment exhibits poor adhesion as it peels off during the Scotch Tape Test.

### Low-Temperature Thermal Treatment

In this particular technique, the samples were carefully positioned within a temperature controlled oven. The oven was equipped with a fan to ensures the homogeneous distribution of heat. The temperature was precisely adjusted to the desired value, while the temperature increase rate was regulated at a steady 5 degrees per minute. Once the temperature reached the designated set point, it was maintained consistently for a specified duration. The experiment was conducted repeatedly, incorporating various samples, each with distinct set points and durations. The details of this study are shown in Table 2.3.

| Sample | Spin coating | Temperature (°C) | Time (h) | Scotch test | Wire bonding |
|---|---|---|---|---|---|
| 1 | 4000 rpm 30 s | 200 | 2.5 | × | × |
| 2 | 6000 rpm 30 s | 200 | 2.5 | × | × |
| 3 | 4000 rpm 30 s | 200 | 4 | ✓ | × |
| 4 | 6000 rpm 30 s | 200 | 4 | ✓ | × |
| 5 | 4000 rpm 30 s | 250 | 2.5 | ✓ | ✓ |
| 6 | 6000 rpm 30 s | 250 | 2.5 | ✓ | ✓ |

**Table 2.3:** Parameters and test results for thermal treatment of SOG samples.

The experiment yielded interesting results regarding the effect of different baking temperatures and durations on the properties of the SOG film. Samples subjected to a baking temperature of 200°C for 2.5 or 4 hours exhibited unsuccessful outcomes in both the scotch tape test and wire bonding tests. However, when the temperature was increased to 250°C for 2.5 hours, significant improvements were observed. The samples treated at 250°C displayed the good adhesive strength, successfully passing both tests. This highlights the importance of baking temperature and duration in achieving the desired characteristics of the SOG film. The findings suggest that a higher temperature of 250°C for 2.5 hours is optimal for densifying the SOG film for insulating InAs-based QCls as it promotes the necessary hardening and enhances adhesion.

It is crucial to acknowledge that the optimizations mentioned above were carried out for

flat samples. However, when we applied the optimized procedure to samples with etched ridges and coated them with a single layer of SOG, we observed a disruption in the insulation layer on the ridge edges. This occurred due to the presence of tall mesa structures and the low viscosity of the SOG, resulting in irregular features depicted as squiggles in Figure 2.24 (Left). As a consequence, the devices experienced short circuits, rendering them non-functional. To address this issue, we implemented two coats of the SOG film. Fortunately, even with the thicker SOG film, we were able to achieve satisfactory film quality by subjecting it to a baking process at 250°C for 2.5 hours. This effectively resolved the discontinuity problem as illustrated in Figure 2.24 (Right) and allowed to fabricate functional devices.

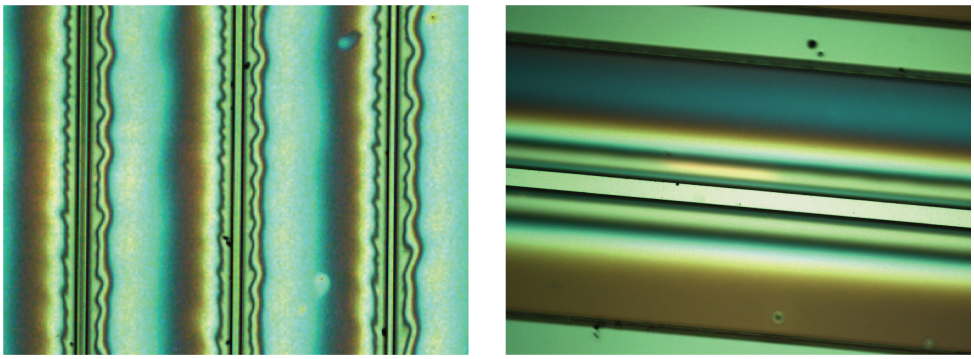

**Figure. 2.24:** (Left) Discontinuity in single coat SOG film. (Right) No discontinuity in two coat SOG film.

Finally, we evaluated two options for removing the SOG film from the mesa top: dilute HF etching and RIE. However, we faced difficulties with HF etching as the etch rate of was high and hard to control. On the other hand, RIE offered better control, although longer etch times and high RF power caused photoresist burning, especially with thinner layers. This issue was mitigated by using thicker photoresist layers. Ultimately, we chose RIE as the preferred method for its controllability while addressing the photoresist burning concern by adjusting the thickness. Figure 2.25 shows the post-etch electron microscopy image of the QCL ridge insulated with $SiO_2$ using SOG technique. A photoresist layer is used to protect the lateral $SiO_2$ layer during etching.

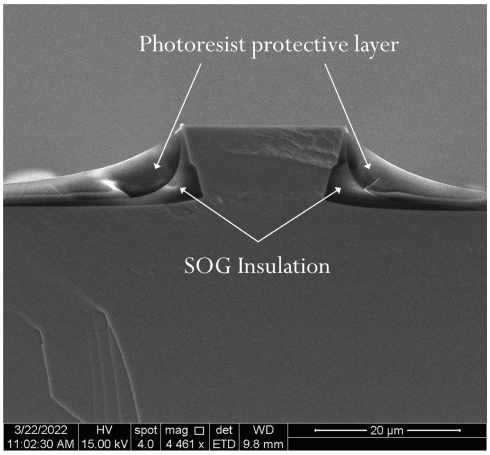


**Figure. 2.25:** Post-etch electron microscopy image of fabricated QCL ridge insulated with $SiO_2$ using SOG, with a photoresist layer utilized to shield the lateral $SiO_2$ layer during etching.

#### 2.4.4.3 Characteristics of QCLs Insulated with $SiO_2$ using SOG

In line with the discussion in Section 2.4.3, a new set of FP ridge lasers insulated with $SiO_2$ using SOG technique was fabricated using the same QCL structure. The PIV characteristics of the new and the reference devices are shown in Figure 2.26 (Left). In contrast to the devices insulated using PECVD, the new devices demonstrated threshold current and optical power comparable to reference devices, if not better. This consistency was observed across multiple devices with different ridge widths, as depicted in Figure 2.26 (Right). The observed high quality of the SOG insulator can be attributed to the low deposition temperature (room temperature) and most importantly the absence of an oxygen-rich environment, particularly nascent oxygen. This finding confirms our previous hypothesis and supports the viability of using SOG technique as an alternative to the photoresist insulation.

Furthermore, to study the effect on the device performance after being subjected to elevated temperatures, the new devices ($\lambda = 14$ $\mu$m) insulated with $SiO_2$ using SOG were fabricated. They were then characterized in two different temperature cycles as discussed before. The PIV characteristics and threshold current density as a function of temperature are presented in Figure 2.27 and Figure 2.28 respectively. The results

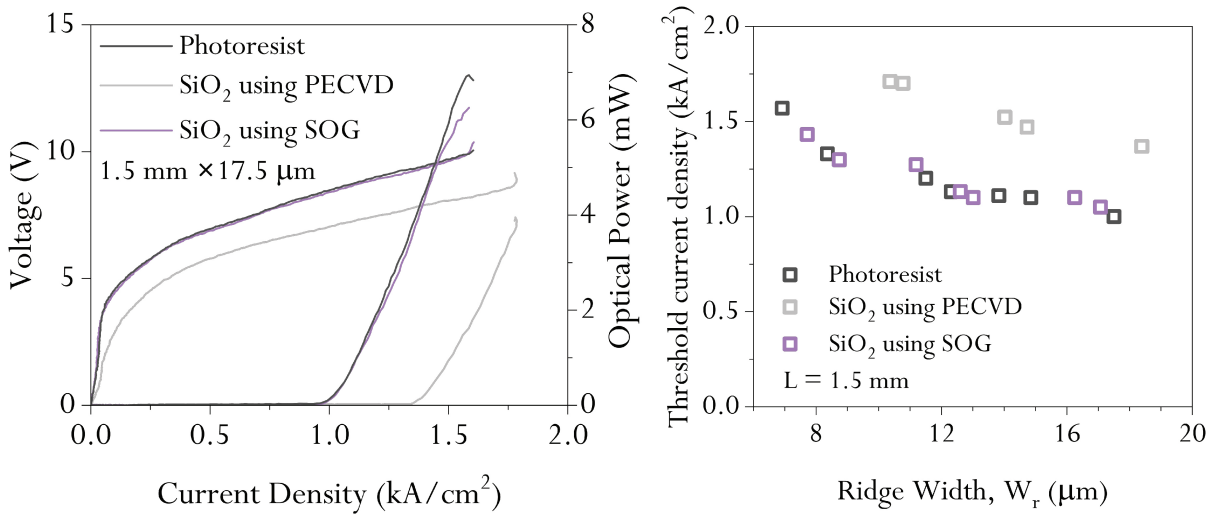


**Figure. 2.26:** (Left) Comparison of pulsed PIV characteristics and (Right) threshold current density as a function of ridge width for QCLs insulated with photoresist, $SiO_2$ using PECVD and SOG.

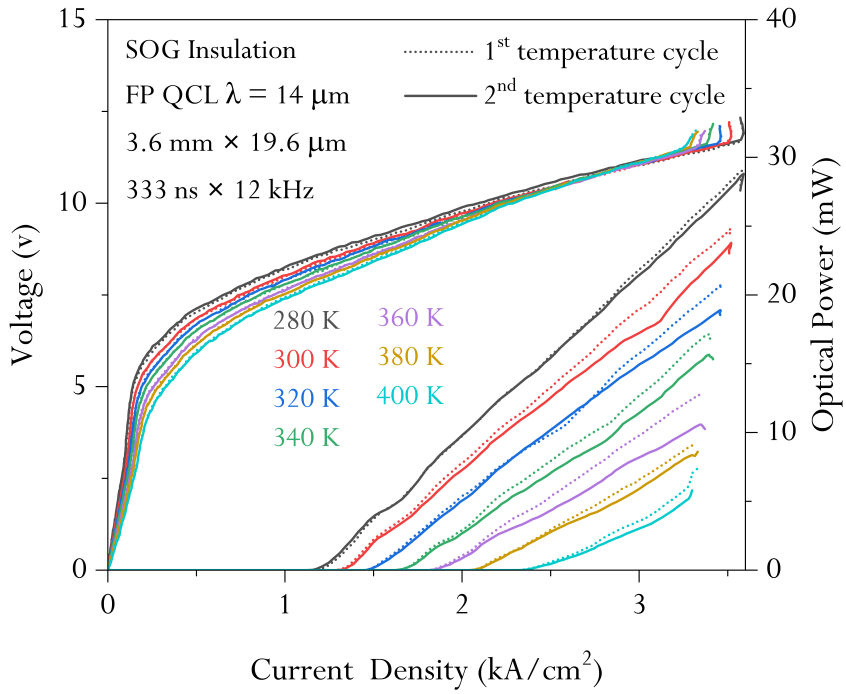


**Figure. 2.27:** PIV characteristics of FP QCL, insulated with $SiO_2$, in different temperature cycles. The emission wavelength is 14 $\mu$m.

show that the devices insulated using SOG do not suffer from the issues presented by the photoresist insulation. In both temperature cycles the threshold current and the optical power remained similar, making the device immune to the effects of elevated temperatures.

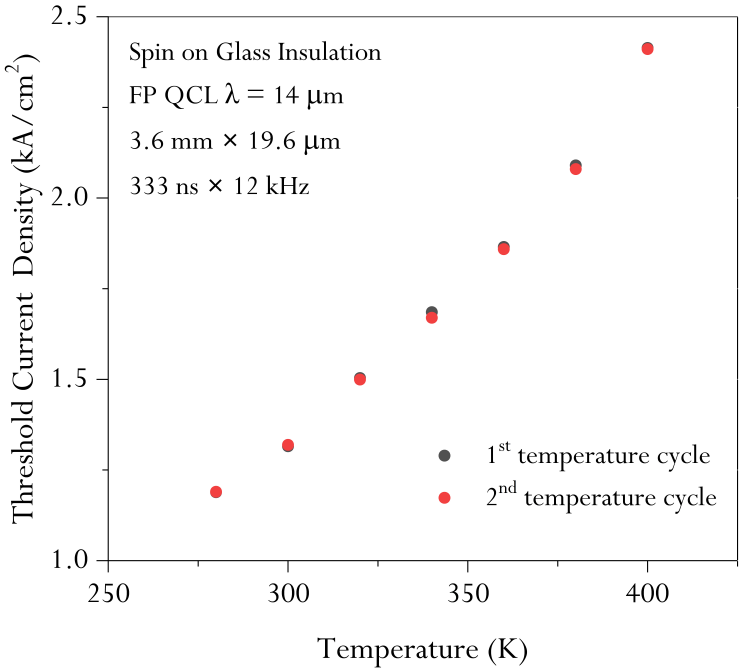


**Figure. 2.28:** Threshold current density as a function of temperature shows no change in different temperature cycles.

To study the effect of improved thermal conductivity of $SiO_2$, we calculated the thermal resistance ($R_{th}$) of the devices using the equation

$$R_{th} = \frac{\Delta T}{V \cdot A \cdot J} \tag{2.5}$$

Where, $\Delta T$ is the difference in temperature where the threshold current density is same in both pulsed and CW operation, $V$ is the bias voltage, $A$ is the product of length and width of the device active zone, and $J$ is the threshold current density. The devices were characterized in pulsed and CW operation. The threshold current density as a function of temperature in both operation modes presented in Figure 2.29. Figure 2.29 (Left) and Figure 2.29 (Right) corresponds to the devices insulated with photoresist and $SiO_2$ using

SOG respectively.

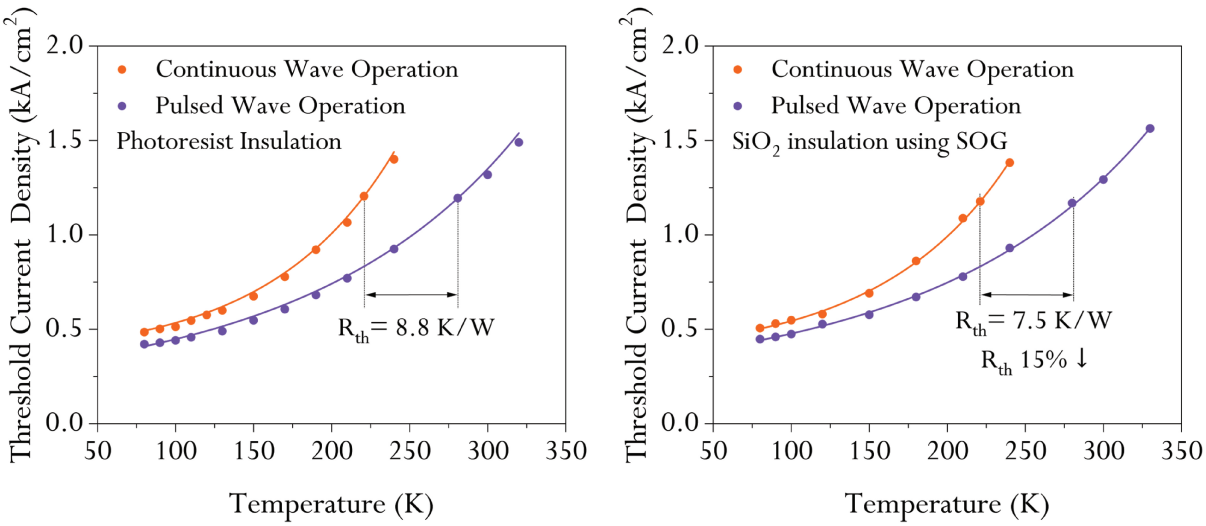


**Figure. 2.29:** Threshold current density as function of temperature in pulsed and continuous wave operation for QCLs insulated with (Left) Photoresist and (Right) $SiO_2$ using Spin on Glass shows the reduction in thermal resistance in later case.

The thermal resistance in both cases is slightly higher than suggested by the simulation. However, the relative improvement remains consistent. In the case of photoresist insulation, the thermal resistance was measured to be 8.8 K/W, whereas for SOG insulation, it was 7.5 K/W, indicating a 15% improvement. Finally, we successfully bonded the gold wires to the SOG-insulated QCLs Using an automatic wire bonding machine as depicted in Figure 2.30.

It is worth noting that all the SOG insulation results discussed above pertain to QCLs that emit at a wavelength of 14 $\mu$m. Unfortunately, the QCLs emitting near 7 $\mu$m were not tested due to time constraints. However, based on the refractive index profile of $SiO_2$ shown in Figure 2.31, it is reasonable to hypothesize that the QCLs emitting near 7 $\mu$m will outperform those emitting at 14 $\mu$m. This is due to the significant decrease in refractive index as well as the extinction coefficient of $SiO_2$ below 9 $\mu$m which should lead to reduced leakage of the optical mode into the insulator and decreased absorption. Thus, $SiO_2$ insulation should improve both the threshold current density and the optical power of the lasers operating in this wavelength range.

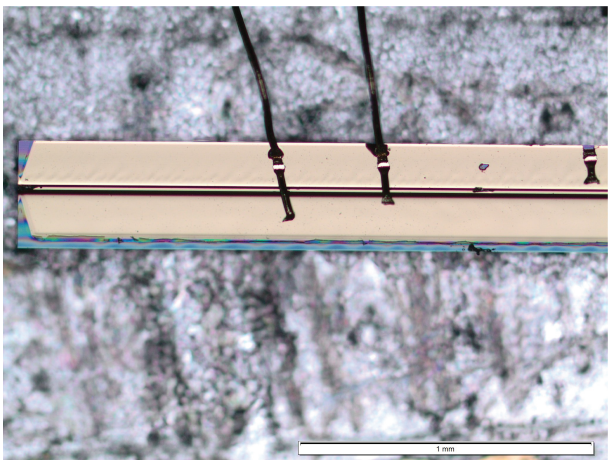

**Figure. 2.30:** An optical image of the fabricated QCLs insulated with $SiO_2$ using spin on glass show successful wire bonding attempts.

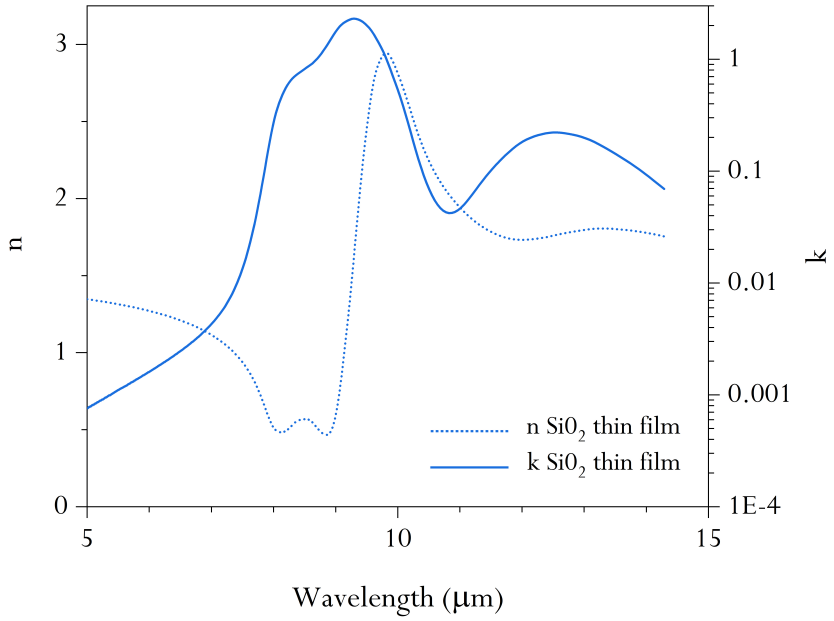


**Figure. 2.31:** n and k of $SiO_2$ thin film as a function of wavelength [24]

## 2.5 Conclusion

This chapter focused on the fabrication of InAs-based QCLs and highlighted the drawbacks of the photoresist insulation commonly used for these devices. A new insulation technology has been developed to address these issues. The use of hard-baked photore-

sist as an insulation material for InAs-based QCLs offers a mature and robust insulation technique with standardized fabrication protocols, whereas its polymeric nature and plastic-like properties pose challenges. Elevated temperatures lead to device performance fluctuations due to modifications of its optical properties caused in particular by residual stress. These fluctuations manifest as temporary modifications in the threshold current, optical power, and emission wavelength.

To ensure the stability of devices, we investigated alternative materials for insulation of InAs-based QCLs. We performed a comprehensive simulation analysis using COMSOL to evaluate the performance of common hard dielectric materials, namely $SiO_2$, $Si_3N_4$, and $TiO_2$. The obtained results showed that $SiO_2$ is an attractive alternative for photoresist insulation.

However, the lasers fabricated using PECVD, a conventional $SiO_2$ deposition technique, exhibited significant leakage currents caused by degradation of initially unprotected etched mesa walls due to the presence of oxygen-rich deposition environment. To overcome this problem, we developed an insulation technology based on spin-on-glass (SOG). The process includes SOG deposition by spin coating followed by bakeout forming a film of solid $SiO_2$. Careful process optimization allowed us to fabricate high performance QCLs, mitigate all the issues related to photoresist insulation.

# Bibliography


[1] Microchemicals GmbH. AZ nLOF 2020 Photoresist. URL: https://www.microchemicals.com/products/photoresists/az_nlof_2020.html.

[2] Kayaku Advanced Materials. Remover PG. URL: https://kayakuam.com/wp-content/uploads/2020/11/KAM-Remover-PG-TDS.10.29.20-final.pdf.

[3] Microchemicals GmbH. AZ 1518 Photoresist. URL: https://www.microchemicals.com/products/photoresists/az_1518.html.

[4] Alexei N. Baranov, Michael Bahriz, and Roland Teissier. Room temperature continuous wave operation of InAs-based quantum cascade lasers at 15 $\mu m$. *Optics Express*, 24, 8 2016. doi:10.1364/OE.24.018799.

[5] Z. Loghmari, M. Bahriz, D. Díaz Thomas, A. Meguekam, H. Nguyen Van, R. Teissier, and A.N. Baranov. Room temperature continuous wave operation of InAs/AlSb-based quantum cascade laser at $\lambda = 11\ \mu m$ . *Electronics Letters*, 54, 8 2018. doi:10.1049/el.2018.5258.

[6] Z. Loghmari, M. Bahriz, A. Meguekam, R. Teissier, and A.N. Baranov. InAs-based quantum cascade lasers emitting close to 25 µm. *Electronics Letters*, 55, 2 2019. doi:10.1049/el.2018.6413.

[7] Microchemicals GmbH. AZ nLoF 2070 Photoresist. URL: https://www.microchemicals.com/products/photoresists/az_nlof_2070.html.

[8] G. Chen, B.-M. Nguyen, A. M. Hoang, E. K. Huang, S. R. Darvish, and M. Razeghi. Elimination of surface leakage in gate controlled type-II InAs/GaSb mid-infrared photodetectors. *Applied Physics Letters*, 99:183503, 10 2011. doi:10.1063/1.3658627.

[9] Elena A. Plis, Maya Narayanan Kutty, and Sanjay Krishna. Passivation techniques for InAs/GaSb strained layer superlattice detectors. *Laser & Photonics Reviews*, 7:45–59, 1 2013. doi:10.1002/lpor.201100029.

[10] Aaron Gin, Yajun Wei, Junjik Bae, Andrew Hood, Jongbum Nah, and Manijeh Razeghi. Passivation of type II InAs/GaSb superlattice photodiodes. *Thin Solid Films*, 447-448:489–492, 1 2004. doi:10.1016/j.tsf.2003.09.002.

[11] B.T. Seok, S.Y. Kim, D.H. Jun, and J.H. Jang. Mesa-type quantum cascade lasers fabricated by using inductively coupled plasma reactive ion etching. *Electronics Letters*, 55:660–661, 5 2019. doi:10.1049/el.2018.7571.

[12] Simon Ferré, Alba Peinado, Enric Garcia-Caurel, Virginie Trinité, Mathieu Carras, and Robson Ferreira. Comparative study of $SiO_2$, $Si_3N_4$ *and* $TiO_2$ thin films as passivation layers for quantum cascade lasers. *Optics Express*, 24, 10 2016. doi:10.1364/OE.24.024032.

[13] P. Laffaille, J. C. Moreno, R. Teissier, M. Bahriz, and A. N. Baranov. High temperature operation of short wavelength InAs-based quantum cascade lasers. *AIP Advances*, 2:022119, 6 2012. doi:10.1063/1.4714363.

[14] Z. Loghmari, J.-B. Rodriguez, A. N. Baranov, M. Rio-Calvo, L. Cerutti, A. Meguekam, M. Bahriz, R. Teissier, and E. Tournié. InAs-based quantum cascade lasers grown on on-axis (001) silicon substrate. *APL Photonics*, 5:041302, 4 2020. doi:10.1063/5.0002376.

[15] Kumar Kinjalk, Daniel Andres Díaz-Thomas, Zeineb Loghmari, Michael Bahriz, Roland Teissier, and Alexei N. Baranov. InAs-Based Quantum Cascade Lasers with Extremely Low Threshold. *Photonics*, 9:747, 10 2022. doi:10.3390/photonics9100747.

[16] Jeffrey Facer Taylor. An experimental evaluation of the state of stress and mechanical performance of a polyacrylate photoresist coating, 1993. URL: https://scholarworks.umass.edu/dissertations_1/810.

[17] A. Schiltz and P.J. Paniez. In-situ determination of photoresist glass transition temperature by wafer curvature measurement techniques. *Microelectronic Engineering*, 27:413–416, 2 1995. doi:10.1016/0167-9317(94)00136-I.

[18] TPT Wire Bonder GmbH. Wire Bonding Technology. URL: https://www.tpt-wirebonder.com/.

[19] G. Rehouma, C. A. Evans, Z. Ikonić, D. Indjin, and P. Harrison. Comparison of $SiO_2$, $Si_3N_4$, $As_2S_3$, *and* $Ge_{0.25}Se_{0.75}$ dielectric layers for InP- and GaAs-based material systems for midinfrared quantum cascade laser waveguides. *Journal of Applied Physics*, 106:053104, 9 2009. doi:10.1063/1.3197858.

[20] JoonHyun Kang, Hyun-Duk Yang, Beom Soo Joo, Joon-Suh Park, Song ee Lee, Shinyoung Jeong, Jihoon Kyhm, Moonsup Han, Jin Dong Song, and Il Ki Han. Quantum cascade lasers with Y2O3 insulation layer operating at 8.1 $\mu m$. *Optics Express*, 25:19561, 8 2017. doi:10.1364/OE.25.019561.

[21] Raffaele Colombelli, Federico Capasso, Claire Gmachl, Albert L. Hutchinson, Deborah L. Sivco, Alessandro Tredicucci, Michael C. Wanke, A. Michael Sergent, and Alfred Y. Cho. Far-infrared surface-plasmon quantum-cascade lasers at 21.5 $\mu m$ and 24 $\mu m$ wavelengths. *Applied Physics Letters*, 78:2620–2622, 4 2001. doi:10.1063/1.1367304.

[22] Carlo Sirtori, Claire Gmachl, Federico Capasso, Jérôme Faist, Deborah L. Sivco, Albert L. Hutchinson, and Alfred Y. Cho. Long-wavelength ($\lambda = 8 - 11.5$ $\mu m$) semiconductor lasers with waveguides based on surface plasmons. *Optics Letters*, 23:1366, 9 1998. doi:10.1364/OL.23.001366.

[23] Zeineb Loghmar. Lasers à cascades quantiques InAs/AlSb au-delà de 10µm : Emission mono-fréquence et génération du THz par différence de fréquences, 2019.

[24] Jan Kischkat, Sven Peters, Bernd Gruska, Mykhaylo Semtsiv, Mikaela Chashnikova, Matthias Klinkmüller, Oliana Fedosenko, Stephan Machulik, Anna Aleksandrova, Gregorii Monastyrskyi, Yuri Flores, and W. Ted Masselink. Mid-infrared optical properties of thin films of aluminum oxide, titanium dioxide, silicon dioxide, aluminum nitride, and silicon nitride. *Applied Optics*, 51:6789, 10 2012. doi:10.1364/AO.51.006789.

[25] Physico-Technical Institute. InAs Thermal properties. URL: http://www.ioffe.ru/SVA/NSM/Semicond/InAs/thermal.html.

[26] T. Borca-Tasciuc D. Achimov, W. L. Li. Thermal conductivity of InAs/ AlSb Superlattice. *Microscale Thermophysical Engineering*, 5:225–231, 7 2001. doi:10.1080/108939501753222896.

[27] S.-M. Lee, David G. Cahill, and Thomas H. Allen. Thermal conductivity of sputtered oxide films. *Physical Review B*, 52:253–257, 7 1995. doi:10.1103/PhysRevB.52.253.

[28] Alexander Fridman. *Plasma Chemistry*. Cambridge University Press, 5 2008. doi:10.1017/CBO9780511546075.

[29] Miguel A. Dominguez, Pedro Rosales, Alfonso Torres, and Mario Moreno. Effects of Curing Time on Properties of Spin-On Glass as Low-Temperature Insulator. *MRS Proceedings*, 1436:mrss12–1436–k05–01, 2 2012. doi:10.1557/opl.2012.1521.

[30] Tomoya Yoshida, Masayoshi Nagao, Hisashi Ohsaki, Takashi Shimizu, and Seigo Kanemaru. Densification of spin-on-glass (SOG) film by RF plasma treatment. *IOP Conference Series: Materials Science and Engineering*, 18:032007, 10 2011. doi:10.1088/1757-899X/18/3/032007.

[31] Li Peng, Wenbin Zhao, Guozhang Wang, and Zongguang Yu. Development of spin-on-glass process for triple metal interconnects. *Journal of Semiconductors*, 31:126003, 12 2010. doi:10.1088/1674-4926/31/12/126003.

[32] Zhibo Ma, Yinan Wang, Qiang Shen, Han Zhang, and Xuetao Guo. Key Processes of Silicon-On-Glass MEMS Fabrication Technology for Gyroscope Application. *Sensors*, 18:1240, 4 2018. doi:10.3390/s18041240.

[33] A. S. Holmes, R. R. A. Syms, Ming Li, and Mino Green. Fabrication of buried channel waveguides on silicon substrates using spin-on glass. *Applied Optics*, 32:4916, 9 1993. doi:10.1364/AO.32.004916.

[34] C. Chiang and D.B. Fraser. Understanding of spin-on-glass (SOG) properties from their molecular structure. pages 397–403. IEEE. doi:10.1109/VMIC.1989.78000.

[35] H. C. Lin, K. L. Chang, G. W. Pickrell, K. C. Hsieh, and K. Y. Cheng. Low temperature wafer bonding by spin on glass. *Journal of Vacuum Science & Technology B: Microelectronics and Nanometer Structures Processing, Measurement, and Phenomena*, 20:752–754, 3 2002. doi:10.1116/1.1464832.

[36] Honeywell. Spin / Bake / Cure Procedure for Spin-On-Glass Materials For Interlevel and Intermetal Dielectric Planarization. URL: https://wiki.nanotech.ucsb.edu/w/images/c/c4/512B-Application-Data-Bake-revA.pdf.

[37] FA van Vught. Spin-on Glass materials and applications in advanced ic technologies, 1999.

[38] H. Ohsaki, Y. Shibayama, N. Yoshida, T. Watanabe, and S. Kanemaru. Room-temperature crystallization of amorphous films by RF plasma treatment. *Thin Solid Films*, 517:3092–3095, 3 2009. doi:10.1016/j.tsf.2008.11.086.

# Chapter 3

# DFB QCLs for BTEX and Propane Detection

## 3.1 Introduction

The spectral coherence of the emitted radiation is a crucial parameter, along with the emission wavelength and spectral tuning range. It plays a vital role in achieving high selectivity for distinguishing various species with similar ro-vibrational frequencies. In gas-phase analysis, particularly, a single frequency emission is required [1] to ensure accurate resolution.

A laser cavity can support multiple longitudinal modes, each with a different resonant frequency, thus forming multi-frequency output. In order to achieve single frequency emission, it is necessary to suppress all but one of the longitudinal modes. In addition, a laser cavity can support multiple transverse modes, each with a different spatial profile and effective refractive index, which further complicate the structure of the emission spectrum and makes the selection of a single longitudinal mode more difficult.

Single frequency emission can be obtained quite easily if the optical gain is homogeneous in frequency and space over the entire volume of the active media. Only the first lasing mode is amplified above the threshold in this case. Any gain nonuniformity caused by spa-

tial or spectral hole burning results in competition between different longitudinal modes depending on the current. This mechanism can be suppressed if the carrier diffusion in the active region is faster than characteristic times of the lasing transition. Unfortunately, due to the fast gain recovery, in the range of picosecond, this preferred single mode emission is not inherently obtained. The gain recovery process is quicker than carrier diffusion, and spatial hole burning takes precedence, favoring multimode operation, often making the devices unsuitable for most applications in spectroscopy [1]. To favor single frequency emission a variety of laser structures have been proposed: short-cavity lasers [2], coupled-cavity lasers [3], injection locked lasers [4], distributed Bragg reflector (DBR) lasers and distributed feedback (DFB) lasers [5]. Among these, DFB lasers employing a diffraction grating delivering selective optical feedback to the gain medium is the most well-established technology to achieve the single frequency operation regime.

In this chapter, we provide a concise introduction to the operational principles of DFB lasers and explore different design variations of gratings in terms of their position in relation to the active zone. We also explore the tuning mechanisms of DFB QCLs. Next, we delve into the optimization of the DFB structure to achieve high-performance devices with effective mode control. Additionally, we discuss the subsequent fabrication steps and highlight the key characteristics of the fabricated devices suitable for detecting BTEX and Propane.

## 3.2 Distributed Feedback Lasers

### 3.2.1 Working Principle

In the conventional FP laser, the optical feedback required for the laser operation is provided by reflection from mirrored facets at the extremities of the laser cavity. The reflection magnitude in such FP resonator remains the same for all longitudinal modes. The only mode discrimination in such a laser is provided by the gain spectrum itself. However, since the gain spectrum is usually much wider than the longitudinal-mode spacing, the resulting emission spectrum is essentially multimode.

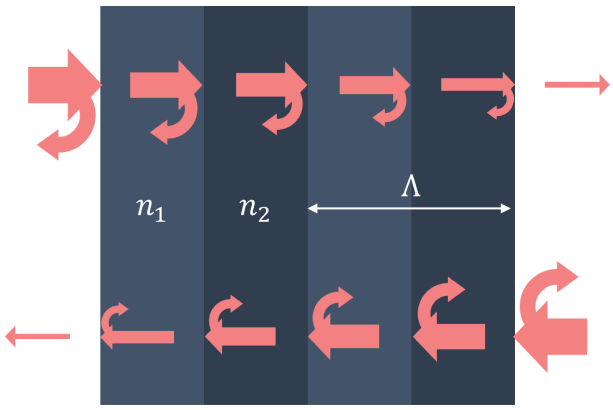


**Figure. 3.1:** A schematic illustration of Bragg resonator showing the reflection occurring at each interface. $n_1$ and $n_2$ are the refractive index of the materials with $n_1 > n_2$.

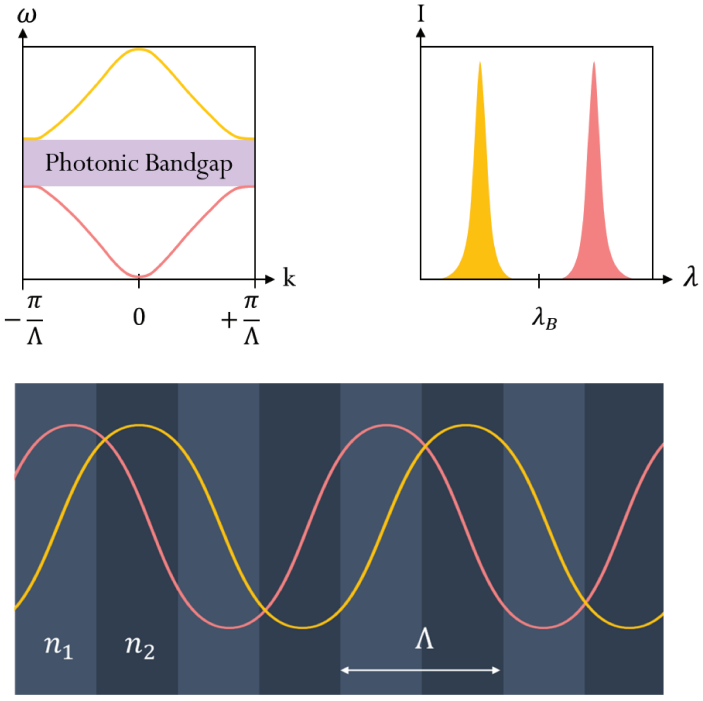


**Figure. 3.2:** (Top Left) Optical band diagram, (Top Right) Spatial response of DFB and (Bottom) Local electric field distribution of two standing waves in a grating with periodic perturbation of refractive index.

One the other hand, in DFB laser, first demonstrated theoretically in 1971 by [6], the feedback necessary for lasing action is distributed throughout the entire laser cavity (which explains the origin of the name), using a Bragg grating providing a periodic variation of the

refractive index. The Bragg grating is incorporated into the laser waveguide along the light propagation direction. The periodic perturbation of the refractive index provides feedback by means of backward scattering, which couples the forward and backward propagating waves [6], as shown in Figure 3.1. This allows for the selection of a single frequency within the gain that is provided by the active medium. The relationship between the grating period ($\Lambda$) and the Bragg wavelength ($\lambda_B$), at which the coherent coupling between the counter propagating waves occurs, is governed by the expression

$$\lambda_B = \frac{2\Lambda n_{eff}}{m} \tag{3.1}$$

where $n_{eff}$ is the effective refractive index of the waveguide and $m$ is an integer denoting the order of the grating.

From Equation (3.1), while it would seem reasonable to expect the grating to filter a single wavelength and thus provide single longitudinal-mode emission, the reality is more complicated because the waveguide supports multiple standing waves as shown in Figure 3.2. These standing waves have different effective refractive index. For a more comprehensive grasp of the spectral behavior of a DFB device, it is beneficial to direct our attention toward the principles of photonic crystal theory [7]. In this context, a photonic crystal can be described as a periodic material where the light travels. Consequently, it becomes evident that a DFB grating is essentially an one-dimensional photonic crystal.

Now, in a periodic layered media, as it is the case for electrons in semiconductor materials, the period induces a zone where no optical frequencies are allowed between the lower and the upper curves of the diagram as shown in Figure 3.2 (Top Left). This zone is called the photonic bandgap ($\Delta\omega$) and the higher the index difference between the layers, the wider the bandgap. The photonic bandgap can be expressed as

$$\Delta\omega = \frac{2\kappa C}{n_{eff}} \tag{3.2}$$

Where, $\kappa$ is coupling coefficient. At the edges of the Brillouin zone, the dispersion relation's slope becomes equal to zero: $\nu_g = d\omega/dk = 0$ at each side of the bandgap. This means that two stationary waves are trapped in the grating as shown in Figure 3.2 (Bottom). Therefore, two mode configurations are possible: the stationary wave can either have its energy mostly concentrated in the layers with higher refractive index ($n_1$) or those with lower refractive index ($n_2$). The low frequency modes have their energy concentrated in high index regions while the high frequency modes have theirs in lower index regions. The lower band in Figure 3.2 (Top Left) corresponds to the case where the electric field is concentrated in the layers with index $n_1$ and the upper band to the case where it is in the layers with index $n_2$. Thus, a DFB laser containing such a grating exhibits two peaks in its spectrum, symmetrically distributed about Bragg wavelength, as displayed on Figure 3.2 (Top Right).

These two modes are equally likely to lase. Therefore, to achieve single frequency emission, the design of the device must be optimized in order to prioritize excitation of only one mode. There are several approaches to accomplish this task. The first approach relies on an unsymmetric gain curve. Typically, the peak of the gain curve does not align precisely with the Bragg frequency. As a result, one of the modes has a higher gain and is preferentially excited. However, this mechanism is relatively weak and lasers relying solely on it lack stability. Another method involves utilizing asymmetry in radiation loss, which is a more efficient selection mechanism. A lower threshold gain for one mode can be obtained. As it will be discussed later, in this thesis we explored DFB with a metal grating deposited on the etched surface of the lasers ridge. The loss asymmetry and optical coupling with the gain medium required to achieve single frequency emission can be obtained in this case by careful optimization of the grating depth and its position relative to the waveguide core. Now we will consider the issues related to the grating design.

### 3.2.2 DFB Design Choice

Diffraction gratings employed in DFB lasers can be of two main configurations depending on their position in the laser waveguide: buried gratings and surface gratings as shown in Figure 3.3. A buried grating, as the name suggests, is embedded within the epitaxial structure through the process of patterning, etching and epitaxial regrowth. By employing this approach, the grating can be positioned in close proximity to the active zone, thereby yielding a substantially high coupling [8]. The increased spatial overlap between the mode and the grating provides a robust mode control although at the cost of reduced index contrast. The reduced index contrast poses the potential risk of escalating the internal loss [9, 10]. Moreover, this approach makes it impossible to adjust the DFB parameters once the grating is integrated into the semiconductor structure, thus limiting the ability to tune the device performance through post-growth wafer processing.

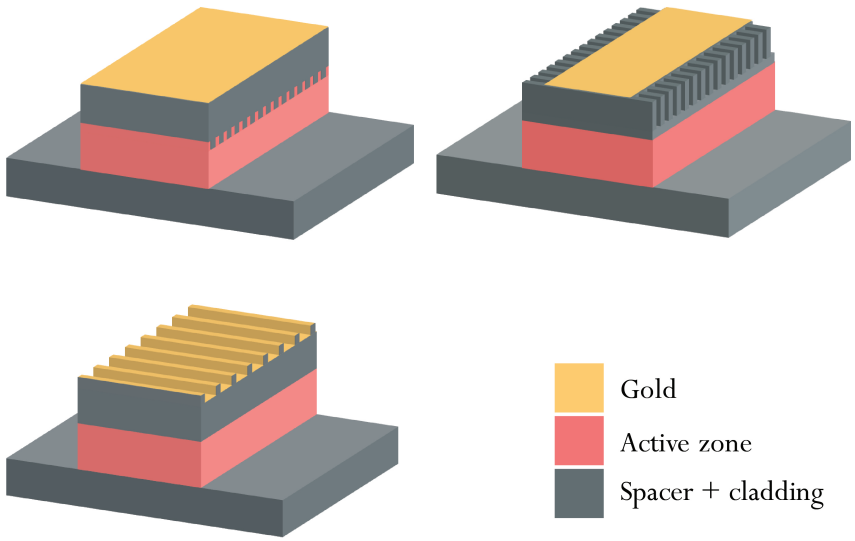


**Figure. 3.3:** Illustration of (Top Left) Buried index, (Top Right) Lateral surface etched and (Bottom Left) Top surface etched gratings.

Additionally, this approach faces another serious issue, especially when working with the Al-containing semiconductors. There is a risk of oxidation and/or contamination of the core of the structure during patterning of the grating. Hence, prior to regrowth, special cleaning procedures are required, which makes the fabrication process particularly

challenging and expensive [11]. In contrast, surface gratings are etched on the fully grown epitaxial structure thus providing a possibility to adjust the device characteristics by modifying the post-growth processing.

Several types of surface etched gratings have been described in the literature [12–14]. The top surface etched grating (Figure 3.3 , Bottom Left) exploits the refractive index variation between the semiconductor and the air or metal. Lateral gratings modulate mainly the losses (Figure 3.3 , Bottom Right). In this work we explore DFB lasers based on the design proposed in [15]. In this design a periodic structure is patterned by etching the top cladding of a QCL structure. A metallic layer is then deposited on the etched grating waveguide providing both modulation of the refractive index and electrical contact to the structure. The loss of the optical mode and its coupling with the DFB region depends on the grating depth and its distance from the active zone of the structure.

### 3.2.3 Wavelength Tuning

Tunable lasers hold immense significance and importance in the field of spectroscopy due to their ability to selectively excite analyte by precisely matching the excitation wavelength to the analyte's absorption line. The large spectral coverage enables the exploration of a wide range of materials. In particular, tunable lasers play a vital role in time-resolved spectroscopy, enabling the capture and analysis of rapid changes occurring in dynamic processes.

In DFB QCLs, the primary mechanism for tuning the wavelength involves the temperature dependent changes in the refractive index. The alterations in temperature lead to shifts in the refractive index, approximately at a rate of $2.6 \times 10^{-5}$ $K^{-1}$ [16], which, in turn, results in a change in the emitted wavelength. Although temperature variations also impact the grating period through thermal expansion and compression, with an estimated rate of around $4.5 \times 10^{-6}$ $K^{-1}$ [17], this effect is relatively weak. The relationship of temperature dependent change in emission wavelength can be expressed as follows:

$$\frac{1}{\lambda_{DFB}}\frac{d\lambda_{DFB}}{dT} = \frac{1}{n_{eff}}\frac{dn_{eff}}{dT} + \frac{1}{\Lambda}\frac{d\Lambda}{dT} \tag{3.3}$$

Where, $\lambda_{DFB}$ and $T$ are the emission wavelength of DFB and the temperature respectively.

Temperature modulation can be accomplished either through an external heater/cooler or by changing the current. The lasing wavelength typically shifts by a few nanometers per K or mA and the tuning range is limited by the maximum operating temperature and the maximum operating current. Typically, a long-wavelength DFB-QCLs can be tuned over a range of about 2 $cm^{-1}$.

## 3.3 DFB Design Optimization

In this section we will discuss optimization of different parameters of the DFB structure required to achieve desired laser performance. Alongside selecting the appropriate grating period ($\Lambda$) for precise wavelength selection, optimisation of the grating etch depth ($d$) and its separation distance ($h = clad - d$) from the active zone, as shown in Figure 3.4, is necessary. The optimal set of these parameters can be established using an iterative combination of simulations and fabrication.

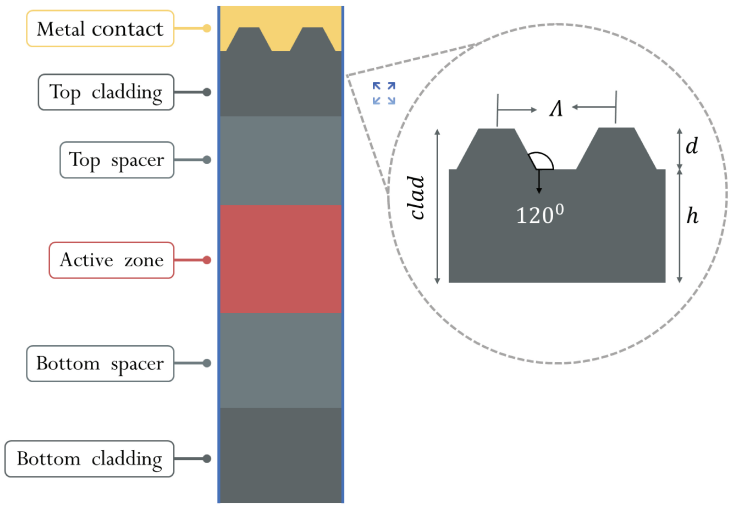


**Figure. 3.4:** Illustration of simulated DFB QCL structure.

We will now consider the DFB optimization process for QCLs operating at 14.3 $\mu$m. First, an index-coupled DFB QCL structure was modeled in the plane of the growth axis and the propagation axis and then numerically simulated using COMSOL. The illustration of the longitudinal section of the modelled structure and its different layers is shown in Figure 3.4. Table 3.1 presents all the layers and their corresponding refractive index.

| Layers | Refractive Index | Thickness |
|---|---|---|
| Top metal | 22.2+i93.2 [18] | 400 nm |
| Top/Bottom cladding | 2.89+i0.009 [19] | 3 $\mu$m |
| Top/Bottom spacer | 3.4 [17] | 3 $\mu$m |
| Active zone | 3.37 | 3.8 $\mu$m |

**Table 3.1:** The refractive indices and the thickness of different layers in the modeled DFB structure.

Furthermore, the surface gratings on the top cladding are almost always created using anisotropic dry etching, resulting in a sloped feature. Hence in accordance with the real grating profile a trapezoidal periodic structure was incorporated in the model. The grating period was 2.12 $\mu$m based on Equation (3.1), and the angle of the trapezoidal shape was 120° . For the grating we chose a fill factor of 50% which is typical for first-order DFBs, as this value maximizes the refractive index contrast [20]. This periodic structure was topped by a thin layer of gold (400 nm). The refractive index of the metal layer is $22.2 + i93.2$ at the considered wavelength [18].

Simulations based on the finite element method solution of the Helmholtz equation as presented below were then performed.

$$\Delta E + K_0^2 \left(n^2 - n_{eff}\right) E = 0 \tag{3.4}$$

where, $\Delta$ is Laplacian operator, $K_0$ is the wave vector of the guided mode, $n$ and $n_{eff}$ are the complex index and effective index of the materials, respectively. $E$ is the electric

field of the guided mode. The simulations were carried out on two periods of grating with periodic boundary conditions (shown as blue vertical lines on either side of the modelled structure in Figure 3.4), which made it possible to simulate an infinitely long laser cavity. The calculations were carried out in a two-dimensional space, with the growth and propagation axis serving as guides. The eigenfrequency study type was used to find resonance frequencies and their associated eigenmodes in resonant cavities. An example of the electric field distribution of the two modes corresponding to the eigen solution of the Helmholtz equation is illustrated in Figure 3.5: the Semiconductor mode has maxima of the electric field under the semiconductor and the Metal mode has maxima of the electric field under the trenches of the grating filled with gold.

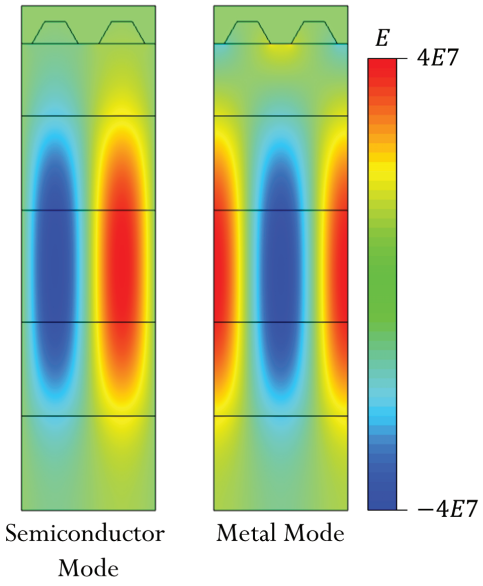


**Figure. 3.5:** Electric field distribution of (Left) Semiconductor and (Right) Metal modes in the DFB laser for grating etch dept of 0.65 $\mu$m.

Throughout the simulations, we played around with the grating etch depth d and the top cladding thickness. The cladding thickness was varied form 2 $\mu$m to 3 $\mu$m, with a parametric sweep of grating etch depth from 0.04 $\mu$m to 0.8 $\mu$m and a step of 0.02 $\mu$m. Figure 3.6 illustrates the variation in mode wavelength in the DFB structure as a function of the etching depth for 2 and 3-$\mu$m-thick claddings represented in purple and teal, respectively.

From Figure 3.6, we observe that the metal mode exhibits anticrossing behavior as function of the grating depth (lines with square markers), while the semiconductor mode exhibits almost no change (lines with circular markers). The dielectric waveguide in the active region of the laser primarily confines the semiconductor mode exhibiting a constant frequency. It is very similar to the optical mode that we typically observe in QCLs that does not have any periodic grating.

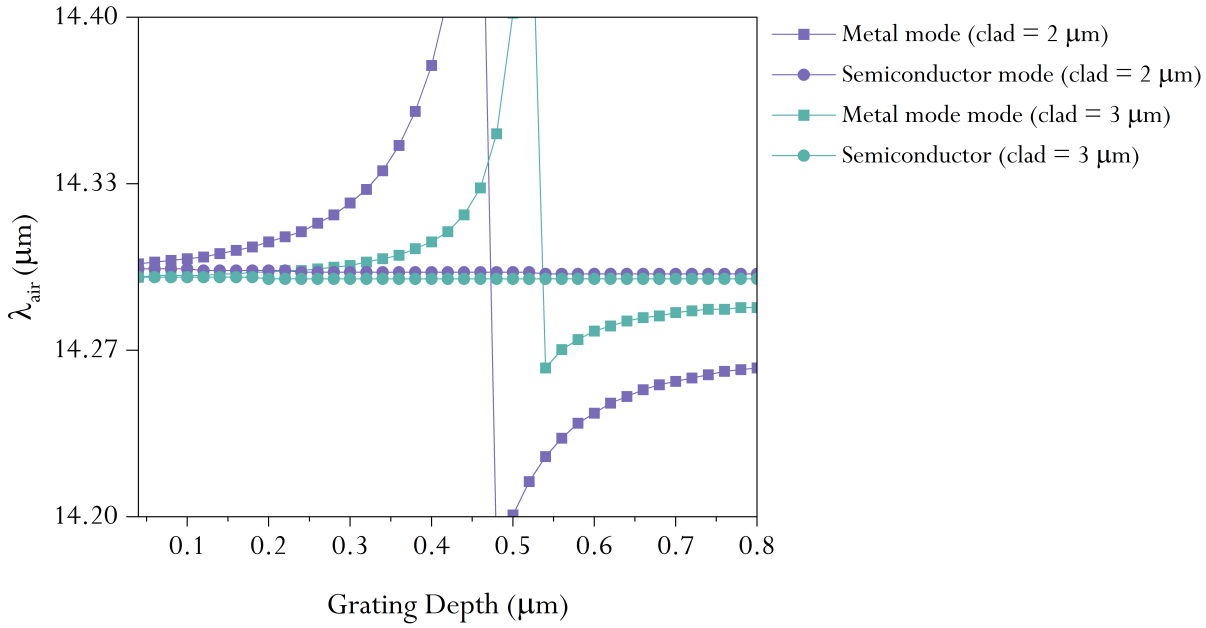


**Figure. 3.6:** The wavelength of the modes in the DFB structure as a function of the grating etch depth for two cladding thicknesses.

On the other hand, the metal mode located beneath the etched region covered by the metal layer can be either symmetrical or antisymmetrical, depending on how close the active region is to the metal. From Figure 3.6, we observe an anti-crossing (symmetric and antisymmetric) of the metal modes at grating etching depth close to 0.45 $\mu$m and 0.5 $\mu$m for cladding thickness of 2 and 3 $\mu$m respectively.

In order to favor one mode over the other, the loss associated with the mode to suppress should be higher. The loss experienced by the semiconductor and metal modes can be deduced from the imaginary part of the mode frequencies according to Equation (1.28). In addition, we used the ratio of the electric field distribution over the active region

($E_{active}$) to that over the complete waveguide ($E_{total}$) to calculate the confinement factor, Γ, Equation (1.29).

The optical loss and the confinement factor of the both modes calculated as a function of the etching depth are shown in Figure 3.7 and Figure 3.8 respectively.

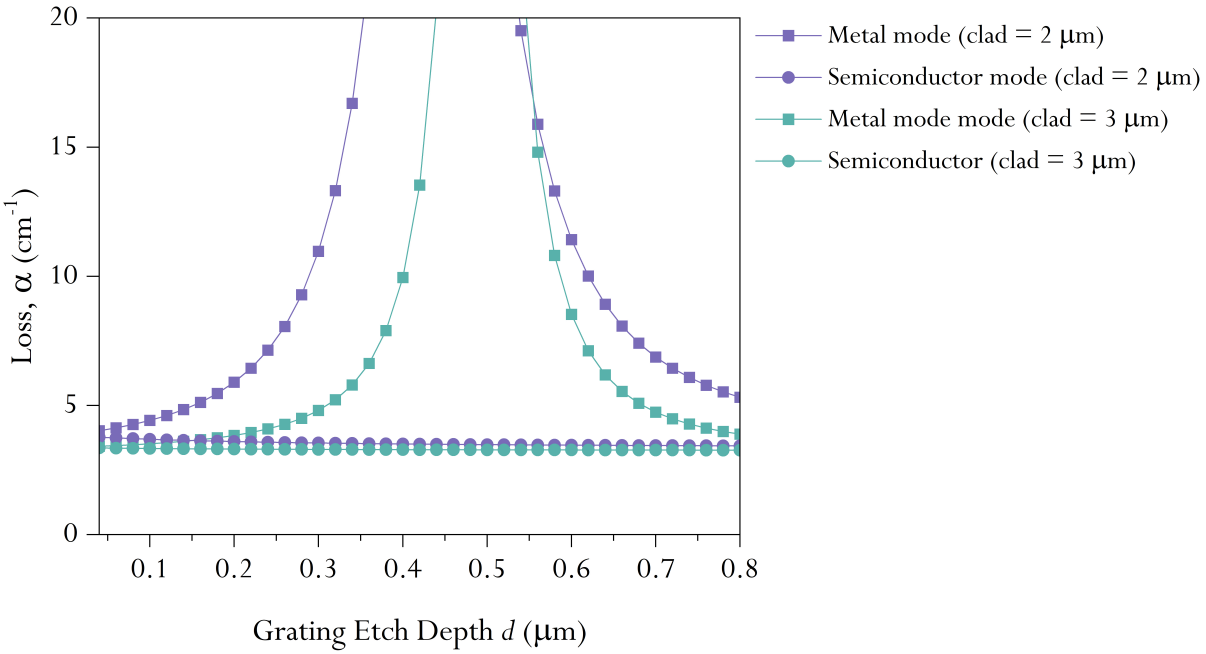


**Figure. 3.7:** The loss experienced by the modes in the DFB structure as a function of grating etch depth for two cladding thicknesses.

As it can be seen From Figure 3.7 the loss associated to the semiconductor mode is nearly constant in the entire range of the grating depth variation. The value of this loss is approximately 3.3 $cm^{-1}$ for both the cladding thickness. While one the other hand, the loss experienced by the metal mode increases and then decreases as the grating depth varies form 0 to 0.45 $\mu$m and 0.45 $\mu$m to 0.8 $\mu$m respectively. We also observe that the metal mode experiences higher loss with the decreasing cladding thickness due to increasing proximity to the metal layer. This is exactly what we hoped for.

Furthermore, from Figure 3.8, we observe a similar trend for semiconductor mode, the optical confinement factor remains mostly constant in the entire range ($\Gamma \approx 0.5$). However, the confinement factor of the metal mode decreases and then increases as the grating

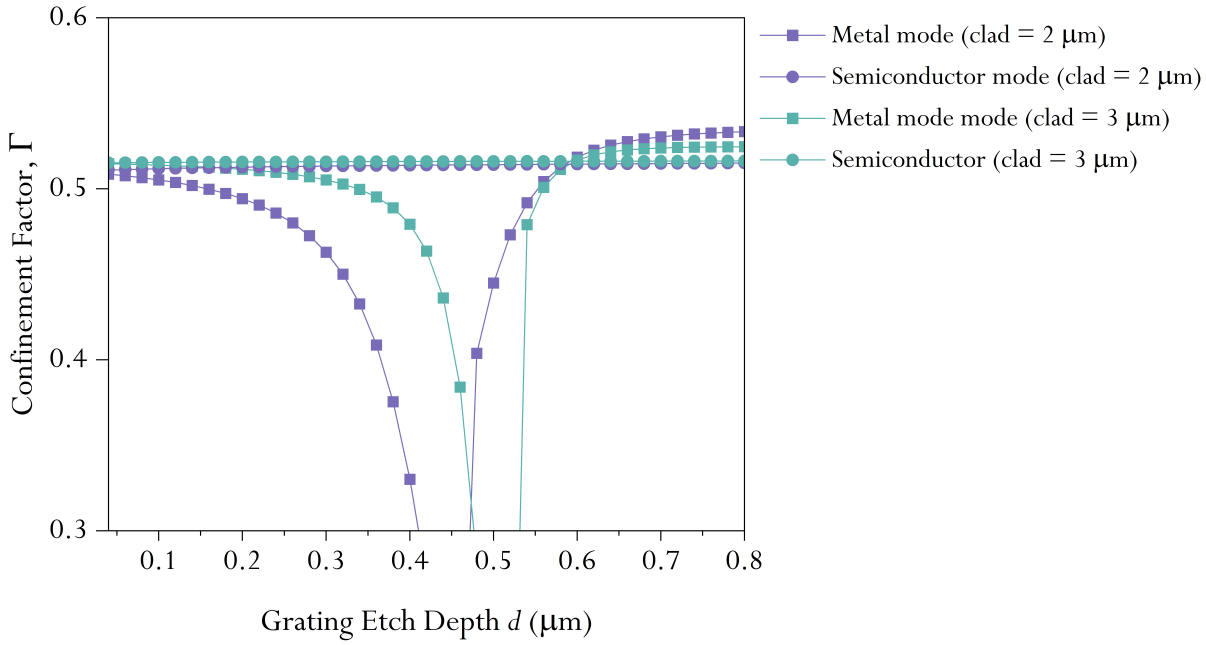


**Figure. 3.8:** The optical confinement factor of modes in the DFB structure as a function of the etching depth for two cladding thicknesses.

depth varies form 0 to 0.45 $\mu$m and 0.45 $\mu$m to 0.8 $\mu$m respectively, which is expected and is consistent with the loss profile i.e., higher the loss, lower the confinement.

To analyze the summary effect of the loss and optical confinement on the mode discrimination we used a figure of merit, $\chi$, determined form Equation (1.28) and Equation (1.29) as follows

$$\chi = \frac{\Gamma}{\alpha} \tag{3.5}$$

The optical mode exhibiting a higher value of the figure of merit should dominate. The figure of merit calculated as a function of the grating depth is shown in Figure 3.9

From the Figure 3.9, we clearly observe that the semiconductor mode has a higher figure of merit in the entire range of the explored grating depths, which should provide its domination over the metal mode. Besides, Figure 3.9 shows that a DFB structure with a thicker cladding performs better.

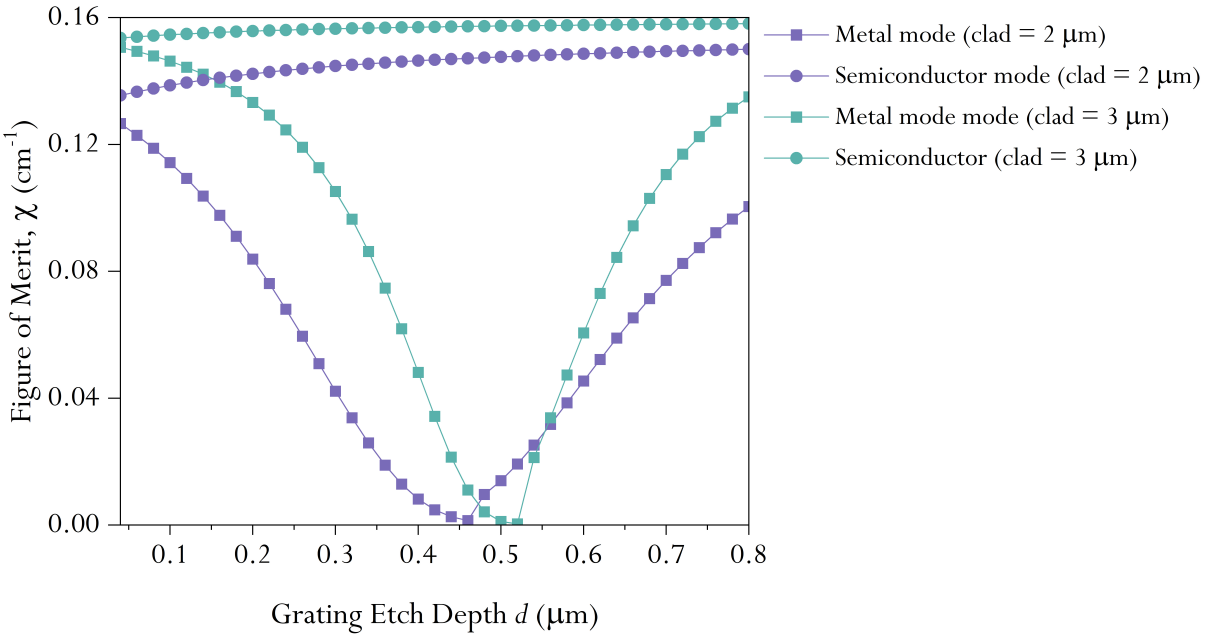


**Figure. 3.9:** The figure of merit of modes in the DFB structure as a function of grating etch depth for two cladding thicknesses.

To determine the optimal grating depth, we should now consider the optical coupling between the grating and the active region of the laser. The coupling coefficient, $\kappa$, is a measure of the backscattering, i.e., optical feedback by the grating. It can be extracted from the real part of the complex frequency of the eigenmodes using the following relation [6]

$$\kappa = \frac{\Delta\omega}{2c} n_{eff} \tag{3.6}$$

Where $\Delta\omega$ is the frequency difference between two modes (photonic bandgap). From the mode control perspective, a high value of $\kappa$ is advantageous as it results in a strong locking of the device into the grating mode, thereby reducing the likelihood of lasing on a FP mode. Nevertheless, a substantially high value of $\kappa$ also results in reduced or potentially negligible optical power output. Therefore, in order to attain single frequency operation with an adequately high optical output power, a compromise must be reached. An additional limitation arises from the need to keep the device length short to maintain

reasonably low threshold currents.

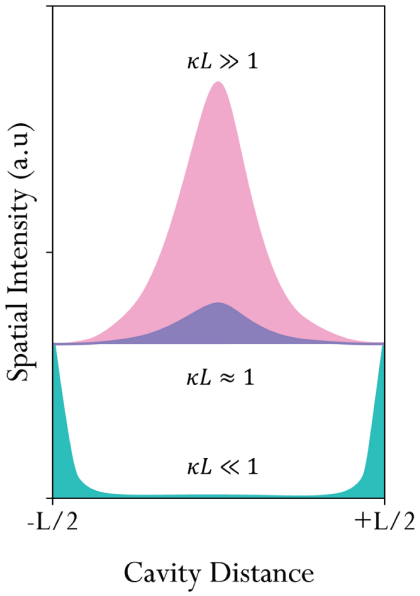


**Figure. 3.10:** Schematic diagrams of longitudinal variation of spatial intensity distribution of a DFB with different coupling levels. Adapted from [6]

Furthermore, it is imperative to ensure that the optical density distribution remains predominantly uniform along the longitudinal axis of the cavity, which is necessary to maintain the gain. This can be better understood considering a product of the coupling coefficient and the laser cavity length $L$. Figure 3.10 shows the optical density distribution along the laser cavity of length $L$. For values far from unity, radiation is concentrated at the ends ($\kappa L \ll 1$, under-coupling) or in the middle ($\kappa L \gg 1$, over-coupled) of the resonator leaving a lot of unused gain in the device, which can then support another mode. Besides, insufficient coupling can result in detrimental effects on the output facet during high power operation, whereas excessive coupling can lead to spatial hole burning and impact the mode stability. There is, however, a middle ground to these two situations where the coupling is optimal ($\kappa L \approx 1$) and the optical power density profile in the cavity is reasonably flat from end to end. This optimal coupling is a preferred value for a DFB design. However, we experimentally found that the devices exhibit better mode control in case of slight over coupling i.e., $\kappa L > 1$ [21].

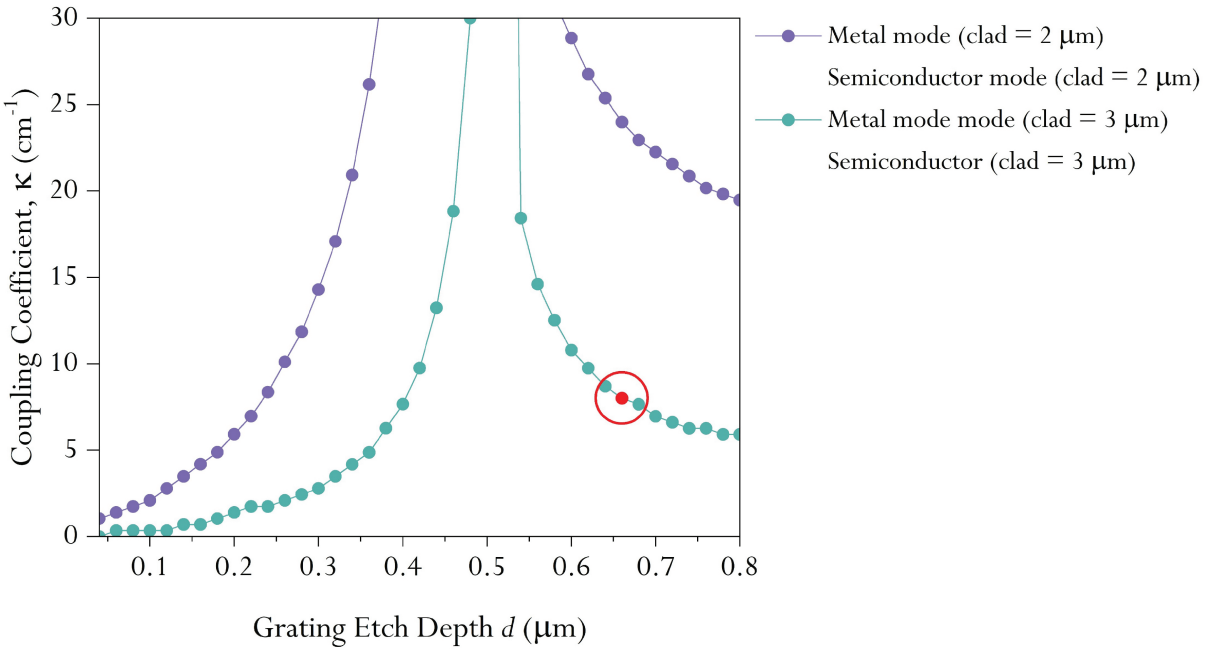


**Figure. 3.11:** (Left) The coupling coefficient of modes in the DFB structure as a function of the etching depth for two cladding thicknesses. (Right) Surface plasmon mode located at the interface of the Bragg grating and the cladding

The coupling coefficients calculated as a function of the grating depth for different cladding thickness are presented in Figure 3.11.

We observe very large coupling in the grating depth range: 0.4 – 0.6 $\mu$m and 0.45 – 0.55 $\mu$m for 2 and 3-$\mu$m-thick cladding respectively. This arises due to the resonance between the surface plasmon mode (located at the interface of Bragg grating with cladding) and the DFB modes. Therefore, we must avoid grating depths within these ranges. It is also crucial to steer clear of shallower grating depths where the coupling coefficient varies rapidly. Therefore, the only acceptable choice remains the region beyond the resonance, where the grating parameters exhibit lower sensitivity to fluctuations in the etching depth.

The entire range beyond the resonance for 2-$\mu$m-thick cladding corresponds to $\kappa L \gg 1$, therefore this cladding thickness is not suitable. The most reasonable coupling coefficient corresponds to the grating depth of 0.65 $\mu$m (marked in red) for a cladding thickness of 3 $\mu$m. This grating etch depth, for a 3.6 mm long device, provides $\kappa L = 2.8$. Moreover,

the loss difference between the two modes, $\sim 2.2$ cm$^{-1}$ from Figure 3.7, is sufficient for mode suppression [15].

In conclusion, based on the simulation, grating period, $\Lambda = 2.12$ $\mu$m, the grating etch depth, $d = 0.65$ $\mu$m and cladding thickness of 3 $\mu$m are optimal parameters for fabricating single mode DFBs emitting at 14.3 $\mu$m. However, this conclusion must be experimentally verified. The characteristics of the fabricated devices are discussed in the following section after a brief presentation of additional processing steps required to incorporate the grating.

## 3.4 Fabrication of DFB QCLs

Fabrication of DFB lasers follow the process described in Section 2.2, along with additional processing steps required to produce a periodic grating on the top of the laser ridge. The grating integration occurs prior to the mesa definition stage and involves cladding thinning, grating patterning, etching, and cleaning.

### 3.4.1 Grating Fabrication

In case of long-wavelength DFB QCLs, the pitch of the first order gratings is typically around 2 $\mu$m and feature size (critical dimension) is half of the pitch. However, for precise selection of the wavelength, the pitch must be tightly controlled in order of a few nanometers. This is not possible by the traditional photolithography where the resolution (0.5 $\mu$m for SUSS MJB4 available in our lab) is inherently limited by the wavelength of light used.

One approach to produce such fine gratings is through Holographic lithography. This technique is based on optical interference of multiple coherent beams. The interference pattern consists of a periodic series of fringes representing intensity minima and maxima. Upon post-exposure lithographic processing, a photoresist pattern corresponding to the periodic intensity pattern emerges. The precise spacing between these fringes can be controlled by varying the angle between the two beams, with the smallest achievable period being half the wavelength of the light used. Although this approach is fast and straightfor-

ward, it is unable to perform simultaneously patterning of gratings with multiple pitches. This limitation becomes critical in laboratory settings where the fabrication of multiple gratings with different pitches is necessary for optimizing emission wavelengths.

Electron beam lithography (EBL) offers a solution to this problem. By employing the EBL technique, one can achieve incredibly fine resolution, measuring just a few nanometers with remarkable flexibility. This technique enables the customization of the masks with different pitch and period, allowing the writing of different patterns in a single write cycle. Although EBL is known for its flexibility, it does entail intricate operational procedures.

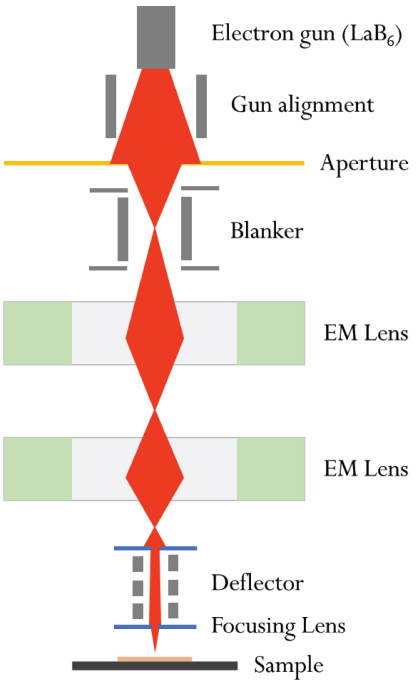


**Figure. 3.12:** Schematic of an electron-beam lithography machine.

Figure 3.12 depicts a schematic of a Raith electron beam lithography machine (EBL) employed in this work. The machine generates an electron beam with an energy up to several kiloelectron volts (keV), which is then focused on a specific resist material with appropriate exposure dose. The electron beam is shaped through the use of electromagnetic lenses that manipulate the electrons emitted by a Field Effect Gun ($LaB_6$ filament in our equipment), accelerating and deflecting them. The focused electron beam is directed

towards the resist-coated sample positioned on a movable stage. The electromagnetic lenses are also responsible for deflecting the electron beam within an area of approximately 100 $\mu$m $\times$100 $\mu$m, referred to as the write field. During the writing process, the EBL machine scans over one write field, and larger displacements are achieved by moving the stage accordingly.

EBL operates under computer control, where the mask design is created using Computer Assisted Design (CAD) software. The mask design is then processed using dedicated software (Elphy Quantum) to ensure compatibility with the machine's input format. Unlike UV optical lithography, EBL is a sequential technology, and the processing time is influenced by the desired resolution and design complexity. The exposure steps for creating gratings, in particular, tend to be time-consuming. However, EBL allows fabricating DFB structures with varying period and pitch in a single run thus effectively saving time by avoiding repeated fabrications.

Firstly, if necessary, the upper cladding layer of the QCL wafer undergoes thinning using plasma etching. However, in the aforementioned DFB design, the cladding thickness was already 3 $\mu$m (Table 3.1), rendering the need for this step unnecessary. The sample was cleaned and spin coated with a photoresist compatible with EBL. In our case we opted for AZ2020 photoresist diluted with Propylene Glycol Monomethyl Ether Acetate (PMGEA) in the proportion of 10: 4. The dilution was necessary because AZ2020 is not inherently compatible with EBL as it produces thick film thus reducing the spatial resolution of the method. The sample, after proper heat treatment, was transferred to the EBL machine. The machine was aligned and the resist was exposed using the mask pattern with an exposure dose factor of 13.7 $\mu$C/cm$^2$.

After writing, the sample was baked and developed. The development step requires extreme care as over development can damage grating patterns. Figure 3.13 shows the optical images of appropriately developed and overdeveloped grating patterns.

The developed grating pattern was etched using 50 W Argon inductive coupled plasma (ICP Oxford). The InAs etching rate was 50 nm/minute. During the etching process

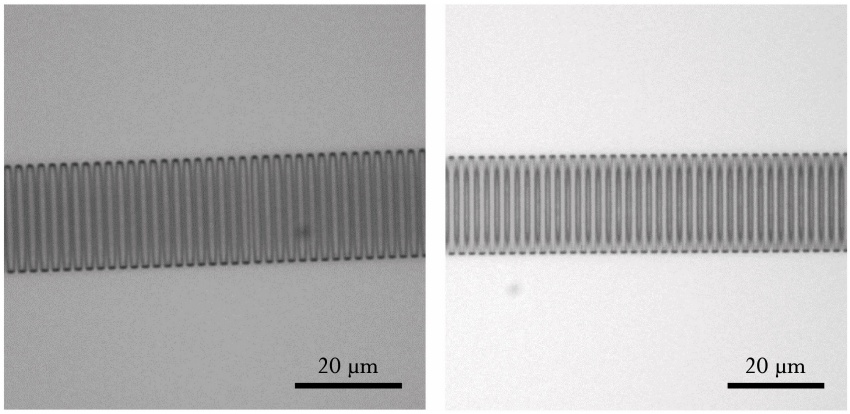


**Figure. 3.13:** (Left) appropriately developed and (Right) over developed grating patterns.

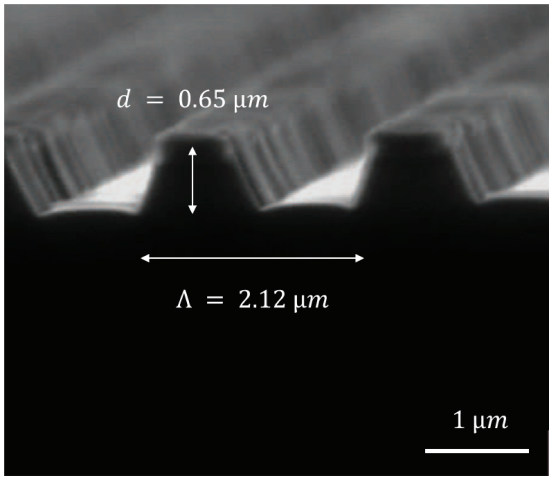


**Figure. 3.14:** Electron microscopy image of gratings etched using ICP.

the resist was also etched however its etching rate was much smaller (2 nm/minute). The remaining photoresist was stripped off using acetone and the rest of the fabrication procedure followed. The final ridge width of the QCL was 14 $\mu$m. Figure 3.14 shows the electron microscopy image of an etched grating.

### 3.4.2 Experimental Results

Before starting a DFB technology on a new structure, we create a standard FP devices to serve as the reference. Figure 3.15 (Left), in solid lines shows the pulsed emission spectra of the 3.6-mm-long FP devices at three temperatures. The devices lased up to 390 K. At

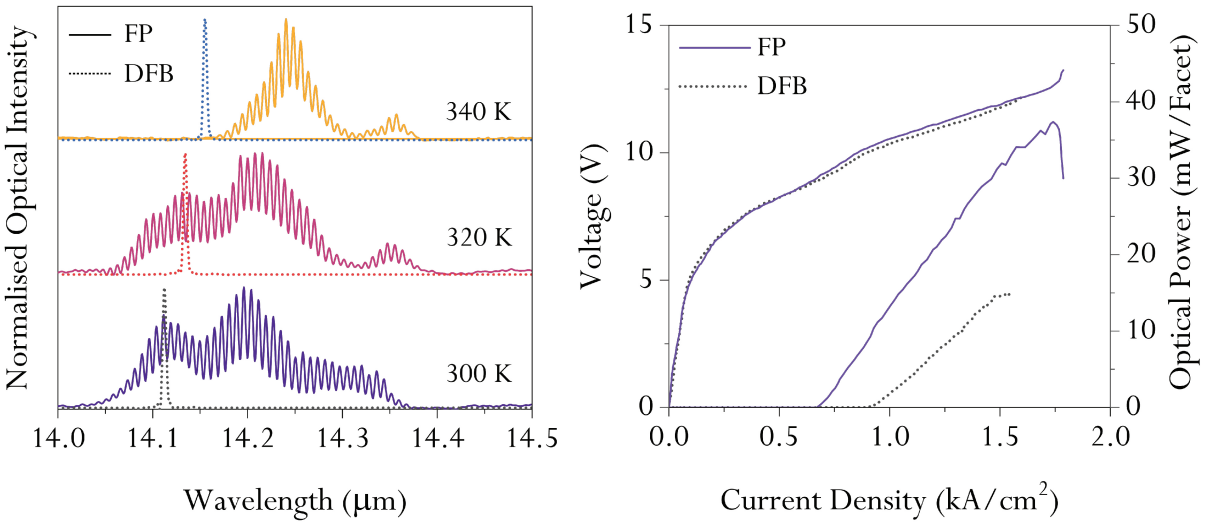


**Figure. 3.15:** (Left) Comparison of position of emission spectra of DFB QCL ($\Lambda = 2.12\ \mu$m) with the emission spectra of FP devices at various temperatures in pulsed operation. (Right) comparison of PIV characteristics of DFB and FP QCLs at 300 K in pulsed operation.

300 K in pulsed operation, they exhibited threshold current density as low as 0.7 kA/cm$^2$ with an optical power of around 40 mW/Facet as shown in Figure 3.15 (Right): solid lines.

Now, for DFB lasers to have single-mode emission, the grating pitch must be matched to the emission wavelength of the active zone. To do this, we need to know from Equation (3.1), the emission wavelength, which we know from measurements with standard FP lasers, and the effective index. However, it should be noted that several factors such as introduction of gratings, variation in ridge width and cladding thickness may change this value. Moreover, this does not correspond to the effective index of the actual DFB modes. It is therefore very often unavoidable to use two DFB technologies before obtaining single-mode emission at the target wavelength. The first technology, with a grating pitch determined by the effective index of the simulations, gives us information on the true effective index of DFB modes, enabling us to adjust the grating period in the second technological realization.

Figure 3.15 (Left), in dotted lines show the pulsed emission spectra of 3.6-mm-long DFB QCLs with the grating period of $\Lambda = 2.12\ \mu$m. These devices lased up to 340 K. On

comparing the positions of the emission spectrum of FB and DFB devices we can see that the DFB emission is far from both the peak gain of FP devices as well as from the desired emission wavelength. The former, in addition to some additional losses introduced by the close proximity of metal on top of gratings explains the increased threshold current density as shown in Figure 3.15 (Right) by dotted lines. This increase was about 25% of that of the FP devices and the maximum optical power was around 15 mW/Facet. The later i.e., the mismatch in desired and the actual emission wavelength can be explained by the discrepancy between estimated effective refractive index used in the simulation and the actual experimental value.

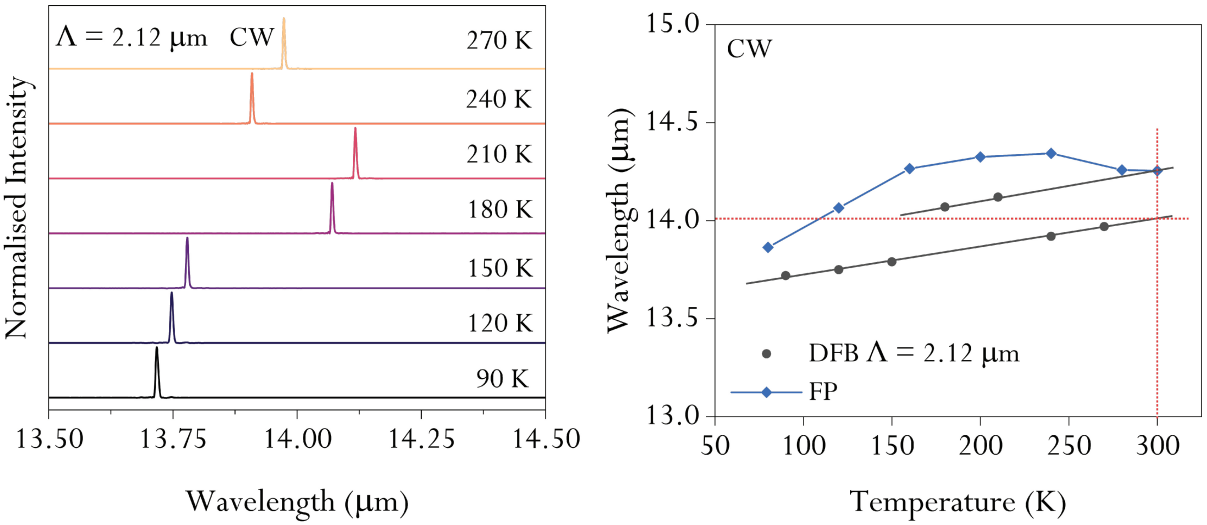


**Figure. 3.16:** (Left) Emission spectra of DFB QCL ($\Lambda = 2.12$ $\mu$m) and (Right) Comparison of emission wavelengths of FP and DFB QCLs at different temperatures in CW regime.

Again, 3.6-mm-long DFB devices were characterized in the CW regime at different temperatures. Devices properly mounted epi-side down onto AlN heatsinks exhibited CW lasing action up to 270 K with a threshold current density of around 1.1 kA/cm$^2$. The maximum operation temperature in this case was considerably lower than that in pulsed operation. This difference arises from the fact that in CW, the core temperature is typically much higher, around 80 K, compared to pulsed operation at same ambient temperature. When the core temperature reaches the maximum pulsed operational temperature, the laser ceases to emit light.

The evolution of the CW emission spectra with temperature is presented in Figure 3.16 (Left). From this figure we can see that the device did not exhibit single mode emission in the entire temperature range. Mode hops occurred however between 180 K to 210 K. Furthermore, the emission wavelength was shifted from the target value of 14.3 $\mu$m. The two wavelengths observed in the emission spectra of DFB lasers belong to different spatial modes. The spectral shift is explained by a difference in the refractive index for these modes, which in turn causes the DFB wavelength to change. Normally, the DFB mode corresponding to the fundamental spatial mode dominates in the emission spectra of DFB lasers. However, DFB modes belonging to higher-order spatial modes can appear and even dominate if their spectral positions are closer to the laser gain peak. The manifestation of such modes in emission can also be attributed to the possible over estimation of the coupling Figure 3.11 i.e., the value of the coupling coefficient obtained by the simulation was exaggerated compared to the true value. The other factor may be the ridge width comparable to the emission wavelength, which can support higher order mode, however it is less likely (Section 1.3.3). Thus, these parameters must be adjusted as well.

Now, to calculate the true effective index of the DFB mode, the emission wavelengths were extrapolated up to 300 K as shown in Figure 3.16 (Right), and the effective refractive index was calculated using Equation (3.1). Interestingly, there was indeed a mismatch: the experimental effective refractive index was determined to be 3.31, while in the simulation we used 3.37.

Based on the obtained results, to achieve single frequency emission at desired wavelength of 14.3 $\mu$m, we are obliged to adjust the grating period and the coupling. The later can be achieved by adjusting the cladding thickness. In the next fabrication we chose the grating period $\Lambda = 2.16$ $\mu$m, based on the experimental effective refractive index. In addition, the upper cladding was thinned down to 2.5 $\mu$m in order to improve the coupling ($\kappa L \sim 5$). Changing the cladding thickness should also changes the effective refractive index, however, we do not expect it to be significant. The grating etch depth was not changed. The adjustments in parameters allowed us to fabricate single frequency devices emitting at the target wavelength.

It must be noted that since the emission wavelength of the new DFBs were still be far from the peak gain, we expect that the they devices will still have higher threshold current density as well as lower optical power output than those of the reference FP devices. The CW threshold current density of the new devices at 270 K was around 1.2 kA/cm$^2$. The characteristics of these DFB QCLs are presented in next section.

## 3.5 Characteristics of DFB QCLs

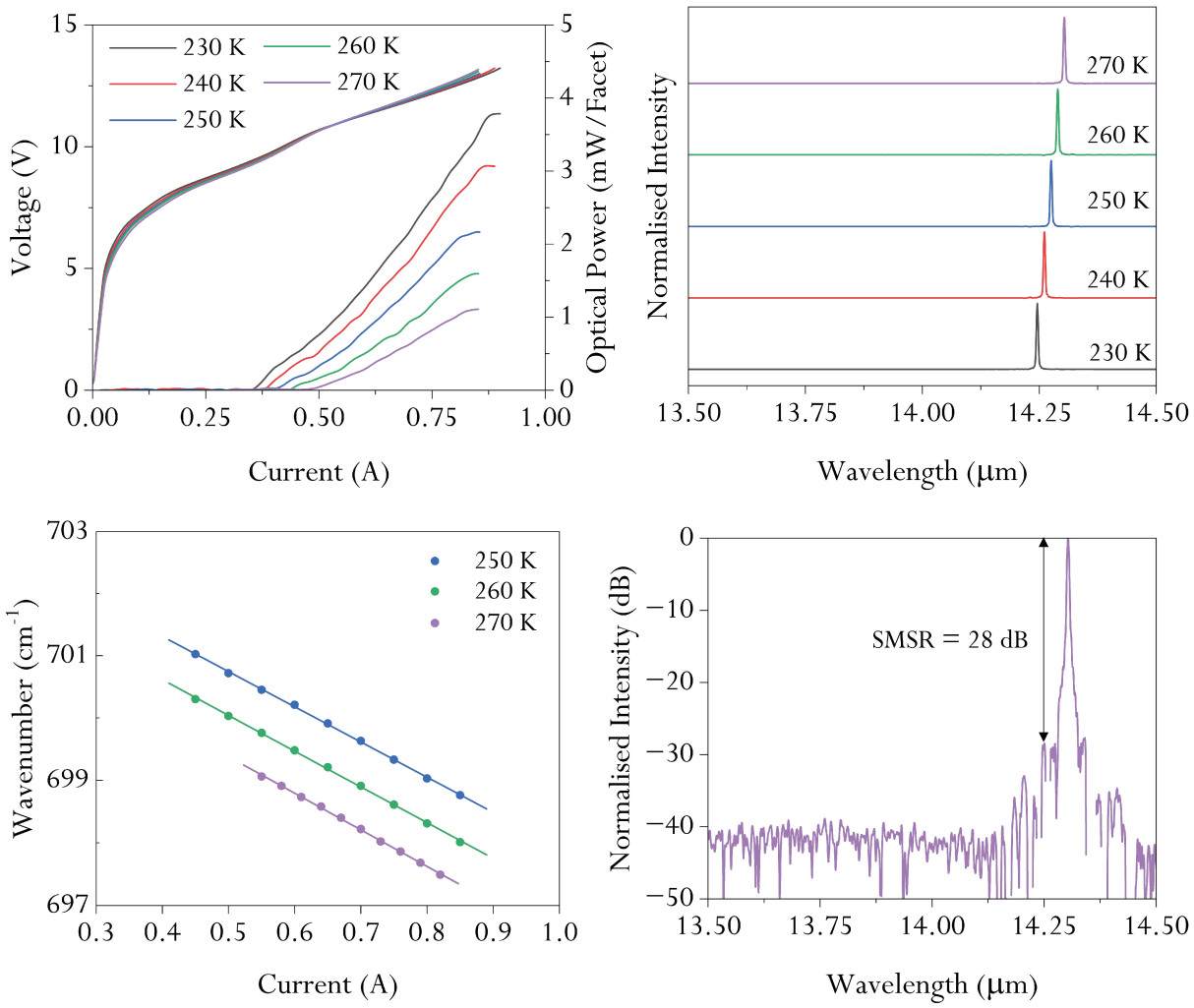


**Figure. 3.17:** (Top Left) CW PIV characteristics, (Top Right) emission wavelength as a function of temperature, (Bottom Left) wavenumber as the function of current at different temperatures accessible by Peltier cooling element and (Bottom Right) emission spectra at 270 K in dB scale showing the SMSR of DFB QCL with $\Lambda = 2.16$ $\mu$m.

Figure 3.17 illustrates the CW operation characteristics of a 3.6-mm-long DFB fabricated

using the revised parameters ($\Lambda$ = 2.16 $\mu$m and cladding thickness of 2.5 $\mu$m). The figure is divided into four sections. In the top left section, the PIV characteristics are presented. The devices were tested in the CW regime up to 300 K and operated at a maximum temperature of 270 K. The laser exhibited an optical power of 1 mW at 270 K. The top right section, displays variation in the emission wavelength as a function of temperature. The wavelength tunning rate was 0.02 nm/K. The devices exhibited single mode operation and emitted at 14.3 $\mu$m when operated at 270 K, matching the absorption line of Ethylbenzene.

The bottom left section demonstrates the wavelength tuning capability (at the temperatures accessible by Peltier cooling element) of the devices as a function of injection current. The tuning rate was measured to be 0.012 nm/mA. Lastly, the bottom right section, showcases the spectral purity of the devices, quantified by the SMSR. The devices exhibited a high SMSR value of 28 dB, indicating excellent spectral purity. Given the emission wavelength's alignment with the absorption line of Ethylbenzene, as well as the single mode emission with good spectral purity, these DFB QCLs are well suited for the detection of Ethylbenzene.

By employing a similar iterative combination of simulation and fabrication techniques, DFB QCLs operating at three distinct wavelengths: 13.71 $\mu$m, 14.85 $\mu$m, and 13.36 $\mu$m were also fabricated from purposely grown QCL wafers. The shift of the emission wavelength was achieved by scaling the thickness of InAs layers in the structure by modifying the MBE growth rate, the AlSb barrier thickness kept unchanged. This approach could be successfully employed to adjust the wavelengths within $\pm$5% of the initial design value without degradation of the device performance. These wavelengths were specifically chosen to target the absorption lines of Toluene, Benzene, and Propane, respectively.

For each wavelength, the process involved measuring the effective refractive index after the initial fabrication step, followed by adjusting the grating period accordingly. The grating periods used were 2.07 $\mu$m, 2.21 $\mu$m, and 1.98 $\mu$m for the respective DFB lasers. Figure 3.18 shows the simulation results for the DFB QCLs operating at 13.7 $\mu$m. These

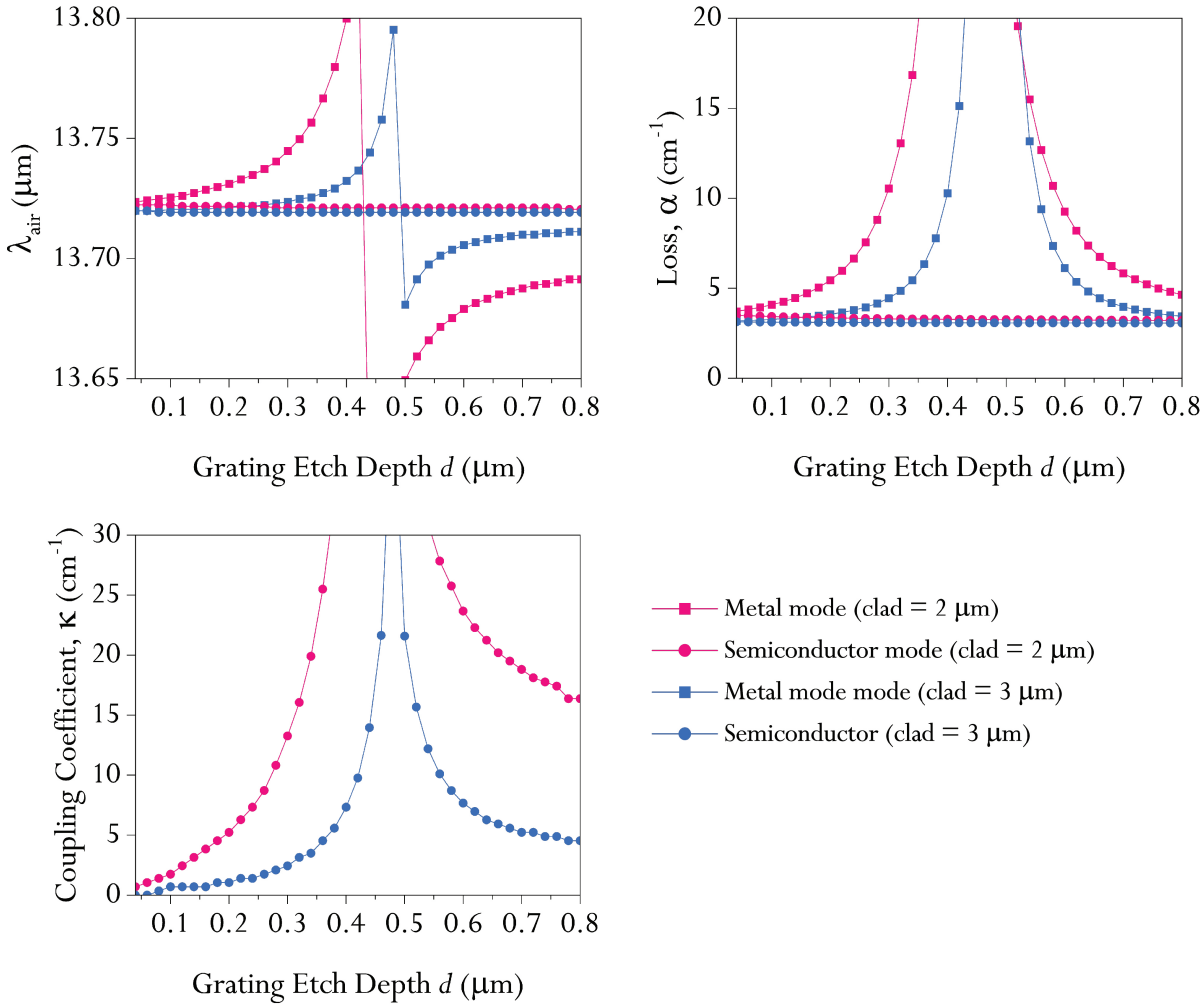


**Figure. 3.18:** Simulation results for the DFB QCLs operating at 13.71 $\mu$m. (Top Left) Wavelength, (Top Right) loss, (Bottom Left) coupling coefficient as the function of grating depth for two cladding thicknesses.

results are similar to those discussed earlier. To optimize the loss separation between modes while maintaining the $\kappa l$ within the range of $2.8 - 5$, both the cladding thickness and grating etch depth were varied. The optimal cladding thickness was 3 $\mu$m, while the grating etch depth was 0.65 $\mu$m. For rest of the wavelengths, these parameters were chosen in a similar fashion.

Figures 3.19 to 3.21 presents CW characteristics of 3.6-mm-long DFB QCLs designed to probe the absorption lines of Toluene, Benzene, and Propane respectively. In these figures, the left side showcases the PIV characteristics, while the right side illustrates the wavelength tuning properties. The lasers exhibited CW optical powers of 2 mW, 1

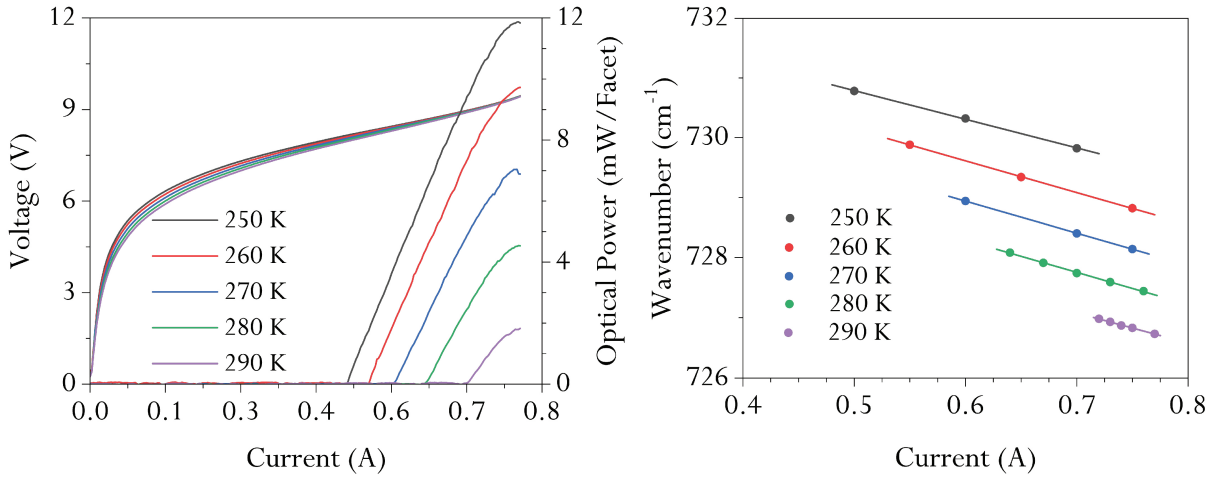


**Figure. 3.19:** (Left) CW PIV characteristics, (Right) wavenumber as the function of current at different temperatures. The laser is suitable for Toluene detection at 13.71 $\mu$m.

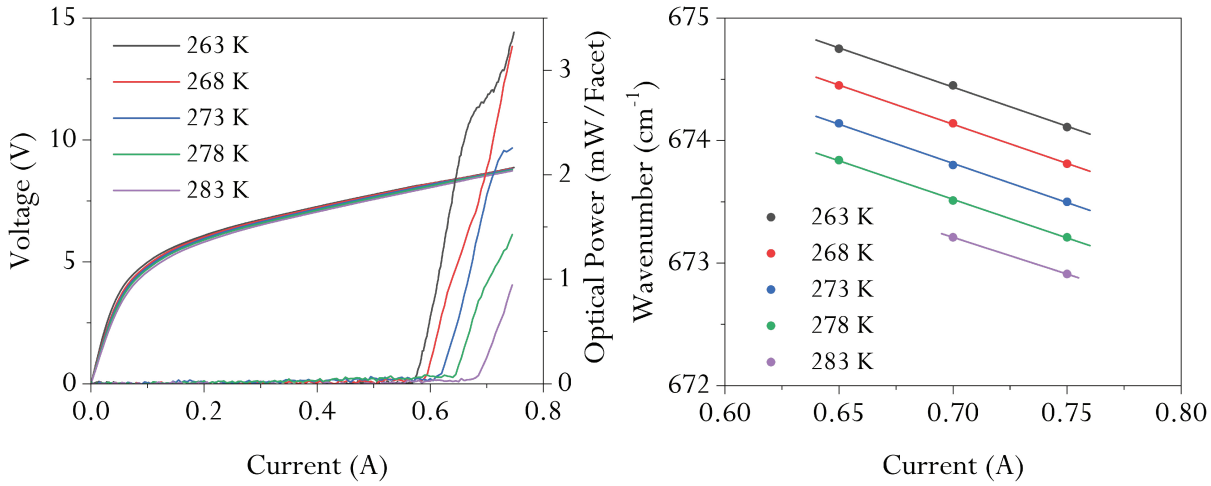


**Figure. 3.20:** (Left) CW PIV characteristics, (Right) wavenumber as the function of current at different temperatures. The laser is suitable for Benzene detection at 14.85 $\mu$m.

mW, and 2 mW at temperatures of 290 K, 283 K, and 310 K, respectively. The PIV data indicates their ability to operate at elevated temperatures. However, they were not tested beyond these temperatures. Furthermore, they displayed single-mode operation with wavelength tuning rate of 0.02 nm/K and 0.012 nm/mA. At 290 K, 283 K, and 270 K, they emitted at wavelengths of 13.71 $\mu$m, 14.85 $\mu$m, and 13.36 $\mu$m, respectively, with SMSR value of 20 dB. This SMSR value attests to their good spectral purity making the devices suitable for spectroscopic applications.

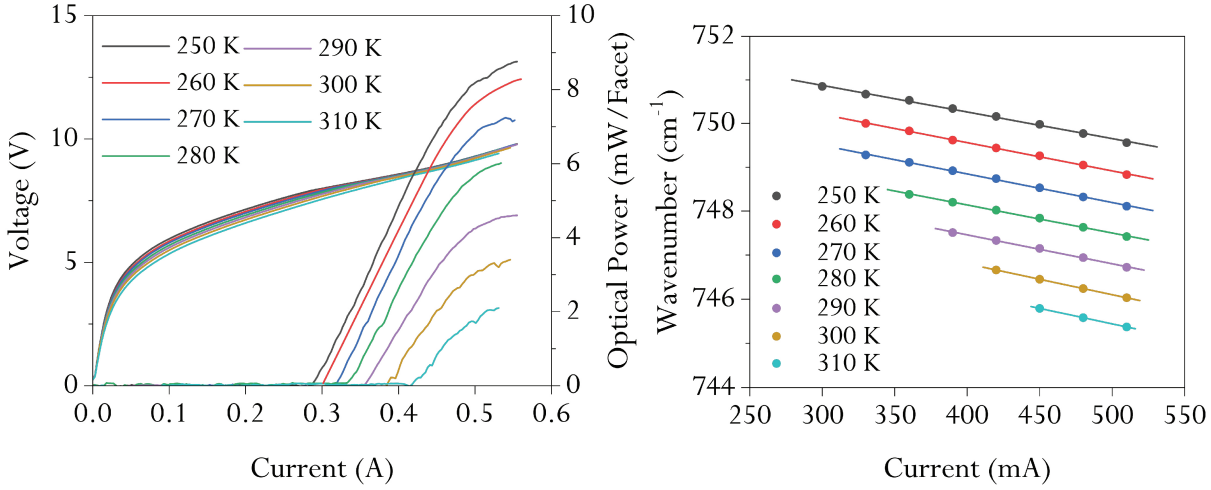


**Figure. 3.21:** (Left) CW PIV characteristics, (Right) wavenumber as the function of current. The laser is suitable for Propane detection at 13.36 $\mu$m.

## 3.6 Conclusion

This chapter discusses the operational principles, design, and fabrication of DFB lasers. After careful consideration of the advantages offered by surface etched gratings compared to buried gratings, we opted to work with the former. Our focus then shifted towards achieving single-frequency emission, capitalizing on the surface plasmon resonance generated by the proximity of a metal contact layer deposited on the etched laser ridge.

By employing an iterative approach that integrates simulation and fabrication, we then successfully identified and optimized key parameters such as grating depth and cladding thickness. This fine-tuning process strikes an optimal balance between coupling factors and losses. Our simulation played a pivotal role in providing invaluable insights for the design of the devices thus allowing us to successfully manufacture InAs-based DFB QCLs designed for long-wavelength operation. These devices exhibit single-mode emission characterized with good spectral purity. The precise alignment of the single-mode emission with the absorption lines of BTEX and Propane positions these devices as ideal candidates for a wide range of spectroscopic applications.

In the next chapter we present the spectroscopic investigation of BTEX and Propane using the fabricated devices.

# Bibliography


[1] Andreas Schwaighofer, Markus Brandstetter, and Bernhard Lendl. Quantum cascade lasers (QCLs) in biomedical spectroscopy. *Chemical Society Reviews*, 46, 2017. doi:10.1039/C7CS00403F.

[2] Binkun Zhou, Jianglin Wang, and Hanyi Zhang. Short-coupled-cavity single-mode semiconductor lasers. *Conference on Lasers and Electro-Optics*, page WO5, 1985. doi:10.1364/CLEO.1985.WO5.

[3] Govind P. Agrawal and Niloy K. Dutta. *Coupled-Cavity Semiconductor Lasers*. Springer US, 1993. doi:10.1007/978-1-4613-0481-4_8.

[4] G. Hadley. Injection locking of diode lasers. *IEEE Journal of Quantum Electronics*, 22:419–426, 3 1986. doi:10.1109/JQE.1986.1072979.

[5] Govind P. Agrawal and Niloy K. Dutta. *Semiconductor Lasers*. Springer US, 1993. doi:10.1007/978-1-4613-0481-4.

[6] H. Kogelnik and C. V. Shank. Coupled-Wave Theory of Distributed Feedback Lasers. *Journal of Applied Physics*, 43:2327–2335, 5 1972. doi:10.1063/1.1661499.

[7] John D. Joannopoulos, Steven G. Johnson, Joshua N. Winn, and Robert D. Meade. *Photonic Crystals: Molding the Flow of Light*. Princeton University Press, 2 edition, 2008.

[8] P. Crump, O. Brox, F. Bugge, J. Fricke, C. Schultz, M. Spreemann, B. Sumpf, H. Wenzel, and G. Erbert. *High-Power, High-Efficiency Monolithic Edge-Emitting GaAs-Based Lasers with Narrow Spectral Widths*. 2012. doi:10.1016/B978-0-12-391066-0.00002-2.

[9] Kais Dridi, Abdessamad Benhsaien, Jessica Zhang, and Trevor J. Hall. Narrow Linewidth 1550 nm Corrugated Ridge Waveguide DFB Lasers. *IEEE Photonics Technology Letters*, 26:1192–1195, 6 2014. doi:10.1109/LPT.2014.2318593.

[10] J. Decker, J. Fricke, A. Maaßdorf, G. Erbert, G. Tränkle, and P. Crump. Non-uniform DFB-surface-etched gratings for enhanced performance high power, high brightness broad area lasers. page 100860R, 2 2017. doi:10.1117/12.2251835.

[11] Kent D. Choquette, M. Hong, R. S. Freund, S. N. G. Chu, J. P. Mannaerts, R. C. Wetzel, and R. E. Leibenguth. Molecular beam epitaxial regrowth on in situ plasma-etched AlAs/AlGaAs heterostructures. *Applied Physics Letters*, 60:1738–1740, 4 1992. doi:10.1063/1.107202.

[12] Chao Ning, Rui-Xuan Sun, Shu man Liu, Jin-Chuan Zhang, Ning Zhuo, Jun-Qi Liu, Li-Jun Wang, Shen qiang Zhai, Feng-Qi Liu, and Zahn-Guo Wang. GaSb surface grating distributed feedback interband cascade laser emitting at 3.25 $\mu m$. *Optics Express*, 30:29007, 8 2022. doi:10.1364/OE.465716.

[13] M.L. Osowski, R. Panepucci, I. Adesida, and J.J. Coleman. A strained-layer InGaAs-GaAs asymmetric cladding gain-coupled DFB laser with titanium surface gratings by metalorganic chemical vapor deposition. *IEEE Photonics Technology Letters*, 9:422–424, 4 1997. doi:10.1109/68.559375.

[14] M. Kamp, J. Hofmann, F. Schäfer, M. Reinhard, M. Fischer, T. Bleuel, J.P. Reithmaier, and A. Forchel. Lateral coupling – a material independent way to complex coupled DFB lasers. *Optical Materials*, 17:19–25, 6 2001. doi:10.1016/S0925-3467(01)00014-3.

[15] M. Carras, M. Garcia, X. Marcadet, O. Parillaud, A. De Rossi, and S. Bansropun. Top grating index-coupled distributed feedback quantum cascade lasers. *Applied Physics Letters*, 93:011109, 7 2008. doi:10.1063/1.2950086.

[16] Glen D. Gillen, Chris DiRocco, Peter Powers, and Shekhar Guha. Temperature-dependent refractive index measurements of wafer-shaped InAs and InSb. *Applied Optics*, 47:164, 1 2008. doi:10.1364/AO.47.000164.

[17] Physico-Technical Institute. IOFFE. URL: http://www.ioffe.ru/SVA/NSM/nk/index.html.

[18] Mark A. Ordal, Robert J. Bell, Ralph W. Alexander, Larry L. Long, and Marvin R. Querry. Optical properties of Au, Ni, and Pb at submillimeter wavelengths. *Applied Optics*, 26:744, 2 1987. doi:10.1364/AO.26.000744.

[19] Olivier Cathabard. Lasers à cascade quantique InAs/AlSb : amélioration des performances et fonctionnement monofréquence, 2009.

[20] Benjamin G. Lee, Mikhail A. Belkin, Christian Pflugl, Laurent Diehl, Haifei A. Zhang, Ross M. Audet, Jim MacArthur, David P. Bour, Scott W. Corzine, Gloria E. Hofler, and Federico Capasso. DFB Quantum Cascade Laser Arrays. *IEEE Journal of Quantum Electronics*, 45:554–565, 5 2009. doi:10.1109/JQE.2009.2013175.

[21] Zeineb Loghmar. Lasers à cascades quantiques InAs/AlSb au-delà de 10 $\mu m$ : Emission mono-fréquence et génération du THz par différence de fréquences, 2019.

# Chapter 4

# Spectroscopic Investigation of BTEX and Propane

## 4.1 Introduction

Researchers have been utilizing infrared sensors to exploit the 3.3 $\mu$m range of Benzene through techniques such as cavity-enhanced spectroscopy [1] and multi-pass sensing via difference frequency generation [2]. Additionally, the $\nu 14$ band at 1023 $cm^{-1}$ has been investigated using TDLAS by employing a Multipass Herriott Cells with a path length of 472 cm [3]. More recently, QCL operating at 14.8 $\mu$m was used in quartz enhanced photoacoustic spectroscopy (QEPAS) employing a standard 32 kHz tuning fork [4] and with a cantilever photoacoustic sensor [5]. These advancements demonstrate the ongoing development and diversification of infrared sensing technologies, expanding the range of applications and improving the detection capabilities in various spectral regions. On the other hand, QEPAS has never been employed for Toluene and rest of the gases in BTEX family.

Moreover, the detection of BTEX compounds, as well as the heavier alkanes like Propane, Butane, Pentane, presents unique challenges stemming from their potential interferences among themselves or from other compounds. The presence of coexisting VOCs charac-

terized by the same bonds can normally introduce spectral interferences especially in the spectral region where the fundamental modes of IR transitions lie, resulting in overlapping absorption bands or distorted signals. For instance, while Methane (C1) and Ethane (C2) have been demonstrated to be easily separated and independently detected even at atmospheric pressure at 3.3 $\mu$m [6, 7], Propane (C3) spectral features seem to be totally overlapping with C2 background absorption, making it difficult to discriminate and quantify C3 except through sophisticated multilinear or even multivariate approaches [8]. This issue of spectral interference can be solved at longer wavelength (13–15 $\mu$m) where BTEX and heavier hydrocarbons show distinct and isolated absorption features, like Propane $\nu$26 transition at 748 $cm^{-1}$ [9]. To achieve selectivity, a gas sensor must be able to probe a single absorption line. This is typically done using narrow linewidth emitters like lasers, as they provide a higher signal-to-noise ratio (SNR) compared to broadband emitters [10]. Unfortunately, the exploitation of this spectral range to develop sensing systems has been impeded due to the unavailability of suitable emitters.

In this chapter, we start with a concise discussion on the available gas detection techniques and their limitations. Following this, we introduce photoacoustic spectroscopy, setting the stage for a theoretical exploration of QEPAS. We then demonstrate the high sensitivity and selectivity of a QEPAS-based sensing system for the detection of BTEX and Propane in the $13 - 15$ $\mu$m range by leveraging specially designed quartz tuning forks (QTF) and long-wavelength DFB QCLs fabricated earlier. We investigate both spectral and non-spectral interference among BTEX as well as the selectivity of Propane detection within gas matrices that contain high concentrations of C1 and C2 hydrocarbons. Finally, we couple the long-wavelength QCL with a Hollow Core Waveguide (HCW) to improve the spatial quality of laser beams and study the optimal coupling conditions, beam quality, and losses associated with this integration process.

## 4.2 Gas Detection Techniques

Over the years, researchers have made significant advancements in developing a wide range of sensors specifically designed to detect trace gases. They have proven invaluable in various fields, including environmental monitoring, industrial safety, and healthcare. These sensors can be broadly divided into two categories: non-optical and optical.

### 4.2.1 Non-Optical

Trace gas analysis has conventionally relied on established techniques, such as the combination of gas chromatography (GC) and mass spectrometry (MS) [11, 12]. With its long-standing reputation, GC-MS [13] has been hailed as the gold standard for trace gas detection. In this approach, GC serves the purpose of separating volatile compounds, while MS determines the mass-to-charge ratio of chemical species present in the sample which then allows to calculate the molecular weight of each constituent, enabling the identification of unknown compounds and the quantification of their presence within the sample. The GC-MS provides a notable degree of selectivity and sensitivity, facilitating precise measurements. Notwithstanding its efficacy, this approach tends to be slow, demands proficient personnel, and entail analysis in a laboratory setting, thereby rendering it less appropriate for rapid on-site surveillance.

Numerous gas sensors, including electrochemical and semiconductor-based devices, have been developed to address these issues. Electrochemical gas sensors detect gases via electrochemical reactions that occur at the electrodes. An electrochemical cell consists of a liquid or solid electrolyte that is in direct contact with two electrodes, namely an active and a reference electrode. The active electrode is subjected to the gas sample that enters the cell, either by direct contact or by passing through a diffusion barrier. When the test gas reacts with the electrolyte, it initiates an electrochemical reaction. This chemical reaction leads to alterations in the electrode potential, or the flow of an electric current, proportional to the gas concentration. This current is then measured and converted into a reading of gas concentration [14].

Solid-state gas sensors on the other hand are based on the reversible interaction that occurs between the gas and the surface of a solid material [15, 16]. These devices employ diverse materials, including porous ceramics or thin films as active layers for detecting and quantifying the trace gases [17]. The interaction between gas molecules and the semiconductor surface changes the active layer's conductivity, permittivity, and work function [18, 19]. These modifications are translated into alterations in electrical parameters, such as resistance, capacitance, and inductance. The concentration of the gas is determined by measuring the amplitude, frequency, and phase of the voltage or current signals.

These sensors offer numerous notable benefits for trace gas detection. They possess high sensitivity, ensuring accurate results. They also provide rapid response and, unlike GC-MS, they are compact, cost-effective, and user-friendly. Additionally, they facilitate in situ and real-time studies [14, 20].

However, there are certain drawbacks associated with these sensors. They exhibit a long recovery time and lack selectivity, resulting in potential interference from other gases. Cross sensitivity is another issue, where the sensors may respond to multiple gases. Furthermore, their lifetime is relatively shorter, and their performance is significantly influenced by environmental conditions such as temperature and humidity levels.

### 4.2.2 Optical

The optical techniques for gas sensing are based on the radiation-matter interaction. Depending on the nature of the interaction they can be categorized in several spectroscopic domains: emission spectroscopy, elastic and inelastic scattering, and absorption spectroscopy, to name a few. The work carried out in this thesis is focused on absorption spectroscopy.

Due to strong fundamental rotational–vibrational transitions, gasses such as BTEX and Propane exhibit unique and highly discriminatory absorption patterns in the mid-IR spectral region [21], also referred to as "molecular fingerprint region". Thanks to these

rotational–vibrational transitions, gas molecules when irradiated with appropriated radiation undergoes excitation from their ground state to excited state through absorption of photons which later relax back to their ground state either through emission of photons or non-radiative processes.

The extent of absorption at a specific wavelength can be utilized to establish a relationship with the concentration of the gas. This correlation follows the principles of the Beer-Lambert law expressed as follows:

$$I(\lambda) = I_0(\lambda) \cdot e^{-\alpha(\lambda) \cdot L} \tag{4.1}$$

where, $I_0(\lambda)$ represents the intensity of the incident radiation, $I(\lambda)$ represents the intensity after it passes through a path length $L$, and $\alpha(\lambda)$ represents the absorption coefficient of the gas as a function of the wavelength $\lambda$. $\alpha(\lambda)$ can further be expanded as

$$\alpha(\lambda) = N_{tot} \cdot c \cdot \sigma(\lambda) \tag{4.2}$$

where, $\sigma(\lambda)$ is the absorption cross-section, $N_{tot}$ is the density of molecules, and $c$ is the concentration. For weak absorption, the exponential trend of Lambert-Beer law reduces to a linear trend

$$I(\lambda) = I_0(\lambda) \cdot (1 - \alpha(\lambda) \cdot L) \tag{4.3}$$

Drawing upon the principles of the Beer-Lambert law several gas detection techniques have been developed. These techniques include Fourier Transform Infrared Absorption Spectroscopy (FTIR), Tunable Diode Laser Absorption Spectroscopy (TDLAS), Cavity Ring-Down Spectroscopy (CRDS), Photoacoustic Spectroscopy (PAS), Quartz Enhanced Photoacoustic Spectroscopy (QEPAS) and various others.

To date it has been demonstrated that trace gas species can be optically detected with de-

tection sensitivities down to parts-per-quadrillion concentration levels [22]. Nevertheless, these techniques do have certain limitations. For instance, FTIR has a restricted spectral range and can be affected by interference. TDLAS sensitivity is directly proportional to the length of the optical path. Consequently, in order to measure trace quantities of gas, the optical path must be large. Nevertheless, multi-pass cells are commercially available and have been successfully employed in several optical sensors over the last years [23]. CRDS encounters the same issue as TDLAS and also necessitates high responsivity detectors and an extremely stable and highly reflective cavity. It is worth emphasizing that both optical cavities and multi-pass cells are typically optimized for specific operational wavelengths. Consequently, their performance significantly declines when paired with broadband sources, making them unsuitable for multi-gas detection applications [24].

These issues make FTIR, TDLAS, CRDS and other detection techniques, complex, bulky and expensive. This is where PAS emerges as the knight in the shining armor. PAS offers outstanding performances for short optical pathlength [10]. It does not require optical cavities and is achromatic, meaning it is wavelength independent. Moreover, it eliminates the need for optical detectors [25] and the sensor size could also be minimized thanks to the signal strength proportional to the laser power. QEPAS, inherits the advantages of PAS while offering additional benefits such as immunity to external vibrations and in general a reduced fingerprint, making the QEPAS module the core a point-sensing system.

Therefore, we choose to work with QEPAS thanks to the numerous advantages, notably its wavelength independence and compactness, which hold significant importance for our purposes. In the subsequent section, we will begin by providing an elaborated discussion of PAS and subsequently transition to a discussion on QEPAS.

## 4.3 Photoacoustic Spectroscopy

The photoacoustic effect is a phenomenon that involves the generation of sound waves due to the absorption of light by a material. The history of the photoacoustic effect dates back to 1880 when Alexander Graham Bell discovered the effect while working on the

development of the telephone. Bell observed that when a beam of sunlight was interrupted by a material, such as a thin metal strip, it produced a sound wave. However, it was not until the $20^{th}$ century that significant advancements were made in understanding and utilizing the photoacoustic effect.

In 1938, Viegerov significantly improved the photoacoustic technique, enabling the first-ever spectroscopic gas analysis [26]. He was able to quantify $CO_2$ in $N_2$ at concentrations as low as 0.2% by using a blackbody as an infrared source. Pioneers like Pfund [27] and Luft [28] made contributions that furthered this technique. But it wasn't until the 1970s, when laser sources, photodetectors, and theory of the photoacoustic effect in solids were developed [29], that photoacoustic spectroscopy (PAS) fully came into its own.

Over time, the photoacoustic effect has gained widespread applications across diverse fields such as biomedical imaging, environmental monitoring, and materials characterization. Nowadays, PAS stands as one of the most reliable and sensitive trace gases optical detection technique.

The molecules in a gas sample are excited when light of a certain wavelength is absorbed by it, which later relax back to their ground state through either emission of photons or non-radiative processes. The non-radiative processes cause localized heating within the gas, resulting in elevated local pressure. When the intensity of the incident light is periodically modulated, the thermal energy generated in the sample also becomes periodic. Consequently, periodic variation of thermal energy provokes pressure wave i.e., an acoustic wave, with the identical frequency as the modulation of the incident light. By selecting a modulating frequency that aligns with the resonant frequency of the sample cell (resonator), the acoustic waves can be amplified. The degree of this amplification is quantified by the quality factor ($Q$) of the acoustic resonance define as

$$Q = \frac{f_0}{\Delta f_{FWHM}} \tag{4.4}$$

where, $f_0$ represents the resonant frequency and $\Delta f_{FWHM}$ represents the full width at

half maximum (FWHM) of the resonance profile. Typically, $f_0$ and $Q$ are in the range of $1-4\ kHz$ and $40-200$ respectively [25].

Moreover, the intensity of the generated acoustic waves (photoacoustic signal, $S$) is linearly related to the concentration of the gas under investigation (form Equations (4.2) and (4.3)), enabling the use of acoustic waves as a means to quantify the concentration.

$$S = C \cdot P_L \cdot \alpha \tag{4.5}$$

where $C$ is the instrumental constant and $P_L$ is the laser optical power.

A microphone can detect acoustic waves, and this capability eliminates the necessity for an optical detector in PAS, providing a significant advantage to this technique. However, the sensitivity of gas sensors based on standard PAS depends on the properties of the resonator cell, such as its resonant frequency and Q-factor, as well as on the performance of the selected microphone, modulation frequency and the noise level. Both external sources of noise and noise generated by the absorption of incident radiation on the PAS cell wall and window contribute to a decrease in signal-to-noise ratio (SNR), consequently limiting the minimum detectable concentration. Thus, various PAS cells design including resonant cells with acoustic buffers [30], windowless cells [31], and a differential cell [32] have been developed and utilized to enhance the SNR.

Thanks to these improvements, PAS has proven to be highly effective in a wide range of trace gas sensing applications and has demonstrated its versatility and reliability in detecting and analyzing trace gases in diverse fields, contributing to advancements in understanding and addressing various environmental, industrial, and health-related challenges.

## 4.4 Quartz Enhanced Photoacoustic Spectroscopy

### 4.4.1 Background

A new approach, quartz-enhanced photoacoustic spectroscopy (QEPAS) was developed to overcome the limitations of standard PAS and to improve noise immunity. This method utilizes quartz tuning forks (QTF), originally developed for timekeeping, to reduce the size of the acoustic cell and take advantage of their intrinsic immunity to environmental noise. The standard QTFs used for timekeeping exhibit high $Q$ of 100,000 or more when encapsulated in a vacuum and $Q$ of 10,000 under normal atmospheric pressure and has a resonance frequency of 32.768 kHz. Moreover, these QTFs are constructed from low loss piezoelectric material (Quartz), enabling them to generate detectable electric charge proportional to the amplitude of the acoustic wave produced by the absorption of modulated incident light. As a result, they function as both an acoustic resonator and a transducer, eliminating the need for traditional acoustic cells and freeing the design from constraints associated with microphone [33].

The Narrow resonance bandwidth of QTF improves external noise (typically <10 kHz ) immunity of the system as only a small number of frequency components falling in this narrow spectral band can produce efficient excitation of the QTF vibrations. It is worth noting that even when external sound waves have frequencies that match the resonance frequency of the QTF do not disrupt the photoacoustic signal, thereby improving the QTF's noise immunity. This can be attributed to the QTF's acoustic quadrupole nature and the small spacing between its two prongs (approximately 0.1 mm), which is much smaller than the acoustic wavelength of such sound waves (around 1 cm). As a result, these sound waves fail to stimulate the piezoelectrically active mode where the two prongs move in opposite directions. Instead, in this case, the prongs move in the same direction, as shown in Figure 4.1 (Left), resulting in zero electrical response.

On the other hand, when the sound source is between the prongs it generates an in-plane antisymmetric vibrational mode as shown in Figure 4.1 (Right), which is further converted

into an electrical signal via the piezoelectric effect [8]. Typically, such configuration of confining photoacoustic wave between the prongs of QTF can be achieved by focusing the laser beam between the prongs as shown in Figure 4.2.

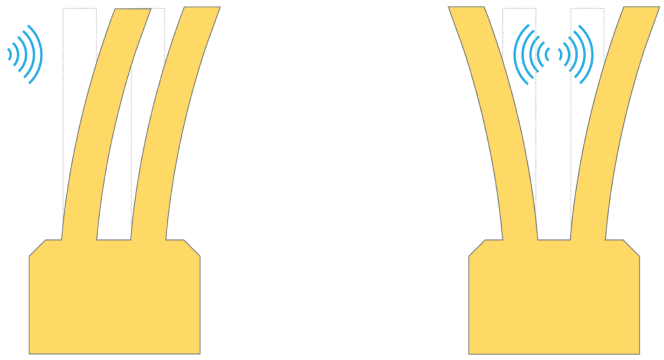

**Figure. 4.1:** (Left) Symmetric and (Right) First in-plane flexural antisymmetric mode of a QTF.

It is important to note that the careful alignment and small spot size of the laser beam is required as illuminating modulated laser light onto the QTF prongs might result in absorption of this light by the quartz crystal. This causes a photothermal excitation which translates to photothermal noise, thereby deteriorating the noise performance of the system. This is especially crucial for standard QTFs due to the small spacing between the prongs.

The generation of a photoacoustic wave involves the energy transfer from internal to translational molecular degrees of freedom. If a rotational-vibrational state is excited, a collision-induced vibrational to translation (V-T) relaxation follows, with a time constant that for a particular molecule is dependent on the presence of other molecules and intermolecular interactions. When QEPAS measurements are performed at a detection frequency of $\sim$ 32.7 kHz, the system will be more sensitive to the V-T relaxation rate compared to the conventional PAS, which is commonly performed at $f_0 < 4$ kHz. In case of a slow V-T relaxation with respect to the modulation frequency, the thermal waves in the gas cannot follow fast changes of the laser induced molecular vibration excitation. Thus, the generated photoacoustic wave is weaker than it would be in case of a fast V-

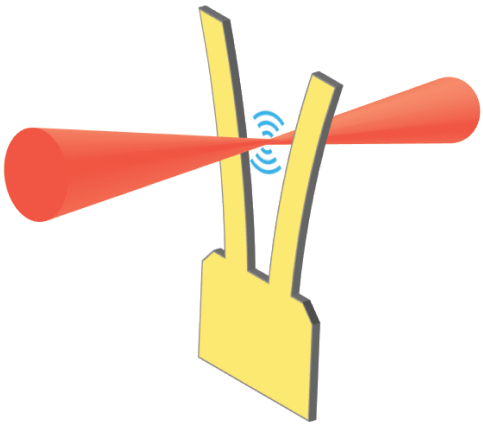

**Figure. 4.2:** Laser beam focused between the prongs of tuning fork to localize the acoustic wave between the prongs.

T energy and effective relaxation [34]. For instantaneous V-T relaxation, the detected photoacoustic signal can be expressed similar to PAS

$$S = Q \cdot P_L \cdot \alpha \cdot \epsilon \tag{4.6}$$

where $\epsilon$ is the optoacoustic transduction efficiency, i.e., the conversion of the absorbed optical radiation power into acoustic energy.

### 4.4.2 Custom Tuning Fork

In the context of gas sensing applications, it is desirable for a QTF design to exhibit certain key attributes. These include a high-quality factor, a resonance frequency that minimizes the influence of environmental noise while effectively detecting acoustic waves produced by gases with slow relaxation, and an adequate prong spacing that allows convenient alignment of laser beam spots without touching the prongs.

Unfortunately, standard QTFs are not well-suited for use in QEPAS sensors due to their small prong spacing. As a result, various research groups have proposed custom QTF designs with different geometries. These design improvements primarily aim to increase

the spacing between the QTF prongs and reduce the resonance frequency. In a study by Patimisco et al. [35], a series of custom QTFs with diverse geometrical parameters, including prong spacing, length, width, and quartz crystal thickness have been successfully demonstrated. These QTFs are shown in Figure 4.3.

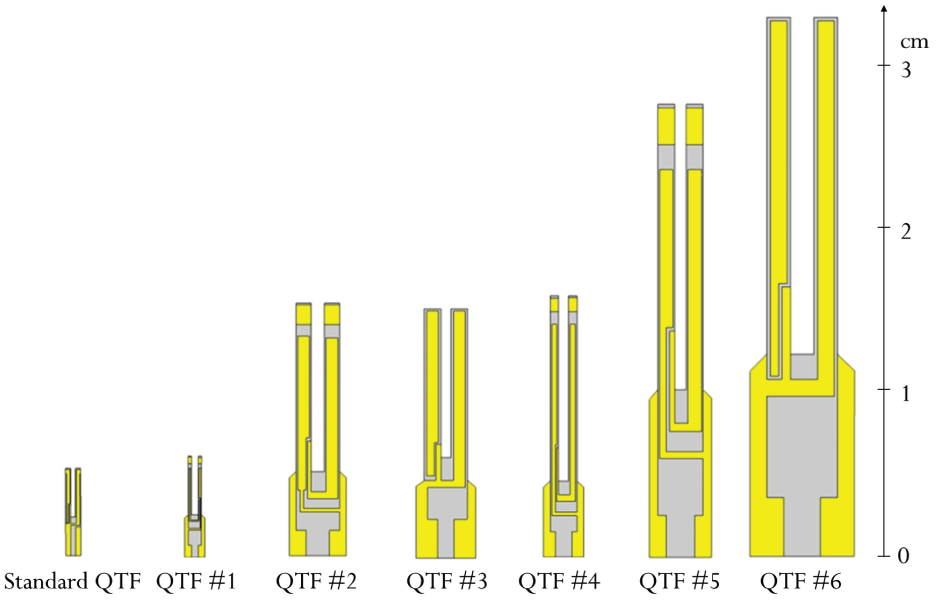


**Figure. 4.3:** Custom tunning forks. Adapted from [35].

Patimisco et al. found that the prong spacing does not influence the electro-elastic properties of the QTFs. This is because the two prongs can be assumed independent of each other. However, the spacing plays a critical role in acoustic-electric transduction efficiency. Furthermore, when the parameters $P_L$, $\alpha$, and $\epsilon$ remain constant, $Q$-factor can be regarded as the figure of merit for QEPAS. Consequently, to enhance the $Q$-factor, one should design a QTF with a larger $T/L$ factor, as $Q$ is directly proportional to the fork constant where $T$ and $L$ represents prong thickness and length respectively [35]. Based on experimental observations the overall $Q$ can be represented in terms of $L$, $T$ and crystal thickness $w$ as [36]

$$Q = 3.78 \times 10^5 \, \frac{wT}{L} \tag{4.7}$$

Additionally, the QEPAS signal is determined by the generated and collected piezoelectric current, and at resonance, the most representative figure of merit for charge generation capability is the electrical conductance, $R^{-1}$, in the electrical model of the QTF. Considering that $R^{-1}$ is approximately proportional to the square root of $R^{-1} \sim (w\sqrt{T})/L^2$ , it becomes necessary to decrease $L$ and increase both $T$ and $w$. Designing QTFs with short $L$ and large $T$ provides a good quality factor and conductance but results in an increase in the resonance frequency [35].

It's crucial to acknowledge that the QEPAS signal is also significantly affected by the gas sample pressure. As the pressure decreases, the Q-factor of the resonator can increase up to $\sim 4$ times the value at atmospheric pressure, when reaching an operating pressure $< 10$ Torr. Decreasing the pressure, the cross-sections of dipole transitions increase whereas V-T and R-T relaxations become less effective due to the reduced number of collisional partners. Hence, at low pressures, it becomes necessary to reduce the QTF resonance frequency to enable efficient relaxation of gas excess energy, allowing thermal waves to follow changes in the laser-induced molecular vibration excitation in the gas. Achieving this requires designing QTFs with small thickness and large prong length to decrease $f_0$. However, this has negative impact on the $Q$.

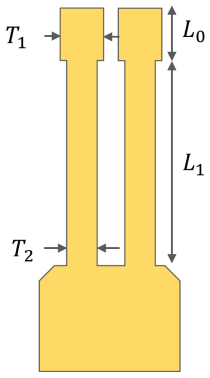


**Figure. 4.4:** QTF with T-shaped prongs where $T_1 = 2$ mm, $T_2 = 1.4$ mm, $L_0 = 2.4$ mm, $L_1 = 7$ mm. Adapted from [35].

To address this concern, a solution involving QTFs with varying prong thickness along prong axis has been proposed, as depicted in Figure 4.4. This geometry in effect adds

an additional mass to the free ends of the prongs, which in turn reduces the resonant frequency. The dimensions of this T-shaped prong QTF are $T_1 = 2$ mm, $T_2 = 1.4$ mm, $L_0 = 2.4$ mm, $L_1 = 7$ mm and $w = 0.25$ mm. This particular QTF model exhibits a resonance frequency of $f_0 = 12460.55$ Hz and a quality factor of $Q = 15540$ at atmospheric pressure. It is worth noting that QTF with this specific prong type has been utilized in the context of this thesis.

### 4.4.3 Spectrophone Design

In a QEPAS spectrophone, typically a pair or a single tube, measuring in the millimeter range, are acoustically coupled to the QTF to enhance and confine the sound wave. These tubes serve as acoustic micro resonators (mRs), and the standing-wave vibrational pattern formed within the tubes enhances the acoustic field intensity between the QTF prongs. These configurations are known as on-beam and off-beam configurations respectively, as illustrated in Figure 4.5.

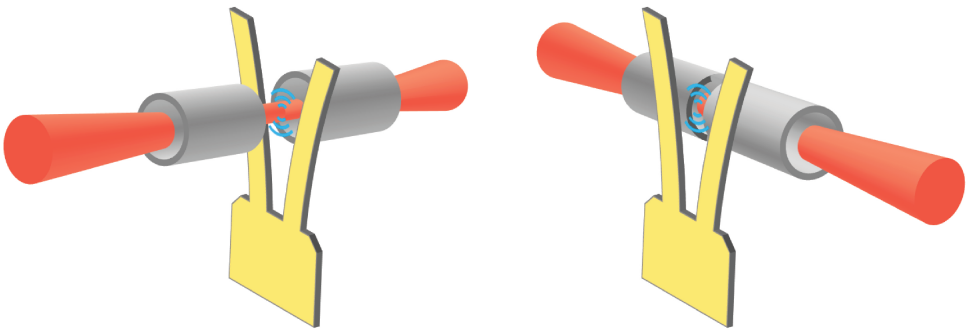

**Figure. 4.5:** (Left) On-beam and (Right) Off-beam QEPAS configuration.

In the on-beam configuration, the micro resonators tubes are positioned on both sides of the QTF perpendicular to its plane, and the excitation laser beam is focused between the prongs through the mRs. The performance of the sensor is influenced by the tubes geometry and the spacing between them. Moreover, it is critical that the laser beam entering the tubes does not touch the tube walls as it will provoke modulated thermal expansions of the acoustic dipole structure, leading also in this case an unwanted background noise

component. On the other hand, the off-beam configuration involves a single resonator tube with a small aperture in its center, allowing for the coupling of acoustic waves with the QTF. This tube is placed adjacent to the QTF. The off-beam configuration offers advantages in terms of alignment but generally results in lower sensitivities compared to the on-beam configuration. As a result, the on-beam QEPAS configuration is typically preferred.

### 4.4.4 Wavelength Modulation

The interaction between the chemical species and the modulated light produces signals at the modulation frequency and its harmonics. These harmonics can be coherently detected using a lock-in amplifier, enabling phase-sensitive detection. This results in a decrease in noise contribution during measurements, leading to an improved signal-to-noise ratio. Only the noise centered around the detection frequency and within the detection bandwidth can impact the measurements. To minimize the impact of $1/f$ laser noise, the detection band is shifted to higher frequencies. While a higher detection band reduces laser noise, it is unnecessary to exceed 100 kHz as the laser noise levels off at this frequency. [37].

Two approaches are commonly employed to modulate the radiation emitted by a laser source: amplitude modulation (AM) and wavelength modulation (WM).

The amplitude modulation (AM) approach involves modulating the laser output by switching it on and off at a fixed frequency. This modulation technique is commonly employed in gas sensors utilizing photoacoustic spectroscopy [38]. However, it's important to note that spectroscopic techniques based on AM are not inherently background-free. Consequently, a comprehensive analysis of the background signal becomes necessary, which adds additional complexity to the technique. Thereby making it less appealing.

On the other hand, wavelength modulation (WM) approach involves periodic variation of the emission wavelength by periodically varying the laser injection current. WM is accomplished by dithering the laser injection current by a sine function. However, sine dithering

changes both the emitted optical power and wavelength resulting in simultaneous AM and WM with a phase shift that is laser dependent [25].

The injection current, $i(t)$, laser emission frequency, $\nu(t)$ and the optical power intensity, $I(t)$ can be represented as

$$i(t) = i_0 + \Delta i \cdot cos(\omega t) \tag{4.8}$$

$$\nu(t) = \nu_0 + \Delta\nu \cdot cos(\omega t) \tag{4.9}$$

$$I(t) = I_0 + \Delta I \cdot cos(\omega t) \tag{4.10}$$

where $\omega = 2\pi f$ is the angular frequency of the modulation. $\Delta i$, $\Delta\nu$ and $\Delta I$ are current, frequency and intensity modulation depths respectively. $\Delta I$ depends on the injection efficiency of the laser and is assumed constant over the wavelength scan range. Furthermore, the absorbed optical intensity depends on the absorption coefficient, $\alpha[\nu(t)]$. From the Taylor series expansion of $\alpha[\nu(t)]$ for small $\Delta\nu$ and considering the weak absorption, we obtain

$$S_{1\omega} = L\Delta I\alpha_0 - L\frac{\delta\alpha}{\delta\nu}\bigg|_{\nu=\nu_0}\Delta\nu \tag{4.11}$$

$$S_{2\omega} = -L\Delta I\frac{\delta\alpha}{\delta\nu}\bigg|_{\nu=\nu_0}\Delta\nu + \frac{I_0}{2}\frac{\delta^2\alpha}{\delta\nu^2}\bigg|_{\nu=\nu_0}(\Delta\nu)^2 \tag{4.12}$$

where, $S_{1\omega}$ and $S_{2\omega}$ are the QEPAS signal at $1\omega$ and $2\omega$ modulation frequency. $\alpha_0$ is the background absorption contribution. We observe that $S_{2\omega}$ is free from background absorption, while background absorption contributes to $S_{1\omega}$.. The first term in $S_{2\omega}$ corresponds to the residual amplitude modulation (RAM) while the second term corresponds to the laser wavelength modulation. The RAM makes the $S_{2\omega}$ distorted, however, the distortion does not affect the peak position since the RAM component vanishes when $\nu = \nu_0$, assuming Lorentzian line shape of the absorption coefficient [39].

Hence, the background free nature of $S_{2\omega}$ makes $2\omega$ modulating more appealing. In practice, the QEPAS signal is usually recovered using a lock-in amplifier. Laser is modulated at $f_0/2$ and QEPAS signal is demodulated at $f_0$. The recovered signal is typically referred to as 2f QEPAS signals.

### 4.4.5 Long-term Stability Analysis of QEPAS Sensor

The sensitivity is a critical factor in any sensing systems. In QEPAS it represents the gas concentration level at which the SNR is unity. Normally, increasing the averaging of measurements can enhance the sensitivity of a QEPAS sensor by improving the signal. However, If the averaging time exceeds a certain point, drift effects begin to appear, leading to a decline in sensor performance. Allan variance analysis offers a way to evaluate the duration for which optical sensor signals can be averaged to enhance detection sensitivity. This analysis takes into account various noise sources, including laser instability, temperature fluctuations, mechanical drift, and the point at which moving fringes become dominant.

The Allan variance $\sigma_y^2(\tau)$ can be represented as

$$\sigma_y^2(\tau) = \frac{1}{M} \sum_{k=1}^{M} \frac{1}{2} \left(y_{k+1} - y_k\right)^2 \tag{4.13}$$

Where, M is the time series data acquired (typically for $2-4$ hours) with and integration time $\tau_0$. $y_k$ is the $k^{th}$ data averaged over $\tau$. $y_{k+1} - y_k$ is the difference between the adjacent values of $y_k$. The data M is collected by setting the lock-in amplifier time constant and recording its readings. The acquisition time of at least three times the lock-in time constant is used.

The values $y_1$ and $y_2$ are averaged to obtain a new $y_1$ averaged over $2\tau_0$. Similarly, the values of $y_3$ and $y_4$ are averaged, to obtain a new $y_2$ averaged over $2\tau_0$. These values are then used in Equation (4.13) to determine $\sigma_y^2(2\tau_0)$. The process is repeated for other integer multiples m of $\tau_0$ and finally yielding $\sigma_y^2(m\tau_0)$ as a function of $m\tau_0$. It is important

to note that all the data are treated as a single uninterrupted time sequence hence the acquired data should avoid dead time between adjacent measurements. This operation is automated by computer routine.

The minimum detection limit as a function of integration time is typically represented as Allan deviation, $\sqrt{\sigma_y^2}$, expressed in terms of the absorption coefficient or the concentration of absorbing gas. The Allan deviation closely follows $1/\sqrt{t}$, indicating that the Johnson noise is the primary noise source, even over extended periods of several hours. This suggests that a QEPAS-based sensor enables unlimited data averaging without experiencing baseline or sensitivity drift [40]. However, in practical applications, after a certain integration time, we often encounter drift effects, leading to a degradation in sensor performance. These drift effects typically arise from the gradual mechanical movements of different components within the sensor system.

## 4.5 Highly Selective QEPAS Detection of BTEX and Propane

### 4.5.1 Experimental Setup

The laser sources employed for the following investigation consist in InAs-based long-wavelength DFB QCLs emitting at wavelengths resonant with absorption bands of Toluene ($QCL_T$ $\lambda = 13.71$ $\mu$m), Benzene ($QCL_B$ $\lambda = 14.85$ $\mu$m) and Propane ($QCL_P$ $\lambda = 13.36$ $\mu$m): Section 3.5. The fabricated DFB QCLs are mounted on ALN heatsink, collimated, and packaged in a customized enclosure equipped with a PT100 [41] temperature sensor and a Peltier cooling element as shown in Figure 4.6. The provision for external water cooling is also available in the enclosure to aid in extraction of generated heat.

While the operating temperature range for these QCLs, in a CW regime, extends from $-20$°C to close to room temperature. In this experiment, specific operating temperatures have been selected to target and allow an efficient exploitation of the identified spectral fingerprints: $-10$°C, $-5$°C and 3°C for $QCL_T$, $QCL_B$ and $QCL_P$, respectively.

Figure 4.7 (a) illustrates the PIV characteristics of $QCL_T$, $QCL_B$ and $QCL_P$ at the specified temperatures. The maximum optical power reaches 11 mW, 4 mW and 3 mW,

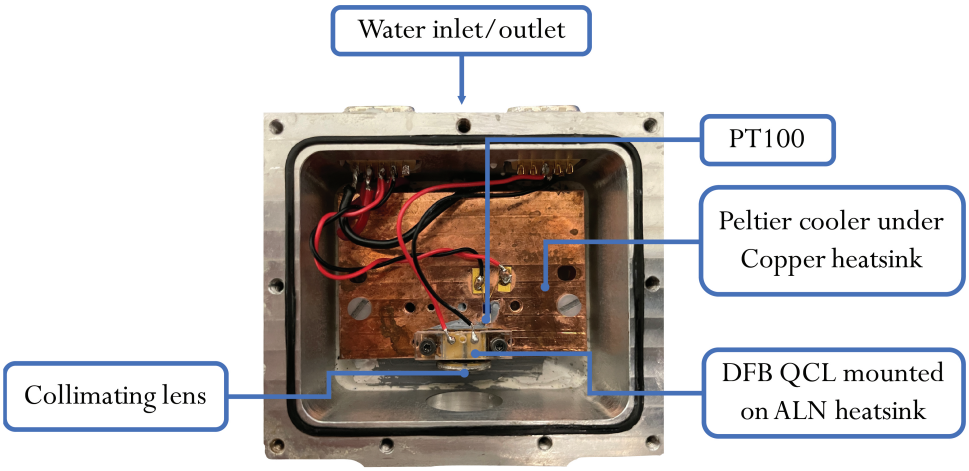


**Figure. 4.6:** Internal view of the collimated and packaged DFB QCLs.

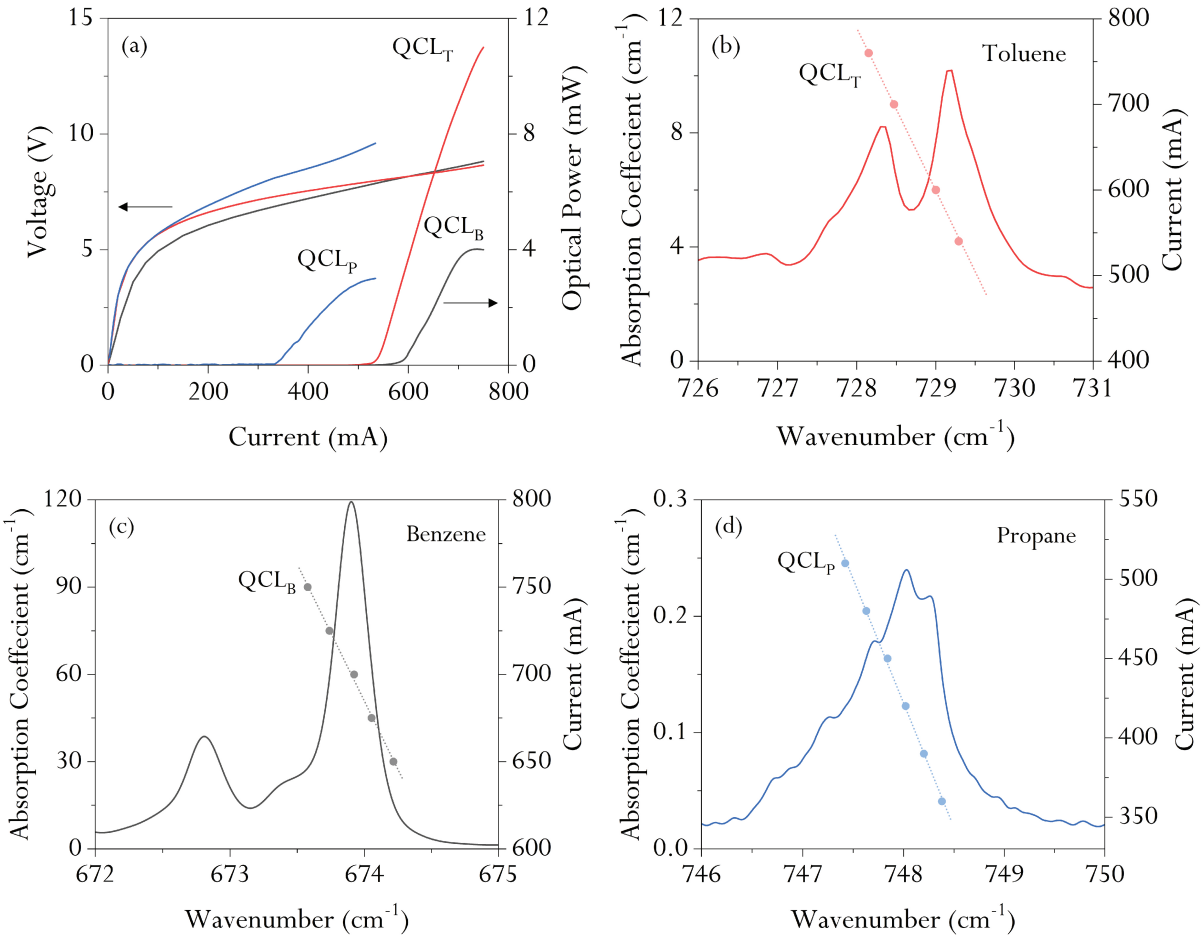


**Figure. 4.7:** (a) PIV characteristics of DFB QCLs operating at −10°C, −5°C and 3°C for $QCL_T$, $QCL_B$ and $QCL_P$ respectively. (b)–(d) Solid lines represent the simulation of the absorption spectrum for pure Toluene, Benzene, and Propane. The absorption spectra of Toluene and Benzene are extracted from the absorption coefficient spectra of the NIST database, while the Propane spectrum is extracted from the cross-sections spectra of the HITRAN spectroscopic database. The dotted lines indicate the QCL wavelength tuning as a function of injected current.

respectively. Figure 4.7 (b–d) displays the absorption coefficient for Toluene, Benzene and Propane at atmospheric pressure: solid lines and wavelength tuning of the QCLs as a function of the injection current: dotted lines with solid circles.

The Benzene and Toluene bands correspond to aryl C–H out-of-plane bending, while the Propane rotational structure refers to C–type $CH_2$–rocking fundamental mode [9]. BTEX bands are both more separated and intense with respect to the $3-4$ $\mu$m spectral window where aryl C–D stretching are mostly involved, while Propane shows absorp-

tion coefficients 50 times stronger at 3369 nm, but an almost total overlap with lighter hydrocarbons too.

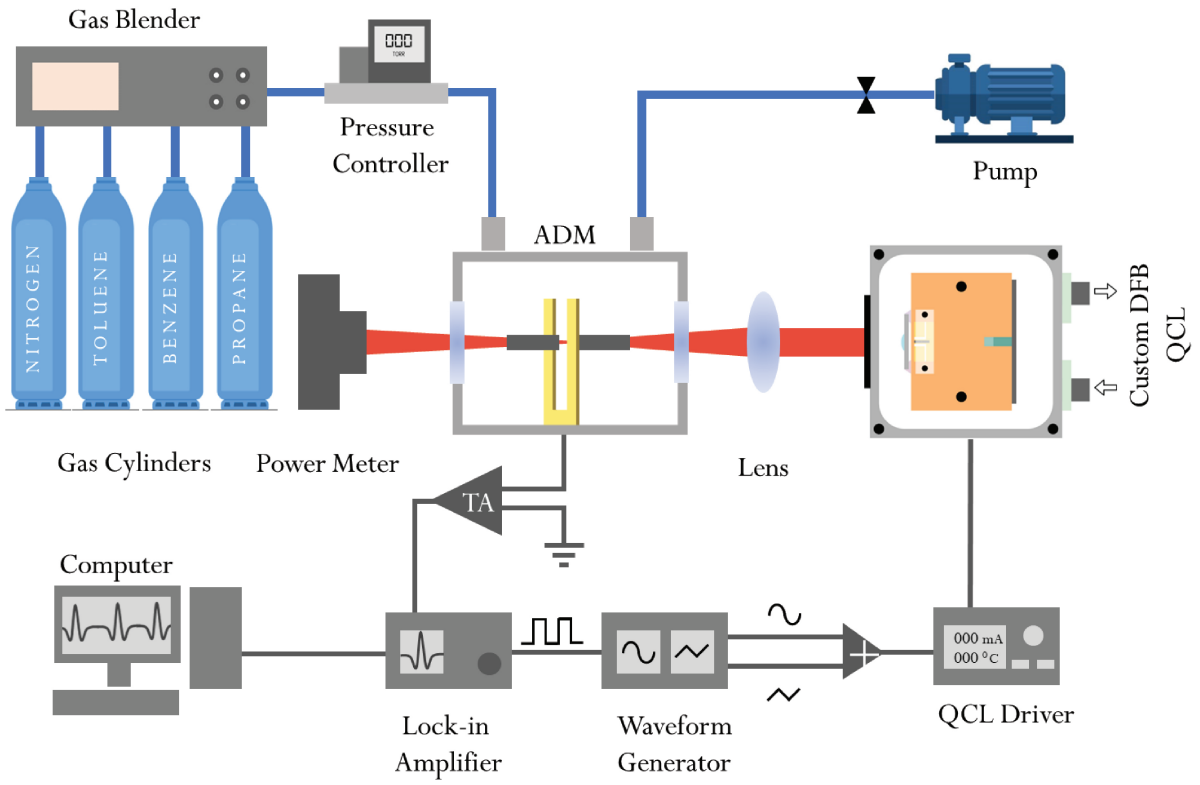


**Figure. 4.8:** The schematic of the QEPAS sensor system employing InAs-base long-wavelength QCL.

The QEPAS sensor system utilizing the fabricated DFB QCLs, is depicted in schematic form in Figure 4.8. The sensing system consists of sensor head, the gas line, and the electronic components used to drive the QCL and acquire data. The sensor head includes an Acoustic Detection Module (ADM) equipped with inlet and outlet connectors to regulate gas flow, and houses a spectrophone composed of a QTF with T-shaped prongs, acoustically coupled with a pair of resonator tubes. The resonator tubes are positioned 2 mm below the top of the QTF, perpendicular to its plane, and are separated by a gap of 0.2 mm. The tubes are 12.4 mm long and have an internal diameter of 1.59 mm and an external diameter of 1.83 mm. The resonance frequency and quality factor of the QTF's fundamental flexural mode have been retrieved via inverse piezoelectric effect, i.e., by

exciting the resonator with a sinusoidal voltage signal and performing a frequency sweep. Both resonance curve and $f$, $Q$ values as a function of pressure are plotted in Figure 4.9. Under atmospheric pressure and in a mixture of pure $N_2$, the QTF exhibits a resonance frequency of $f_0 = 12.45727$ kHz and a quality factor of $Q = 9296$.

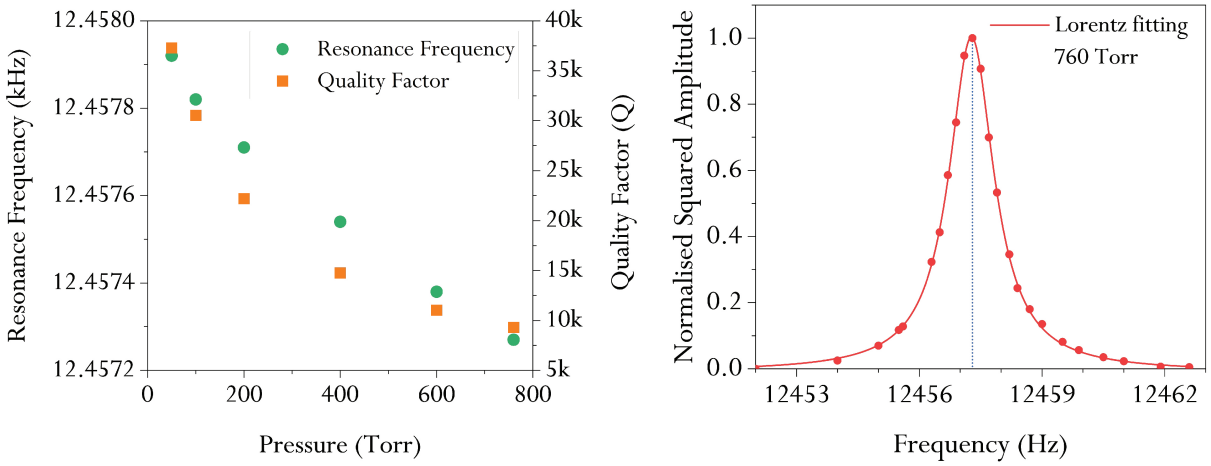


**Figure. 4.9:** (Left) The electrical characteristics of the QTF showing the resonance frequency and quality factor as a function of pressure. (Right) Resonance profile of the QTF at 760 Torr.

Components of the gas line include certified gas cylinders, a gas blender, a pressure regulator, a needle valve, and a vacuum pump. With pure $N_2$ as the carrier gas, the Gas Blender (MCQ Instrument) is used to precisely control the flow rate of each individual gas channel and produce the desired gas mixture. An Alicat pressure controller/flow meter, in conjunction with a needle valve and a pump, is used to precisely regulate gas pressure and flow rate within the gas line. The gas flow rate is maintained at a constant value of 50 sccm, with a precision of 1% for the flow setpoint of every channel.

To control the QCLs, a combined laser current driver and TEC controller (Thorlabs ITC4002QCL) is used. The current driver provides the necessary current to operate the QCLs and the TEC controls operation temperature.

The collimated beam enters the ADM through the Ge optical windows and is focused between the prongs of the QTF, through the resonator tubes, using a ZnSe plano-convex lens with a focal length of 50 mm having 3–12 $\mu$m antireflection coating. The ADM is

mounted on a five-axis stage to ensure precise alignment. The alignment process is aided by an optical power meter (THORLABS PM100D).

To carry out QEPAS measurements, the wavelength modulation and $2f$ detection method is employed. This involves applying a sinusoidal dither, which matches half of the QTF resonance frequency, to the QCL current driver. A transimpedance amplifier (TA) is then used to convert the resulting piezoelectric charge into an electrical signal. The transduced QTF signal is demodulated by a lock-in amplifier (MFIA500kHz Lock-in Amplifier, Zurich Instruments) at the QTF resonance frequency. A lock-in time constant of 100 ms is used in this process. The demodulated signal is then digitized and saved on a personal computer using a data acquisition board, with the sampling time set to three times the lock-in time constant.

### 4.5.2 Sensor Optimization, Calibration and Minimum Detection Limit

#### Sensor Optimization

In QEPAS, the optimization of gas pressure and modulation amplitude is of critical importance in order to enhance the sensitivity and improve the overall signal-to-noise ratio (SNR). When dealing with purely Lorentzian and isolated optical transitions, the operating pressure optimization has the main goal of finding a trade-off between the number of target molecules available for signal generation, the number of overall molecules facilitating the energy relaxation versus the QTF's quality factor deterioration due to increasing the working pressure. In case of complex absorption bands and presence of interferents, the identification of the optimum working pressure becomes more a matter of trade-off between collisional broadening and spectral overlaps. In this context, the optimization of the modulation depth becomes a critical issue as well. In fact, once selected the operating pressure, the modulation depth for a purely Lorentzian and isolated feature is mainly determined by its linewidth with the aim of maximizing the efficiency of the wavelength modulation, while in presence of structured absorption bands and interferents the main

criticality is selectivity. The broadband absorbers in general pose also the issue of the fingerprinting potential of the target features. For example, in terms of modulation depth, the effect of overmodulation may provide a generally high signal spectrum, which could generate as a drawback, a less-characteristic features for signal discrimination with respect to potential interferents. In fact, it is crucial to avoid exceeding an optimal threshold to prevent non-linear effects that could distort the signals and compromise accuracy and linearity. The experimental determination of the optimal pressure practically consists in the assessments of the SNR at various pressure levels, allowing for the selection of the pressure value that maximizes the system's sensitivity. To accomplish modulation depth optimization, a systematic exploration of different amplitudes is conducted, evaluating the resulting photoacoustic signal amplitude to identify the point that strikes the right balance between signal enhancement and maintaining linearity.

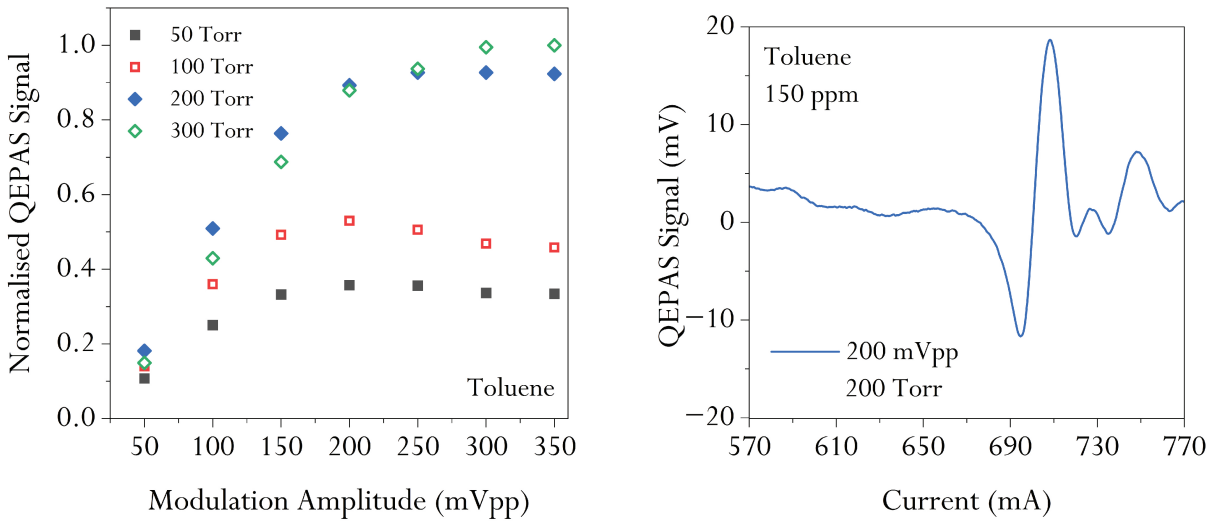


**Figure. 4.10:** (Left) Normalized QEPAS signal of Toluene plotted against modulation amplitude at various pressures. (Right) QEPAS spectra of 150 ppm of Toluene at optimal working conditions.

Figures 4.10 to 4.12 (Left) illustrates the normalized QEPAS signal as a function of modulation depth at different pressures for Toluene, Benzene and Propane respectively. In this case, the concentration of Toluene and Propane matched the certified levels in the gas cylinders: 150 ppm and 10,000 ppm, respectively. Nevertheless, we opted for a lower

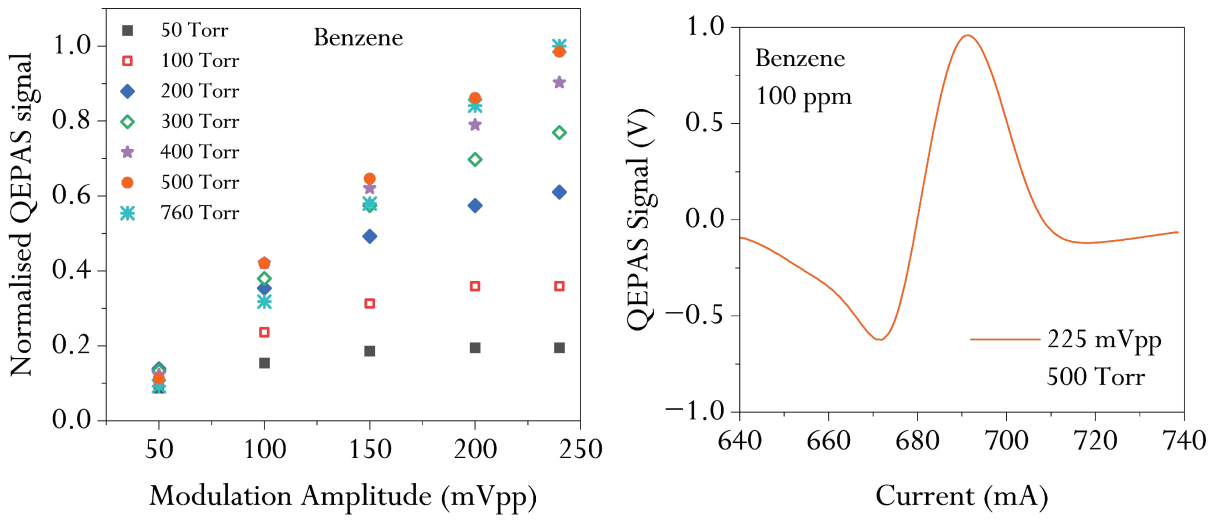


**Figure. 4.11:** (Left) Normalized QEPAS signal of Benzene plotted against modulation amplitude at various pressures. (Right) QEPAS spectra of 100 ppm of Benzene at optimal working conditions.

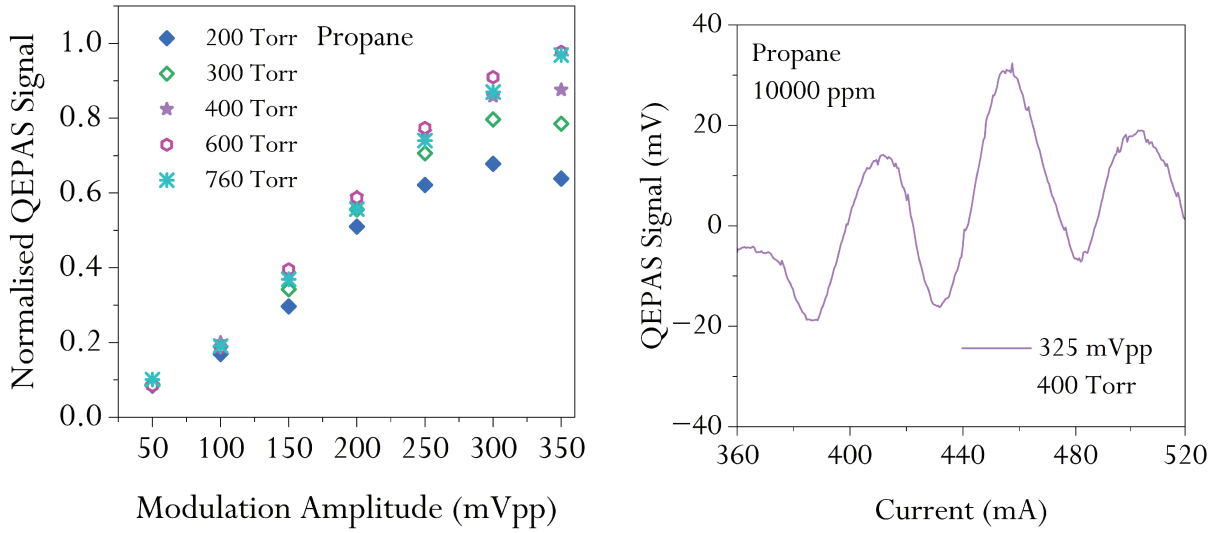


**Figure. 4.12:** (Left) Normalized QEPAS signal of Propane plotted against modulation amplitude at various pressures. (Right) QEPAS spectra of 10000 ppm of Propane at optimal working conditions.

concentration (100 ppm) of Benzene due to the fact that the amplified QEPAS signal was nearing the maximum gain provided by the transimpedance amplifier. Any further increase in signal would have caused the amplifier to saturate.

The pressure ranges of investigation are different from each gas and have been identified using the following criteria: SNR> 10 for the lower pressure value and preservation of the shape of the most representative feature for the higher value. It is evident from Figures 4.10 to 4.12 (Left) that as the pressure increases, there is a corresponding rise in the QEPAS signal. However, at higher pressures, the signals tend to overlap and intersect when varying the modulation depth. This is due to the increasing overlap of nearby absorption features. Concerning modulation amplitude, QEPAS signals tend to flatten out or even slightly decrease beyond a certain value, compatibly with the linewidth of each excited transition of the absorption band. Based on these observations and always preserving the characteristic shape of the spectra for selectivity issues, the optimal pressure and modulation depth were selected, considering the maximum signal amplitude recorded for the most intense feature of each gas spectrum. For Toluene, the optimal pressure was determined to be 200 Torr, with a corresponding optimal modulation amplitude of 200 mVpp. Similarly, for Benzene, the optimal pressure was found to be 500 Torr, with an optimal modulation amplitude of 225 mVpp. Lastly, for Propane, the optimal pressure was determined to be 400 Torr, accompanied by an optimal modulation amplitude of 325 mVpp. The QEPAS spectrum for each gas at their respective optimal working conditions are presented in the Figures 4.10 to 4.12 (Right), showcasing the absorption peaks.

**Sensor Calibration and Minimum Detection Limit**

Sensor calibration is an important step to establish the relationship between the measured signal and the concentration of the target gas. To calibrate the QEPAS sensor for each gas, a calibration process was conducted by acquiring a gas target spectral scan while diluting the certified gas mixture with humidified nitrogen ($N_2$) as shown in Figures 4.13 to 4.15 (Left).

The peak value of the most intense absorption feature for each analyte was extracted and plotted as a function of the target molecule concentration. These data have been fitted by a linear interpolation, showing a perfect linearity for each molecule, as depicted in

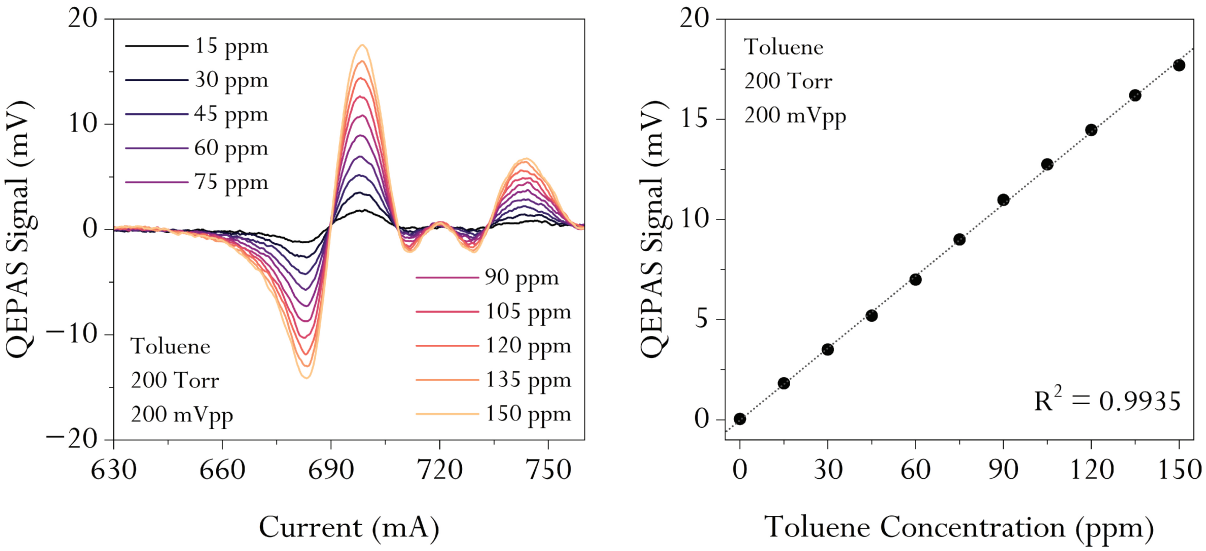


**Figure. 4.13:** (Left) QEPAS spectra of Toluene depicted as a function of laser current at optimal working conditions for various concentration levels. (Right) Peaks of most intense features plotted against concentration for Toluene

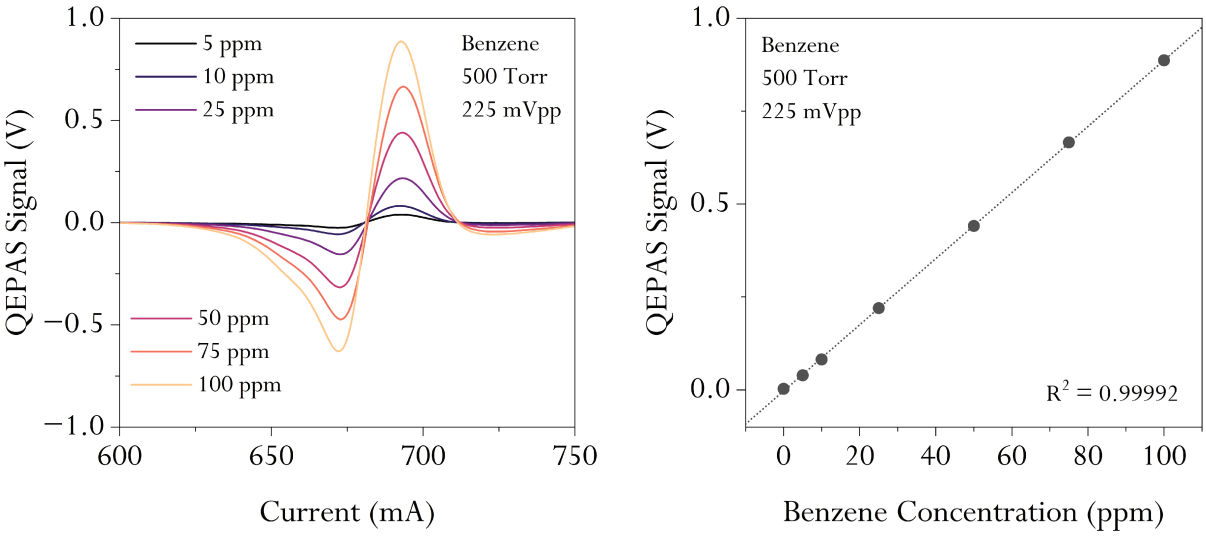


**Figure. 4.14:** (Left) QEPAS spectra of Benzene depicted as a function of laser current at optimal working conditions for various concentration levels. (Right) Peaks of most intense features plotted against concentration for Benzene

Figures 4.13 to 4.15 (Right). These calibrations allowed us to determine the detection limits through the relative slopes and by evaluating the ground noise . The noise level is calculated as the standard deviation ($1\sigma$) of the sensor response when there is no optical

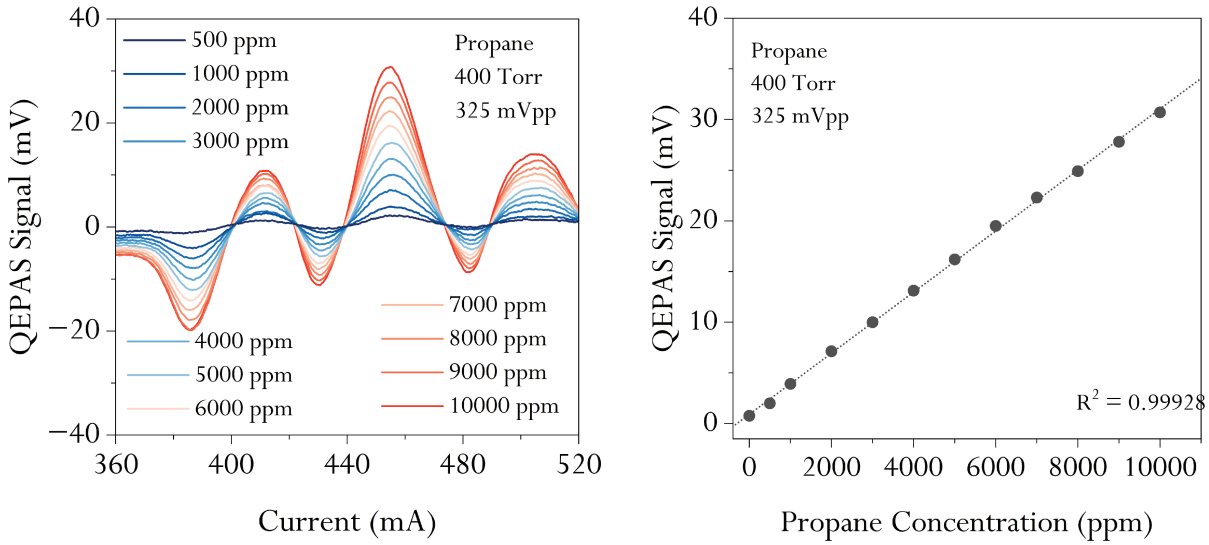


**Figure. 4.15:** (Left) QEPAS spectra of Propane depicted as a function of laser current at optimal working conditions for various concentration levels. (Right) Peaks of most intense features plotted against concentration for Propane

absorption, typically achieved by flowing pure nitrogen ($N_2$) through the absorption cell. To estimate the achievable minimum detection limit (MDL), an Allan-Werle deviation analysis was performed on noise acquired for 2.5 hours.

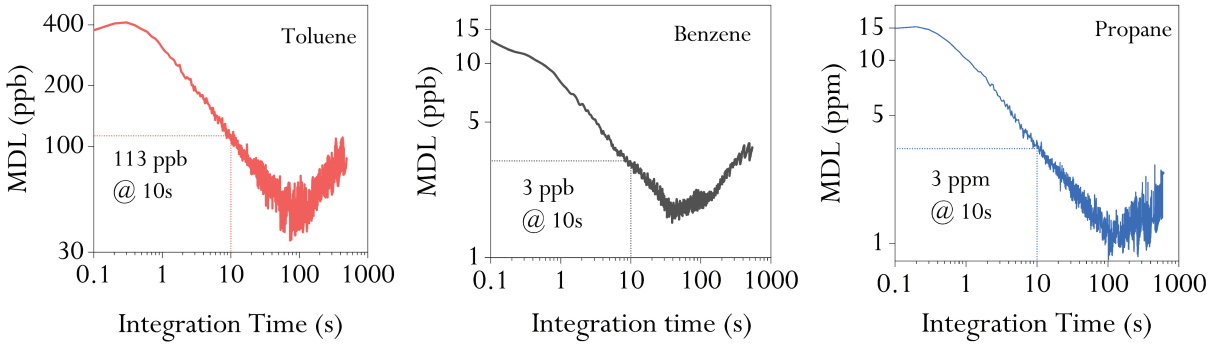


**Figure. 4.16:** (a)-(c) Allan-Werle deviation analysis of Toluene, Benzene, and Propane, respectively, demonstrating the minimum detection limit (MDL) as a function of lock-in integration time.

This analysis provides insights into the $1\sigma$ noise level and, consequently, the MDL as a function of the lock-in integration time as shown in Figure 4.16. The sensor exhibited

an MDL of 113 ppb, 3 ppb and 3 ppm for Toluene, Benzene and Propane respectively at a lock-in integration time of 10s. Furthermore, by increasing the integration time, it is possible to enhance the sensitivity and thus improve the detection limit of the sensing system. The Allan deviation analysis demonstrates that for integration times less than 100 seconds (Toluene and Propane) and 60 seconds (benzene), the noise level closely follows a $1/\sqrt{t}$ dependence. This observation suggests that the dominant source of noise in QEPAS is the thermal noise in the Quartz Tuning Fork (QTF). Beyond this, a sensitivity drift is observed where the noise level deviates from the thermal noise trend and starts to deteriorate for longer integration times. This deviation can be primarily attributed to the occurrence of other long-term effects, such as laser and mechanical instabilities, as well as temperature drifts.

### 4.5.3 Selectivity Analysis

To ensure accuracy and reliability in detecting specific gasses, the importance of selectivity in sensors cannot be overstated. High selectivity allows for precise measurements by concentrating on the target gas while reducing the impact of other compounds, thus eliminating false readings. Additionally, high selectivity enhances sensitivity, enabling sensors to detect even lower concentrations or subtle changes in gas levels.

In this study, we investigate the potential spectral interference caused by BTEX on Toluene and Benzene, as well as the interference caused by Methane and Ethane on Propane. We conduct a comparative analysis of the QEPAS signals obtained in pure nitrogen, without the presence of BTEX or Propane, with the signals obtained in the presence of Toluene, Benzene, and Propane. Furthermore, we analyze the mixture of these gases to assess any potential alterations in the spectral features or the maximum strength of the QEPAS signal. This analysis aims to verify whether the complex gas mixture affects the efficiency of radiation-to-sound conversion ($\epsilon$).

Figure 4.17 (Left) illustrates a comparison of the QEPAS signal obtained for 240 ppm of Benzene, 150 ppm of Ethylbenzene, and pure nitrogen. We employed $\mathrm{QCL}_T$ in this

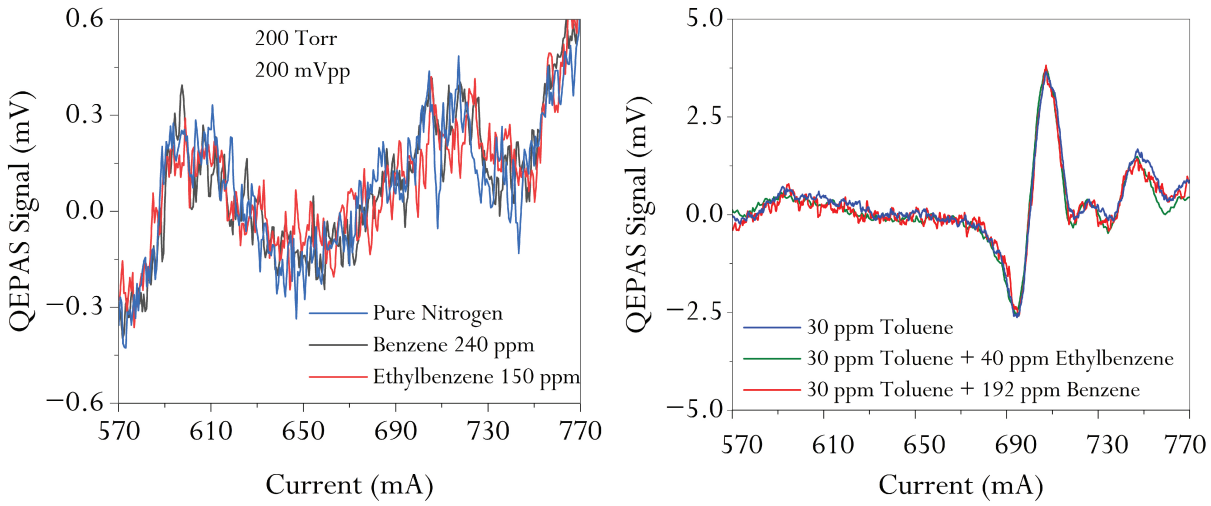


**Figure. 4.17:** Left) Comparison of QEPAS spectra obtained for 240 ppm of Benzene and 150 ppm of Ethylbenzene with the spectrum obtained for pure Nitrogen. (Right) Comparison of QEPAS signals for 30 ppm Toluene with two mixtures: 30 ppm of Toluene mixed with 40 ppm Ethylbenzene, and 30 ppm Toluene mixed with 192 ppm of Benzene at 200 Torr and 200 mVpp modulation depth.

investigation. From this figure we can see that there are no discernible spectral features observed even at high concentrations of Benzene and Ethylbenzene with respect to the $2f$ spectrum of pure nitrogen. In fact, the QEPAS signals align with that of pure nitrogen. This was evaluated by verifying that the point-by-point difference among the three spectra is actually lower that the $1\sigma$ fluctuations of the QEPAS signal at any fixed current value, indicating that within the whole tuning range of the $\mathrm{QCL}_T$, Benzene and Ethylbenzene do not exhibit absorption.

The further verification to carry out is whether Toluene detection would be affected by the presence of Benzene and Ethylbenzene in terms of radiation-to sound conversion efficiency,due to matrix effect.

Figure 4.17 (Right) compares the QEPAS signal obtained at 30 ppm of Toluene with two different gas mixtures: 30 ppm of Toluene combined with 40 ppm of Ethylbenzene, and 30 ppm of Toluene combined with 192 ppm of Benzene. These concentrations correspond to 20% and 80% of the certified Toluene, Ethylbenzene, and Benzene concentrations,

respectively. The figure clearly indicates that both the QEPAS signal features and the peak amplitude remain the same, within the $1\sigma$ fluctuations of the QEPAS signal for the strongest peak. This spectra comparison is the confirmation that the presence of the BTEX mixture does not affect the efficiency of radiation-to-sound conversion in the sensor system. Consequently, the calibration curve of the system remains highly reliable.

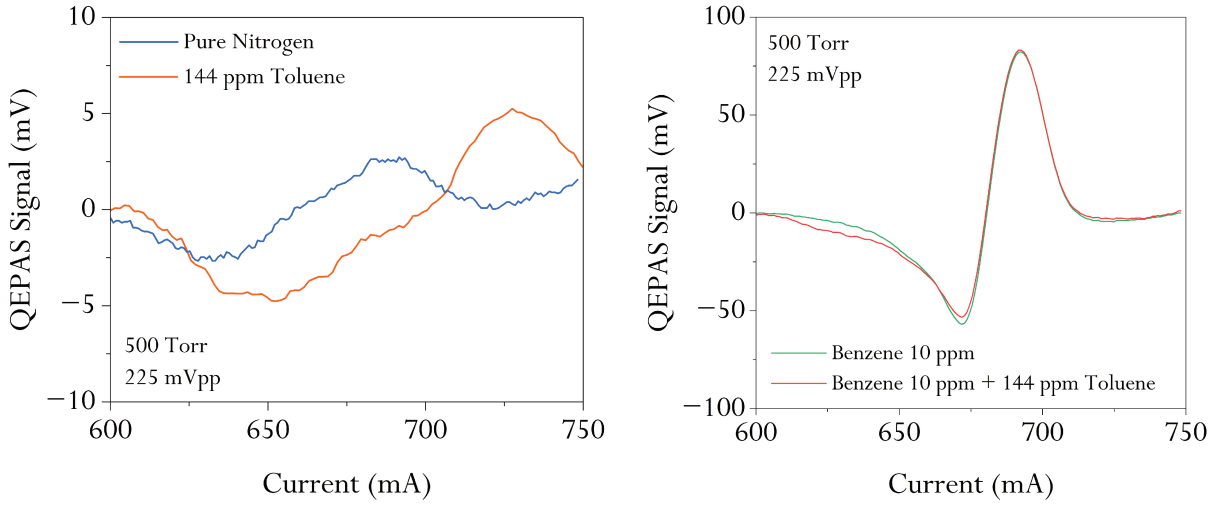


**Figure. 4.18:** (Left) Comparison of QEPAS spectra obtained for 144 ppm of Toluene with the spectrum obtained for pure Nitrogen. (Right) Comparison of QEPAS signals for 10 ppm Benzene with a mixture of 10 ppm of Benzene and 144 ppm Toluene at 500 Torr and 225 mVpp modulation depth.

Similarly, Figure 4.18 (Left) presents a comparison of the QEPAS signal obtained for 144 ppm of Toluene and pure nitrogen. We employed $QCL_B$ in this investigation.

Unlike the previous case (Figure 4.17) the QEPAS signal for Toluene does not coincide with that of pure nitrogen. Instead, a discernible feature is observed in the laser current range of 700 mA to 750 mA. However, the prominence of the feature is relatively low, with a maximum value of 5 mV. This indicates that Toluene does absorb within the tuning range of the $QCL_B$, but not so different in intensity with respect to the signal background. Moreover, Figure 4.18 (Right) compares the QEPAS signal obtained at 10 ppm of Benzene with a gas mixture comprising 10 ppm of Benzene and 144 ppm of Toluene. These concentrations correspond to 5% and 95% of the certified Benzene and

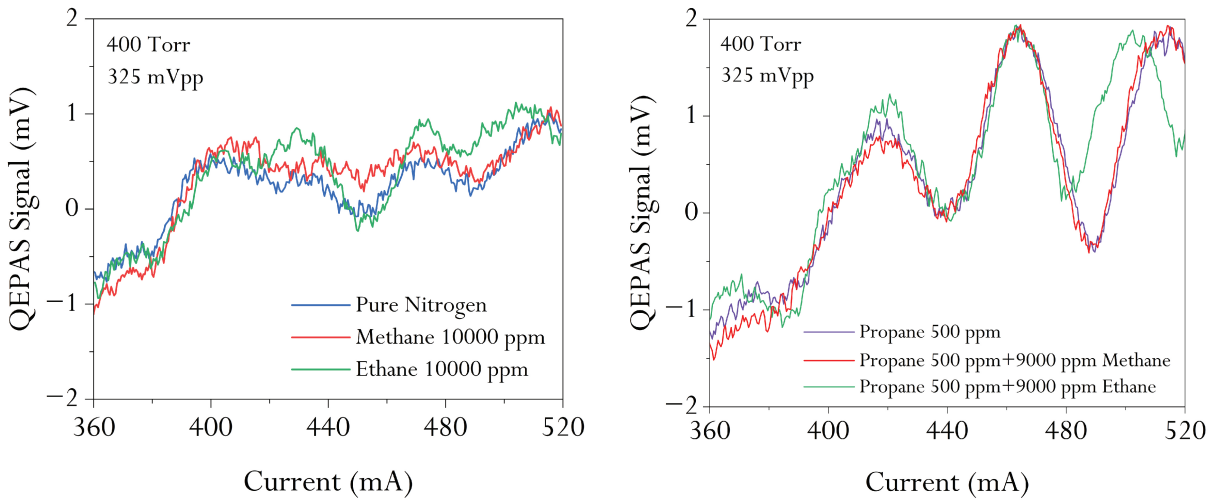


**Figure. 4.19:** (Left) Comparison of QEPAS spectra obtained for 10000 ppm of Methane and Ethane with the spectrum obtained for pure Nitrogen.(Right) Comparison of QEPAS signal for 500 ppm Propane with two mixtures: 500 ppm of Propane mixed with 9000 ppm Methane, and 500 ppm Propane mixed with 9000 ppm of Ethane at 400 Torr and 325 mVpp modulation depth.

Toluene concentrations, respectively. Here as well, both the QEPAS signal features and the peak amplitude remain the same, within the $1\sigma$ fluctuations of the QEPAS signal for the strongest peak, indicating no change in the radiation to sound conversion efficiency.

Finally, Figure 4.19 (Left) illustrates a comparison between the QEPAS signals obtained for 10000 ppm of Methane, Ethane, and pure nitrogen. We employed $QCL_P$ in this investigation. From this figure, it is evident that the QEPAS signal for Methane and even more for Ethane is different from the $N_2$ background signal. However, it is important to note that this difference is very small and is only distinguishable from $N_2$ background signal at a very high concentration (around 10000 ppm).

Furthermore, Figure 4.19 (Right) compares the QEPAS signals obtained for 500 ppm of Propane with two different gas mixtures. The first mixture comprises 500 ppm of Propane combined with 9000 ppm of Methane, while the second mixture consists of 500 ppm of Propane combined with 9000 ppm of Ethane. These concentrations represent 10% and 90% of the certified Propane, Methane, and Ethane concentrations, respectively.

Regarding the QEPAS signal of the mixture of Propane with Methane, the signal aligns with that of 500 ppm of Propane across almost the entire tuning range. However, Ethane QEPAS signal show major differences especially at the beginning and at the end of laser scan. Nevertheless, if the only Propane central peak occurring at 450 mA is considered, for which the linearity and the calibration were carried out, this figure show us that, within the $1\sigma$ Propane peak signal fluctuations, the 3 spectra are perfectly overlapping. These findings confirm the possibility to selectively perform on peak measurements without any kind of spectral/non spectral interference for Propane, even in presence of other lighter alkanes, which are normally expected at higher abundances in natural gas-like mixtures.

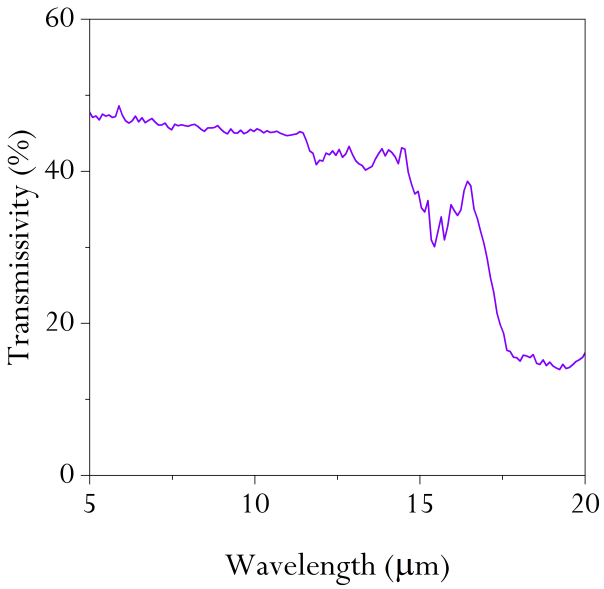


**Figure. 4.20:** Transmissivity of uncoated Ge optical window as a function of wavelength. Adapted from [42].

It is important to note that due to the wavelength modulation we observe a periodic variation in the $2f$ QEPAS spectra of $N_2$ as shown in Figures 4.17 to 4.19 (Left). This variation can be attributed to slight changes in the transmissivity of Ge window at longer wavelengths, as illustrated in Figure 4.20, showing the transmission profile of an uncoated Ge optical window [42]. It is essential to mention that in our experimental setup, we utilized an AR coated Ge window since the transmissivity of uncoated windows is significantly lower compared to coated ones. However, we must acknowledge that the AR

coating is specifically designed for the $7 - 12$ $\mu$m range, and we lack information on how its transmissivity behaves beyond 12 $\mu$m. Therefore, we assumed the possibility that the used window may experience transmission fluctuations beyond the specified range.

## 4.6 Coupling of Long-Wavelength QCLs with Hollow Core Waveguide

Hollow Core Waveguides (HCWs) structure is composed of a hollow glass capillary tube with a metallic/dielectric film deposited inside the bore [43]. HCWs are of particular interest for mid-IR and terahertz radiation, where it is otherwise difficult to find materials suitable to use in solid-core optical fibers. They are ideal for transmitting infrared laser radiation due to their advantageous characteristics, including easy handling, flexibility, and high output beam quality. HCWs exhibit exceptional coupling efficiency, absence of back reflection and cladding modes, as well as superior energy/power handling capabilities [43, 44]. These features make HCWs well-suited for applications such as in QEPAS, where the quality of the exciting laser beam directly impacts the optical noise.

Another significant attribute of HCW is their ability to achieve quasi-single mode propagation, despite their relatively large bore size [45]. However, the effectiveness of single mode propagation and mode filtering in HCWs is heavily influenced by the optical coupling conditions between laser source and HCW and the HCW length. The bore size determines the overall losses and mode quality, whereas the thickness of the dielectric/metallic layers determines the spectral response.

While HCWs operating in single mode for $3.5 - 10.5$ $\mu$m wavelengths have already been demonstrated [46, 47], the exploration of HCWs for longer wavelengths is limited or non-existent primarily, due to the lack of suitable laser sources. Therefore, in this section, we investigate the performance of HCWs at 13.71 $\mu$m.

We analyze two sets of HCWs of different lengths and a bore diameter of 500 $\mu$m. We assess the mode quality of the output beams by comparing them with the mode profiles

obtained at the exit of the employed QCL. Additionally we evaluate the contributions to total losses from the coupling conditions and propagation losses and compare the experimental results with theoretical predictions.

### 4.6.1 Theoretical Overview

The coupling conditions between the laser and the HCW have a significant impact on both the propagation losses and the quality of the HCW output beam. When a collimated laser beam is coupled to the HCW using a focusing lens, the losses during propagation and the beam quality at the waveguide exit are affected by the beam quality of the input laser beam and the ratio between the beam waist and the core diameter.

To estimate the beam waist radius, $w_0$, at the focal plane of the lens, we consider a diffraction-limited collimated Gaussian beam with a radius of, $W$, illuminating a lens with a radius of curvature of $R$. $w_0$ can be estimated as

$$w_0 = \frac{W}{\sqrt{1 + \left(\frac{\pi W^2}{\lambda R}\right)^2}} \tag{4.14}$$

An approximation for the intensity distribution profile of the Gaussian laser beam at the entrance of the waveguide can be given by:

$$G(r) = G_0 e^{-\frac{r^2}{w_0^2}} \tag{4.15}$$

When this Gaussian beam is precisely focused into a HCW along the optic axis, only the $HE_{1m}$ hybrid modes are selectively excited within the waveguide.

The spatial profiles of $HE_{1m}$ waveguide modes can be approximated by the zero order Bessel functions $J(u_{1m}r/a)$ where a is the bore radius and $u_{1m}$ is the $m^{th}$ root of zero-order Bessel function. The amount of optical power coupled with the $m^{th}$ waveguide mode can be expressed in terms of power coupling efficiency defined as

$$\eta_{1m} = \frac{\left| \int_0^a G(r) J\left(u_{1m}\frac{r}{a}\right) r dr \right|^2}{\int_0^a G(r)^2 r dr \int_0^a J^2\left(u_{1m}\frac{r}{a}\right) r dr} \tag{4.16}$$

Since $\eta_{1m}$ is dependent on the ratio $w_0/a$, it is necessary to use a suitable focal length lens in order to optimize the coupling of the laser beam into the HCW.

The lowest order mode $HE_{11}$ exhibits a Gaussian spatial profile with circular symmetry. Therefore, a single-mode Gaussian-like circular-symmetric beam delivery at the HCW exit is obtained when the laser power is coupled with the $HE_{11}$ mode. The highest coupling efficiency to the $HE_{11}$ mode is obtained for $w_0/a = 0.64$ [45].

Furthermore, while propagating in the waveguide, each $m^{th}$ HCW mode undergoes an attenuation, depending on the waveguide length, $L$, the optical properties of the metallic and dielectric HCW layers and the $u_{1m}$ coefficient. To estimate the propagation losses, the equation derived by Miyagi and Kawakami to determine the attenuation coefficients $\alpha_{1m}$ for the $HE_{1m}$ waveguide modes can be employed [48]

$$\alpha_{1m} = \left(\frac{u_{1m}}{2\pi}\right)^2 \frac{\lambda^2}{a^3} \left(\frac{n}{n^2+k^2}\right) \frac{1}{2} \left[1 + \frac{n_d^2}{(n_d^2-1)^{1/2}}\right]^2 \tag{4.17}$$

Where, n and k are the real and imaginary parts of the complex index of metallic layer, while $n_d$ is the refractive index of the dielectric film. It is worth to notice that the attenuation coefficient increases with the order number m, resulting in a significant attenuation experienced by the higher order modes as compared to the $HE_{11}$ mode. Therefore, only the $HE_{11}$ mode can propagate effectively through a HCW long enough to suppress the other modes. Finally, the total propagation losses, $L_p$, of the $HE_1$ mode can be calculated in terms of the coupling efficiency coefficients $\eta_{1m}$ and the attenuation coefficients $\alpha_{1m}$, as follows

$$L_p(dB) = -10 \cdot log_{10}\left(\sum_m \eta_{1m} e^{-2\alpha_{1m}L}\right) \tag{4.18}$$

### 4.6.2 Experimental Setup

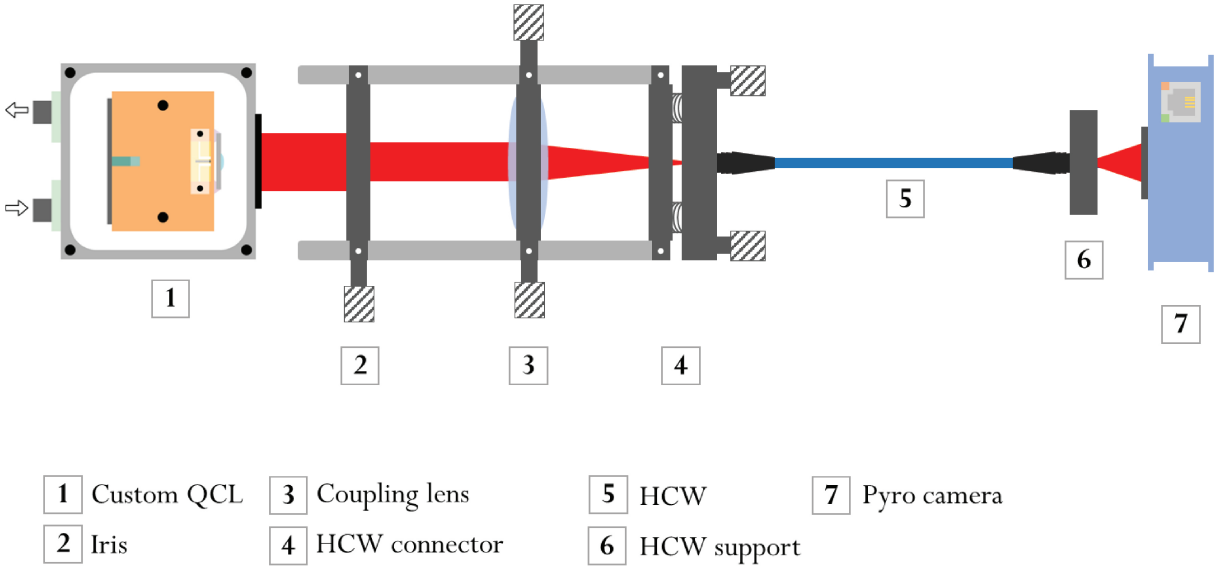


**Figure. 4.21:** Schematic of the experimental setup used to optically couple long-wavelength QCL with the HCW.

The experimental setup to evaluate the performance of HCW is depicted in a schematic form in Figure 4.21. We used 20 cm and 40 cm long HCWs with a cylindrical bore of diameter 500 $\mu$m equipped with SMA connector, produced by Guiding Photonics. The Ag/AgI coatings in HCWs were designed to provide low propagation losses in the mid-IR spectral range from 2 $\mu$m to 16 $\mu$m [49]. The HCWs were coupled with the $QCL_T$ emitting at 13.71 $\mu$m. Both the temperature and current is controlled by the QCL driver from Thorlabs (ITC40002).

To achieve precise adjustments of the optical coupling between the laser beam and the HCWs, we have designed a cage system. This system consists of an Iris, a mount that enables fine-tuning of the coupling lens (1" diameter) position in the x–y plane and a fiber connector holder to secure the HCW in place as shown in Figure 4.21. The cage system

also allows fine adjustments of the distance between the lens and the HCW entrance along the optical z–axis. The HCW connector facilitates precise changes to the HCW's entrance position relative to the focused laser spot. This optomechanical system allows for fine adjustments of both the azimuthal and polar angles of the waveguide entrance with respect to the direction of the laser beam.

The far-field mode profile of the laser beam as it exits the HCW was captured using an infrared pyro-camera (Pyrocam III, Ophir Spiricon, 160 × 160 pixels) with a spatial resolution of 80 $\mu$m. The pyro-camera was positioned at a distance of 2 cm from the HCW exit. Additionally, to measure the optical power of the laser beam exiting the HCW, the pyro-camera was replaced with an infrared power meter (Thorlabs PM100D equipped with Thermal Power Sensors S401C).

### 4.6.3 Results and Discussion

The beam profiles of the QCL were recorded using an infrared pyro-camera positioned close to the QCL exit, and is shown in Figure 4.22, Top Left. The laser exhibits a poor spatial quality, with a secondary spot on the left side and two lobes in the center. However, a Gaussian function was used to fit the data and calculate an average beam radius, $W = 1.6$ mm.

Based on the theoretical model, the optimal choice of the focal length of the coupling lens for this wavelength guaranteeing a ratio $w_0/a = 0.64$ is $f = 59.3$ mm. However, due to the unavailability of such lens we choose to work with lenses with $f = 75$ mm and $f = 50$ mm. Table 4.1 displays the measured radius, $W$, and the calculated beam waist radius, $w_0$, at the focal plane for each lens using Equation (4.14). The optimal coupling conditions were determined by maximizing the HCW output power [50].

The beam profiles exiting the 20 cm and 40 cm long HCWs for both coupling lenses are shown in Figure 4.22. It can be noticed that even with a low input beam quality, cylindrical HCWs with a core size as small as 500 $\mu$m enable single-mode output with a circular-symmetric beam profile.

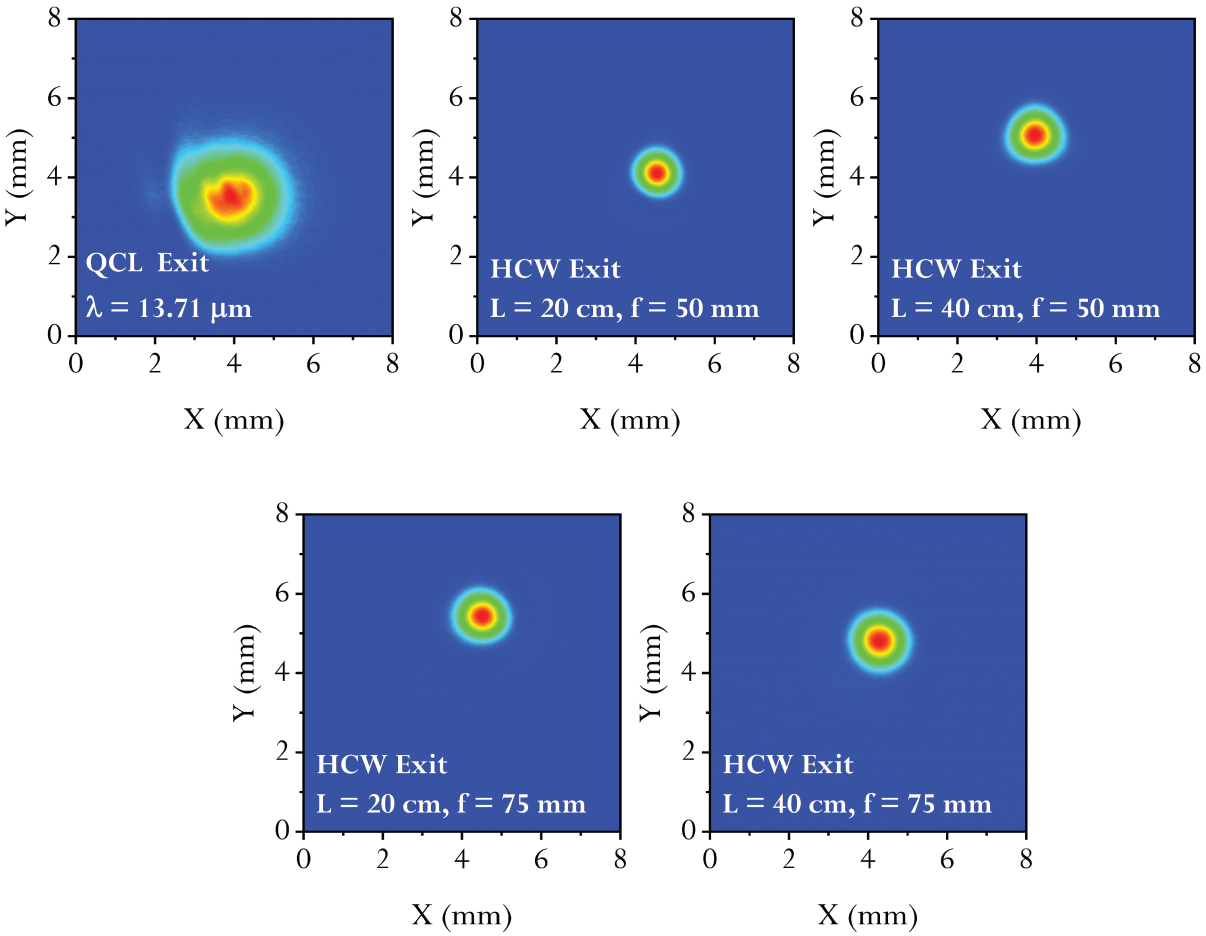


**Figure. 4.22:** Beam profiles of the $QCL_T$ emitting at 13.71 $\mu$m recorded by positioning the infrared pyro-camera (Top Left) close to the QCL exit, (Top Middle) and (Top Right) close to the exit of the HCW of length 20 cm and 40 cm coupled with lens of focal length 50 mm respectively, (Bottom Left) and (Bottom Right) close to the exit of the HCW of length 20 cm and 40 cm coupled with lens of focal length 75 mm respectively.

| $QCL_T$ $\lambda = 13.71$ $\mu$m | | |
|---|---|---|
| $f$ (mm) | 50 | 75 |
| $W$ (mm) | 1.6 | 1.6 |
| $w_0$ ($\mu$m) | 136 | 203 |

**Table 4.1:** Measured beam radius, $W$, and calculated beam waist radius, $w_0$, at the focal plane of the coupling lens having focal length $f$.

To evaluate the spatial quality of the HCW output beam in comparison to the input beam, we employed the parameter $M^2$. This parameter allows us to quantify the beam's angular divergence, with reference to a diffraction-limited Gaussian beam (where $M^2 = 1$). $M^2$ for the beam exiting QCL is defined as

$$M^2_{QCL} = \theta_{QCL}\frac{\pi w}{\lambda} \tag{4.19}$$

where, $\lambda/\pi w$ is the beam divergence angle of a diffraction limited Gaussian beam and $\theta_{QCL}$ is the divergence angle of the QCL beam. The $M^2$ of the beam exiting the HCW can be defined as the ratio of the divergence of the beam to the theoretical beam divergence.

$$M^2_{QCL} = \theta_{HCW}\frac{2\pi a}{u_{11}\lambda} \tag{4.20}$$

Where, $(u_{11}\lambda)/2\pi a$ is the theoretical divergence angle, $u_{11} = 2.4048$, calculated by assuming that only the $HE_{11}$ guided mode exits from the waveguide and $\theta_{HCW}$ is the divergence angle of the HCW exit beam. $\theta_{HCW}$ is extracted from the beam profiles obtained at various distances from HCW exit [51]. Table 4.2 shows the $M^2$ values for the beam at the QCL and HCWs exit, for both coupling lenses.

Table 4.2 clearly demonstrates a substantial improvement in the $M^2$ values of the beams exiting the HCWs. This improvement indicates a significant enhancement in the spatial quality of the beams compared to the input beam. However, it is important to understand the effect of HCW on the total loss experienced by the excited mode. This can be determined by measuring the optical power at the entrance ($I_{in}$) and exit ($I_{out}$) of the HCW. The loss can be defined as

$$Loss(dB) = 10 \cdot log_{10}\left(\frac{I_{in}}{I_{out}}\right) \tag{4.21}$$

Figure 4.23 shows the total loss measured for 20 cm and 40 cm long HCW having a

| QCL$_T$ $\lambda = 13.71$ $\mu$m | | | | |
|---|---|---|---|---|
| $w$(mm) | 1.6 | | | |
| $\theta_{QCL}(mrad)$ | 6.1 | | | |
| $M^2_{QCL}$ | 2.23 | | | |
| $f$(mm) | 50 | | 75 | |
| HCW length (cm) | 20 | 40 | 20 | 40 |
| $\theta_{HCW}$ (mrad) | 28.15 | 30 | 27.6 | 29.65 |
| $M^2_{HCW}$ | 1.34 | 1.42 | 1.31 | 1.41 |

**Table 4.2:** Divergence angles and $M^2$ values for both QCL and HCWs, coupled using lens of focal length $f$.

bore diameter of 500 $\mu$m, coupled to the QCL emitting at 13.71 $\mu$m using lens of focal lengths 50 mm and 75 mm. This figure also includes the theoretical losses, calculated by using Equation (4.18), as a function of the HCWs length assuming that only $HE_{11}$ mode propagates inside the waveguide.

We can see that the measured optical losses are higher than the calculated ones for both the lenses, with measured loss being much higher than the calculated ones for lens with $f = 75$ mm. Using the intercept of the fitted line we calculate the coupling efficiency for each case and is presented in Table 4.3. We see that the experimental coupling efficiency in case of lens with $f = 50$ mm is comparable to theoretical value where as for lens with $f = 75$ mm the efficiency is significantly lower. These discrepancies can be attributed to the poor spatial laser beam quality, which impacts: (i) the estimation of theoretical coupling efficiencies (calculated by assuming a perfect two-dimensional Gaussian profile for the laser beam) and the consequent propagation losses; and (ii) the beam waist sizes at the waveguide entrance.

The beam profiles shown in Figure 4.22, together with the comparison between the theoretical and experimental losses in Figure 4.23, the calculated $M^2$ values and coupling

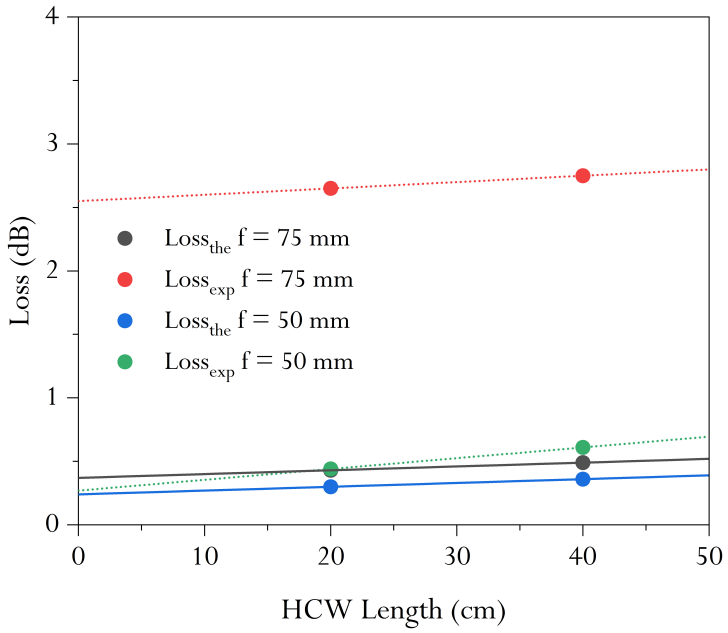


**Figure. 4.23:** Measured and theoretical total loss as a function of HCW length for coupling lens of different focal lengths.

| | QCL$_T$ $\lambda = 13.71$ $\mu$m | |
|---|---|---|
| | $f = 50$ mm | $f = 75$ mm |
| $\eta_{the}$ | 0.95 | 0.92 |
| $\eta_{exp}$ | 0.93 | 0.56 |

**Table 4.3:** Comparison of measured and calculated coupling efficiency.

efficiency values in Table 4.2 and Table 4.3, respectively lead to the conclusion that a single-mode Gaussian-like low-loss beam delivery can be obtained by optically coupling the low spatial quality 13.71 $\mu$m QCL with a HCW having core size of 500 $\mu$m and length of 20 cm using a lens with focal length f = 50 mm.

## 4.7 Conclusion

This chapter discusses the spectroscopic investigation of BTEX and Propane using QEPAS. Before delving into this investigation, the chapter provides an overview of various available sensing techniques and presents arguments for selecting QEPAS as the preferred approach. Subsequently, it introduces the fundamental principles of photoacoustic spectroscopy, followed by a comprehensive exploration of the theoretical foundations of QEPAS. This includes discussions on custom-tuned forks, spectrophone design, and different modulation techniques. Additionally, the chapter covers the development of the QEPAS sensing system, its optimization, calibration, and the determination of the minimum detection limit.

Toluene, Benzene, and Propane undergo calibration and characterization with respect to their most common interferents. The results reveal response linearity and detection limits of 113 ppb, 3 ppb, and 3 ppm, respectively, for an integration time of 10 seconds in pure nitrogen matrix conditions. Importantly, the study highlights a high degree of selectivity and robustness even in case of varying gaseous matrix compositions for each of the three analytes considered. This outcome is particularly significant given that it was achieved with a QEPAS sensing system—a technology known for its compactness and robustness, albeit relying on an indirect technique that could potentially be influenced by the gaseous matrix.

Finally, the chapter details the successful integration of a long-wavelength QCL with a HCW. A thorough investigation is conducted into the optimal coupling conditions, beam quality, and losses associated with this integration process. Findings indicate that achieving optimal coupling necessitates the use of a lens with a suitable focal length. Additionally, the study confirms that wavelengths as high as 13 $\mu$m can be efficiently guided through hollow-core waveguides with minimal loss. Moreover, the spatial quality of laser beams can be enhanced through HCW filtering, resulting in a Gaussian-like spatial beam profile at the output, even when the input laser beam quality is suboptimal. It is crucial to note that the extent of loss experienced depends on factors such as the length

of HCW, input beam quality, and the specific lens chosen for the coupling setup.

# Bibliography


[1] Mhanna Mhanna, Guangle Zhang, Noushad Kunnummal, and Aamir Farooq. Cavity-Enhanced Measurements of Benzene for Environmental Monitoring. *IEEE Sensors Journal*, 21:3849–3859, 2 2021. doi:10.1109/JSEN.2020.3026981.

[2] J. Cousin, W. Chen, D. Bigourd, M. Fourmentin, and S. Kassi. Telecom-grade fiber laser-based difference-frequency generation and ppb-level detection of benzene vapor in air around 3 $\mu m$. *Applied Physics B*, 97:919–929, 12 2009. doi:10.1007/s00340-009-3669-7.

[3] J. Waschull, B. Sumpf, Y. Heiner, and H.-D. Kronfeldt. Diode laser spectroscopy in the $\nu 14$ band of benzene. *Infrared Physics & Technology*, 37:193–198, 2 1996. doi:10.1016/1350-4495(95)00112-3.

[4] Diba Ayache, Wioletta Trzpil, Roman Rousseau, Kumar Kinjalk, Roland Teissier, Alexei N. Baranov, Michael Bahriz, and Aurore Vicet. Benzene sensing by Quartz Enhanced Photoacoustic Spectroscopy at 14.85 $\mu m$. *Optics Express*, 30:5531, 2 2022. doi:10.1364/OE.447197.

[5] Juho Karhu, Hadrien Philip, Alexei Baranov, Roland Teissier, and Tuomas Hieta. Sub-ppb detection of benzene using cantilever-enhanced photoacoustic spectroscopy with a long-wavelength infrared quantum cascade laser. *Optics Letters*, 45:5962, 11 2020. doi:10.1364/OL.405402.

[6] Angelo Sampaolo, Sebastian Csutak, Pietro Patimisco, Marilena Giglio, Giansergio Menduni, Vittorio Passaro, Frank K. Tittel, Max Deffenbaugh, and Vincenzo Spagnolo. Methane, ethane and propane detection using a compact quartz enhanced photoacoustic sensor and a single interband cascade laser. *Sensors and Actuators B: Chemical*, 282:952–960, 3 2019. doi:10.1016/j.snb.2018.11.132.

[7] Pan Luo, Jonathan Harrist, Giansergio Menduni, Rabah Mesdour, Nathan StMichel, and Angelo Sampaolo. Simultaneous Detection of Methane, Ethane, and Propane by QEPAS Sensors for On-Site Hydrocarbon Characterization and Production Monitoring. *ACS Omega*, 7:3395–3406, 2 2022. doi:10.1021/acsomega.1c05645.

[8] Angelo Sampaolo, Pietro Patimisco, Marilena Giglio, Andrea Zifarelli, Hongpeng Wu, Lei Dong, and Vincenzo Spagnolo. Quartz-enhanced photoacoustic spectroscopy for multi-gas detection: A review. *Analytica Chimica Acta*, 1202:338894, 4 2022. doi:10.1016/j.aca.2021.338894.

[9] G. Gassler, B. Reißenauer, and W. Hüttner. Tunable Diode Laser Spectra and Assignment of the 748 $cm^{-1}$ Band of Propane. *Zeitschrift für Naturforschung A*, 44:316–324, 4 1989. doi:10.1515/zna-1989-0412.

[10] Jane Hodgkinson and Ralph P Tatam. Optical gas sensing: a review. *Measurement Science and Technology*, 24:012004, 1 2013. doi:10.1088/0957-0233/24/1/012004.

[11] F.W. Karasek and R.E. Clement. *Gas Chromatography–Mass Spectrometry*. Elsevier, 1988. doi:10.1016/B978-0-444-42760-1.50007-0.

[12] Jürgen H Gross. *Mass Spectrometry*. Springer International Publishing, 2017. doi:10.1007/978-3-319-54398-7.

[13] D.O. Sparkman, Z.E. Penton, and F.G. Kitson. *Gas Chromatography and Mass Spectrometry: A Practical Guide*. Elsevier, 2011. doi:10.1016/B978-0-12-373628-4.00055-1.

[14] František Opekar and Karel Štulík. *Electrochemical Gas Sensors*. John Wiley & Sons, Ltd, 9 2009. doi:10.1002/9780470027318.a9074.

[15] Marc J. Madou and S. Roy Morrison. *Chemical Sensing with Solid State Devices*. Elsevier, 1989. doi:10.1016/C2009-0-22258-6.

[16] Andreas Mandelis, Constantinos Christofides, and James D. Winefordner. *Physics, Chemistry and Technology of Solid State Gas Sensor Devices*. Wiley, 1993.

[17] M Ivanovskaya, P Bogdanov, G Faglia, and G Sberveglieri. The features of thin film and ceramic sensors at the detection of CO and $NO_2$. *Sensors and Actuators B: Chemical*, 68:344–350, 8 2000. doi:10.1016/S0925-4005(00)00455-X.

[18] I. Eisele, T. Doll, and M. Burgmair. Low power gas detection with FET sensors. *Sensors and Actuators B: Chemical*, 78:19–25, 8 2001. doi:10.1016/S0925-4005(01)00786-9.

[19] Huankiat Seh, Takeo Hyodo, and Harry L. Tuller. Bulk acoustic wave resonator as a sensing platform for NOx at high temperatures. *Sensors and Actuators B: Chemical*, 108:547–552, 7 2005. doi:10.1016/j.snb.2004.11.083.

[20] G. Korotcenkov. Metal oxides for solid-state gas sensors: What determines our choice? *Materials Science and Engineering: B*, 139:1–23, 4 2007. doi:10.1016/j.mseb.2007.01.044.

[21] Andreas Schwaighofer, Markus Brandstetter, and Bernhard Lendl. Quantum cascade lasers (QCLs) in biomedical spectroscopy. *Chemical Society Reviews*, 46, 2017. doi:10.1039/C7CS00403F.

[22] I. Galli, S. Bartalini, S. Borri, P. Cancio, D. Mazzotti, P. De Natale, and G. Giusfredi. Molecular Gas Sensing Below Parts Per Trillion: Radiocarbon-Dioxide Optical Detection. *Physical Review Letters*, 107:270802, 12 2011. doi:10.1103/PhysRevLett.107.270802.

[23] Lei Dong, Frank K. Tittel, Chunguang Li, Nancy P. Sanchez, Hongpeng Wu, Chuantao Zheng, Yajun Yu, Angelo Sampaolo, and Robert J. Griffin. Compact TDLAS based sensor design using interband cascade lasers for mid-IR trace gas sensing. *Optics Express*, 24:A528, 3 2016. doi:10.1364/OE.24.00A528.

[24] Gianluca Gagliardi and Hans-Peter Loock, editors. *Cavity-Enhanced Spectroscopy and Sensing*, volume 179. Springer Berlin Heidelberg, 2014. doi:10.1007/978-3-642-40003-2.

[25] Angela Elia, Pietro Mario Lugarà, Cinzia Di Franco, and Vincenzo Spagnolo. Photoacoustic Techniques for Trace Gas Sensing Based on Semiconductor Laser Sources. *Sensors*, 9:9616–9628, 12 2009. doi:10.3390/s91209616.

[26] M. L Viengerov. New method of gas analysis based on tyndall-roentgen optoacoustic effect. *Dokl. Akad. Nauk. USSR*, 19:687, 1938.

[27] A. H. Pfund. Atmospheric contamination. *Science*, 90:326–327, 10 1939. doi:10.1126/science.90.2336.326.

[28] K. F Luft. On a new method of registering gas analysis using the absorption of ultra-red rays without spectral decomposition. *Z. tech. Phys*, 24:97–104, 1943.

[29] Allan Rosencwaig and Allen Gersho. Theory of the photoacoustic effect with solids. *Journal of Applied Physics*, 47:64–69, 1 1976. doi:10.1063/1.322296.

[30] F. G. C. Bijnen, J. Reuss, and F. J. M. Harren. Geometrical optimization of a longitudinal resonant photoacoustic cell for sensitive and fast trace gas detection. *Review of Scientific Instruments*, 67:2914–2923, 8 1996. doi:10.1063/1.1147072.

[31] A. Miklos and A. Lorincz. Windowless resonant acoustic chamber for laser-photoacoustic applications. *Applied Physics B Photophysics and Laser Chemistry*, 48:213–218, 3 1989. doi:10.1007/BF00694347.

[32] V. Zeninari, V.A. Kapitanov, D. Courtois, and Yu.N. Ponomarev. Design and characteristics of a differential Helmholtz resonant photoacoustic cell for infrared gas detection. *Infrared Physics & Technology*, 40:1–23, 2 1999. doi:10.1016/S1350-4495(98)00038-3.

[33] A. A. Kosterev, Yu. A. Bakhirkin, R. F. Curl, and F. K. Tittel. Quartz-enhanced photoacoustic spectroscopy. *Optics Letters*, 27:1902, 11 2002. doi:10.1364/OL.27.001902.

[34] G. Wysocki, A.A. Kosterev, and F.K. Tittel. Influence of molecular relaxation dynamics on quartz-enhanced photoacoustic detection of $CO_2$ at $\lambda = 2\ \mu m$. *Applied Physics B*, 85:301–306, 11 2006. doi:10.1007/s00340-006-2369-9.

[35] P. Patimisco, A. Sampaolo, L. Dong, M. Giglio, G. Scamarcio, F.K. Tittel, and V. Spagnolo. Analysis of the electro-elastic properties of custom quartz tuning forks for optoacoustic gas sensing. *Sensors and Actuators B: Chemical*, 227:539–546, 5 2016. doi:10.1016/j.snb.2015.12.096.

[36] Pietro Patimisco, Angelo Sampaolo, Marilena Giglio, Stefano dello Russo, Verena Mackowiak, Hubert Rossmadl, Alex Cable, Frank K. Tittel, and Vincenzo Spagnolo. Tuning forks with optimized geometries for quartz-enhanced photoacoustic spectroscopy. *Optics Express*, 27:1401, 1 2019. doi:10.1364/OE.27.001401.

[37] David S. Bomse, Alan C. Stanton, and Joel A. Silver. Frequency modulation and wavelength modulation spectroscopies: comparison of experimental methods using a lead-salt diode laser. *Applied Optics*, 31:718, 2 1992. doi:10.1364/AO.31.000718.

[38] M.D. Wojcik, M.C. Phillips, B.D. Cannon, and M.S. Taubman. Gas-phase photoacoustic sensor at 8.41 $\mu m$ using quartz tuning forks and amplitude-modulated quantum cascade lasers. *Applied Physics B*, 85:307–313, 11 2006. doi:10.1007/s00340-006-2394-8.

[39] K. Ruxton, A.L. Chakraborty, W. Johnstone, M. Lengden, G. Stewart, and K. Duffin. Tunable diode laser spectroscopy with wavelength modulation: Elimination of residual amplitude modulation in a phasor decomposition approach. *Sensors and Actuators B: Chemical*, 150:367–375, 9 2010. doi:10.1016/j.snb.2010.06.058.

[40] Anatoliy A. Kosterev, Frank K. Tittel, Dmitry V. Serebryakov, Alexander L. Malinovsky, and Igor V. Morozov. Applications of quartz tuning forks in spectroscopic gas sensing. *Review of Scientific Instruments*, 76:043105, 4 2005. doi:10.1063/1.1884196.

[41] Thorlabs. PT100. URL: https://www.thorlabs.com/drawings/9e38a79580c3fa3f-F2895ACB-FB0C-FAC0-8B708A640660C59A/TH100PT-SpecSheet.pdf.

[42] Thorlabs. Total Transmission of 5 mm Thick Uncoated Ge Window ($0.2 - 25\ \mu m$). URL: https://www.thorlabs.com/newgrouppage9.cfm?objectgroup_id=3980&gclid=CjwKCAjwvfmoBhAwEiwAG2tqzPVYZtwLMNdhxMOQ46kA_wMauMH3V1h2Ws_cdSCHxjv0SG7LYtVgAhoC0HcQAvD_BwE.

[43] James A. Harrington. *Infrared Fibers and Their Applications*, volume PM135. 2004.

[44] P. Patimisco, V. Spagnolo, M. S. Vitiello, A. Tredicucci, G. Scamarcio, C. M. Bledt, and J. A. Harrington. Coupling external cavity mid-IR quantum cascade lasers with low loss hollow metallic/dielectric waveguides. *Applied Physics B*, 108:255–260, 8 2012. doi:10.1007/s00340-012-4891-2.

[45] Rick K. Nubling. Launch conditions and mode coupling in hollow-glass waveguides. *Optical Engineering*, 37:2454, 9 1998. doi:10.1117/1.601768.

[46] P. Patimisco, L. Mihai, M. Giglio, A. Sampaolo, P. P. Calabrese, J. M. Kriesel, D. Sporea, G. Scamarcio, F. K. Tittel, and V. Spagnolo. Hollow-core waveguide for single-mode laser beam propagation in the spectral range of $3.7 - 7.3\ \mu m$. page 97552M, 2 2016. doi:10.1117/12.2209533.

[47] Angelo Sampaolo, Pietro Patimisco, Jason M. Kriesel, Frank K. Tittel, Gaetano Scamarcio, and Vincenzo Spagnolo. Single mode operation with mid-IR hollow fibers in the range $5.1 - 10.5\ \mu m$. *Optics Express*, 23:195, 1 2015. doi:10.1364/OE.23.000195.

[48] M. Miyagi and S. Kawakami. Design theory of dielectric-coated circular metallic waveguides for infrared transmission. *Journal of Lightwave Technology*, 2:116–126, 1984. doi:10.1109/JLT.1984.1073590.

[49] Guiding Photonics. Mid-infrared (mid-ir) fiber optic solutions. URL: https://guidingphotonics.com/mid-infrared-mid-ir-fiber-optic-solutions/#specifications.

[50] Pietro Patimisco, Angelo Sampaolo, Laura Mihai, Marilena Giglio, Jason Kriesel, Dan Sporea, Gaetano Scamarcio, Frank Tittel, and Vincenzo Spagnolo. Low-Loss Coupling of Quantum Cascade Lasers into Hollow-Core Waveguides with Single-Mode Output in the 3.7–7.6 $\mu m$ Spectral Range. *Sensors*, 16:533, 4 2016. doi:10.3390/s16040533.

[51] Pietro Patimisco, Vincenzo Spagnolo, Miriam Vitiello, Gaetano Scamarcio, Carlos Bledt, and James Harrington. Low-Loss Hollow Waveguide Fibers for Mid-Infrared Quantum Cascade Laser Sensing Applications. *Sensors*, 13:1329–1340, 1 2013. doi:10.3390/s130101329.

# Summary and Future Perspective

The necessity to detect BTEX (Benzene, Toluene, Ethylbenzene and Xylene) arises from their severe detrimental effects on human health and their potential as a biomarker for noninvasive disease detection. Additionally, Propane detection is essential to ensure safer industrial practices. However, detecting BTEX compounds and heavier alkanes like Propane poses distinctive challenges due to potential interferences, either among themselves or from other compounds. The coexistence of species sharing similar bonds often leads to spectral interferences, particularly in the spectral region where fundamental IR transitions occur, causing overlapping absorption bands or signal distortions. This spectral interference issue can be resolved at longer wavelengths (13–15 $\mu$m), where these molecules exhibit distinct and isolated absorption features. However, the lack of appropriate laser sources in this wavelength range has hindered the progress of sensor development in this area.

This thesis seeks to bridge the divide between the need for precise BTEX and Propane detection and the constraints posed by current technologies. By harnessing the potential of long wavelength QCLs, this research strives to open up fresh avenues in the field of detection, providing a means to surmount present obstacles and lay the foundation for more effective monitoring, enhanced air quality, and safer industrial practices.

We harnessed the potential of the InAs/AlSb-based material system to advance the development of long-wavelength QCLs emitting in 13–15 $\mu$m wavelength range. This achievement was made possible by exploiting the low electron effective mass of InAs, which in turn leads to significant intersubband gain. Our novel design approach aimed to enhance

the energy gap between the upper lasing level ($e_3$) and the immediately adjacent level ($e_4$). This adjustment was crucial in mitigating shunt-like leakage currents resulting from the direct recombination of thermally excited carriers from level $e_4$ to lower levels. However, due to the design limitations inherent in the vertical transition scheme typically utilized in InAs-based QCLs, we introduced a thin quantum well after the injection barrier. This modification gave the transition a slightly diagonal orientation and allowed to increase the separation between levels $e_3$ and $e_4$ to 65 meV. As a result, we successfully reduced the population of carriers in $e_4$ level by 38%.

In the middle of the injector region, we incorporated two highly doped quantum wells to counteract unintentional residual doping. Additionally, we increased the thickness of the injector barrier to minimize the direct tunneling of carriers from the injector level to $e_2$. This design configuration led to the development of QCLs with extremely low threshold emitting at a wavelength of 14.2 $\mu$m. Notably, these lasers exhibited a remarkable achievement, boasting a record-breaking low threshold current density of 0.6 kA/cm$^2$ at 300 K, surpassing previous results without the need for facet treatment. Furthermore, our design contributed to improved temperature stability, characterized by characteristic temperatures $T_0 = 180\ K$ and $T_1 = 280\ K$. These values exceeded those reported in earlier studies on long-wavelength InAs-based QCLs.

We addressed the challenges arising from hard-baked photoresist insulation typically used in fabrication of these devices, revealing that its polymeric nature leads to stability issues at elevated temperatures, causing temporary shifts in threshold current, emission wavelength, and optical power. This phenomenon is attributed to the alteration in the optical properties of the insulation provoked by slow relaxing residual stress buildup within the photoresist.

In response, we explored alternative insulation options, ultimately favoring silicon dioxide ($SiO_2$) based on COMSOL simulations. However, initial attempts with $SiO_2$ using the conventional PECVD technique encounter issues with increased threshold current density and decreased optical power due to oxygen-rich deposition environment. The oxygen-rich

environment caused rapid oxidation of exposed active zone leading to elevated leakage current. Therefore, we proposed a novel insulating technique involving Spin-on-Glass (SOG) for $SiO_2$ deposition, overcoming these challenges by carefully optimizing the thermal treatment parameters such as the annealing temperature and its duration. This achievement resolved all the issues related to photoresist insulation and enabled successful automatic wire bonding. The performance of the devices was similar to reference devices, we did not observe any degradation unlike in case of PECVD deposition.

Subsequently we developed single frequency DFB QCLs using the iterative process of simulation and fabrication aimed at optimizing crucial parameters, including grating period, grating etch depth, cladding thickness, and coupling. This optimization capitalized on the surface plasmon resonance triggered by the proximity of a metal contact layer deposited on the etched laser ridge, effectively suppressing multimode operation to achieve single longitudinal mode operation. We identified the optimal grating etch depth and cladding thickness as 0.65 $\mu$m and 2.5–3 $\mu$m, respectively, while the ideal coupling-device-length-product ranges between 2.8 and 5. The gratings were produced atop the laser ridges by employing electron beam lithography for precise control of the grating period. The resulting devices exhibit single frequency emission matching the absorption lines of BTEX and Propane, with optical power output in the milliwatt range in continuous wave operation. They had good spectral purity characterized by a side mode suppression ratio (SMSR) exceeding 20 dB. The relatively low threshold current density of the fabricated DFB lasers can be further reduced by using a QCL material with the gain maximum located closer to the targeted wavelengths.

Using these DFB QCLs, we performed spectroscopic investigation of BTEX and Propane through QEPAS. Out of the various techniques at our disposal, we have chosen QEPAS due to its numerous benefits, including immunity to external noise, wavelength independence, elimination of the need for optical detectors, and a compact footprint. The sensing system was calibrated and characterized for Toluene, Benzene, and Propane with regard to their most common interferents. The sensor exhibited linear and repeatable response with detection limits of 113 ppb, 3 ppb, and 3 ppm, respectively, for an integration time

of 10 seconds in pure nitrogen matrix conditions. Most importantly, even in the complex matrix involving other gas components from BTEX family as well as lighter alkanes, peak amplitude variations of the target analyte's QEPAS signals were demonstrated to be unperturbed within $1\sigma$ fluctuation of the most representative QEPAS feature of each target molecule. This proved a high level of selectivity and robustness of the developed sensing system. This achievement holds particular significance as it was accomplished using an indirect absorption technique that could potentially be influenced by the gaseous matrix.

Finally, we successful coupled the QCL emitting at 13.71 $\mu$m with a Hollow Core Waveguide (HCW). We investigated the optimal coupling conditions, beam quality, and losses associated with this integration process. We verified how the choice of the focal length is of crucial importance to achieve optimal coupling conditions. Additionally, the study confirms that wavelengths as high as 13.71 $\mu$m can be efficiently transmitted through HCW with minimal loss. The loss depends on factors such as the waveguide length, input beam quality, and the specific lens chosen for coupling. Moreover, the spatial quality of laser beams was enhanced through HCW filtering, resulting in a Gaussian-like spatial beam profile at the output, even when the input laser beam power distribution was not perfectly Gaussian.

In this thesis several interesting results have been achieved. However, there is still wide margin for improvement. In the proposed design we see that the operating voltage is quite high because of the large injector miniband, helpful to reduce the thermal backfilling, which penalized the CW operation. It is necessary to explore alternative approaches for solving this problem. For instance, we can make the structure to be less sensitive to the backfilling by further increasing the design diagonality. Additional efforts will be required in this case to optimize the profile of the electron wavefunctions in order to decrease their overlap with interfaces and thus to reduce the interface recombination that kills the QCL performance. Novel designs with lower barriers in the active quantum wells can also be considered to moderate the effect of interface scattering.

We see a direct proportionality between the QEPAS signal and the optical power of the

laser. Therefore, in order to enhance sensitivity, it becomes necessary to increase the optical power. Besides the QCL design improvements, this can be achieved by employing an Anti-Reflection (AR) coating on the output facet, which can allow us to eliminate the problem of the phase of the DFB mode that is usually random in the cleaved lasers and to reliably obtain the maximum possible output power. High-Reflection (HR) coating on the opposite facet can also be useful. However, as the thickness of optical coatings scales with the wavelength this task is not trivial in the case of long-wavelength QCLs. Another parameter which we can play with is waveguide geometry, we can perhaps employ tapered waveguide to increase the active volume of the device, which would increase the output power.

Additionally, exploring the enhanced spatial characteristics of the beam through HCW is an interesting possibility in QEPAS. This improved beam quality is expected to improve SNR, resulting in better sensitivity. As a direct absorption based technique still employing tuning forks as sensitive element, Light Induced Thermo-Elastic Spectroscopy (LITES) can be also considered as a serious candidate as reliable sensors for real time and in situ measurements.

I hope that my work will contribute to further development of laser spectroscopy in the long-wavelength mid-infrared spectral range and its results will be useful for the scientists working in this field.

# List of Publications

## Journals

1. **Kinjalk, K.**, A. Gilbert, A. Remis, Z. Loghmari, L. Cerutti, G. Patriarche, M. Bahriz, et al. 2022. 'Quantum Cascade Lasers Monolithically Integrated on Germanium'. Optics Express 30 (25): 45259. doi:10.1364/OE.472473

2. **Kinjalk, Kumar**, Daniel Andres Díaz-Thomas, Zeineb Loghmari, Michael Bahriz, Roland Teissier, and Alexei N. Baranov. 2022. 'InAs-Based Quantum Cascade Lasers with Extremely Low Threshold'. Photonics 9 (10): 747. doi:10.3390/photonics9100747

3. Ayache, Diba, Wioletta Trzpil, Roman Rousseau, **Kumar Kinjalk**, Roland Teissier, Alexei N. Baranov, Michael Bahriz, and Aurore Vicet. 2022. 'Benzene Sensing by Quartz Enhanced Photoacoustic Spectroscopy at 14.85 $\mu$m'. Optics Express 30 (4): 5531. doi:10.1364/OE.447197

4. **Kumar Kinjalk**, Francesco Paciolla, Bo Sun, Andrea Zifarelli, Giansergio Menduni, Marilena Giglio, Hongpeng Wu, Lei Dong, Diba Ayache, Davide Pinto, Aurore Vicet, Alexei Baranov, Pietro Patimisco, Angelo Sampaolo and Vincenzo Spagnolo. 2023. 'Highly Selective and Sensitive Detection of Volatile Organic Compounds using Long Wavelength InAs-based QCLs through QEPAS'. Applied Physics Review, Submitted

## Communications at Conferences

1. **Kinjalk, Kumar**, Giansergio Menduni, Andrea Zifarelli, Marilena Giglio, Roland Teissier, Alexei N. Baranov, Angelo Sampaolo. 'Highly Selective Toluene Detection using Quartz Enhanced Photoacoustic Spectroscopy at $\lambda = 13.71\ \mu m$. Mid-Infrared Optoelectronics: Materials and Devices (MIOMD 2023) and Conference on photonics for advanced spectroscopy and sensing (C-PASS 2023) (Oral Presentations)

2. **Kinjalk, Kumar**, Audrey Gilbert, Andres Remis, Zeineb Loghmari, Laurent Cerutti, Michael Bahriz, Roland Teissier, Alexei Baranov, Jean-Baptiste Rodriguez, and Eric Tournié. 2023. 'Monolithic Integration of InAs-Based Quantum Cascade Lasers on Germanium'. Silicon Photonics XVIII, SPIE Photonics West. doi:10.1117/12.2649886 (Oral Presentation)

3. **Kinjalk, Kumar**, Ariane Meguekam, Daniel Andres Diaz-Thomas, Zeineb Loghmari, Michael Bahriz, Roland Teissier, and Alexei N. Baranov. 2023. 'Spin-on-Glass in the Technology of InAs-Based Quantum Cascade Lasers'. Novel In-Plane Semiconductor Lasers XXII, SPIE Photonics West.
doi:10.1117/12.2647567 (Poster Presentation)

4. Pinto, Davide, **Kumar Kinjalk**, Ariane Meguekam, Michael Bahriz, and Alexei N. Baranov. 2023. 'Tapered Quantum Cascade Lasers in the Long-Wavelength Mid-Infrared Region'. Quantum Sensing and Nano Electronics and Photonics XIX, SPIE Photonics West doi:10.1117/12.2649669

5. **Kinjalk, K.**, D. Andres Diaz-Thomas, A. Meguekam, Z. Loghmari, M. Bahriz, R. Teissier, and A.N. Baranov. 2022. 'Very Low Threshold InAs-Based Quantum Cascade Lasers'. In 2022 International Conference Laser Optics (ICLO), 1–1. IEEE. doi:10.1109/ICLO54117.2022.9840243 (Oral Presentation)

6. Paciolla, Francesco, Andrea Zifarelli, Vincenzo Spagnolo, Pietro Patimisco, Angelo Sampaolo, Marilena Giglio, **Kumar Kinjalk**, Roland Teissier, and Alexei N. Baranov. 2022. 'Benzene and Toluene Detection with a Quartz-Enhanced Photoacoustic Sensor'. In 2022 IEEE International Symposium on Medical Measurements and Applications (MeMeA), 1–2. IEEE. doi:10.1109/MeMeA54994.2022.9856434

7. **Kinjalk, K.**, D. Andres Diaz-Thomas, A. Meguekam, Z. Loghmari, M. Bahriz, R. Teissier, and A.N. Baranov. 2021. 'InAs-based quantum cascade lasers for spectroscopy of methane'. In 2021, European Semiconductor Laser Workshop 2021 (Oral Presentation)

## Abstract

Sensitive and selective sensing of BTEX and Propane is of great interest for environmental, biomedical, and petrochemical applications. However, detecting these compounds poses unique challenges due to potential interferences, either among themselves or from other compounds. This issue can be resolved by using laser spectroscopy in the long-wavelength mid-infrared spectral region (13–15 $\mu$m), where they exhibit highly discriminating absorption features. Yet, this wavelength range is almost unexplored due to the lack of suitable sources. This thesis aims to bridge this gap by developing high-performing long-wavelength QCLs and leveraging QEPAS for ultra-sensitive and selective detection.

A novel design is proposed to improve the performance of long-wavelength InAs-based QCLs, which allowed us to demonstrate a record-breaking low threshold current density of 0.6 kA/cm$^2$ at 300 K. Additionally, a novel insulation technique using SOG is also proposed to improve device stability issues provoked by the alteration of properties of photoresist insulation (typically used for InAs-based QCLs) at elevated temperatures. Subsequently, single-frequency DFB QCLs with SMSR $>$ 20 dB and optical output power in the mW range operating in the continuous wave regime are developed, targeting the absorption lines of these gasses. Using these DFBs, a sensing system based on QEPAS is developed, calibrated, and characterized for Toluene, Benzene, and Propane detection. Exceptionally low detection limits of 113 ppb, 3 ppb, and 3 ppm are achieved in a pure nitrogen matrix over a 10-second integration time. The system maintains selectivity and robustness, even in complex gas mixtures. Finally, a 13.71 $\mu$m QCL is successfully coupled with a HCW, where optimal coupling conditions, beam quality, and loss are explored. The study confirms the efficient transmission of such wavelength through HCW with minimal loss and improved spatial beam quality.

## Résumé

La détection sensible et sélective des BTEX et du propane présente un grand intérêt pour les applications environnementales, biomédicales et pétrochimiques. Cependant, la détection de ces composés est compliquée à cause des interférences potentielles, soit entre eux, soit avec d'autres composés. Ce problème peut être résolu par la spectroscopie laser à de grandes longueurs d'onde (13–15 $\mu$m), où ils présentent des caractéristiques d'absorption très discriminantes. Pourtant, cette gamme spectrale est pratiquement inexplorée en raison du manque de sources appropriées. Cette thèse vise à combler cette lacune en développant des LCQ émettant à des grandes longueurs d'onde élevées et en exploitant le QEPAS pour une détection ultra-sensible et sélective.

Un nouveau design est proposé pour améliorer les performances des LCQ à base d'InAs de grande longueurs d'onde. Cette conception nous a permis de démontrer une densité de courant de seuil record de 0,6 kA/cm$^2$ à 300 K. En outre, une nouvelle technique d'isolation utilisant le SOG est également proposée pour améliorer les problèmes de stabilité du dispositif provoqués par l'altération des propriétés de l'isolation de la résine photosensible (généralement utilisée pour les LCQ à base d'InAs) à des températures élevées. Par la suite, des LCQ DFB monomodes avec un SMSR $>$ 20 dB et une puissance de sortie optique de l'ordre du mW ont été développé, ciblant les lignes d'absorption de ces gaz. En utilisant ces lasers, un système de détection basé sur le QEPAS a été développé, calibré et caractérisé pour la détection du toluène, du benzène et du propane. Des limites de détection exceptionnellement basses de 113 ppb, 3 ppb et 3 ppm sont atteintes dans une matrice d'azote pur sur un temps d'intégration de 10 secondes. Le système conserve sa sélectivité et sa robustesse, même dans des mélanges de gaz complexes. Enfin, une LCQ de 13,71 $\mu$m est couplée avec succès à un HCW, où les conditions optimales de couplage, la qualité du faisceau et la perte sont explorées. L'étude confirme la transmission efficace d'une telle longueur d'onde à travers le HCW avec une perte minimale et une qualité de faisceau spatial améliorée.